US-CE-C PROPERTY OF THE
UNITED STATES GOVERNMENT

DREDGING RESEARCH PROGRAM

TECHNICAL REPORT DRP-92-6

ADCIRC: AN ADVANCED THREE-DIMENSIONAL CIRCULATION MODEL FOR SHELVES, COASTS, AND ESTUARIES

Report 3
DEVELOPMENT OF A TIDAL CONSTITUENT DATABASE FOR THE WESTERN NORTH ATLANTIC AND GULF OF MEXICO

by

J. J. Westerink

Department of Civil Engineering and Geological Sciences
University of Notre Dame
Notre Dame, Indiana   46556

R. A. Luettich, Jr.

University of North Carolina at Chapel Hill
Institute of Marine Sciences
Morehead City, North Carolina   28557

Norman Scheffner

Coastal Engineering Research Center
DEPARTMENT OF THE ARMY
Waterways Experiment Station, Corps of Engineers
3909 Halls Ferry Road, Vicksburg, Mississippi   39180-6199

June 1993

Report 3 of a Series

Approved For Public Release; Distribution Is Unlimited
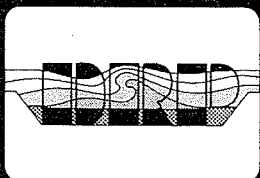
The Dredging Research Program (DRP) is a seven-year program of the US Army Corps of Engineers. DRP research is managed in these five technical areas:

Area 1 - Analysis of Dredged Material Placed in Open Water

Area 2 - Material Properties Related to Navigation and Dredging

Area 3 - Dredge Plant Equipment and Systems Processes

Area 4 - Vessel Positioning, Survey Controls, and Dredge Monitoring Systems

Area 5 - Management of Dredging Projects

PRINTED ON RECYCLED PAPER

Dredging Research Program

Technical Report DRP-92-6
June 1993

ADCIRC: An Advanced Three-Dimensional Circulation Model for Shelves, Coasts, and Estuaries

Report 3
Development of a Tidal Constituent Database for the Western North Atlantic and Gulf of Mexico

by   J. J. Westerink

Department of Civil Engineering and Geological Sciences
University of Notre Dame
Notre Dame, Indiana   46556

R. A. Luettich, Jr.
University of North Carolina at Chapel Hill
Institute of Marine Sciences
Morehead City, North Carolina   28557

Norman Scheffner
Coastal Engineering Research Center

U.S. Army Corps of Engineers
Waterways Experiment Station
3909 Halls Ferry Road, Vicksburg, MS   39180-6199
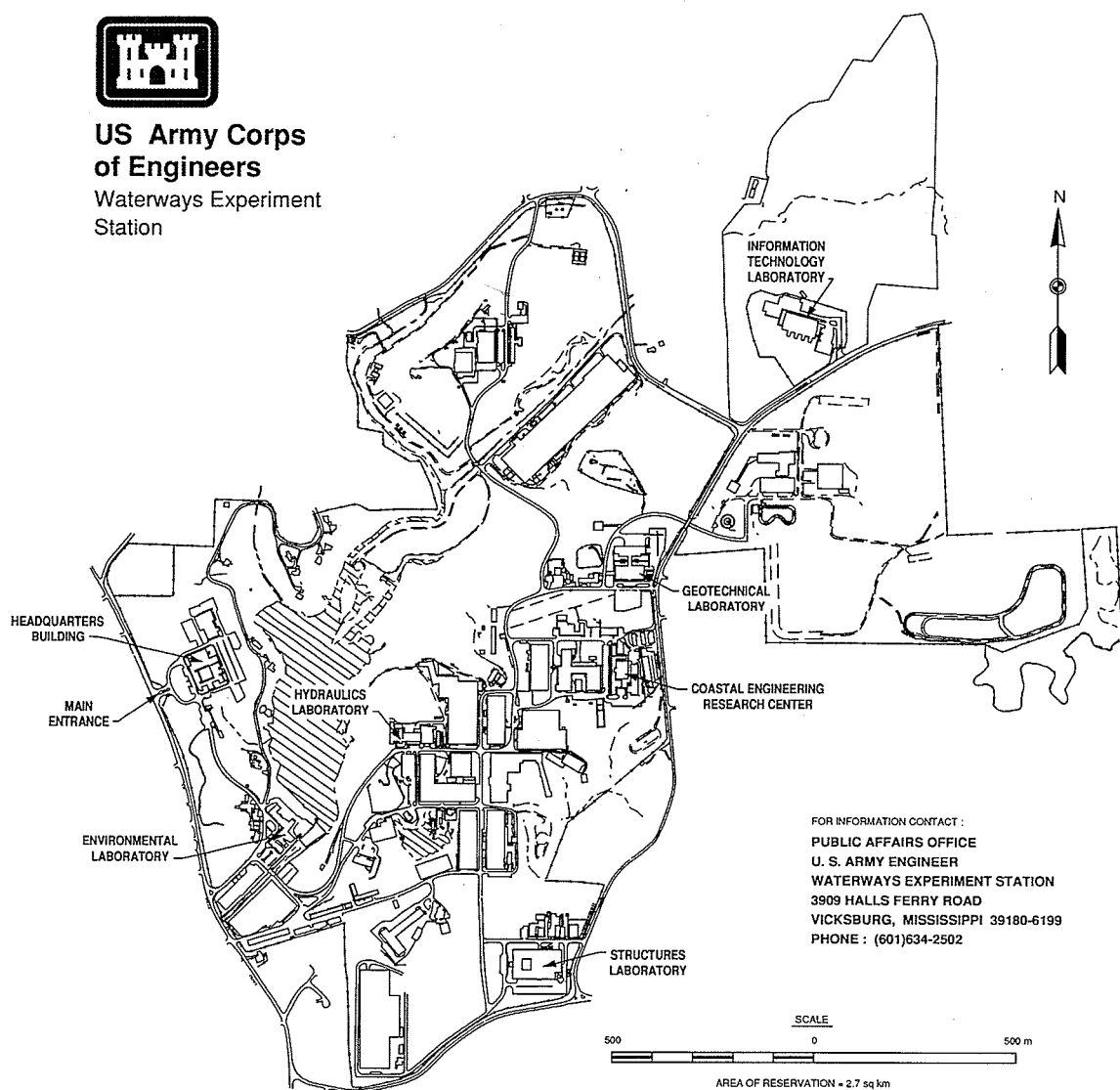
Report 3 of a series

**US Army Corps
of Engineers**
Waterways Experiment
Station

Dredging Research Program
Report Summary

US Army Corps
of Engineers
Waterways Experiment
Station

ADCIRC: An Advanced Three-Dimensional Circulation Model for Shelves, Coasts, and Estuaries; Report 3 , Development of a Tidal Constituent Database for the Western North Atlantic and Gulf of Mexico (TR DRP-92-6)

ISSUE: Dredged material disposal sites located in open water are classified as either dispersive or nondispersive depending on whether local water velocities are strong enough to erode and transport dredged material from the deposited mound. The Corps needs the capability to predict stability of the mound and long-term migration patterns of eroded material to (1) identify acceptable disposal-site locations, and (2) provide a quantitative approach for gaining site-designation approval.

RESEARCH: The overall work-unit objective is development of a systematic approach for predicting the dispersion characteristics of a specific open-water disposal site. This objective includes the following goals:

● Identify realistic wind-, wave-, tide-, and storm-generated velocity boundary conditions.

● Develop numerical models capable of simulating dispersion characteristics of dredged-material mounds for periods of time in excess of one year.

● Provide site-designation technology to field engineers as a tool in site identification and designation.

This study reports the tidal-constituent database developed for locations along the East and Gulf coast of the United States, which is a part of the first two goals listed above.

SUMMARY: The numerical model ADCIRC-2DDI (a two-dimensional depth-integrated finite-element-based hydrodynamic circulation code) was applied to the western North Atlantic, Gulf of Mexico, and Carribbean Sea to develop a tidal constituent database. The report presents initial results from a tidal model of the western North Atlantic (WNAT) that encompasses the coastal ocean as well as the deep ocean. The domain for the model includes the entire area of interest.

AVAILABILITY OF REPORT: The report is available through the Interlibrary Loan Service from the U.S. Army Engineer Waterways Experiment Station (WES) Library, telephone number (601)634-2355. National Technical Information Service (NTIS) numbers may be requested from WES librarians.

To purchase a copy of the report, call NTIS at (703)487-4780.

About the Authors: Dr. J. J. Westerink is a member of the Department of Civil Engineering and Geological Sciences of the University of Notre Dame; Dr. R. A. Luettich, Jr., the Institute of Marine Sciences, University of North Carolina at Chapel Hill; and Dr. Norman W. Scheffner, the Coastal Engineering Research Center, WES. For further information about the DRP, contact Mr. E. Clark McNair, Jr., Manager, DRP, at (601)634-2070.
Point of Contact: Dr. Scheffner, Principal Investigator for the work unit.

Contents

List of Figures

astronomical tidal constituents used in the boundary and interior domain forcing functions

Preface

The research described in this report was authorized and funded under Work Unit 32466, "Numerical Simulation Techniques for Evaluating Long-Term Fate and Stability of Dredged Material Disposed in Open Water," of Technical Area 1 (TA1), "Analysis of Dredged Material Placed in Open Water," of the Dredging Research Program (DRP). The DRP is sponsored by Headquarters, U.S. Army Corps of Engineers (HQUSACE). Administrative responsibility is assigned to the U.S. Army Engineer Waterways Experiment Station (WES) Coastal Engineering Research Center (CERC), Dr. James R. Houston, Director, and Mr. Charles C. Calhoun, Jr., Assistant Director.

Mr. John H. Lockhart, Jr., HQUSACE, was DRP TA1 Technical Monitor. Mr. E. Clark McNair, Jr., was DRP Program Manager (PM), and Dr. Lyndell Z. Hales was assistant PM. Dr. Nicholas C. Kraus, Senior Research Scientist, CERC, was the TA1 Technical Area Manager, and Dr. Norman W. Scheffner, Coastal Processes Branch (CPB), Research Division (RD), CERC, was the Principal Investigator for the work unit. Dr. Scheffner worked under the administrative supervision of Mr. H. Lee Butler, Chief, RD, CERC, and Mr. Bruce A. Ebersole, Chief, CPB, RD, CERC.

This study was performed and the report was prepared over the period 1 September 1990 through 15 December 1992. The numerical modeling goals, concepts, and methodology were developed by Dr. Scheffner and two DRP contractors: Dr. Joannes J. Westerink of the University of Notre Dame and Dr. Richard A. Luettich, Jr., of the University of North Carolina at Chapel Hill. Development and implementation of the model were completed by Drs. Westerink and Luettich.

At the time of publication of this report, Director of WES was Dr. Robert W. Whalin. Commander was COL Leonard G. Hassell, EN.

Additional information on this report can be obtained from Mr. E. Clark McNair, Jr., DRP Program Manager, at (601) 634-2070 or Dr. Norman W. Scheffner, Principal Investigator, at (601) 634-3220.

Summary

This report describes the application of model ADCIRC-2DDI, a two-dimensional, depth-integrated, finite-element-based hydrodynamic circulation code, to the western North Atlantic, Gulf of Mexico, and Caribbean Sea in order to develop a tidal constituent database. Issues that are emphasized in the development of the Western North Atlantic Tidal (WNAT) model include definition of hydrodynamically simple open ocean boundaries; the use of large domains; the importance of a high degree of grid resolution in coastal regions; and the use of finite element meshes with highly varying nodal densities in order to minimize the size of the discrete problem. The development of an optimal graded finite-element mesh is based on regular and graded grid convergence studies using an M_2 tidal forcing function on the boundary and within the domain.

The optimal graded mesh is then forced for eight diurnal and semidiurnal astronomical tidal constituents (K_1, O_1, P_1, Q_1, M_2, S_2, N_2, and K_2) on the open ocean boundary by coupling to Schwiderski's (1979; 1981 a-g) global model results as well as within the interior domain using a tidal potential forcing function. Structures of the various tides are examined and results are compared to field data at 77 stations.

1 Introduction

There has been a recent trend in coastal ocean tidal modeling towards using increasingly larger computational domains, which extend up to or beyond the continental shelf break and slope. For example, Flather (1987), Gerritsen and Bijlsma (1988), and Vincent and Le Provost (1988) have all developed tidal and/or storm surge models of a large portion of the eastern North Atlantic. These studies indicate that accurate tidal predictions can be conveniently obtained using large computational domains. This report presents initial results from a tidal model of the western North Atlantic, which encompasses the coastal ocean as well as the deep ocean. Key features of the Western North Atlantic Tidal (WNAT) model are the definition of hydrodynamically simple open ocean boundaries to facilitate the specification of boundary conditions, the use of a high degree of selective grid refinement to resolve the flow physics on a localized basis, and the coupling of the coastal ocean with a global tidal model.

The domain for the WNAT model encompasses the Western North Atlantic Ocean, the Caribbean Sea, and the Gulf of Mexico. The WNAT model has an eastern open ocean boundary that lies along the 60° W meridian and is situated almost entirely in the deep ocean. The location of this open ocean boundary was specifically selected to simplify the difficult task of specifying an accurate set of boundary conditions for a coastal ocean tidal model. The WNAT model open ocean boundary offers a variety of significant advantages. First, the boundary is geometrically simple and includes no discontinuities or corners. Second, the boundary lies almost entirely in the deep ocean where tides vary gradually. This avoids the difficulty of specifying complex and highly variable cross shelf boundary conditions over most of the open ocean boundary. Furthermore, this open ocean boundary is ideally suited for coupling with global tidal models, which should be most accurate in the deep ocean. Third, nonlinear tidal constituents will not be significant on this open ocean boundary since they are generated on the continental shelf and are largely trapped on the shelf due to the out-of-phase reflective character of the continental slope.

The size of the resulting computational domain of the WNAT model exceeds 8×10^6 km^2 and is therefore very large in terms of coastal ocean tidal models. It is clear that uniformly discretizing the entire domain with the resolution required in regions of rapidly varying flow would substantially

increase the size of the discrete problem. In fact, in deep ocean regions, which account for more than three quarters of the domain, a relatively coarse discretization should resolve all flow features of interest. However, on the continental shelf, the propagation speed and wavelength of tidal waves decrease with decreasing bathymetric depth and therefore require an increasingly finer discretization. Flow also varies much more quickly in regions of rapidly varying topography, such as in the vicinity of the continental shelf break and the continental slope, as well as near the coastal boundary. Therefore, these regions should require a greater resolution than deep ocean regions.

In order to realize tidal computations on grids with a very high degree of grid flexibility, a Generalized Wave Continuity Equation (GWCE)-based finite element (FE) shallow water model (Lynch and Gray 1979, Kinnmark 1984, Luettich et al. 1992) has been implemented. GWCE-based FE solutions to the shallow water equations have been demonstrated to lead to highly accurate and robust hydrodynamic circulation predictions within the coastal and deep oceans (Lynch 1983, Le Provost and Vincent 1986, Foreman 1988, Vincent and Le Provost 1988, Walters 1988, Gray 1989, Walters and Werner 1989, Werner and Lynch 1989, Westerink et al. 1992).

In this report, resolution requirements for the WNAT model are systematically examined using the entire model domain. It is vital to establish the level of convergence achieved with the grid resolution used in a computational domain (Le Provost and Vincent 1986; Dietrich, Roache, and Marietta 1990). Computations for a sequence of regularly discretized grids, ranging from a very coarse (1.6° x 1.6°) mesh to a very fine (6' x 6' to 12' x 12') mesh are presented. These computations are compared to a sequence of irregularly graded grids with resolutions varying between 1.6° and 5' within each mesh. In the development of an optimal graded grid, the resolution requirements in regions of rapidly varying topography, as well as the resolution of the coastal boundary, have been carefully considered. The final optimal graded grid has a tidal response that is comparable to that of the finest regular grid in most regions. The WNAT model, using the optimal graded grid, is then coupled with Schwiderski's (1979, 1980, 1981a-g) global model. Computed cotidal charts are presented for eight astronomical constituents and comparisons are made between the computed results and field data at 77 stations within the WNAT domain.

2 Governing Equations and Numerical Discretization

The computations described in this report were performed using ADCIRC-2DDI, the depth-integrated option of a system of two- and three-dimensional hydrodynamic codes named ADCIRC (Luettich, Westerink, and Scheffner 1992). ADCIRC-2DDI uses the depth-integrated equations of mass and momentum conservation, subject to the incompressibility, Boussinesq, and hydrostatic pressure approximations. Using the standard quadratic parameterization for bottom stress and neglecting baroclinic terms and lateral diffusion/dispersion effects leads to the following set of conservation statements in primitive non-conservative form expressed in a spherical coordinate system (Flather 1988, Kolar et al. 1992):

$$
\frac{\partial \zeta}{\partial t} + \frac{1}{R \cos \varphi} \left[\frac{\partial UH}{\partial \lambda} + \frac{\partial (VH \cos \varphi)}{\partial \varphi} \right] = 0 \tag{1}
$$

$$
\frac{\partial U}{\partial t} + \frac{1}{R \cos \varphi} U \frac{\partial U}{\partial \lambda} + \frac{1}{R} V \frac{\partial U}{\partial \varphi} - \left(\frac{\tan \varphi}{R} U + f \right) V =
$$
$$
- \frac{1}{R \cos \varphi} \frac{\partial}{\partial \lambda} \left[\frac{p_s}{\rho_0} + g (\zeta - \eta) \right] + \frac{\tau_{s\lambda}}{\rho_0 H} + -\tau_* U \tag{2}
$$

$$
\frac{\partial V}{\partial t} + \frac{1}{R \cos \varphi} U \frac{\partial V}{\partial \lambda} + \frac{1}{R} V \frac{\partial V}{\partial \varphi} + \left(\frac{\tan \varphi}{R} U + f \right) U =
$$
$$
- \frac{1}{R} \frac{\partial}{\partial \varphi} \left[\frac{p_s}{\rho_0} + g (\zeta - \eta) \right] + \frac{\tau_{s\varphi}}{\rho_0 H} - \tau_* V \tag{3}
$$

where

t = time

λ, φ = degrees longitude (east of Greenwich positive) and degrees latitude (north of the equator positive)

ζ = free surface elevation relative to the geoid

U, V = depth-averaged horizontal velocities

R = radius of the earth

$H = \zeta + h$ = total water column

h = bathymetric depth relative to the geoid

$f = 2\Omega \sin \varphi$ = Coriolis parameter

Ω = angular speed of the earth

p_s = atmospheric pressure at the free surface

g = acceleration due to gravity

η = effective Newtonian equilibrium tide potential

ρ_0 = reference density of water

$\tau_{s\lambda}, \tau_{s\varphi}$ = applied free surface stress

$$\tau_* = C_f \frac{\left(U^2 + V^2\right)^{1/2}}{H}$$

C_f = bottom friction coefficient

A practical expression for the effective Newtonian equilibrium tide potential is given by Reid (1990) as:

$$\eta (\lambda, \varphi, t) = \sum_{n,j} \alpha_{jn} C_{jn} f_{jn} (t_0) L_j (\varphi) \cos \left[\frac{2\pi (t - t_0)}{T_{jn} + j\lambda + \nu_{jn} (t_0)} \right] \qquad (4)$$

where

C_{jn} = constant characterizing the amplitude of tidal constituent n of species j

α_{jn} = effective earth elasticity factor for tidal constituent n of species j

f_{jn} = time-dependent nodal factor

ν_{jn} = time-dependent astronomical argument

$j = 0,1,2$ = tidal species ($j = 0$, declinational; $j = 1$, diurnal; $j = 2$, semidiurnal)

$$L_0 = 3 \sin^2 \varphi - 1$$

$$L_1 = \sin (2 \varphi)$$

$$L_2 = \cos^2 (\varphi)$$

λ, φ = degrees longitude and latitude, respectively

t_0 = reference time

T_{jn} = period of constituent n of species j

Values for C_{jn} are presented by Reid (1990). The value for the effective earth elasticity factor is typically taken as 0.69 for all tidal constituents (Schwiderski 1980, Hendershott 1981) although its value has been shown to be slightly constituent dependent (Wahr 1981, Woodworth 1990).

To facilitate an FE solution to Equations 1-3, these equations are mapped from spherical form into a rectilinear coordinate system using a Carte Parallelogrammatique (CP) projection (Pearson 1990):

$$x' = R (\lambda - \lambda_0) \cos \varphi_0 \tag{5}$$

$$y' = R \varphi \tag{6}$$

where λ_0, φ_0 = center point of the projection. Applying the CP projection to Equations 1-3 gives the shallow-water equations in primitive non-conservative form expressed in the CP coordinate system:

$$\frac{\partial \zeta}{\partial t} + \frac{\cos \varphi_0}{\cos \varphi} \frac{\partial (UH)}{\partial x'} + \frac{1}{\cos \varphi} \frac{\partial (VH \cos \varphi)}{\partial y'} = 0 \tag{7}$$

$$\frac{\partial U}{\partial t} + \frac{\cos \varphi_0}{\cos \varphi} U \frac{\partial U}{\partial x'} + V \frac{\partial U}{\partial y'} - \left(\frac{\tan \varphi}{R} U + f \right) V \tag{8}$$

$$= -\frac{\cos \varphi_0}{\cos \varphi} \frac{\partial}{\partial x'} \left[\frac{p_s}{\rho_0} + g (\zeta - \eta) \right] + \frac{\tau_{s\lambda}}{\rho_0 H} - \tau_* U$$

$$\frac{\partial V}{\partial t} + \frac{\cos\varphi_0}{\cos\varphi} U \frac{\partial V}{\partial x'} + V \frac{\partial V}{\partial y'} + \left(\frac{\tan\varphi}{R} U + f \right) U$$

$$= -\frac{\partial}{\partial y'} \left[\frac{p_s}{\rho_0} + g(\zeta - \eta) \right] + \frac{\tau_{s\varphi}}{\rho_0 H} - \tau_* V \tag{9}$$

Utilizing the FE method to resolve the spatial dependence in the shallow-water equations in their primitive form gives inaccurate solutions with severe artificial near $2 \cdot \Delta x$ modes (Gray 1982). However, reformulating the primitive equations into a GWCE form gives highly accurate, noise-free, FE-based solutions to the shallow-water equations (Lynch and Gray 1979, Kinnmark 1984). The GWCE is derived by combining a time-differentiated form of the primitive continuity equation and a spatially differentiated form of the primitive momentum equations recast into conservative form, reformulating the convective terms into non-conservative form, and adding the primitive form of the continuity equation multiplied by a constant in time and space, τ_0 (Lynch and Gray 1979; Kinnmark 1984; Luettich, Westerink, and Scheffner 1992). The GWCE in the CP coordinate system is:

$$\frac{\partial^2 \zeta}{\partial t^2} + \tau_0 \frac{\partial \zeta}{\partial t} + \frac{\cos\varphi_0}{\cos\varphi} \frac{\partial}{\partial x'} \frac{\partial \zeta}{\partial t} \left\{ U - \frac{\cos\varphi_0}{\cos\varphi} UH \frac{\partial U}{\partial x'} - VH \frac{\partial U}{\partial y'} \right.$$

$$+ \left(\frac{\tan\varphi}{R} U + f \right) VH - H \frac{\cos\varphi_0}{\cos\varphi} \frac{\partial}{\partial x'} \left[\frac{p_s}{\rho_0} + g(\zeta - \eta) \right]$$

$$- (\tau_* - \tau_0) UH + \frac{\tau_{s\lambda}}{\rho_0} \right\} + \frac{\partial}{\partial y'} \left\{ V \frac{\partial \zeta}{\partial t} - \frac{\cos\varphi_0}{\cos\varphi} UH \frac{\partial V}{\partial x'} \right. \tag{10}$$

$$- VH \frac{\partial V}{\partial y'} - \left(\frac{\tan\varphi}{R} U + f \right) UH - H \frac{\partial}{\partial y'} \left[\frac{p_s}{\rho_0} + g(\zeta - \eta) \right]$$

$$- (\tau_* - \tau_0) VH + \frac{\tau_{s\varphi}}{\rho_0} \right\} - \frac{\partial}{\partial t} \left(\frac{\tan\varphi}{R} VH \right) + - \tau_0 \left(\frac{\tan\varphi}{R} VH \right) = 0$$

The GWCE (Equation 10) is solved in conjunction with the primitive momentum equations in non-conservative form (Equations 8 and 9).

The high accuracy of GWCE-based FE solutions is a result of their excellent numerical amplitude and phase propagation characteristics. In fact, Fourier analysis indicates that in constant depth water and using linear interpolation, a linear tidal wave resolved with 25 nodes per wavelength is more than adequately resolved over the range of Courant numbers ($C = \sqrt{gh}\Delta t / \Delta x \le 1.0$ (Luettich, Westerink, and Scheffner 1992)). Furthermore, the monotonic dispersion behavior of GWCE-based FE solutions avoids generating artificial near $2 \cdot \Delta x$ modes, which plague primitive-based FE solutions (Platzman 1981, Foreman 1983). The monotonic dispersion behavior of GWCE-based FE solutions is very similar to that associated with staggered finite difference solutions to the primitive shallow-water equations (Westerink and Gray 1991). GWCE-based FE solutions to the shallow-water equations allow for extremely flexible spatial discretizations, which result in a highly effective minimization of the discrete size of any problem (Le Provost and Vincent 1986, Foreman 1988, Vincent and Le Provost 1988, Westerink et al. 1992).

The details of ADCIRC, the implementation of the GWCE-based solution to the shallow-water equations, are described by Luettich, Westerink, and Scheffner (1992). As most GWCE-based FE codes, ADCIRC applies three-noded linear triangles for surface elevation, velocity, and depth. Furthermore, the decoupling of the time and space discrete form of the GWCE and momentum equations, time-independent and/or tri-diagonal system matrices, elimination of spatial integration procedures during time-stepping, and full vectorization of all major loops results in a highly efficient code.

3 Description of the Computational Domain

The WNAT model domain is shown in Figure 1. The open ocean boundary extends from the vicinity of Glace Bay in Nova Scotia, Canada to the vicinity of Corocora Island in eastern Venezuela. The computational domain is bounded on the north, west, and south by the North, Central, and South American coastlines. The topography within the domain, shown in Figure 2, includes the continental shelf (depths typically range from 0 m to 130 m), the continental slope (depths typically range from 130 m to 3,000 m), and the continental rise and deep ocean (depths from approximately 3,000 m to almost 8,500 m).

The WNAT model open ocean boundary lies almost entirely in the deep ocean, well away from the continental shelf and slope. As was discussed in the introduction, it is highly advantageous to specify boundary conditions in deep water since tides vary slowly, global tidal models tend to be more accurate, and nonlinear constituents are small in deep water. In water where the model open ocean boundary does cross or come near the continental shelf or slope, there are nearby islands with long-term tidal data which allow for adjustments if the global model data prove to be inaccurate in these shallow waters. For example, the very northern portion of the model open ocean boundary crosses the continental shelf and slope but also intersects Sable Island, Canada, which has available tidal data. Furthermore, the southern portion of the open ocean boundary nears or crosses the continental shelf and slope but also is in the vicinity of the lesser Antilles Islands for which long-term constituent data exist.

Within the WNAT model domain, 147 stations have been defined at which tidal elevation time histories were recorded for all model runs. These stations, shown in Figure 2, provide a basis for inter-grid comparisons and/or comparisons with field measured data.

Stations 1 through 77 have field-measured long-term tidal elevation data available in harmonically decomposed constituent form (long-term indicates that the time history records used to determine the constituent data are typically a year in duration). Details regarding the locations of the stations and source of the tidal data are listed in Table 1. Data at a given

8

station from the various sources generally agree. These tidal elevation stations lie predominantly in open waters near the coast along the eastern U.S. seaboard (stations 1-20), within the Gulf of Mexico (stations 21-38), and within the Caribbean Sea (stations 39-58). The remaining stations (stations 59-77) are generally located away from the coast either near small islands or in deep waters throughout the WNAT model domain. Stations 1 through 77 were used in the grid convergence studies as well as in comparing the computed tides with the measured field data.

In addition to stations with field-measured tidal data, an additional 70 stations were defined throughout the domain in order to achieve a more homogeneous distribution of stations within the domain. The additional stations were placed on the continental shelf (stations 78-87), in the vicinity of the continental shelf break (stations 88-109), near the toe of the continental slope (stations 110-130), and in the deep ocean (stations 131-147). These stations provide a more thorough basis for intercomparisons of responses for the grid convergence studies.

4   Grid Convergence Studies

In this section, the resolution requirements for the WNAT-model for the semidiurnal astronomical M_2 tide are examined. A sequence of three numerical experiments was conducted to establish the resolution required to obtain a converged M_2 response on a regular grid, to develop an optimal graded grid which minimized the number of nodes within the domain yet gave an M_2 solution that was equivalent to the finest regular grid and to examine the effect of resolution of the boundary on the M_2 solution. The three numerical experiments involved five regular grids (R1 - R5) and three graded grids (V1 - V3). The grid properties are summarized in Table 2. The coarsest and finest regular grids are shown in Figures 3 and 4, while the three graded meshes are shown in Figures 5 through 7. All grids were generated using GREDIT, a flexible interactive grid generation code developed by Turner and Baptista (1991).

The bathymetry of each grid was obtained by interpolating values from the ETOP05 database from the National Center for Atmospheric Research, which has a resolution of 5′ by 5′. However, the actual representation of the bathymetry for each grid depends on the grid itself, since depth is interpolated linearly on the three-noded triangular finite elements. A specified minimum bathymetry between 4 m (for the Caribbean Sea and Gulf of Mexico) and 7 m (for the northeast U.S. and Canadian coasts) was specified to avoid the drying of elements.

The open ocean boundary for each grid was forced with an M_2 tidal amplitude and phase interpolated onto the open ocean boundary modes using data from Schwiderski's (1979) global model results. This results in slightly different boundary forcings in space for grids R1, R2, and R3. Grids R4, R5, and V1 through V3 have essentially identical boundary forcing functions. An effective tidal potential forcing was applied within the domain for the M_2 constituent using an amplitude of 0.242334 m (Reid 1990). A theoretical value for the effective earth elasticity factor (which reduces the magnitude of the tidal potential forcing due to earth tides) of 0.69 was used (Schwiderski 1980, Hendershott 1981). Zero normal flow specified boundary conditions were applied to all coastal and island boundaries.

The fully nonlinear form of the shallow-water equation (Equations 1-3) was used for all grids. The nonlinear bottom friction coefficient C_f was specified equal to 0.003 throughout the domain. The GWCE parameter τ_0 was specified equal to 0.001, which represents a balance between the primitive continuity and wave equation portions of the GWCE equation.

Time-steps used with each grid are listed in Table 2. These time-steps were selected to maintain the maximum Courant number based on wave celerity less than unity. Each run was spun up from a cold start applying a very smooth hyperbolic tangent ramp function, which acts over approximately 12 days, to both the boundary and direct forcing functions. The use of this ramp function avoids exciting short period gravity modes and vortex modes in the subinertial frequency range due to start-up transients (Reid and Whitaker 1981). Nonetheless, free Helmholtz modes did appear to be excited in the Gulf of Mexico and the Caribbean Sea. However, the use of the 12-day ramp minimized the amplitude of these modes and they were almost entirely dissipated after about 30 days. Simulations were run for 50 days and tidal elevations were recorded at the 147 defined elevation stations. The last 10 days of these tidal elevation records were analyzed using a least square harmonic analysis and decomposed into amplitudes and phases for the M_2 tide and its overtides.

Comparisons of M_2 elevation amplitudes and phases are the basis for all grid intercomparisons. Global and regional error measures established by comparing the computed amplitudes and phases to a converged solution (which for our studies was obtained using grid R5) are presented in Tables 3 and 4. M_2 amplitude errors were computed as a proportional standard deviation for each grid as follows:

$$
E_{M_2-amp}^{grid-R5} \equiv \left\{ \frac{\displaystyle\sum_{\iota=1}^{L} \left[\hat{\eta}_{M_2}^{grid}(x_\iota, y_\iota) - \hat{\eta}_{M_2}^{R5}(x_\iota, y_\iota) \right]^2}{\displaystyle\sum_{\iota=1}^{L} \left[\hat{\eta}_{M_2}^{R5}(x_\iota, y_\iota) \right]^2} \right\}^{1/2}
$$

(11)

where

L = the total number of elevation stations within a given region

(x_ι, y_ι) = the location of an elevation station

$\hat{\eta}_{M_2}^{grid}(x_\iota, y_\iota)$ = the M_2 elevation amplitude for a given grid at station coordinates (x_ι, y_ι)

$\hat{\eta}_{M_2}^{R5}(x_\iota, y_\iota)$ = the M_2 elevation amplitude for the converged solution obtained using grid R5 at station coordinates (x_ι, y_ι)

$E_{M_2-amp}^{grid-R5}$ may be interpreted as the standard deviation in terms of a fraction of a regional representative measure of M_2 amplitude or roughly as an average percentage of error (when multiplied by 100) for the M_2 amplitude within a specified region. M_2 phase errors were computed for each grid as an absolute average error over a defined region as follows:

$$E_{M_2-phase}^{grid-R5} \equiv \frac{1}{L} \sum_{\iota=1}^{L} \left| \varphi_{M_2}^{grid}(x_\iota, y_\iota) - \varphi_{M_2}^{R5}(x_\iota, y_\iota) \right| \tag{12}$$

where

$\varphi_{M_2}^{grid}(x_\iota, y_\iota)$ = the M_2 elevation phase for a given grid at measurement location (x_ι, y_ι)

$\varphi_{M_2}^{R5}(x_\iota, y_\iota)$ = the M_2 elevation phase for the converged solution obtained with grid R5 at measurement location (x_ι, y_ι)

$E_{M_2-amp}^{grid-R5}$ and $E_{M_2-phase}^{grid-R5}$ are presented in Tables 3 and 4 for all grids considered for the entire domain (i.e., at all 147 elevation stations discussed in the previous section) as well as for various groups of stations defined in the previous section.

Resolution Requirements for Tidal Computations

In the first numerical experiment, the sensitivity of the solution to the level of refinement was examined using a regular grid structure by comparing simulations for grids R1 through R5. Grid R1, shown in Figure 3, is very coarsely discretized with a resolution of approximately 1.6° x 1.6° (this corresponds roughly to 140 km x 140 km). The degree of resolution for both bathymetry and the coastal boundary is identical to that of the grid itself. The only islands included in grid R1 are Cuba and Hispaniola. Figure 8 shows the M_2 wavelength-to-grid size ratio ($\lambda_{M_2}/\Delta x$) based on inviscid linear long-wave theory and indicates that large portions of the continental shelf are significantly underresolved (regions where $\lambda_{M_2}/\Delta x \leq 12.5$). In fact, Table 2 indicates that the shallowest regions of the domain are quite poorly resolved, with $\lambda_{M_2}/\Delta x$ as low as 1.5.

Grid R2 is derived from grid R1 by splitting each element into four elements. This halves the resolution to approximately 0.8° x 0.8° (roughly 70 km x 70 km). The coastal boundary remains identical to that of grid R1 although the bathymetric resolution was updated to be consistent with the resolution in the grid. This effectively steepens the gradient of the continental slope and improves the representation of the continental shelf. Grids R3 and R4 were subsequently generated in the same manner as grid R2, each increasing the grid resolution by a factor of 2 as compared to the previous grid, while maintaining the same coastal boundary as grid R1 and updating the bathymetry to the resolution of the grid itself. Consequently grid R4 is finely discretized over the domain with a resolution of approximately 12' x 12' (roughly 17 km x 17 km). Finally, grid R5 was generated by increasing the grid resolution by a factor of 2 in regions with bathymetry less than 3,500 m while maintaining the same resolution as grid R4 in waters deeper than 3,500 m. The resulting grid is shown in Figure 4. Figure 9 plots the $\lambda_{M_2} / \Delta x$ ratio for grid R5. The minimum

$\lambda_{M_2} / \Delta x$ ratio is equal to approximately 23, which should be sufficient to resolve M_2 waves accurately in regions where topography does not vary rapidly. This assertion is based on the results of Fourier analysis briefly discussed in the section on the governing equations and the numerical discretization. Figure 9 also indicates that all regions in grid R5 with rapidly varying topography, i.e., the continental shelf break and slope, as well as the deep ocean, are resolved with $\lambda_{M_2} / \Delta x$ ratios ranging from approximately 100 to over 500.

The computed M_2 response at the 147 established elevation stations indicated that amplitudes typically tend to increase when comparing grids R1 and R2 and may increase or decrease when comparing grids R2 and R3, grids R3 and R4, and grids R4 and R5. There are a variety of factors which come into play when considering the convergence of these solutions. First, as the grid resolution improves, the M_2 wave is better resolved in the shallowest portions of the domain, at least on a local basis, and in regions of rapidly varying flow such as in the vicinity of the continental shelf break and slope. This improved resolution leads to reduced truncation errors in these regions. Second, as grid resolution increases, the continental shelf and slope are more accurately represented. Therefore, the interaction between the tides and topography, as well as the importance of the bottom friction term, will be altered.

Error measures for M_2 amplitude and phase are presented in Tables 3 and 4. In general, the differences between solutions for subsequent grids become increasingly smaller with the finer grids. Errors tend to be largest in the Gulf of Mexico and Caribbean Sea and smallest in deep water. The relatively large amplitude and phase errors in the Gulf of Mexico are predominantly caused by large errors at a few stations along the coast of northern Florida and the Mississippi delta (stations 24, 25, 26, 27, 28, 96 and 98) in addition to stations near the center of the Gulf (stations 37, 82, and 102). The absolute phase differences between grids R4 and R5 associated with these stations range between 8.8 deg and 17.6 deg. These stations

lie in the vicinity of very high gradients in phase which occur on the Florida shelf, off the Mississippi delta, and near the center of the Gulf associated with amphidromes. The increased error levels within the Caribbean are associated with stations in the vicinity of Puerto Rico and Hispaniola (stations 50 and 54), which are again located in the vicinity of high gradients in phase associated with an amphidrome. Based on the errors in Tables 3 and 4, the resolution provided in grid R5 is judged to allow M_2 amplitudes to be predicted with less than 1 deg error and M_2 phase with less than 2 deg error (based on the diminishing error trends, since the accuracy of grid R5 must be better than that of grid R4) except at a few specific locations in the Gulf of Mexico and the Caribbean mentioned above. The M_2 constituent solution obtained with grid R5 is considered to be a converged solution for most of the WNAT domain with a coarse coastal boundary. Finally, it is noted that the errors in the computed overtides were not as good as for the astronomical M_2 tide. For example, the M_6 constituent differed by an average of 21 percent in amplitude and 18 deg in phase between grids R4 and R5 within the domain. Thus grid R5 does not lead to converged overtide solutions.

Development of an Optimal Graded Mesh

In the second experiment, optimally graded grids were developed with the goal of obtaining M_2 solutions that were comparable to the finest regular mesh, grid R5. While grid R5 adequately resolves the M_2 tide in the shallowest portions of the domain, it significantly over-resolves the M_2 tide in the deepest portions of the domain. In fact, Table 2 indicates that there are more than 1,322 nodes per M_2 wavelength for the deepest waters. Over-resolving a grid to this extent is, of course, extremely inefficient from a computational perspective. Therefore grids V1 and V2 were developed.

Grid V1, shown in Figure 5, was generated by starting with grid R1 and systematically refining regions for which $\lambda_{M_2} / \Delta x \leq 25$ until the shallowest regions within the domain as well as the coastal boundary were discretized to approximately the same level of detail as grid R5. Thus, grid V1 is coarsely resolved in deep water (1.6° resolution) and very finely resolved in the shallowest portions of the domain (5′ resolution). Regions with steep gradients in bathymetry such as in the vicinity of the continental shelf break and over the continental slope were generally refined to satisfy the minimum criterion $50 \leq \lambda_{M_2} / \Delta x \leq 100$. This criterion was based on one-dimensional numerical experiments and truncation error analysis, which indicated that the $\lambda_{M_2} / \Delta x = 25$ is not adequate to give accurate solutions over the shelf break and slope (Westerink, Muccino, and Luettich 1992). Transition regions between small and large elements were provided with additional resolution to create a smooth transition between element sizes and to control element skewness. Grid V1 maintains the same coarse coastal boundary as grids R1 through R5. Figure 10

shows the distribution of $\lambda_{M_2} / \Delta x$ contours for grid V1 and indicates that the $\lambda_{M_2} / \Delta x$ ratio is generally between 25 and 50 on the continental shelf and ranges between 75 and 100 in deep waters. Over the continental shelf break and slope, $\lambda_{M_2} / \Delta x$ generally varies between 50 and 100, although in the Caribbean Sea, the ratio is as high as 250.

The computed errors in Tables 3 and 4 indicate that grid V1 gives almost the same response as grid R5. In fact, differences in M_2 amplitude between grids R5 and V1 are on the order of 2 percent and differences in phase are on the order of 3 deg. As was the case in the regular grid convergence studies, the Gulf of Mexico and Caribbean exhibit larger amplitude and phase errors than other portions of the domain. In particular, the Gulf of Mexico has large phase errors associated with stations along the coast of northern Florida and the Mississippi delta (stations 24 through 28 and 96), in the center of the Gulf (station 37), in addition to the southwestern portion of the Gulf (stations 82, 99, 102, 127). Again, these errors correspond to the large gradients in phase associated with amphidromes on the Florida shelf and in the center of the Gulf.

Finally, a second graded grid, Figure 6, was developed to determine whether insufficient resolution over the shelf break, slope, and selected deep regions was a limiting factor in the agreement between grids R5 and V1. Grid V2 was developed from grid V1 by providing resolution of at least 5' in the vicinity of the continental shelf break (typically between 100 m and 500 m) and of at least 10' on the slope (typically between 500 m and 4,000 m). Again, additional resolution was provided in adjacent regions in order to control the ratio of adjacent element sizes as well as element skewness. Additional resolution was also provided in the deep regions of the Gulf and Caribbean. Grid V2 also maintains a coarse coastal boundary. Figure 11 presents the $\lambda_{M_2} / \Delta x$ ratios for grid V2 and indicates that the $\lambda_{M_2} / \Delta x$ ratio in the vicinity of the continental shelf break, slope, and in deep waters in the Gulf and Caribbean is much greater than for grid V1 (i.e., $\lambda_{M_2} / \Delta x$ is equal to at least 250 and often greater than 500), whereas other regions are similarly discretized.

Tables 3 and 4 compare the M_2 amplitude response obtained with grids R5 and V2 at the 147 elevation stations. The response of the graded grid V2 is almost identical to the response of the graded grid V1. Thus, the resolution provided by grid V1 over the shelf break, slope, and in deep waters in the Gulf and Caribbean does not limit the accuracy of the solution. In fact, it can be concluded that grid V2 unnecessarily over-resolves the shelf break and slope regions.

Influence of the Resolution of the Coastal Boundary on the M_2 Response

The third experiment examined the sensitivity of the solution to the degree of resolution of the coastal boundary itself. Grids R1 through R5, as well as grids V1 and V2, all represented the coastal boundary with the resolution of the coarsest grid R1. Therefore, grid V3, shown in Figure 7, was generated from grid V1 by updating all coastal boundaries to a resolution of roughly 5′ (equivalent to the resolution of the most resolved regions in grid V1). The islands of Puerto Rico, Andros, and Jamaica, in addition to 50 smaller islands, were also added. Tables 3 and 4 indicate that the M_2 elevation response changes substantially in some regions with the improved representation of the coastal boundary. Particularly in near-coastal regions and on the continental shelf, the resolution of the coastal boundary will strongly influence the computed response. Differences in phase in the Gulf of Mexico are particularly large. Differences in amplitude and phase are less in remote and deep waters.

5 Comparison Between Computed and Observed Tidal Elevations in the WNAT Model

Computations are now presented using grid V3 driven on the open ocean boundary using results from an existing global model and within the interior domain with eight diurnal and semidiurnal astronomical tidal constituents. These computations allow for realistic comparisons between the coupled global/WNAT model results and the measurement data at the 77 stations previously defined, since the constituents are allowed to fully interact through the various nonlinear terms in the shallow-water equations (Westerink et al. 1989). The computations were intended to be entirely predictive and therefore no calibration/tuning procedures were performed.

The open ocean boundary was forced using tidal elevations for the K_1, O_1, P_1, Q_1, M_2, S_2, N_2, and K_2 constituents from Schwiderski's global model (Schwiderski 1979; 1981, a-g). An effective tidal potential forcing within the interior domain was applied for the same eight constituents that were forced on the open ocean boundary. Tidal potential amplitudes and the associated effective earth elasticity factors for the eight constituents are listed in Table 5. In particular, the diurnal tides have associated effective earth elasticity factors ranging between 0.695 and 0.782 (Wahr 1981, Woodworth 1990) instead of the widely used value of 0.69 (Schwiderski 1980, Hendershott 1981). Equilibrium tides were directly computed and therefore no nodal factors or astronomical arguments were used in either the boundary or the interior domain forcing functions.

A constant bottom friction coefficient equal to $C_f = 0.003$ was applied throughout the domain. Furthermore, all nonlinearities in the shallow-water equations (Equations 1-3) were included in the computations. The model was spun up from homogeneous initial conditions using a 12-day hyperbolic tangent ramp function. Due to the presence of free Helmholtz modes within the Gulf of Mexico and Caribbean, results were only recorded after 40 days when these free modes had been entirely dissipated. The simulations were

run for 225 days; during the last 185 days data were recorded every half hour at elevation stations for which measurement data are available (stations 1-77) and every hour at all nodes within the domain. A time-step of 37.5 sec was used, giving a Courant number between 0.01 and 1.1.

The computed time histories at all nodes within the domain as well as at the 77 measurement tidal elevation stations were harmonically analyzed over the recorded 185-day period. Cotidal charts for the four diurnal constituents and the four semidiurnal constituents are presented in Figures 12 and 13, respectively. These figures also indicate the relative error between the predicted and measured values at the 77 measurement stations for which data are available. Figures 12 and 13 indicate a marked similarity between each of the diurnal and each of the semidiurnal constituents. The diurnal constituent amplitudes tend to increase significantly within the Gulf of Mexico. The diurnal constituents exhibit an amphidrome in the North Atlantic off the coast of Nova Scotia as well as dual amphidromes in the vicinity of the Bahamas. The semidiurnal constituents experience rapid increases in amplitude in the Gulf of Maine, on the Blake Plateau, on the Florida Shelf, and on the Nicaragua Rise, as well as in the vicinity of Trinidad. Semidiurnal amplitudes generally tend to be significantly smaller in the Gulf of Mexico and the Caribbean than in the Atlantic. Full or degenerate amphidromes exist off of Puerto Rico and on the Florida Shelf. A full amphidrome exists in the center of the Gulf of Mexico for the M_2 and N_2 constituents, while this feature appears as a degenerate amphidrome off of Cancun for the S_2 and K_2 constituents. A full amphidrome exists in the northwest Gulf of Mexico for the K_2 constituent.

The accuracy of the predicted tides was quantified by comparing predicted values at the 77 measurement stations for the eight astronomical constituents to the available field data in harmonic form. The amplitude error for constituent j for each of the eight astronomical constituents was computed as a proportional standard deviation for a defined region as:

$$E_{j-amp}^{V3-meas} \equiv \left\{ \frac{\sum_{l=1}^{L} \left[\hat{\eta}_j^{V3}(x_l, y_l) - \hat{\eta}_j^{meas}(x_l, y_l) \right]^2}{\sum_{l=1}^{L} \left[\hat{\eta}_j^{meas}(x_l, y_l) \right]^2} \right\}^{\frac{1}{2}} \tag{13}$$

where

$\quad L$ = total number of elevation stations within a given region

$\quad (x_l, y_l)$ = location of an elevation station

$$\hat{\eta}_j^{V3}(x_\iota, y_\iota) = \text{computed elevation amplitude for constituent } j \text{ at}$$
$$\text{station coordinates } (x_\iota, y_\iota)$$

$$\hat{\eta}_j^{meas}(x_\iota, y_\iota) = \text{measured elevation amplitude for constituent } j \text{ at}$$
$$\text{station coordinates } (x_\iota, y_\iota)$$

The phase error for each constituent j was computed as an absolute average error defined over a region as:

$$E_{j\text{-}phase}^{V3-meas} \equiv \frac{1}{L} \sum_{\iota=1}^{L} \left| \varphi_j^{V3}(x_\iota, y_\iota) - \varphi_j^{meas}(x_\iota, y_\iota) \right| \qquad (14)$$

where

$$\varphi_j^{V3}(x_\iota, y_\iota) = \text{computed elevation phase for constituent } j \text{ at}$$
$$\text{measurement location } (x_\iota, y_\iota)$$

$$\varphi_j^{meas}(x_\iota, y_\iota) = \text{measured elevation phase for constituent } j \text{ at}$$
$$\text{measurement location } (x_\iota, y_\iota)$$

Amplitude and phase errors are presented in Tables 6 and 7 for the entire domain as well as on a regional basis for each of the eight astronomical constituents. The constituents are predicted with an average amplitude error between 18.2 and 45.3 percent and an average phase error between 8.3 and 27.5 deg. Typically, the larger constituents, the K_1, O_1, M_2, S_2 and N_2 tides, have smaller relative amplitude errors while the smaller constituents, the P_1, Q_1 and K_2 tides, have larger relative amplitude errors. There are no predominant trends with respect to spatial variability in amplitude errors, with the exception of relatively lower errors in the Caribbean for diurnal constituents and relatively higher errors in the Caribbean and Gulf of Mexico for semidiurnal constituents. The distribution of amplitude ratio errors is presented in Table 8 and indicates that the diurnal constituent amplitude predictions are evenly and closely clustered about the measured values, while the semidiurnal constituent amplitude predictions are typically over-predicted with quite a few outliers. Phase errors for the diurnal tides, ranging between 8.6 and 12.4 deg, are much smaller than phase errors for the semidiurnal tides, which range between 19.6 and 27.5 deg. Phase errors tend to be especially large for the semidiurnal constituents within the Gulf of Mexico and Caribbean. A consistent feature of the results is that stations which had poor convergence properties also showed the poorest comparison to the measurement data. Again these stations typically lie in the vicinity of amphidromes. Finally, the relative distribution of phase errors is presented in Table 9, which indicates that predicted diurnal constituent phases generally lead and are clustered

closely about the measured phase, while predicted semidiurnal constituent errors are distributed over a much wider range of values.

Resynthesized time histories for surface elevation from harmonically decomposed computed constituent data (i.e. resynthesized ADCIRC-2DDI results) are compared to synthesized time histories of the available measurement data at every other station for stations 1 through 77 in Figure 14. These time histories were all synthesized using up to eight astronomical constituents applied in the forcing functions or a sub-set of these constituents when all eight were not available in the measurement data at the station. Procedures for resynthesis are presented in Appendix A. Errors in these time histories are dominated by the constituent errors of the largest constituent or constituents. In regions where semidiurnal tides dominate, such as the U.S. east coast, the ADCIRC-2DDI results are almost always over-predicted. This relates directly to the over-prediction of the M_2 constituent. On the other hand, in regions of mixed or diurnal tides, such as in the Gulf of Mexico, errors in the time histories are closer to the more modest errors associated with the dominant O_1 and K_1 constituents in the region.

On a Cray YMP-6128, ADCIRC-2DDI ran at 0.46 central processing unit seconds per time-step for the WNAT domain using grid V3.

6   Discussion

The overall accuracy of a numerical model depends on the physics included in the model, on the numerical accuracy (which depends on the algorithm as well as the grid) and on the precision of the forcing functions. Two-dimensional barotropic tidal models generally give comparisons between model predictions and measurements within 10 percent accuracy for amplitude and 10 percent accuracy for phase. Therefore, it is assumed that the physics incorporated in the model used in this report should be generally satisfactory.

The WNAT model grid convergence studies demonstrate that convergence to solutions within 1-2 percent error in amplitude and 2° to 3° in phase have generally been achieved, with the exception of the Gulf of Mexico and Caribbean, where persistent errors occur in semidiurnal constituent phases. The latter problem appears to be associated with amphidromes, whose locations shift readily. The performance characteristics of the finest regular grid (6′ x 6′ to 12′ x 12′ in very deep water) and the graded V1 and V2 grids were very similar. All three grids appear to have difficulties in phase in the Gulf of Mexico and Caribbean, with an average error of up to 10°. The results from grids V1, V2, and R5 indicate that the lack of convergence in the Gulf as well as in the Caribbean is not associated with insufficient resolution over the shelf break, slope, in deep waters, or in the immediate vicinity of the amphidromes. Rather, these problems appear to be due to factors that control the structure and location of the amphidromes. Previous studies in the Gulf indicate that the semidiurnal response was very sensitive to the grid resolution and bathymetry, as well as the bottom friction coefficient (Westerink et al. 1992). Insufficient resolution over the shelf, particularly in the shallowest regions, may be responsible for the relatively poor numerical convergence in these regions. Finally, grid V3 clearly demonstrated the importance of providing detailed resolution for the coastal boundary. Phase response in the Gulf was again the most sensitive.

Results of the uncalibrated simulation in which grid V3 is forced with Schwiderski's (1979, 1981a-g) global model indicate that the differences between the WNAT model predictions and field data significantly exceed the level of estimated numerical convergence error throughout the entire domain. Nonetheless the largest errors again occur in the Gulf of Mexico as well as

the Caribbean. Many of the largest semidiurnal constituent station errors occur in the vicinity of amphidromic points. This suggests that the amphidromes are sensitive not only to numerical truncation errors and the resolution provided for the coastal boundary but also to the precision of the forcing function. Indeed, a systematic error for all constituents exists in amplitude and phase throughout the entire domain in deep as well as shallow waters. In particular, all the semidiurnal tides and especially the M_2 constituent are predominantly over-predicted. Thus, it is highly likely that Schwiderski's model is not sufficiently accurate on the WNAT model open ocean boundary. This is not entirely surprising, considering that Schwiderski's model does not properly account for dissipation on the shelf due to a lack of grid resolution and the linear character of the model. In fact, Cartwright and Ray (1991) computed root mean square errors at 80 deep-ocean stations throughout the world and found average amplitude errors of 4.1 cm for M_2, 1.86 cm for S_2, 1.49 cm for O_1, and 1.76 cm for K_1. How these globally average errors exactly impact the constituent values used on the WNAT model open ocean boundary is difficult to determine. However, since the tides are typically small in deep waters, errors in Schwiderski's results on this boundary may be significant. Adjusting the constituents on the open ocean forcing boundaries downwards from Schwiderski's values will decrease the errors at the 77 measurement stations. Sensitivity and calibration studies for the forcing functions on the open ocean boundary are currently being performed to improve the match between the data and predictions. These findings will be detailed in a subsequent report.

7 Conclusions

The WNAT model is a large domain coastal model with a geometrically and hydrodynamically simple open ocean boundary. WNAT is ideally located to facilitate tidal predictions with minimum requirements for open ocean boundary condition calibration. The open ocean boundary lies almost entirely in deep water where astronomical tides vary slowly, nonlinear tides are small, and global models, to which the WNAT model can be coupled, are likely to be most accurate. Due to the resulting large domain and the required resolution in shallow regions as well as regions of rapidly varying flow, it is highly desirable to vary nodal densities to fully resolve flow features on a local basis. The FE shallow-water equation model, ADCIRC-2DDI, easily accommodates the required highly flexible meshes.

Resolution requirements have been systematically studied using the entire WNAT model domain and a sequence of regular grids (with grids ranging from a very coarse 1.6° x 1.6° mesh to a very fine 6′ x 6′ to 12′ x 12′ mesh) as well as a sequence of non-uniformly graded grids with resolution varying between 1.6° and 5′ within each mesh. Elevation response computations with the sequence of regular grids indicate that the semidiurnal M_2 tide typically converges to better than 1 percent accuracy in elevation amplitude and 2 deg in phase using the 6′ x 6′ to 12′ x 12′ mesh with the exception of specific locations in the Gulf of Mexico and Caribbean in which shifting amphidromes lead to consistently larger phase errors. The overtide constituents did not satisfactorily converge, even with the finest 6′ x 6′ to 12′ x 12′ mesh. The elevation response computed using the non-uniformly graded meshes achieves about the same level of performance as the finest nearly uniform grid. Overall, these studies indicate that grids can be developed based on a $\lambda / \Delta x \cong 25$ criterion with some additional resolution over the shelf break and slope. This is in sharp contrast with one-dimensional studies, which indicated the need for a much higher level of resolution over the continental shelf break and slope (Westerink, Muccino, and Luettich 1992b). This indicates the importance of performing grid convergence studies in two dimensions as opposed to one dimension. However, it appears that the shallow regions in the Gulf of Mexico and Caribbean need to be more highly resolved in order to converge to the same level of precision as in other parts of the domain. Finally, it was

noted that the representation of the coastal boundary can also substantially influence tidal response.

Predictive computations were performed with the optimal graded mesh driven by the eight constituents from Schwiderski's global ocean model results and by tidal potential functions. Comparisons of measurement data at 77 stations for the K_1, O_1, P_1, Q_1, M_2, S_2, N_2 and K_2 constituents indicate that these constituents are predicted with average errors in amplitude between 18.2 percent and 45.3 percent and average errors in phase between 8.3° and 27.5°. Phase errors in the Gulf of Mexico and Caribbean for semidiurnal constituents are quite sensitive to the shifting amphidromes. Even in deep water, there is no close match between predictions and measurements. It is felt that Schwiderski's model results contribute substantially to these error levels. The sensitivity of response to perturbations in the boundary forcing function and driving the model boundary with more accurate global models are currently being investigated.

24

References

Cartwright, D. E., and Ray, R. D. (1991). "Energetics of global ocean tides from geosat altimetry," *Journal of Geophysical Research* 96(C9), 16897-16912.

Dietrich, D. E., Roache, P. J., and Marietta, M. G. (1991). "Convergence studies with the Sandia ocean modeling system," *International Journal for Numerical Methods in Fluids* 11, 127-150.

Flather, R. A. (1987). "Estimates of extreme conditions of tide and surge using a numerical model of the North-west European continental shelf," *Estuarine, Coastal and Shelf Science* 24, 69-73.

_____ . (1988). "A numerical model investigation of tides and diurnal-period continental shelf waves along Vancouver Island," *J. of Physical Oceanography* 18, 115-139.

Foreman, M. G. G. (1977). "Manual for tidal heights analysis and prediction," Pacific Marine Science Report 77-10, Institute of Ocean Sciences, Patricia Bay, Sidney B.C.

_____ . (1983). "An analysis of the wave equation model for finite element tidal comparisons," *Journal of Computational Physics* 52, 290-312.

_____ . (1988). "A comparison of tidal models for the southwest coast of Vancouver Island." *Proceedings of the VII International Conference on Computational Methods in Water Resources*, held in Cambridge, MA, Elsevier.

Gerritsen, H., and Bijlsma, A. C. (1988). "Modelling of tidal and winddriven flow: The Dutch continental shelf model." *Computer Modelling in Ocean Engineering*. Schrefler & Zienkiewicz, eds., Balkema, Rotterdam.

Gray, W. G. (1982). "Some inadequacies of finite element models as simulators of two-dimensional circulation," *Advances in Water Resources* 5, 171-177.

Gray, W. G. (1989). "A finite element study of tidal flow data for the North Sea and English Channel," *Advances in Water Resources*, 12, 143-154.

Hendershott, M. C. (1981). "Long Waves and Ocean Tides," *Evolution of Physical Oceanography*, B. A. Warren and C. Wunsch, eds., MIT Press, Cambridge, MA, 292-341.

International Hydrographic Organization Tidal Constituent Bank. (1991). "Station Catalogue." Ocean and Aquatic Sciences, Department of Fisheries and Oceans, Ottawa.

Kinnmark, I. P. E. (1984). "The shallow water wave equations: Formulation, analysis and application," Ph.D. dissertation, Department of Civil Engineering, Princeton University, NJ.

Kolar, R. L., Gray, W. G., Westerink, J. J., and Luettich, R. A. (1992). "Shallow water modeling in spherical coordinates: Equation formulation, numerical implementation, and application," submitted to *Journal of Hydraulic Research*.

Le Provost, C., and Vincent, P. (1986). "Some tests of precision for a finite element model of ocean tides," *Journal of Computational Physics* 65, 273-291.

Luettich, R. A., Westerink, J. J., and Scheffner, N. W. (1992). "ADCIRC: An advanced three-dimensional circulation model for shelves, coasts and estuaries; Report 1, Theory and methodology of ADCIRC-2DDI and ADCIRC-3DL," Technical Report DRP-92-6, U.S. Army Engineer Waterways Experiment Station, Vicksburg, MS.

Lynch, D. R. (1983). "Progress in hydrodynamic modeling, review of U.S. Contributions, 1979-1982," *Reviews of Geophysics and Space Physics* 21(3), 741-754.

Lynch, D. R., and Gray, W. G. (1979). "A wave equation model for finite element tidal computation," *Computers and Fluids* 7, 207-228.

Pearson, F. (1990). *Map projections: Theory and applications*. CRC Press, Inc., Boca Raton, FL.

Platzman, G. W. (1981). "Some response characteristics of finite element tidal models," *Journal of Computational Physics* 40, 36-63.

Reid, R. O., and Whitaker, R. E. (1981). "Numerical model for astronomical tides in the Gulf of Mexico," Technical report for the U.S. Army Corps of Engineers, Department of Oceanography, Texas A&M University.

Reid, R. O. (1990). "Waterlevel changes." *Handbook of coastal and ocean engineering*, J. Herbich, ed., Gulf Publishing, Houston, TX.

Schureman, P. (1941). "Manual of harmonic analysis and prediction of tides," Special Publication No. 98, Coast and Geodetic Survey, U.S. Department of Commerce, U.S. Government Printing Office, Washington, D.C.

Schwiderski, E. W. (1979). "Global ocean tides; Part II: The semidiurnal principle lunar tide (M_2)," *Atlas of tidal charts and maps*, NSWC TR 79-414.

_____ . (1980). "On charting global ocean tides," *Reviews in Geophysics and Space Physics* 18, 243-268.

_____ . (1981a). "Global ocean tides; Part III: The Semidiurnal principle solar tide (S_2)," *Atlas of tidal charts and maps*, NSWC TR 81-122.

_____ . (1981b). "Global ocean tides; Part IV: The diurnal luni-solar declination tide (K_1)," *Atlas of tidal charts and maps*, NSWC TR 81-142.

_____ . (1981c). "Global ocean tides; Part V: The diurnal principle lunar tide (O_1)," *Atlas of tidal charts and maps*, NSWC TR 81-144.

_____ . (1981d). "Global ocean tides; Part VI: The semidiurnal elliptical lunar tide (N_2)," *Atlas of tidal charts and maps*, NSWC TR 81-218.

_____ . (1981e). "Global ocean tides; Part VII: The diurnal principle solar tide (P_1)," *Atlas of tidal charts and maps*, NSWC TR 81-220.

_____ . (1981f). "Global ocean tides; Part VIII: The semidiurnal luni-solar declination tide (K_2)," *Atlas of tidal charts and maps*, NSWC TR 81-222.

_____ . (1981g). "Global ocean tides; Part IX: The diurnal elliptical lunar tide (Q_1)," *Atlas of tidal charts and maps*, NSWC TR 81-224.

Turner, P. J., and Baptista, A. M. (1991). "ACE/GREDIT users manual: Software for semi-automatic generation of two-dimensional finite element grids," CCALMR Software Report SDS2(91-2), Oregon Graduate Institute, Beaverton, OR.

U.S. Geological Survey. (1984). "Atlas of tidal elevation and current observations on the Northeast American continental shelf and slope," U.S. Geological Survey Bulletin No. 1611.

Vincent, P., and Le Provost, C. (1988). "Semidiurnal tides in the Northeast Atlantic from a finite element numerical model," *Journal of Geophysical Research* 93(C1), 543-555.

Wahr, J. M. (1981). "Body tides on an elliptical, rotating, elastic and oceanless earth, *Geophys. J. R.* Astr. Soc. 64, 677-703.

Walters, R. A. (1988). "A finite element model for tides and currents with field application," *Comm. Applied Numerical Methods* 4, 401-411.

Walters, R. A., and Werner, F. E. (1989). "A comparison of two finite element models of tidal hydrodynamics using a North Sea data set," *Advances in Water Resources* 12(4), 184-193.

Werner, F. E., and Lynch, D. R. (1989). "Harmonic structure of English Channel/Southern Bight tides from a wave equation simulation," *Advances in Water Resources* 12, 121-142.

Westerink, J. J., and Gray, W. G. (1991). "Progress in surface water modeling," *Reviews of Geophysics*, April supplement, 210-217.

Westerink, J. J., Luettich, R. A., Baptista, A. M., Scheffner, N. W., and Farrar, P. (1992). "Tide and storm surge predictions using a finite element model," *Journal of Hydraulic Engineering* 118, 1373-1390.

Westerink, J. J., Muccino, J. C., and Luettich, R. A. (1992). "Resolution requirements for a tidal model of the Western North Atlantic and Gulf of Mexico," *Proceedings of the IX International Conference on Computational Methods in Water Resources*, Denver, CO. T. F. Russell et al., eds., Computational Mechanics Publications, Southampton, UK.

Westerink, J. J., Stolzenbach, K. D., and Connor, J. J. (1989). "General spectral computations of the nonlinear shallow water tidal interactions within the Bight of Abaco," *Journal of Physical Oceanography* 19, 1348-1371.

Woodworth, P. L. (1990). "Summary of recommendations to the UK Earth Observation Data Centre (UK-EODC) by the Proudman Oceanographic Laboratory (POL) for tide model corrections on ERS-1 geophysical data records," Proudman Oceanographic Laboratory Communication.
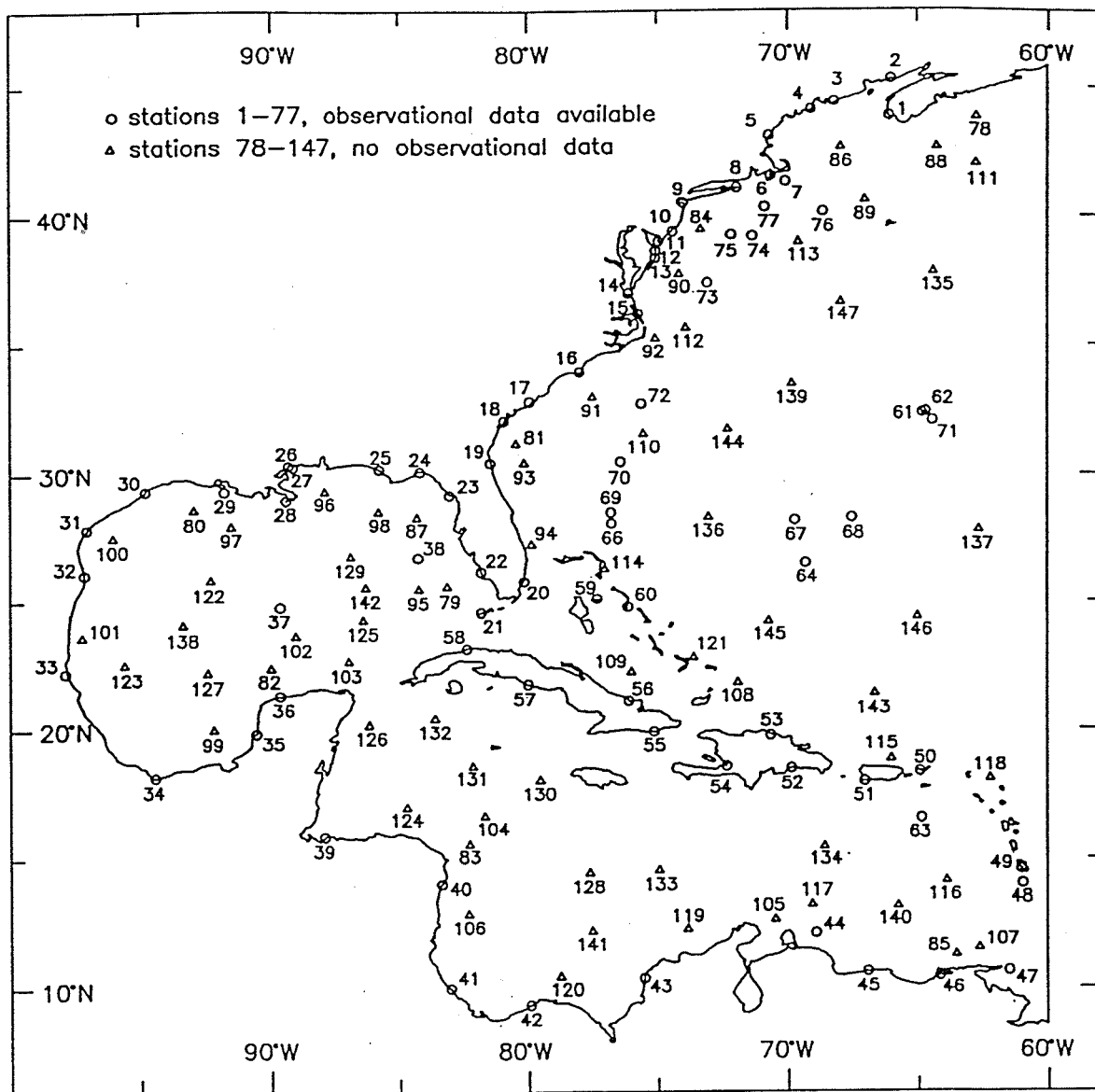
Figure 1.   The Western North Atlantic Tidal (WNAT) model computational domain, including the locations of tidal elevation stations with available field data and tidal elevation stations without field data
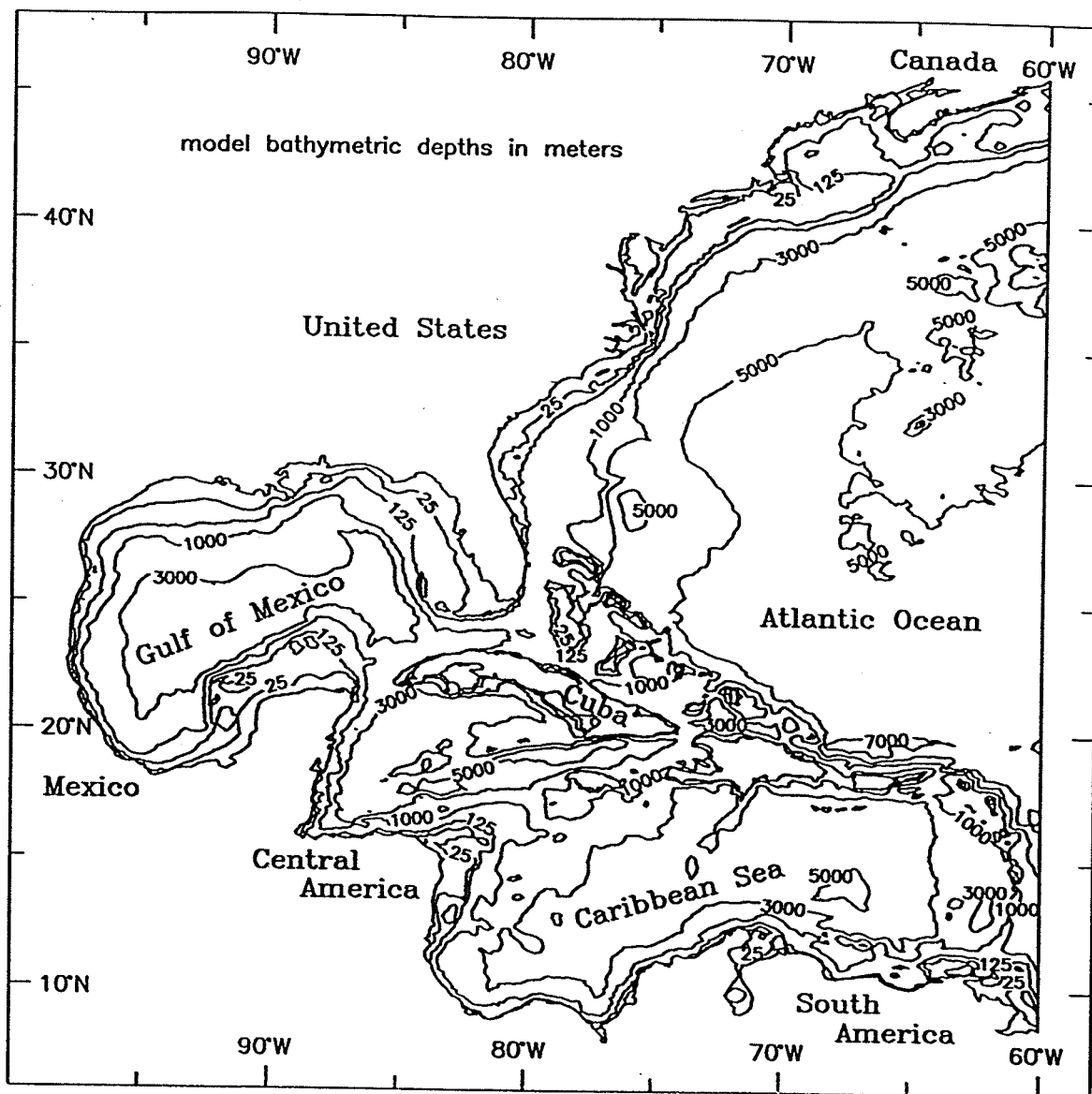
Figure 2.   Topography (in meters) within the WNAT computational domain
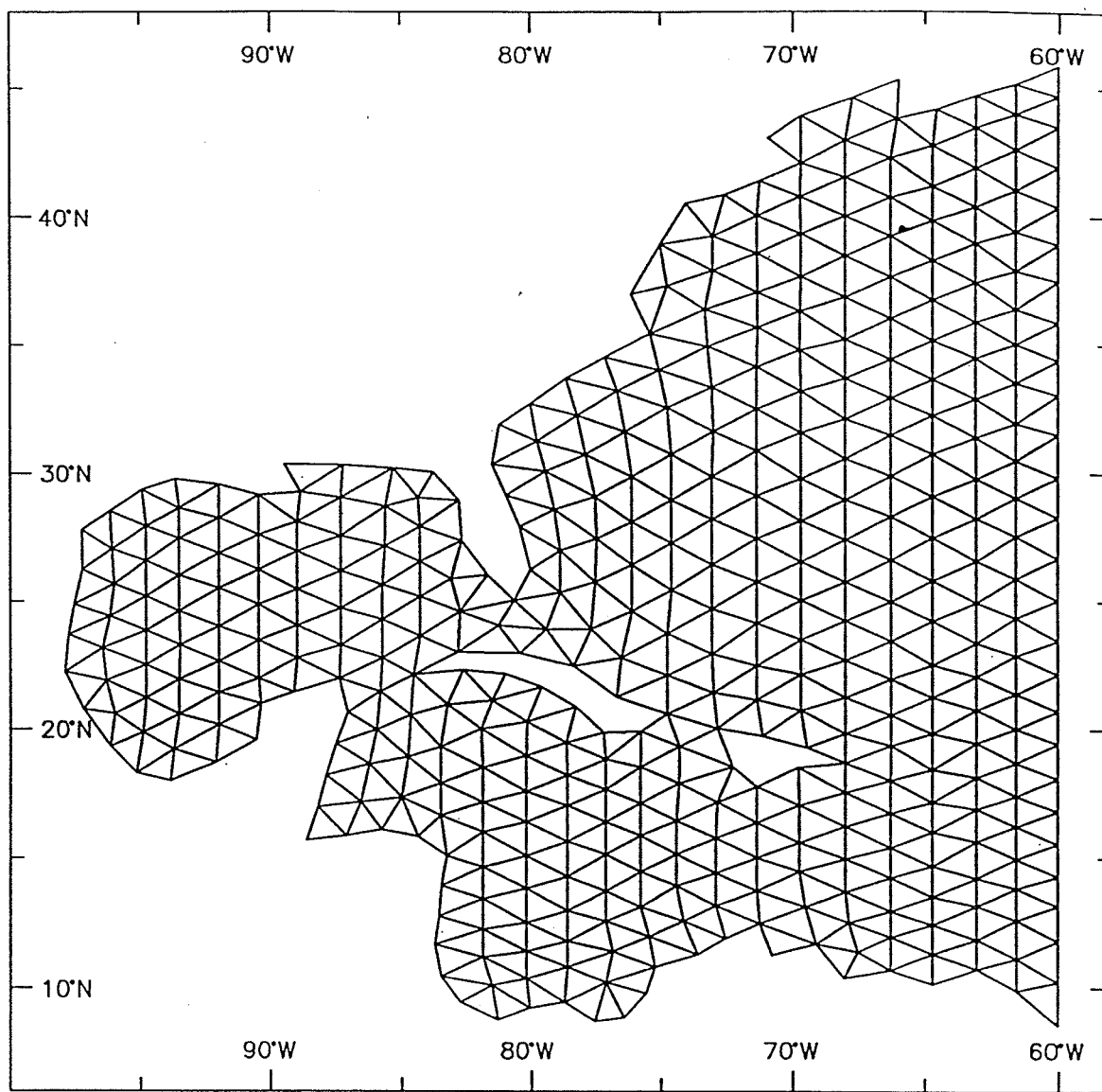
Figure 3.   Grid R1: Regular finite element 1.6° × 1.6° discretization of the domain with a
coarse representation of the coastal boundary
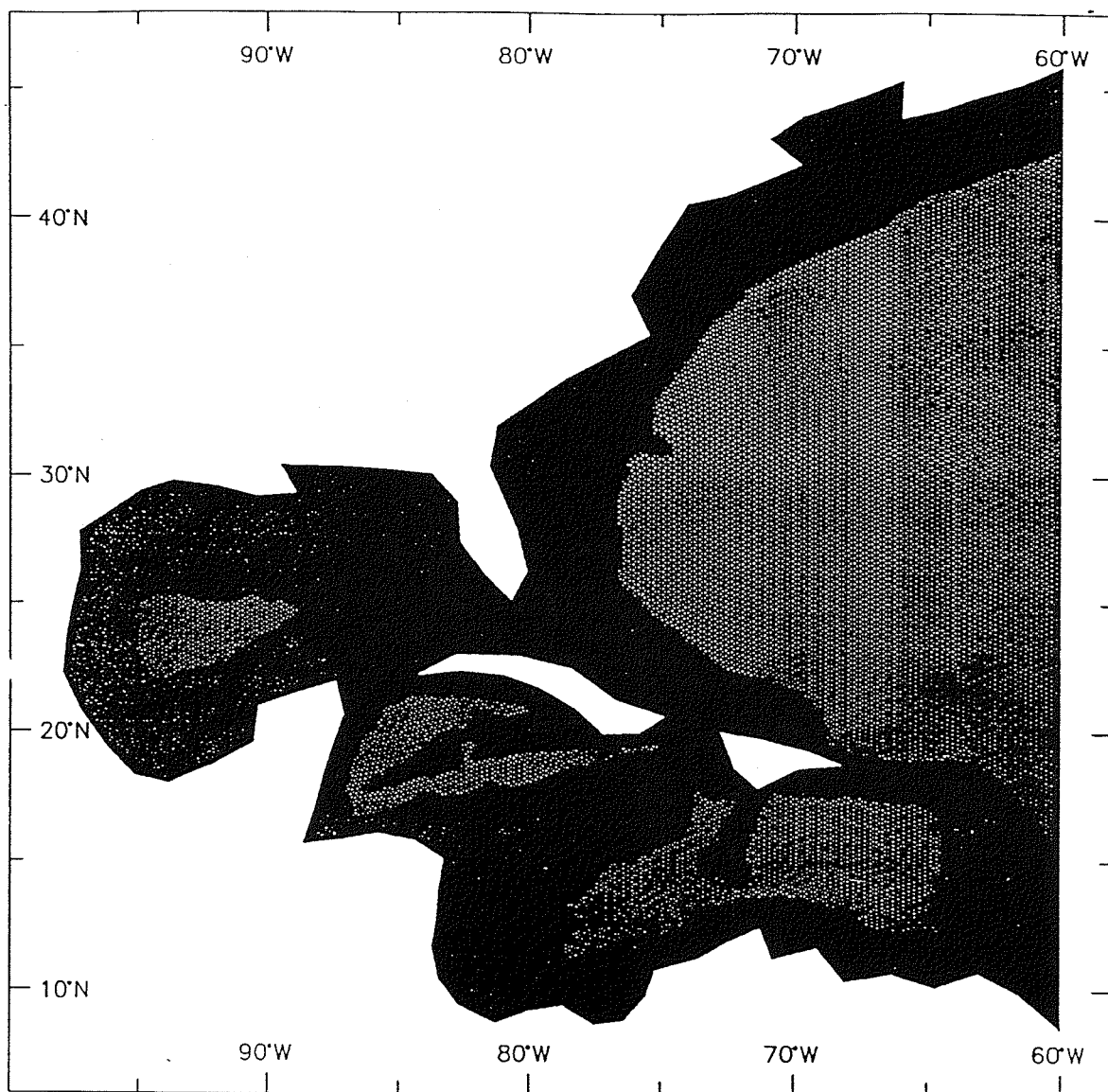
Figure 4.   Grid R5: Nearly regular finite element 6′ × 6′ to 12′ × 12′ discretization of the domain with a coarse representation of the coastal boundary
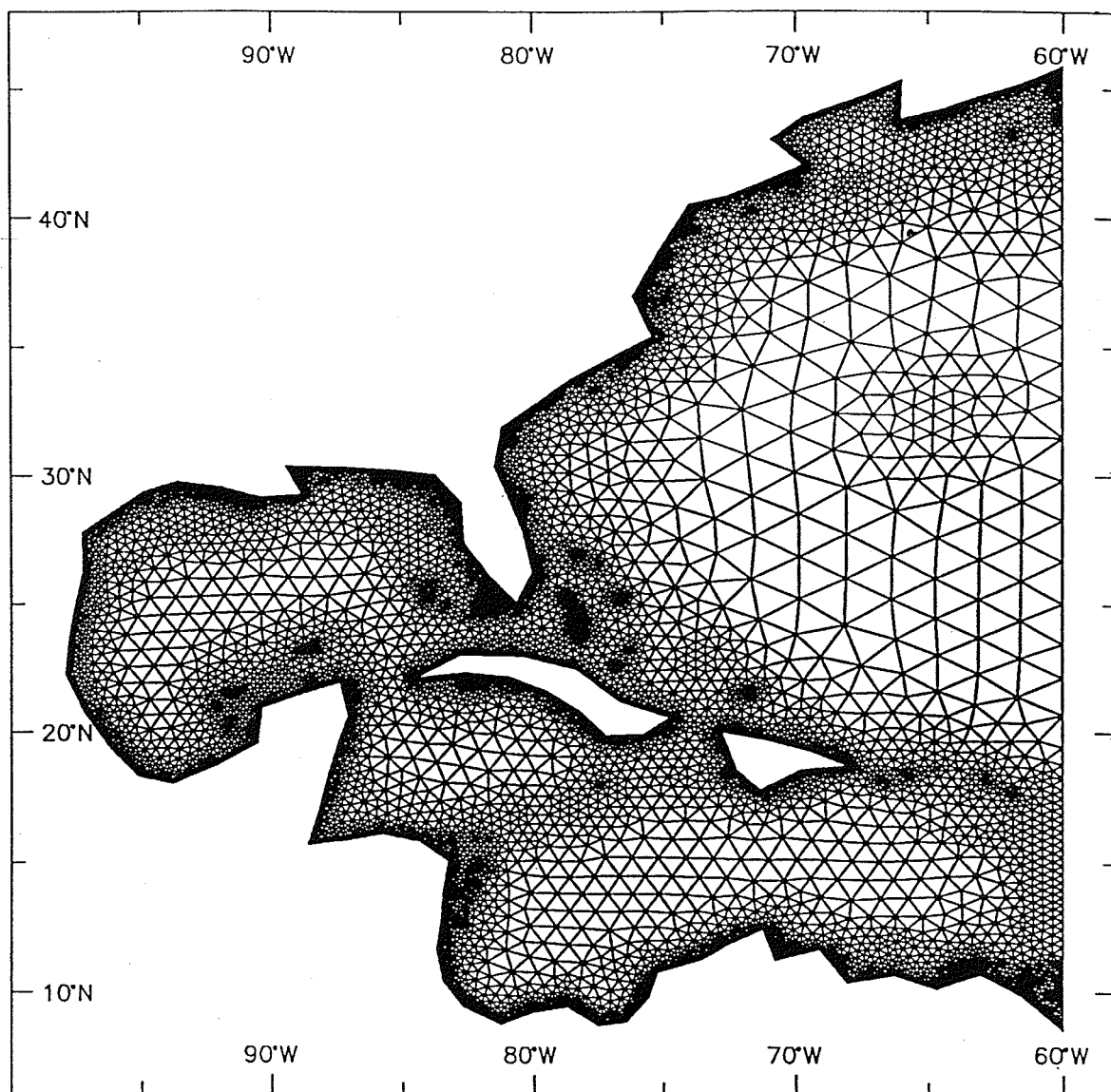
Figure 5.   Grid V1: Graded finite element discretization of the domain based on a
$\lambda_{M_2}/\Delta x \geq 25$ criterion with a coarse representation of the coastal boundary
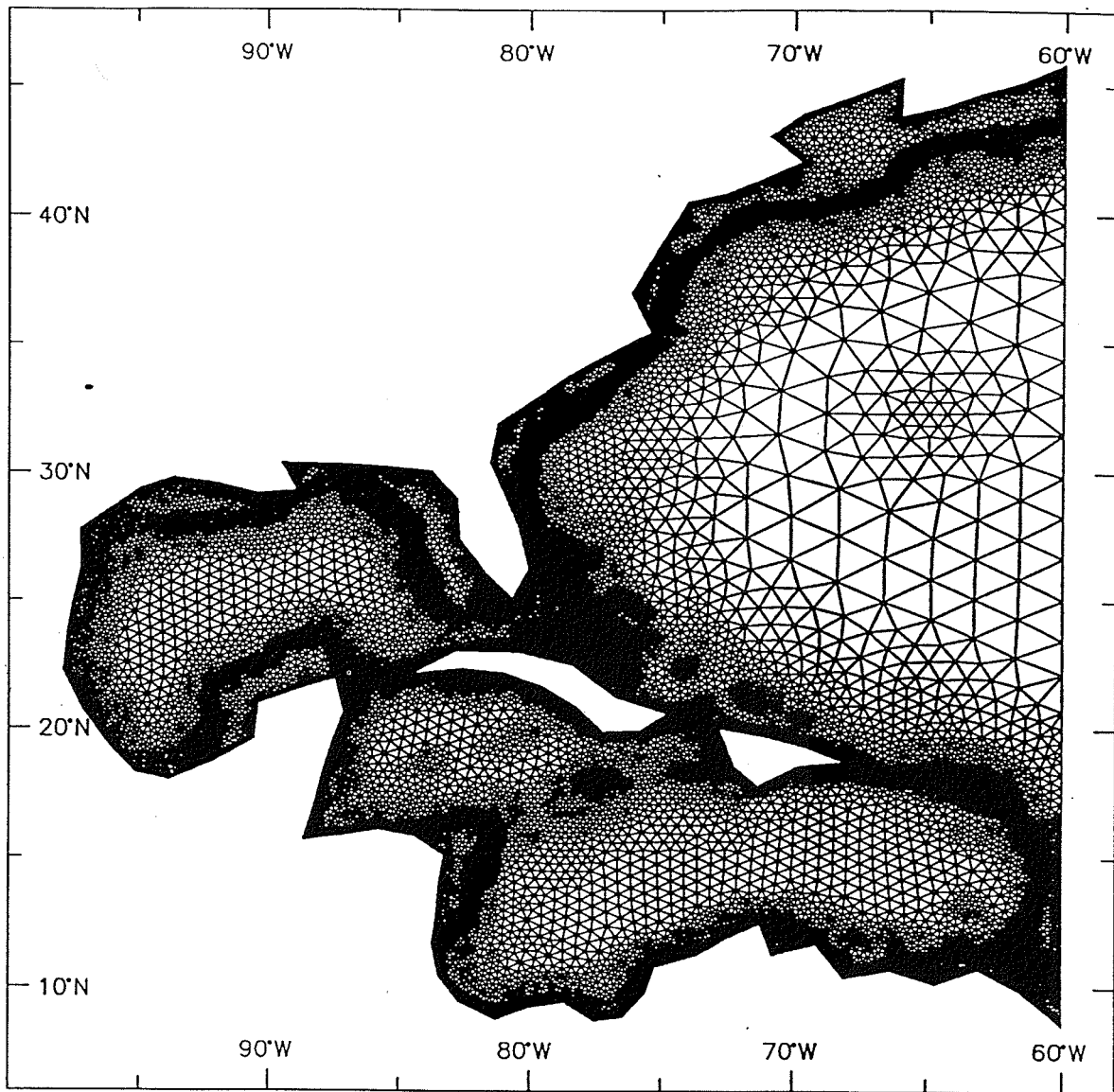
Figure 6. Grid V2: Graded finite element discretization of the domain based on a
$\lambda_{M_2}/\Delta x \geq 25$ criterion with additional resolution in the vicinity of the continental

shelf break and with coarse representation of the coastal boundary
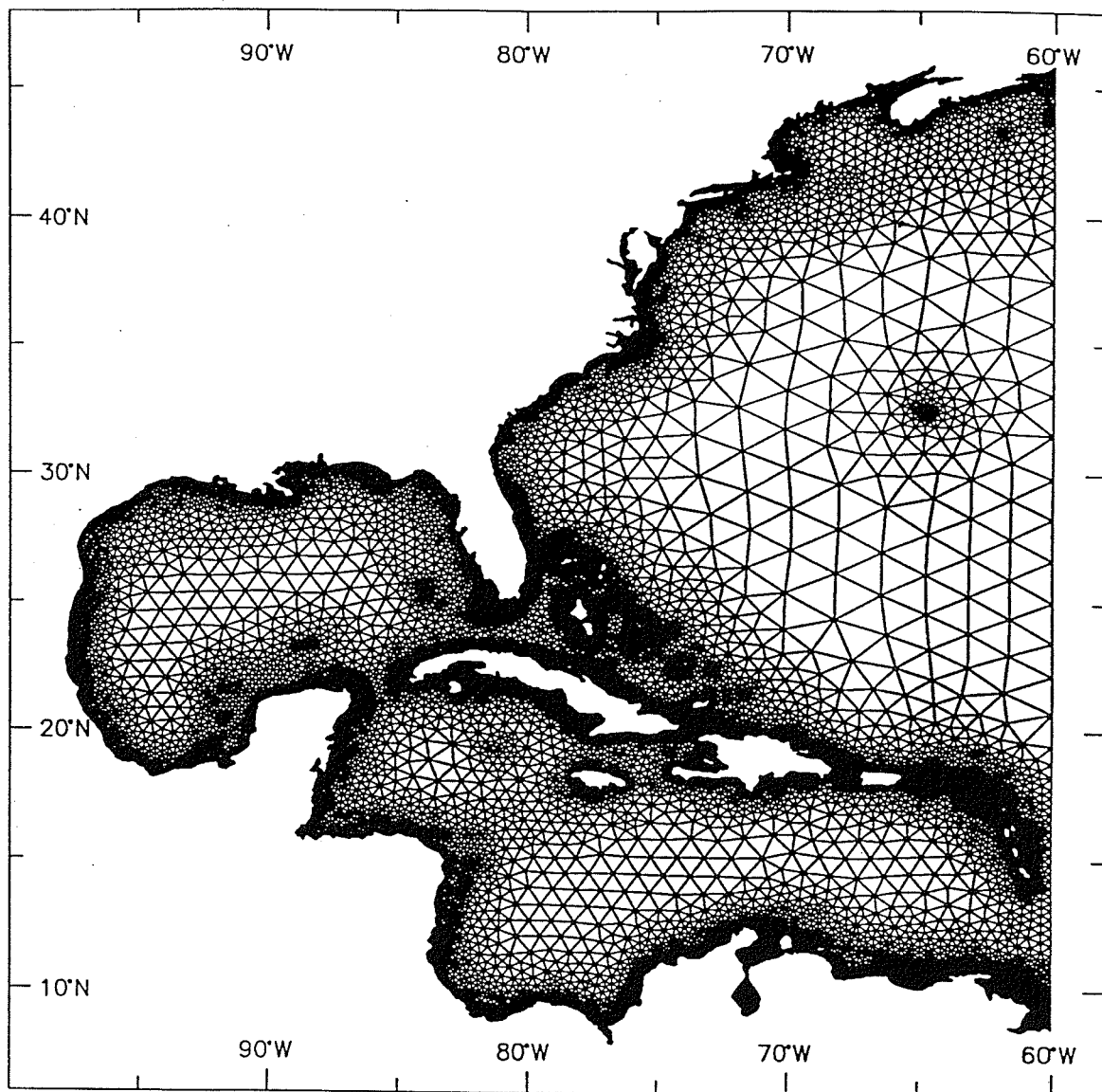
Figure 7.   Grid V3: Graded finite element discretization of the domain based on a $\lambda_{M_2}/\Delta x \geq 25$ criterion with additional resolution in the vicinity of the continental shelf break and with fine representation of the coastal boundary
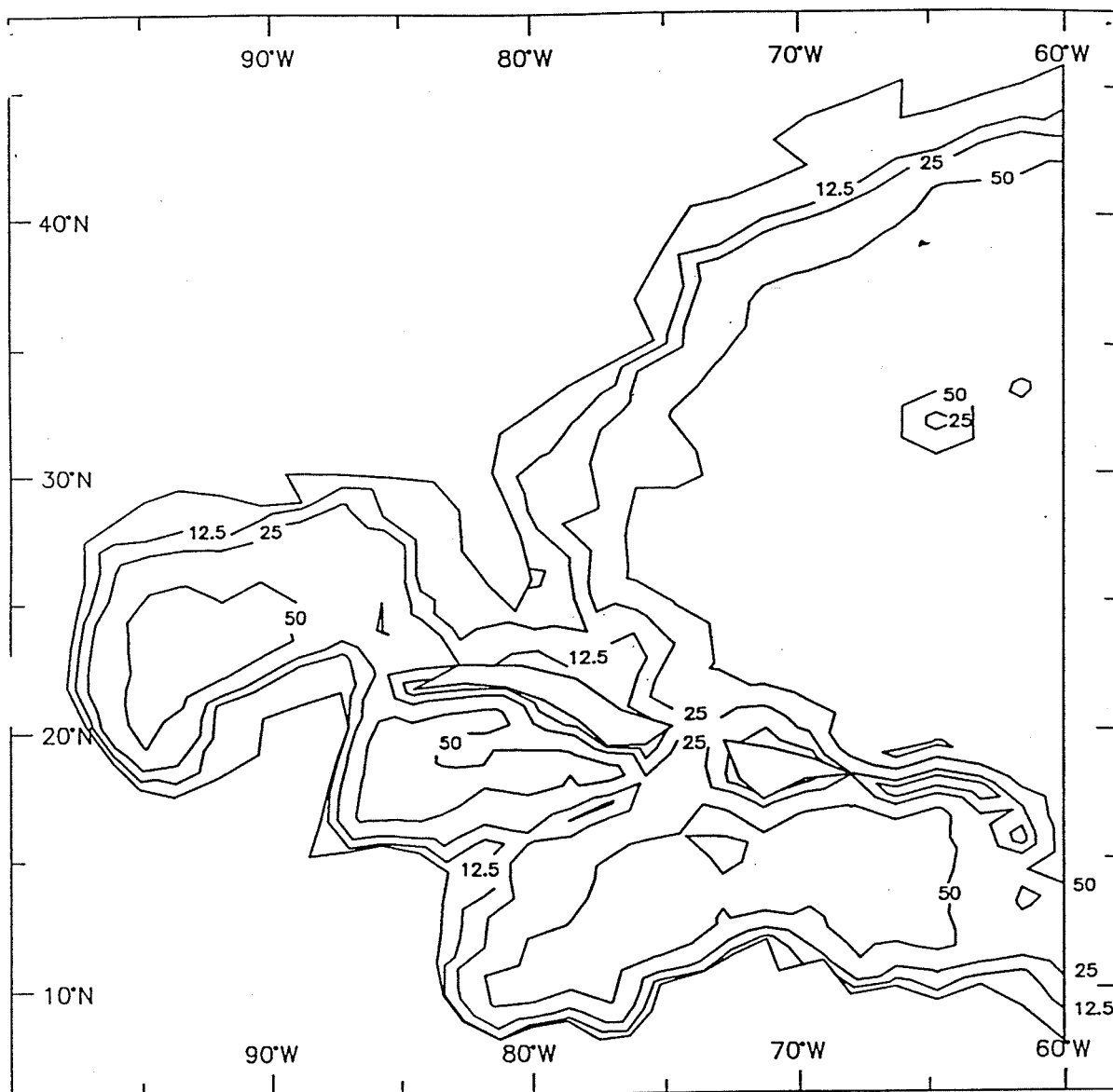
Figure 8.   Distribution of $\lambda_{M_2}/\Delta x \geq 25$ contours for grid R1
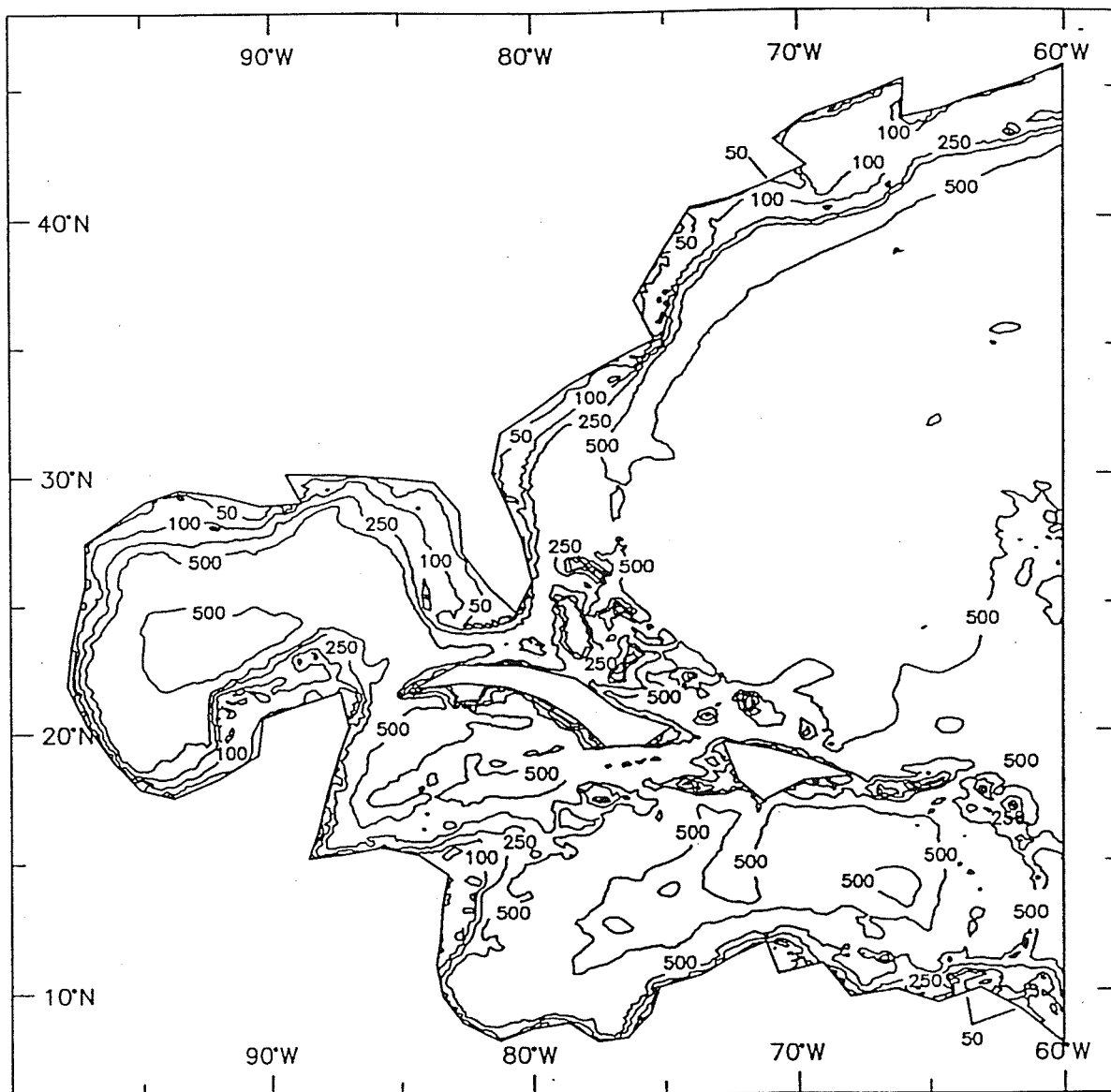
Figure 9. Distribution of $\lambda_{M_2}/\Delta x \geq 25$ contours for grid R5
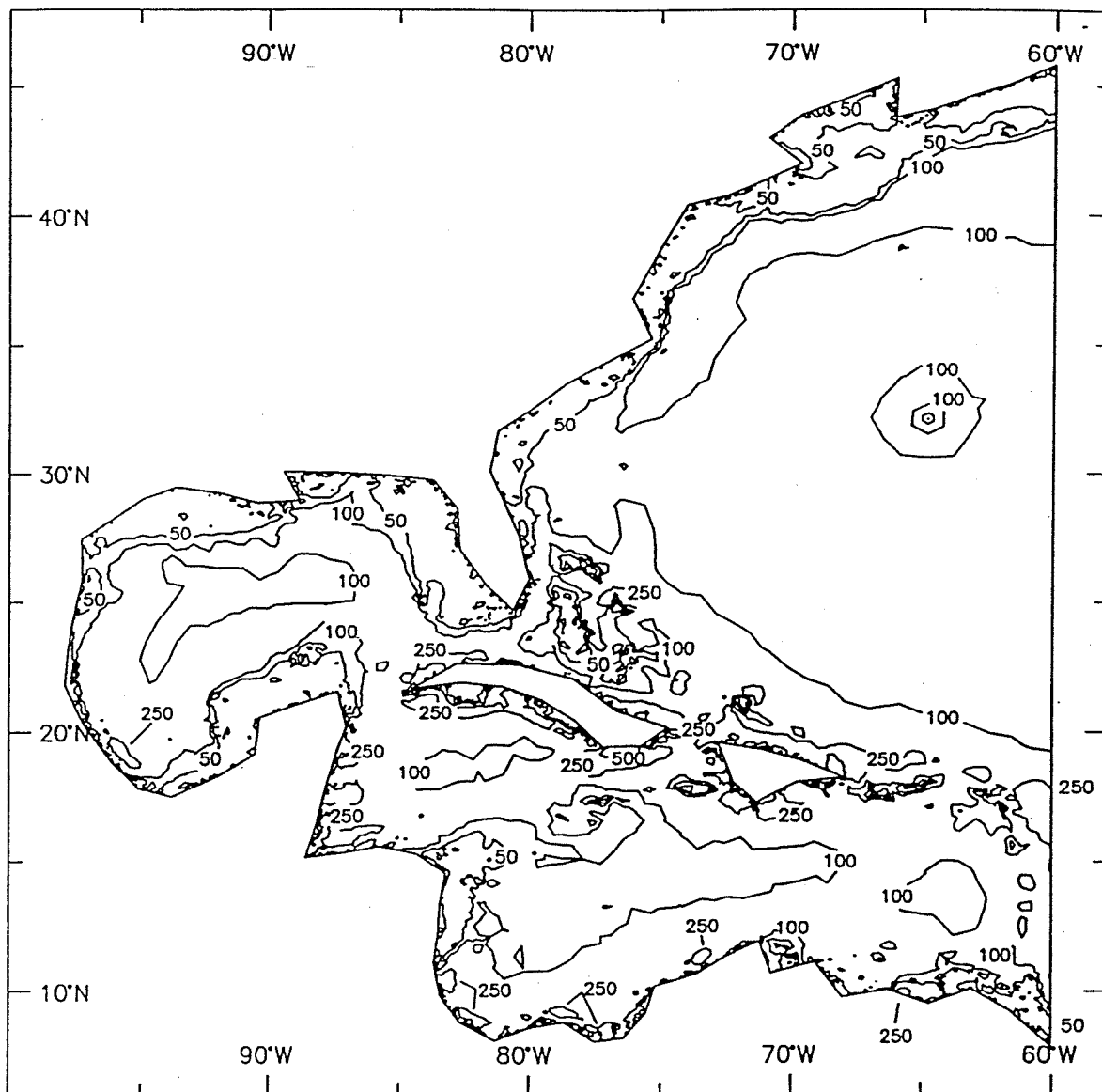
Figure 10.   Distribution of $\lambda_{M_2}/\Delta x \geq 25$ contours for grid V1
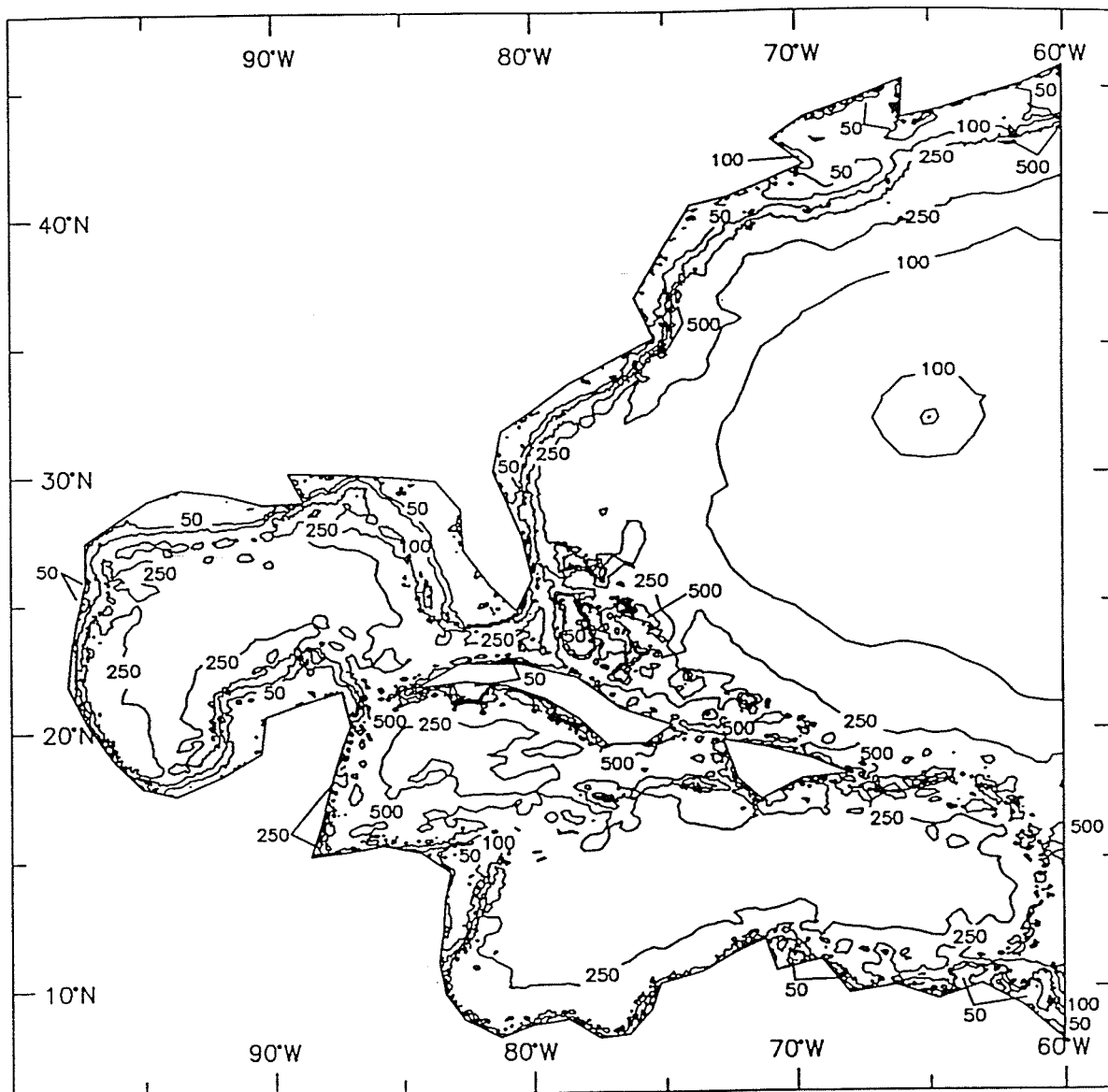
Figure 11.   Distribution of $\lambda_{M_2}/\Delta x \geq 25$ contours for grid V2
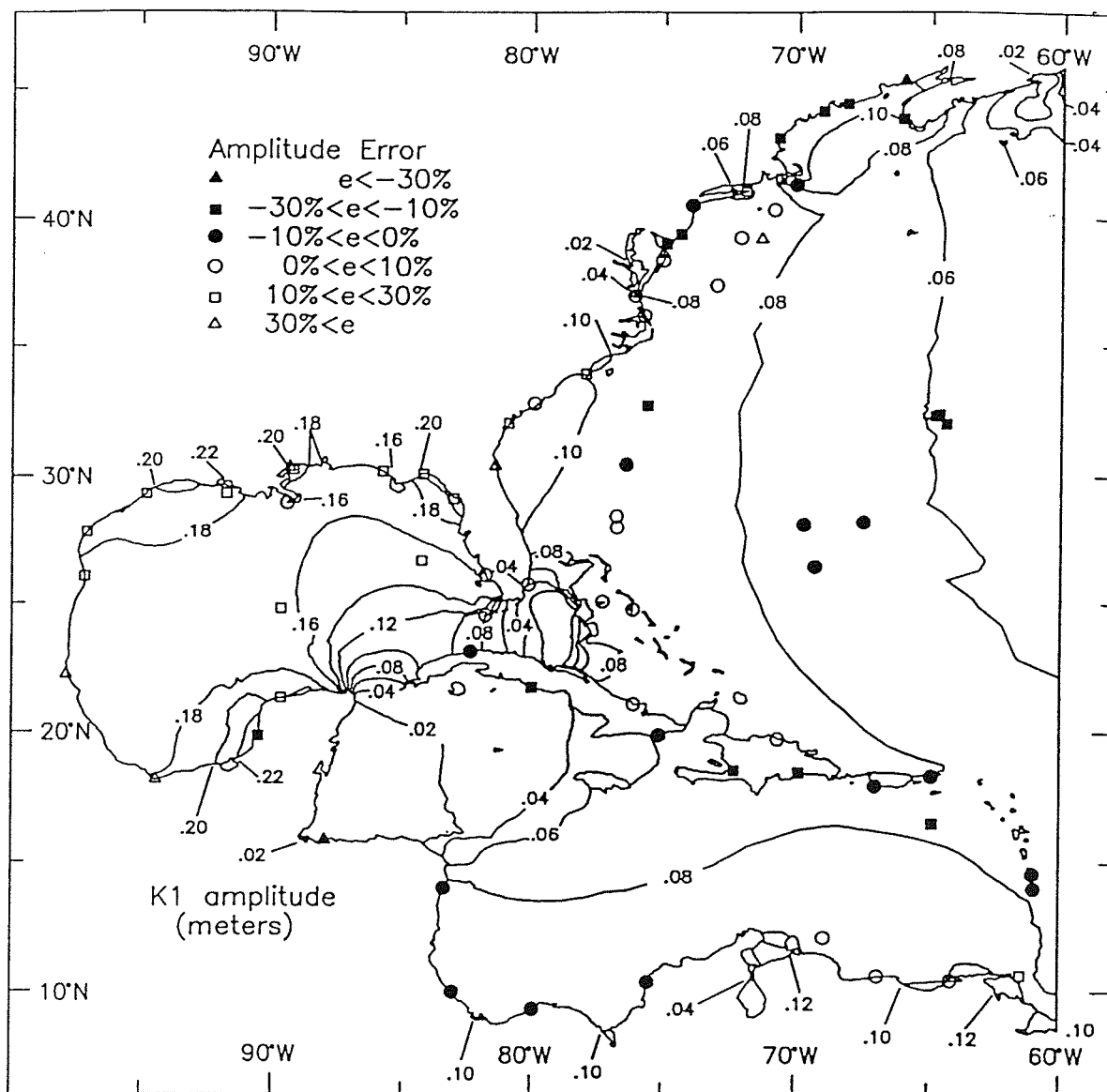
Figure 12.   Computed contours for elevation amplitudes (in meters) and phases (in degrees relative to GMT) for the four diurnal astronomical tidal constituents used in the boundary and interior domain forcing functions (Sheet 1 of 8)
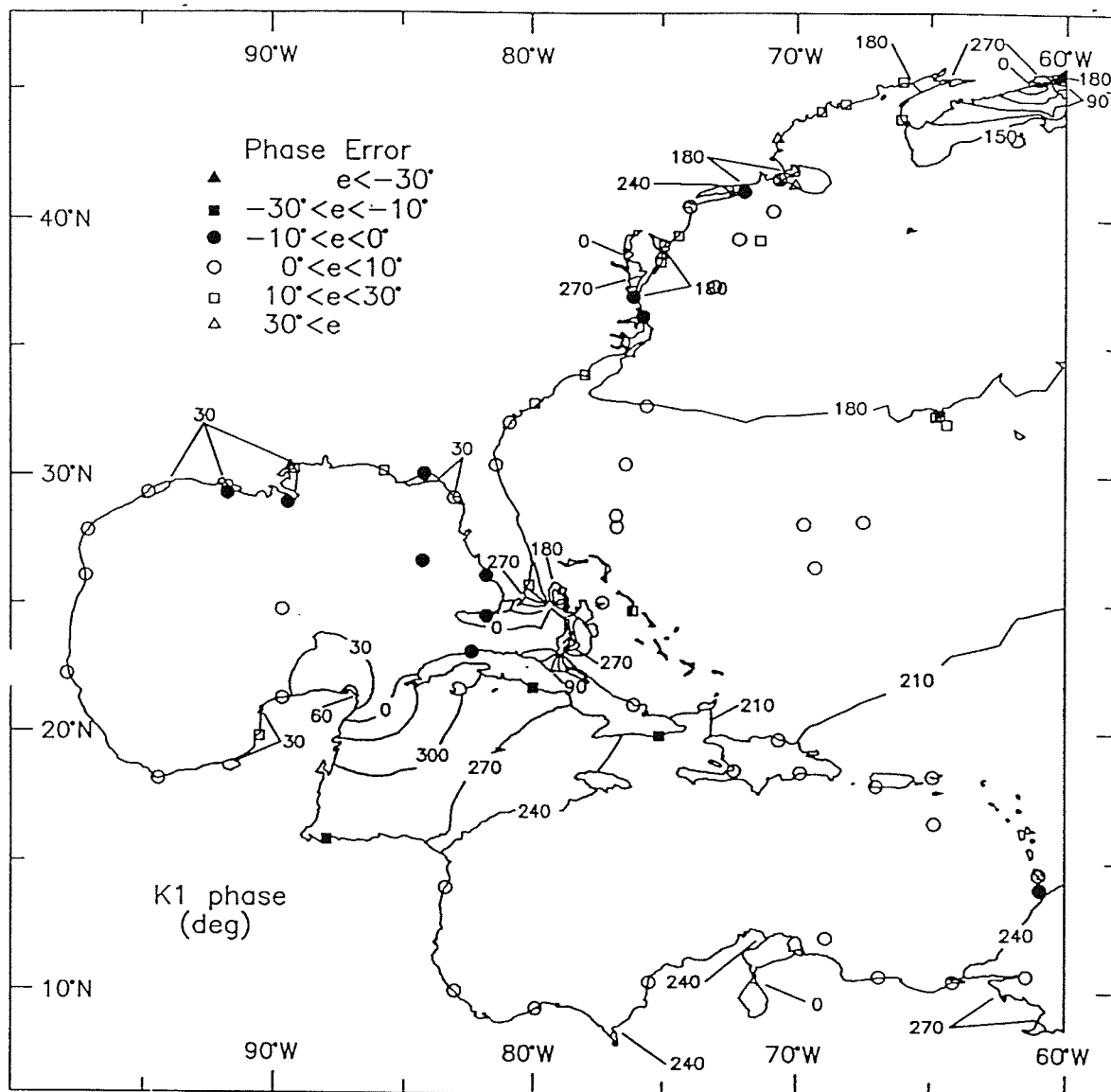
Figure 12.   (Sheet 2 of 8)
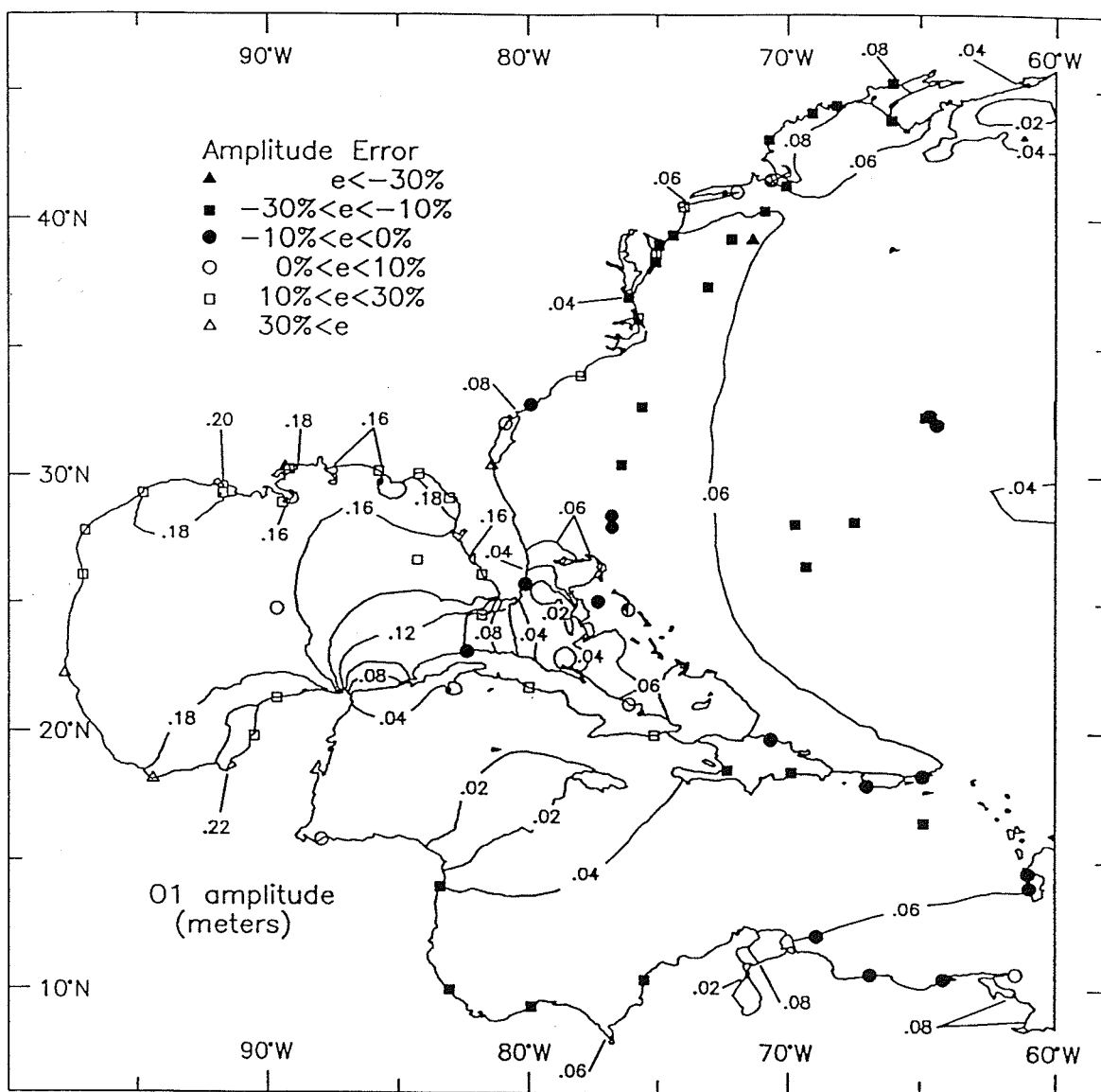
Figure 12.   (Sheet 3 of 8)
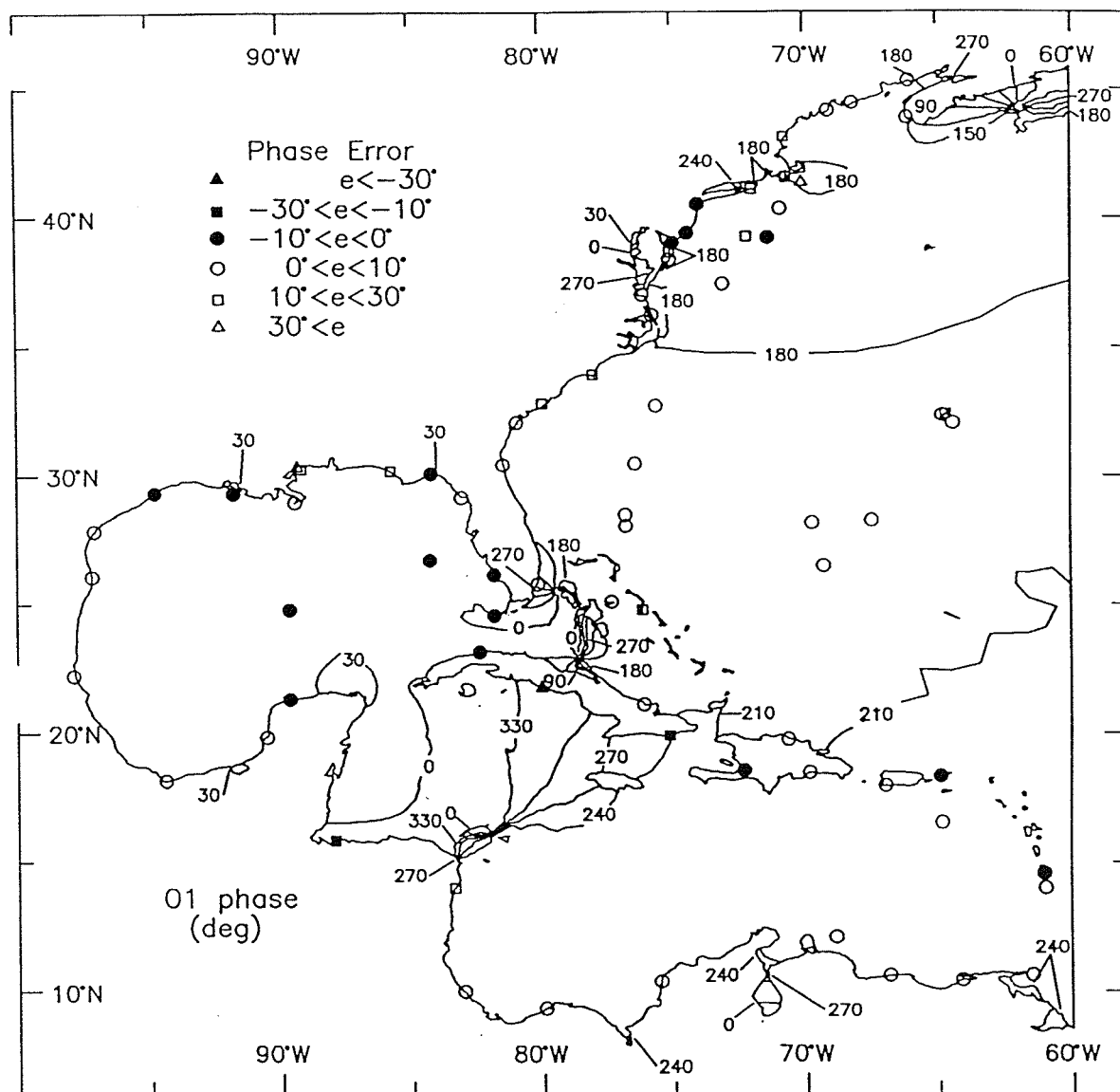
Figure 12.   (Sheet 4 of 8)
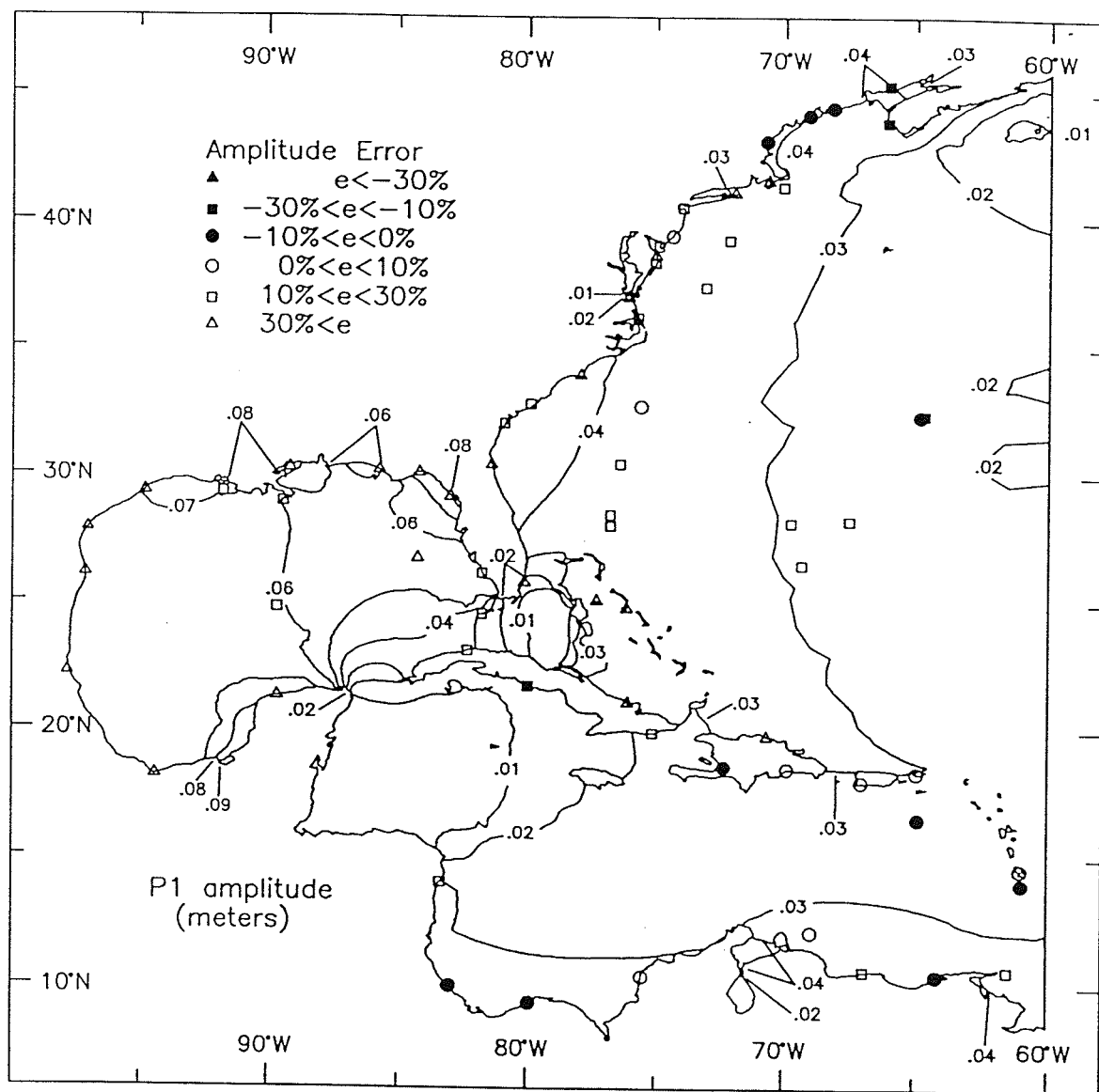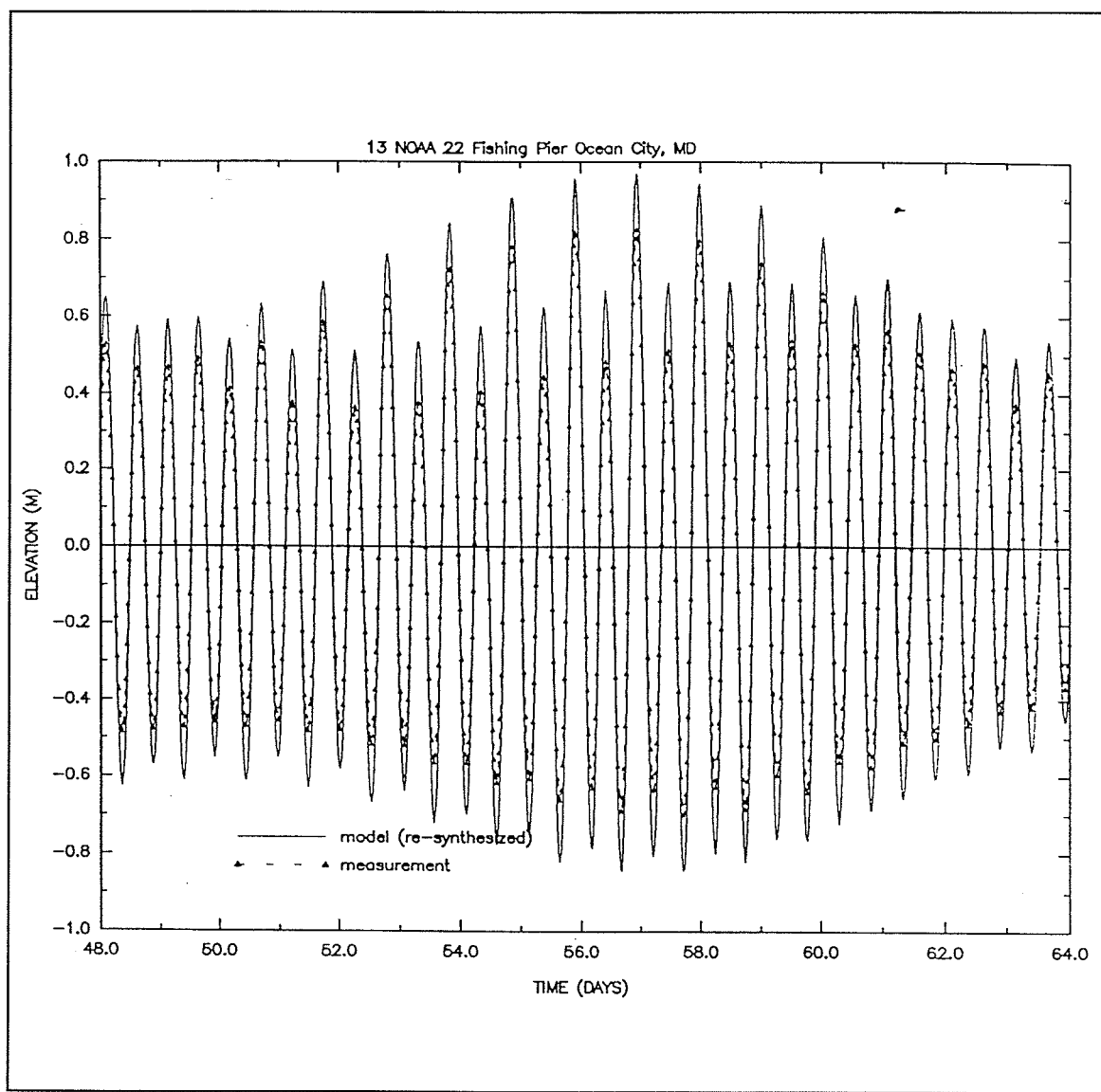
Figure 12.   (Sheet 5 of 8)
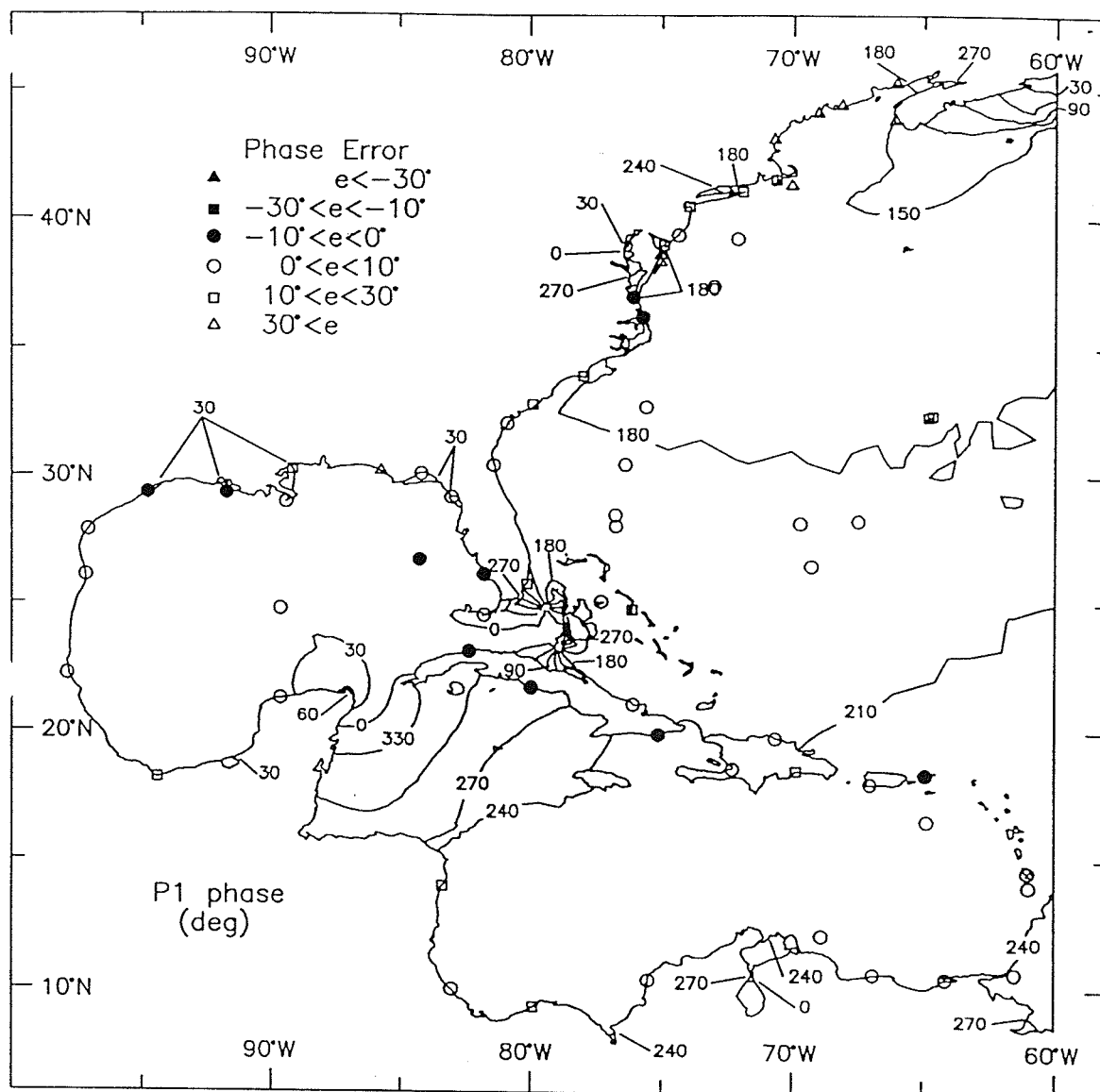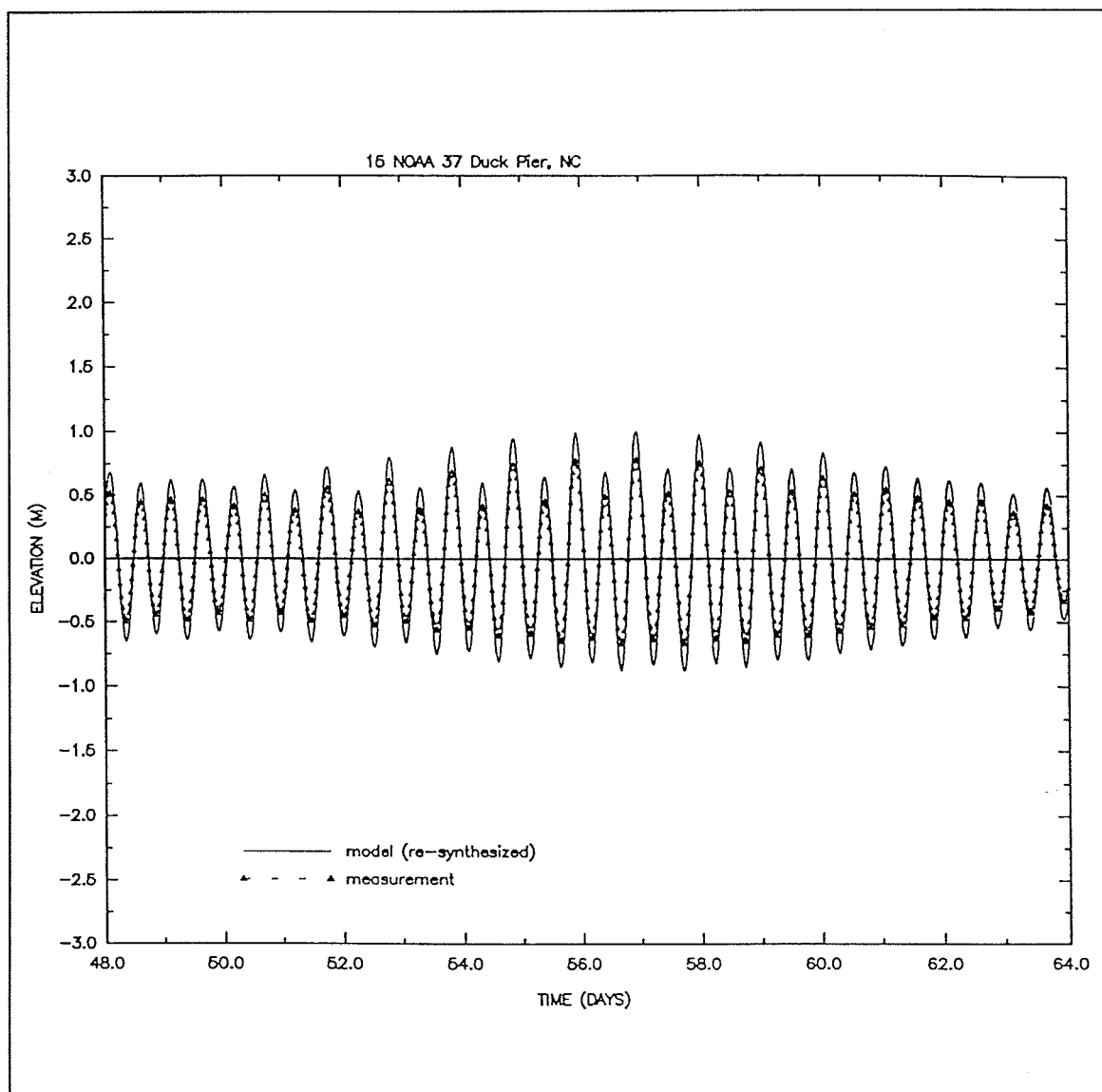
Figure 12. (Sheet 6 of 8)
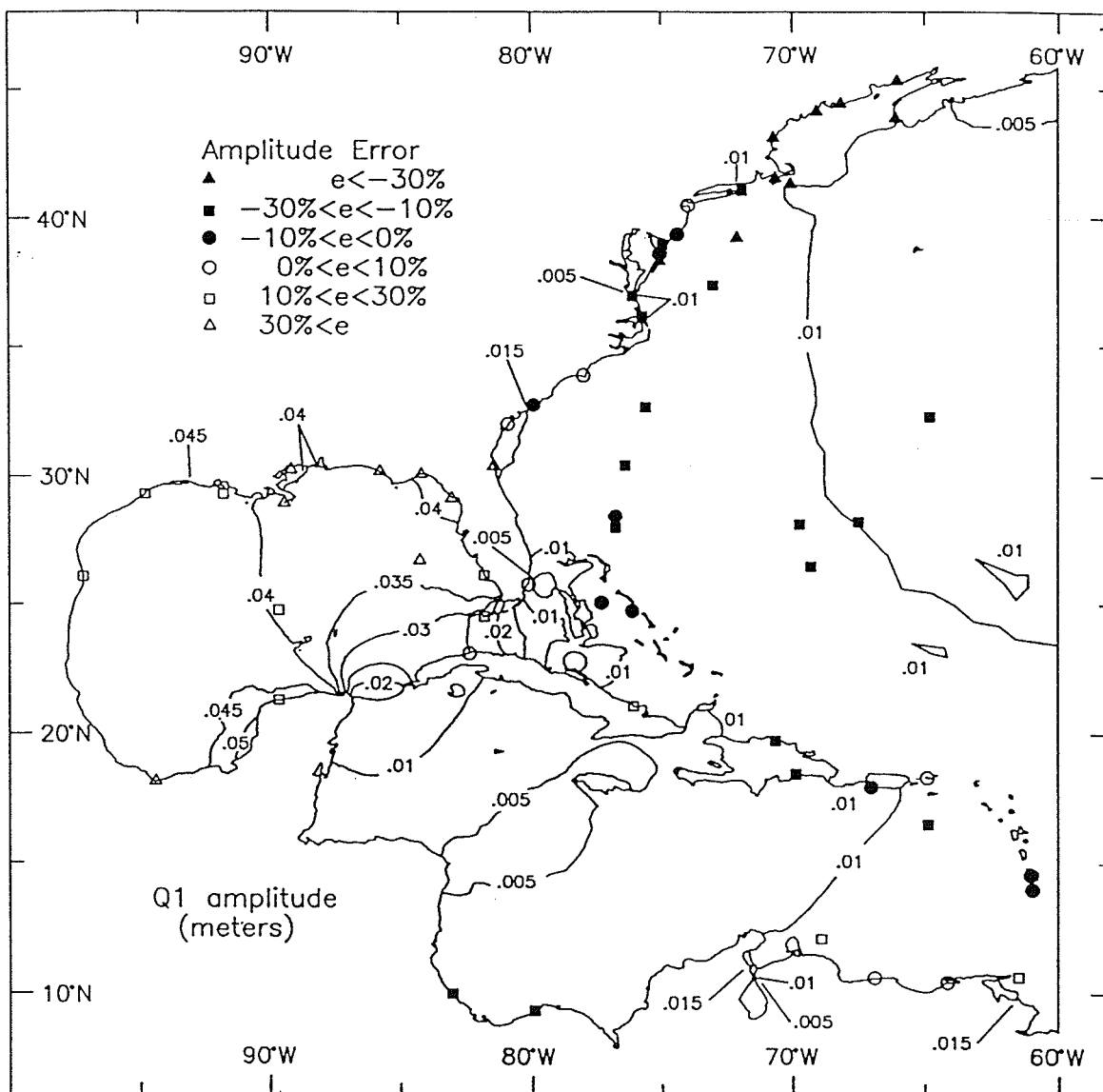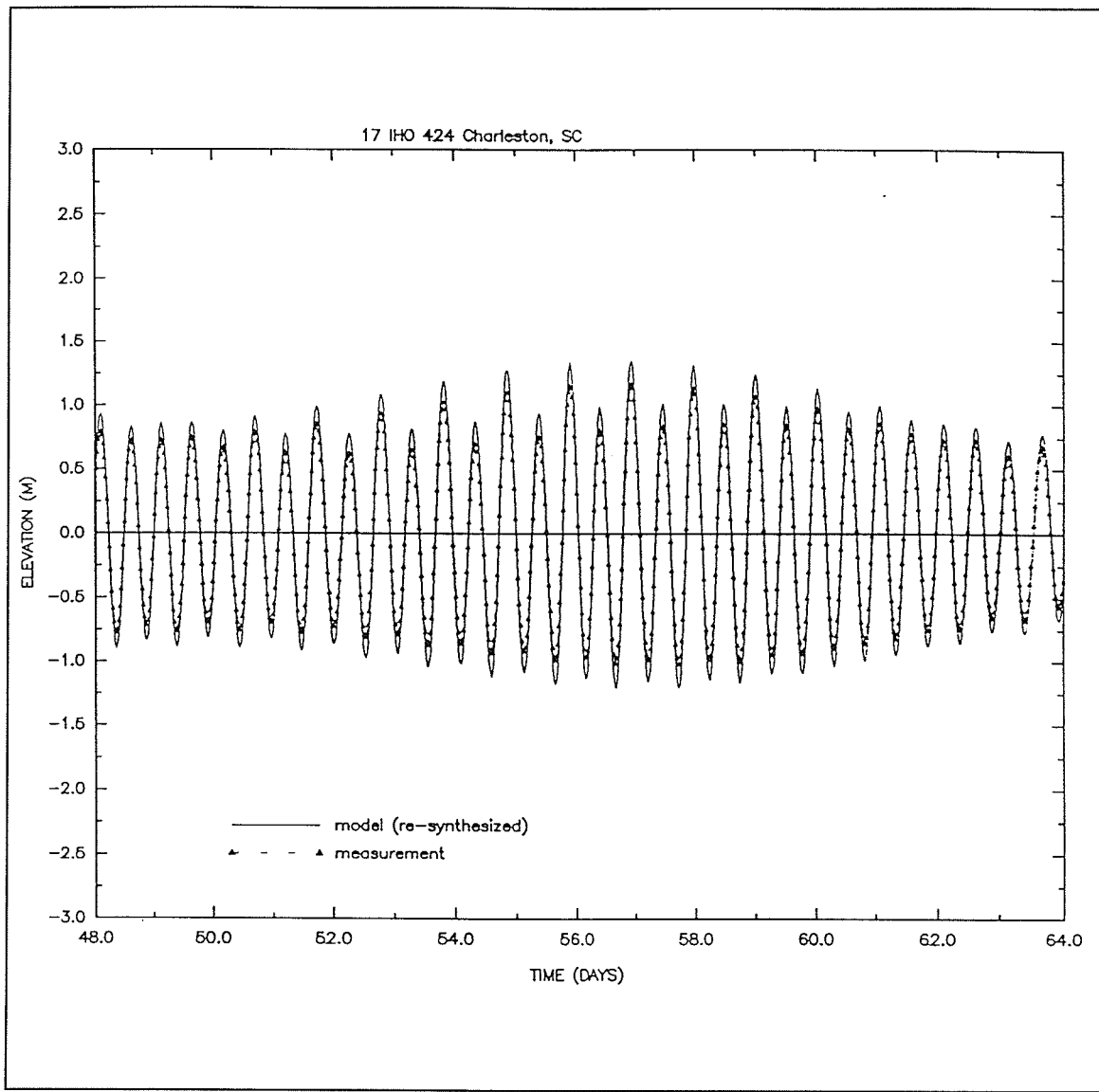
Figure 12. (Sheet 7 of 8)
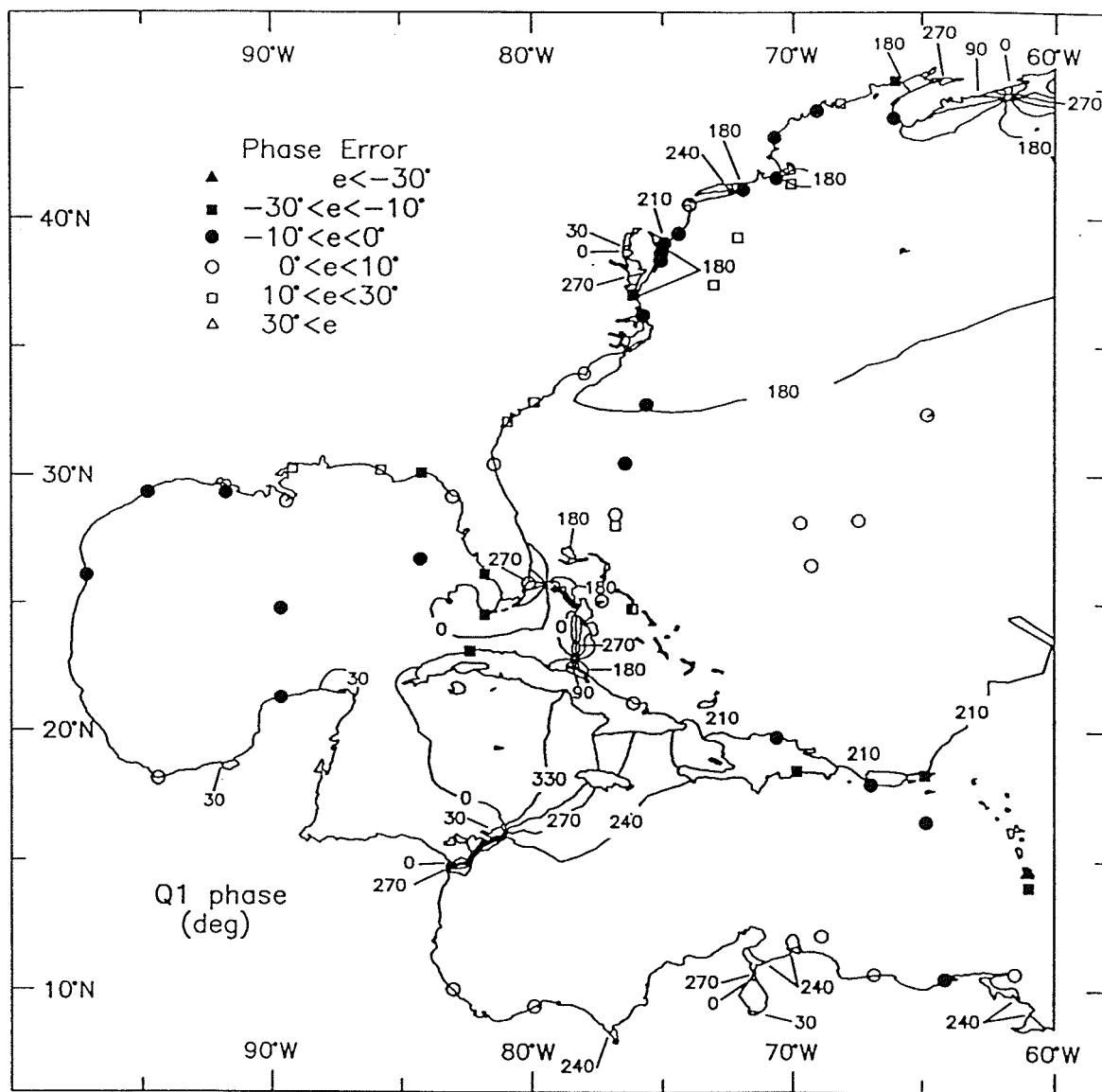
Figure 12. (Sheet 8 of 8)
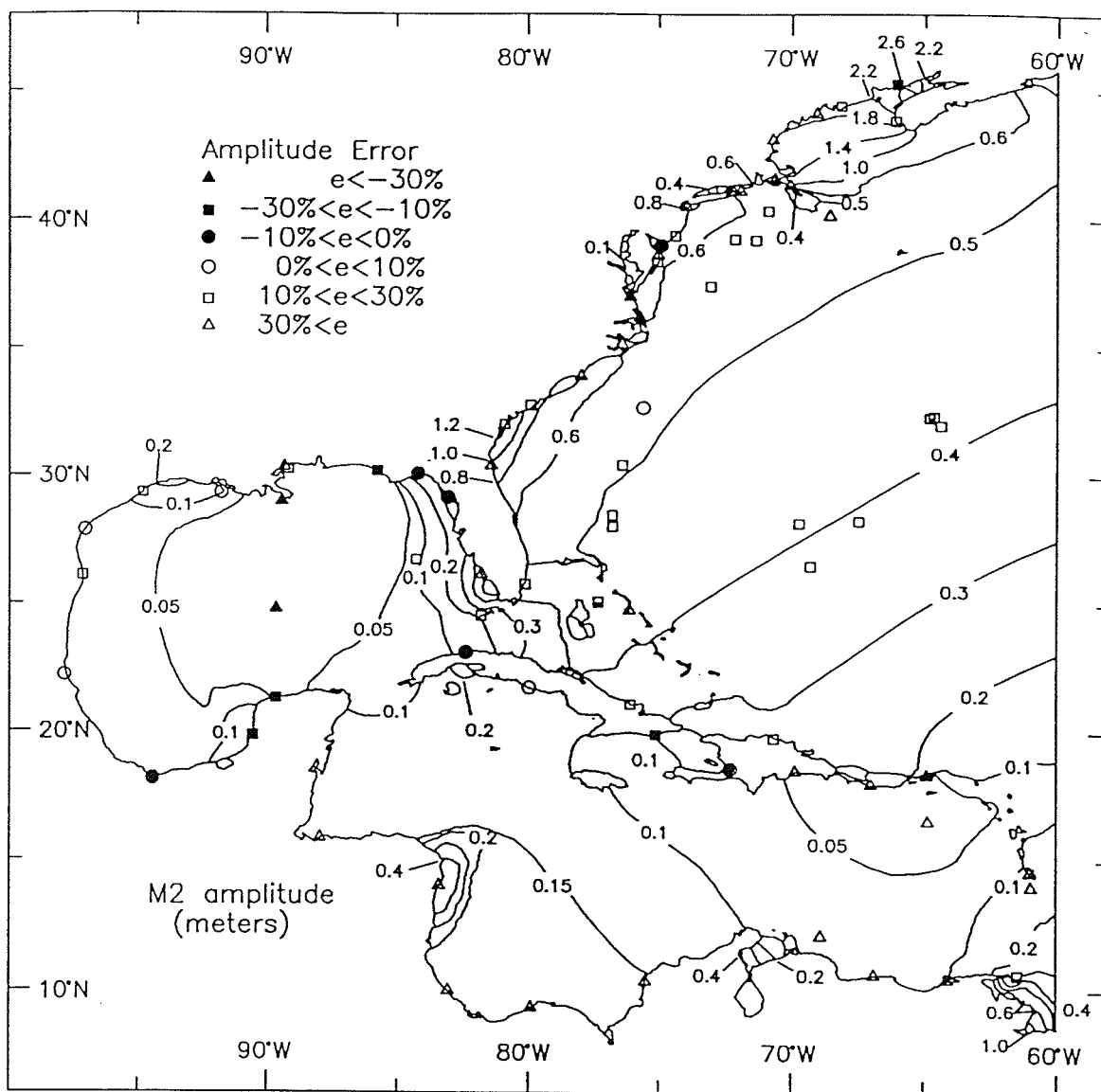
Figure 13.   Computed contours for elevation amplitudes (in meters) and phases (in degrees relative to GMT) for the four semidiurnal astronomical tidal constituents used in the boundary and interior domain forcing functions (Sheet 1 of 8)
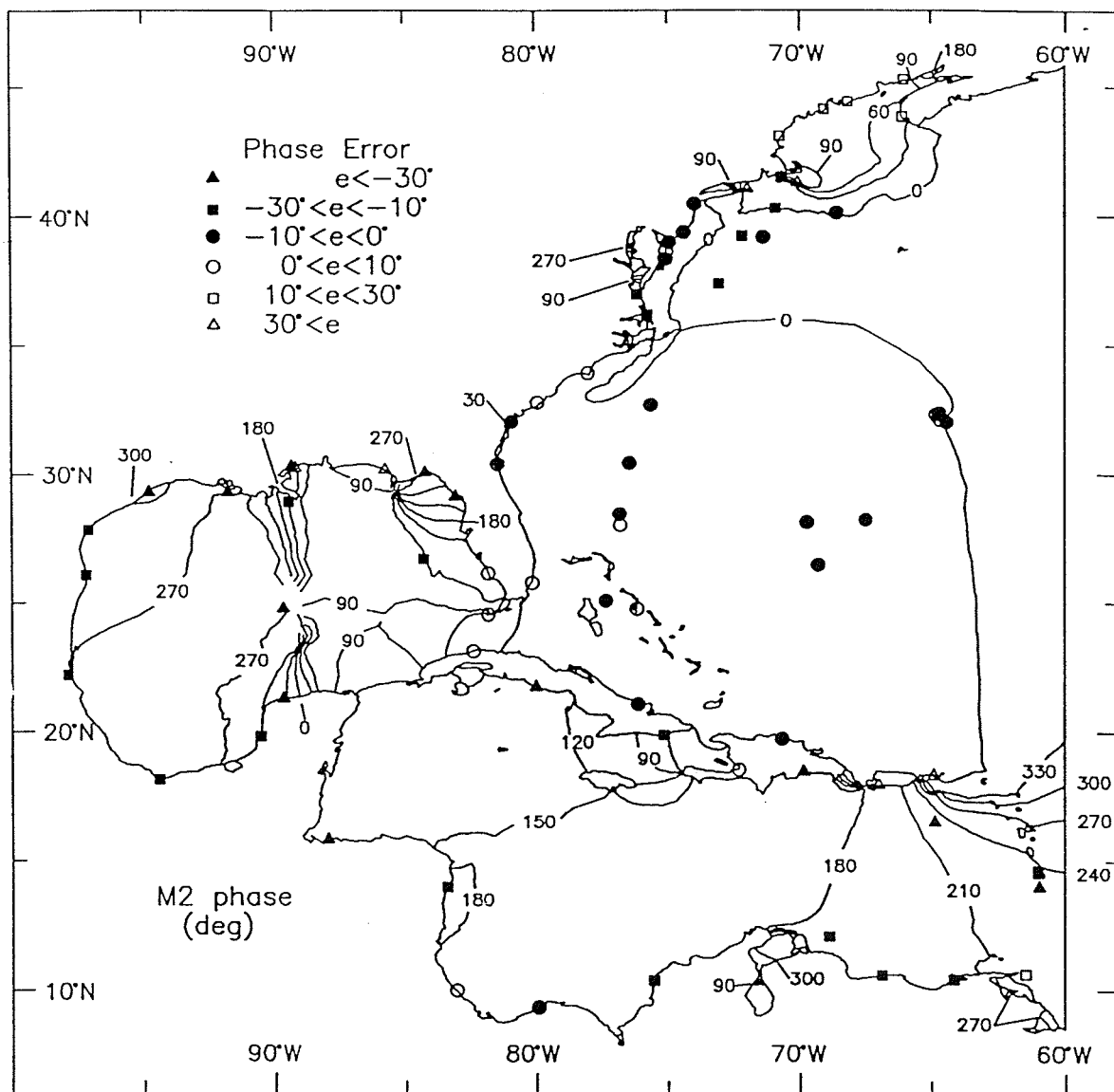
Figure 13.   (Sheet 2 of 8)

Figure 13. (Sheet 3 of 8)
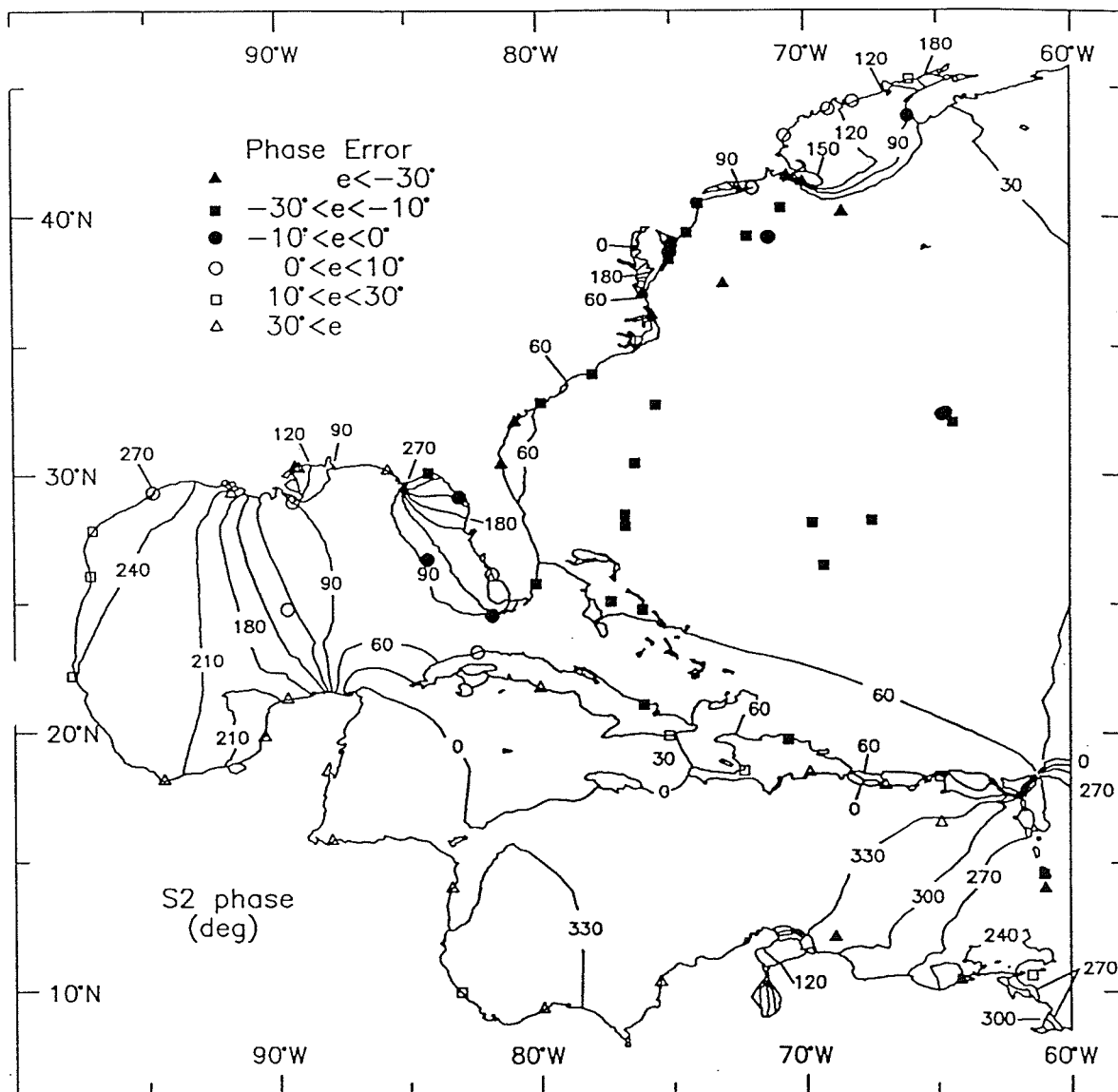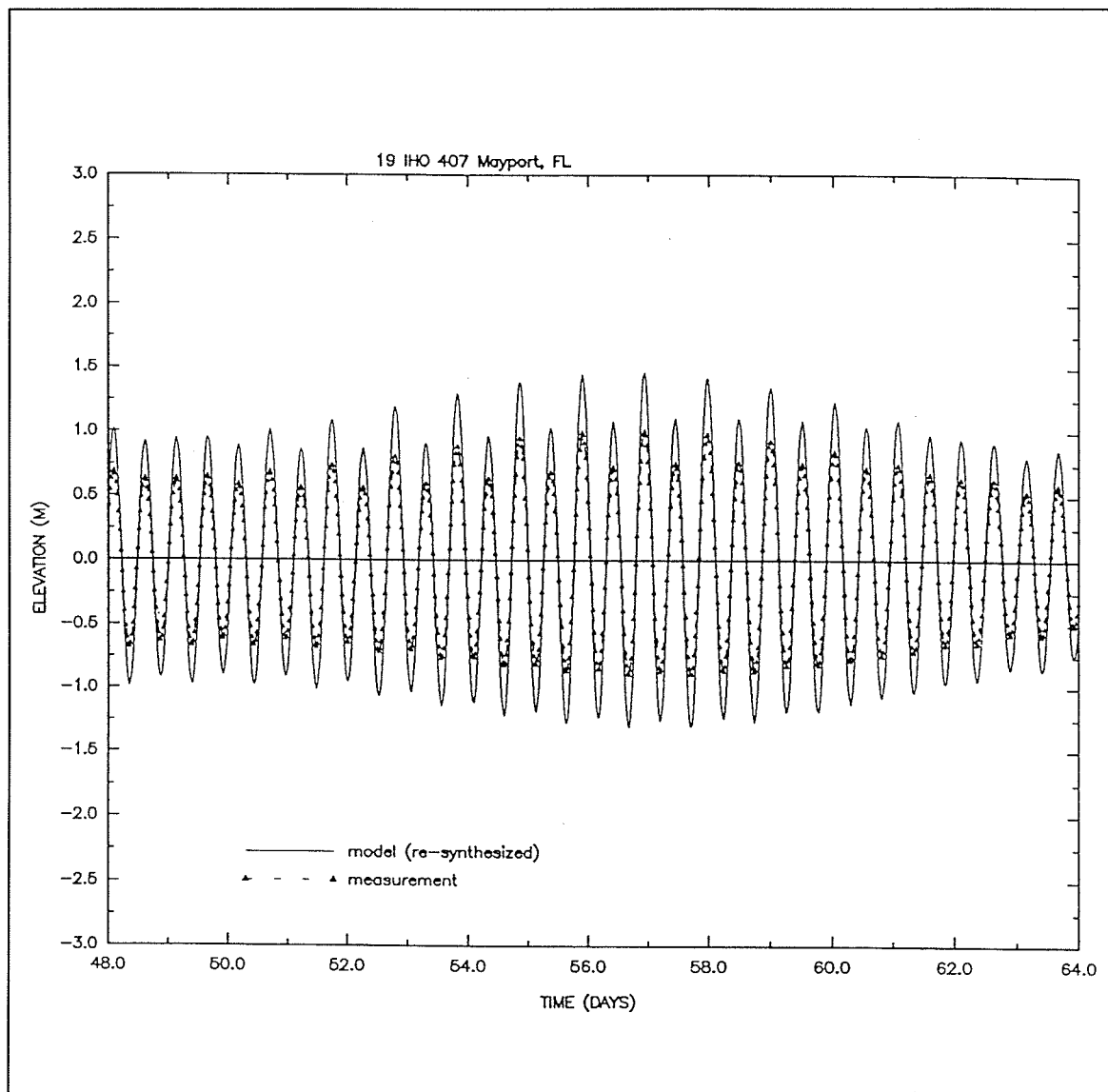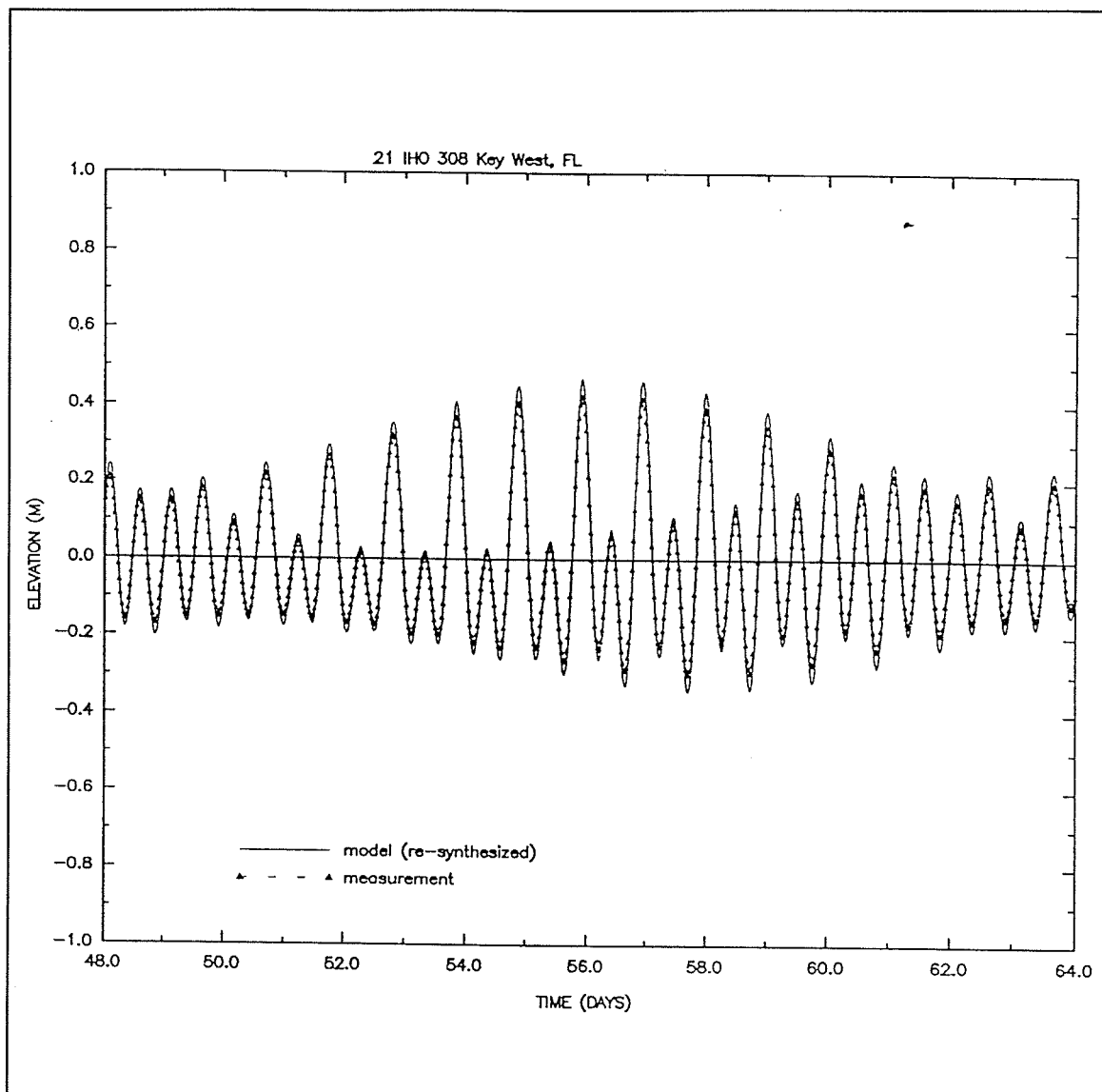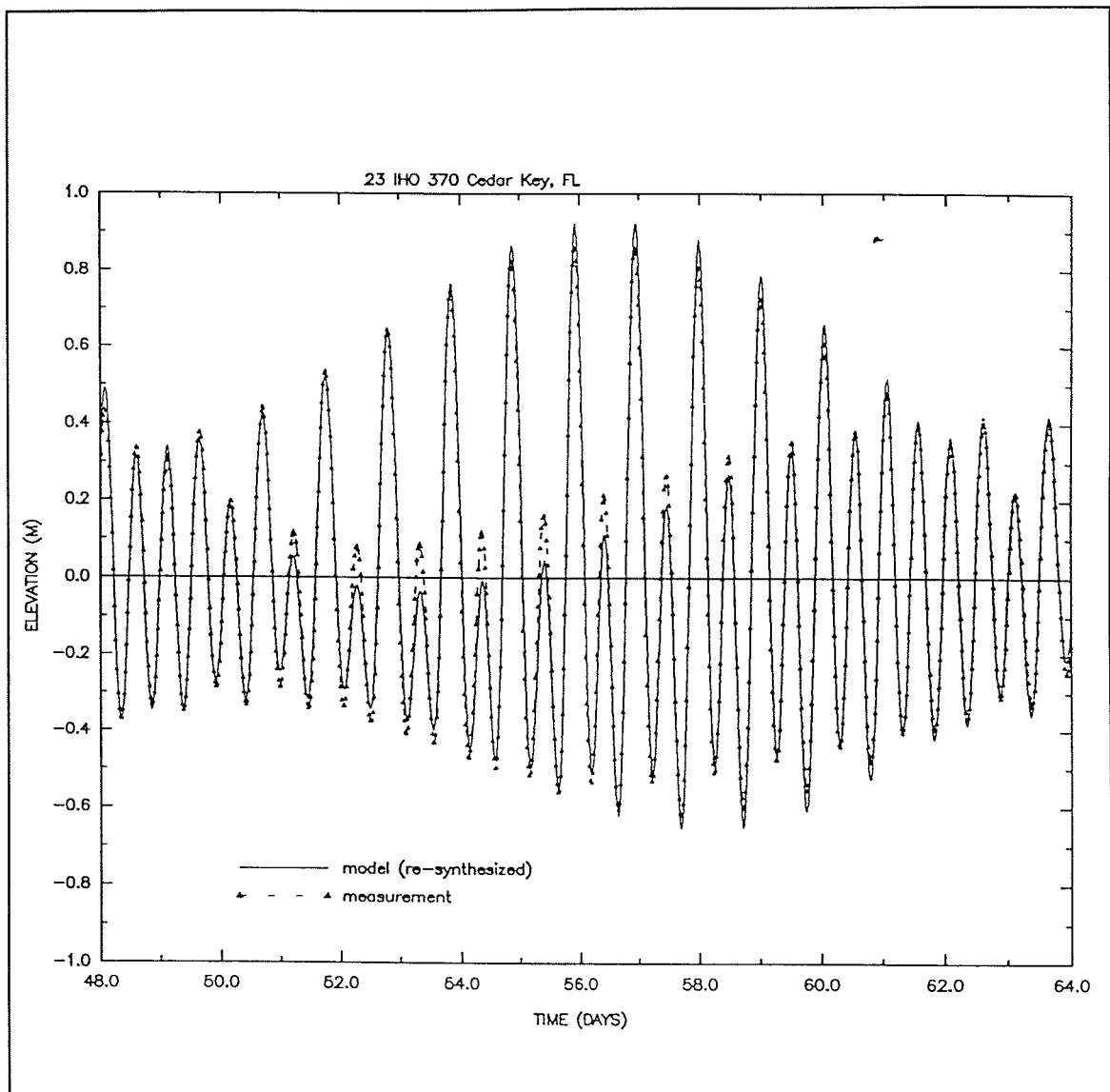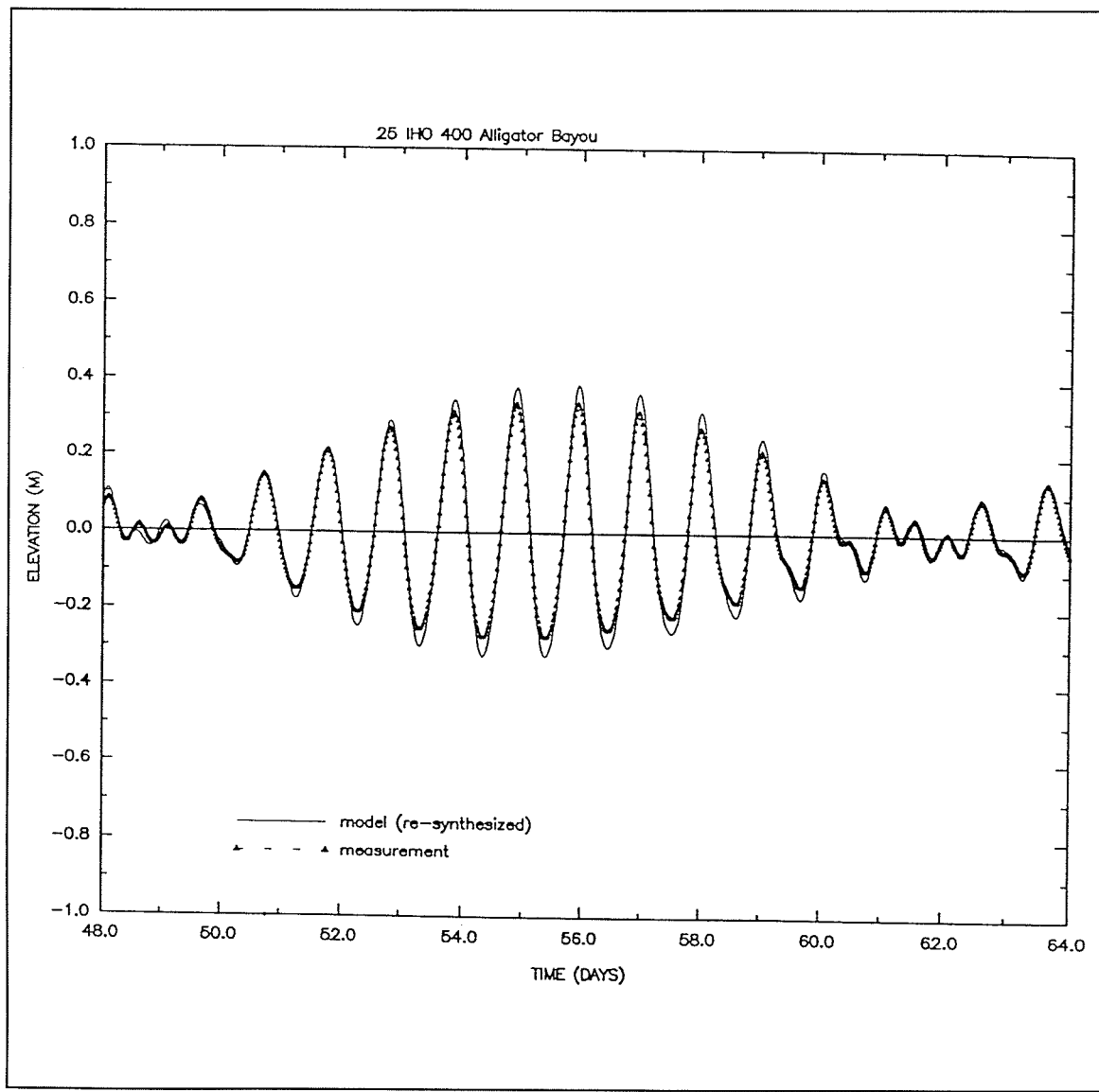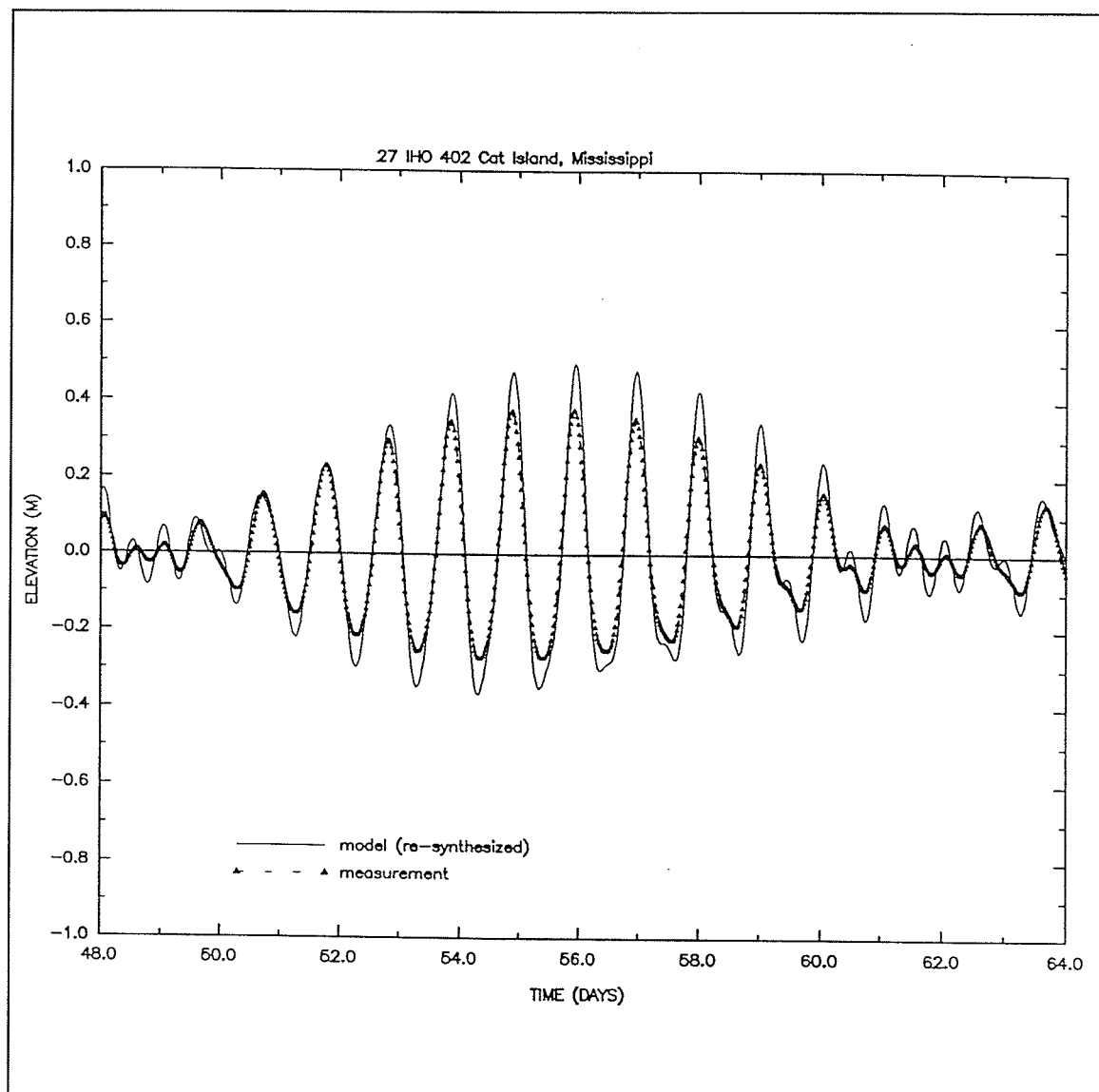
Figure 13.   (Sheet 4 of 8)
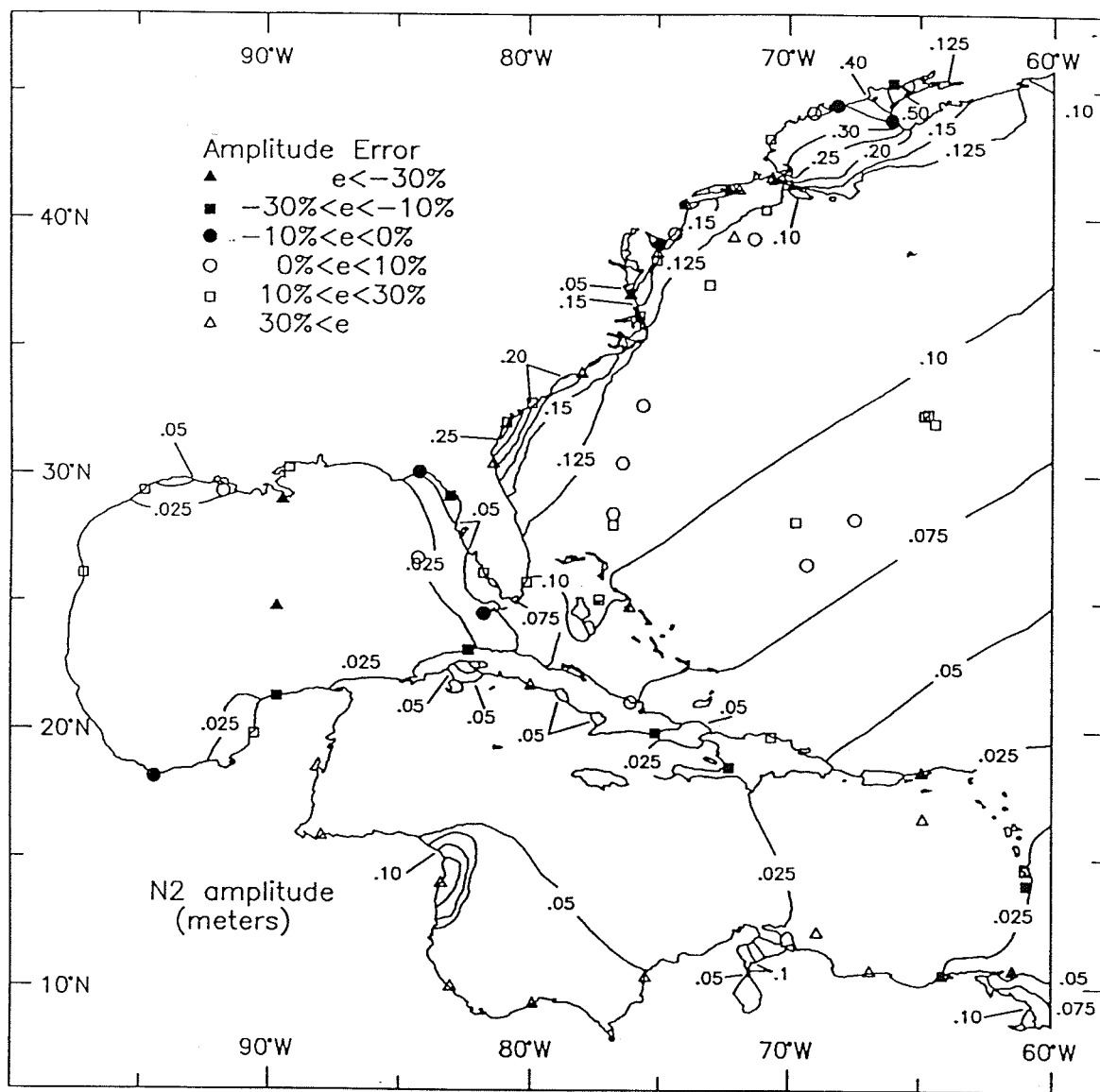
Figure 13.   (Sheet 5 of 8)
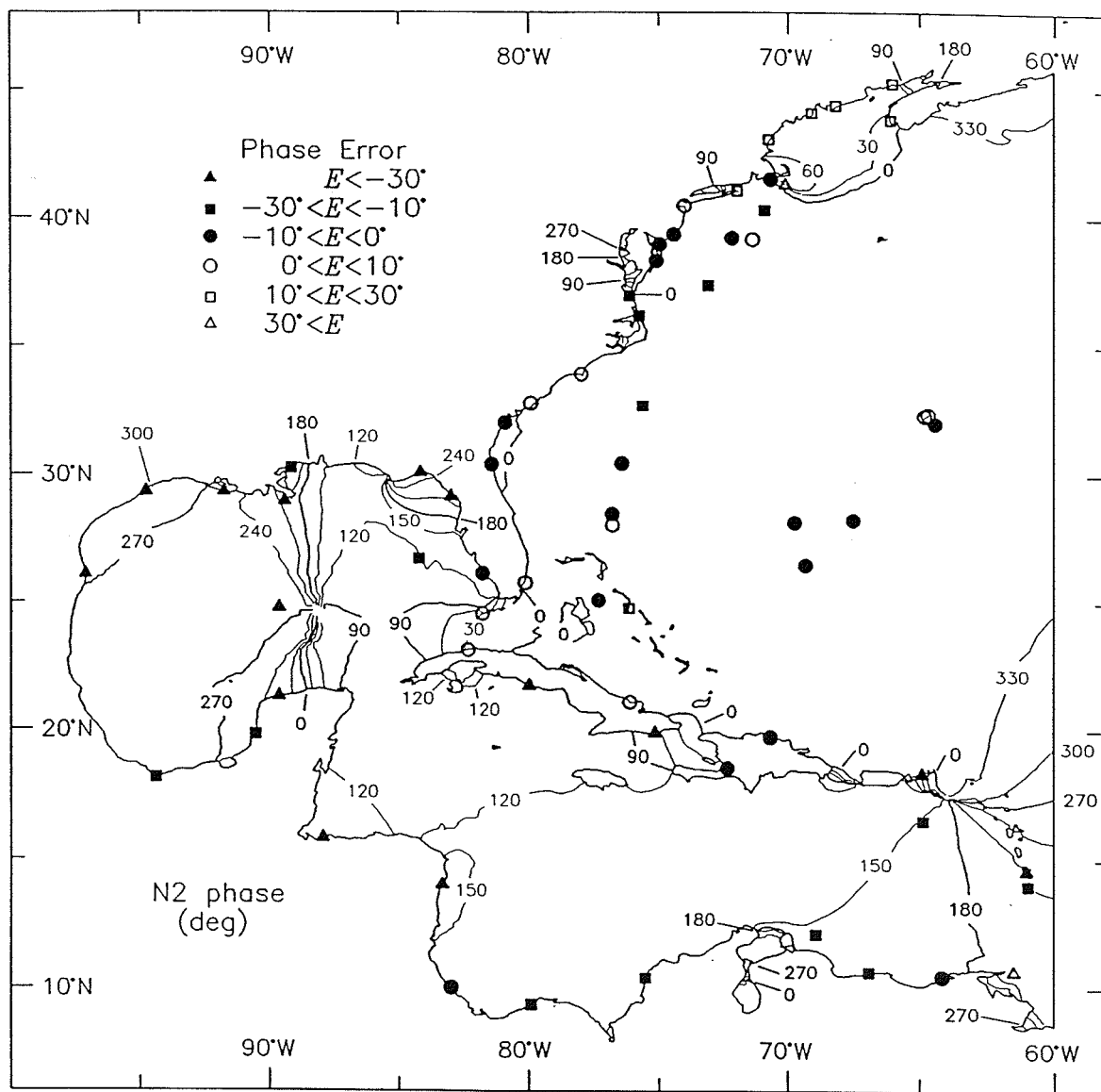
Figure 13. (Sheet 6 of 8)
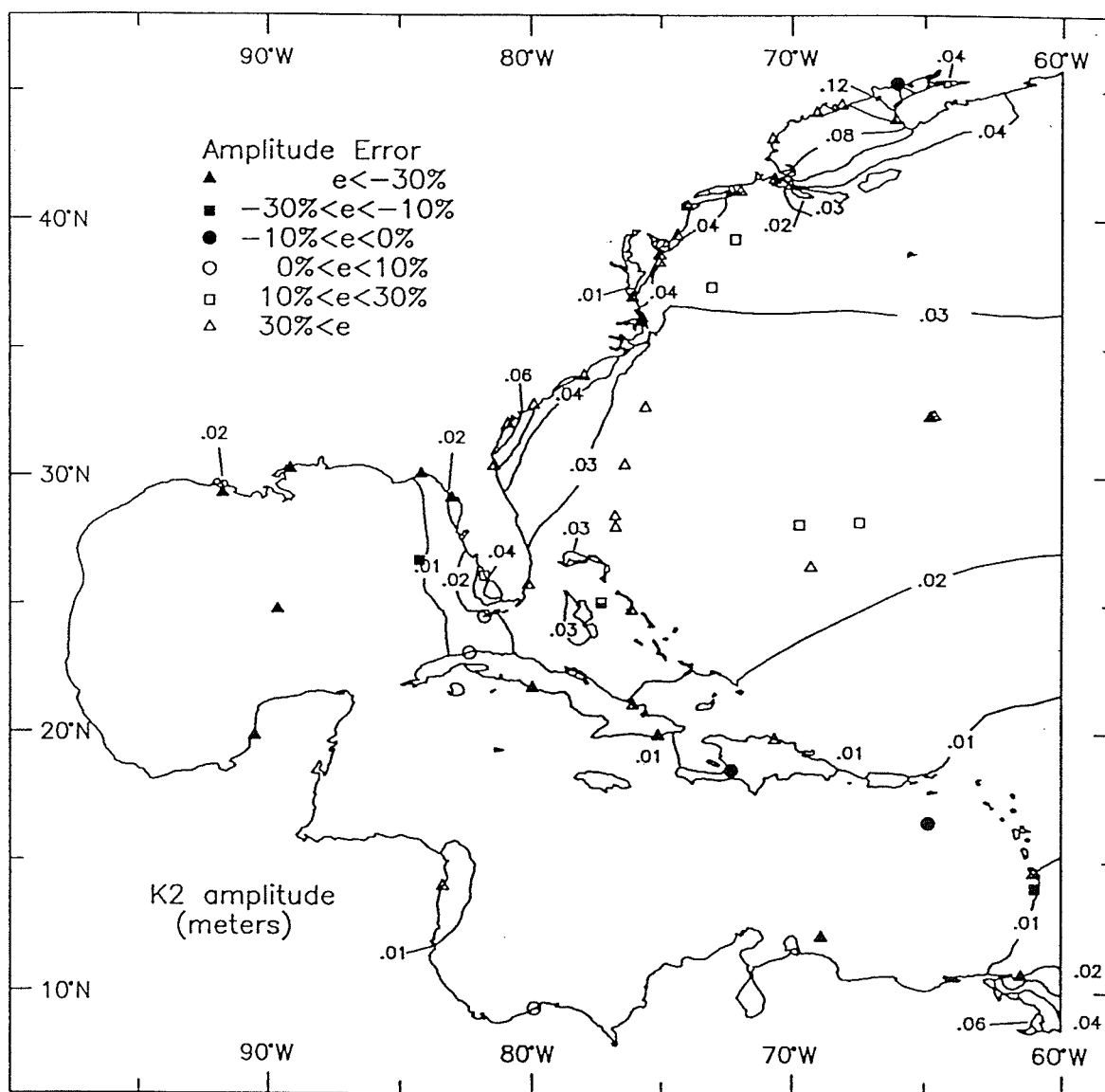
Figure 13. (Sheet 7 of 8)
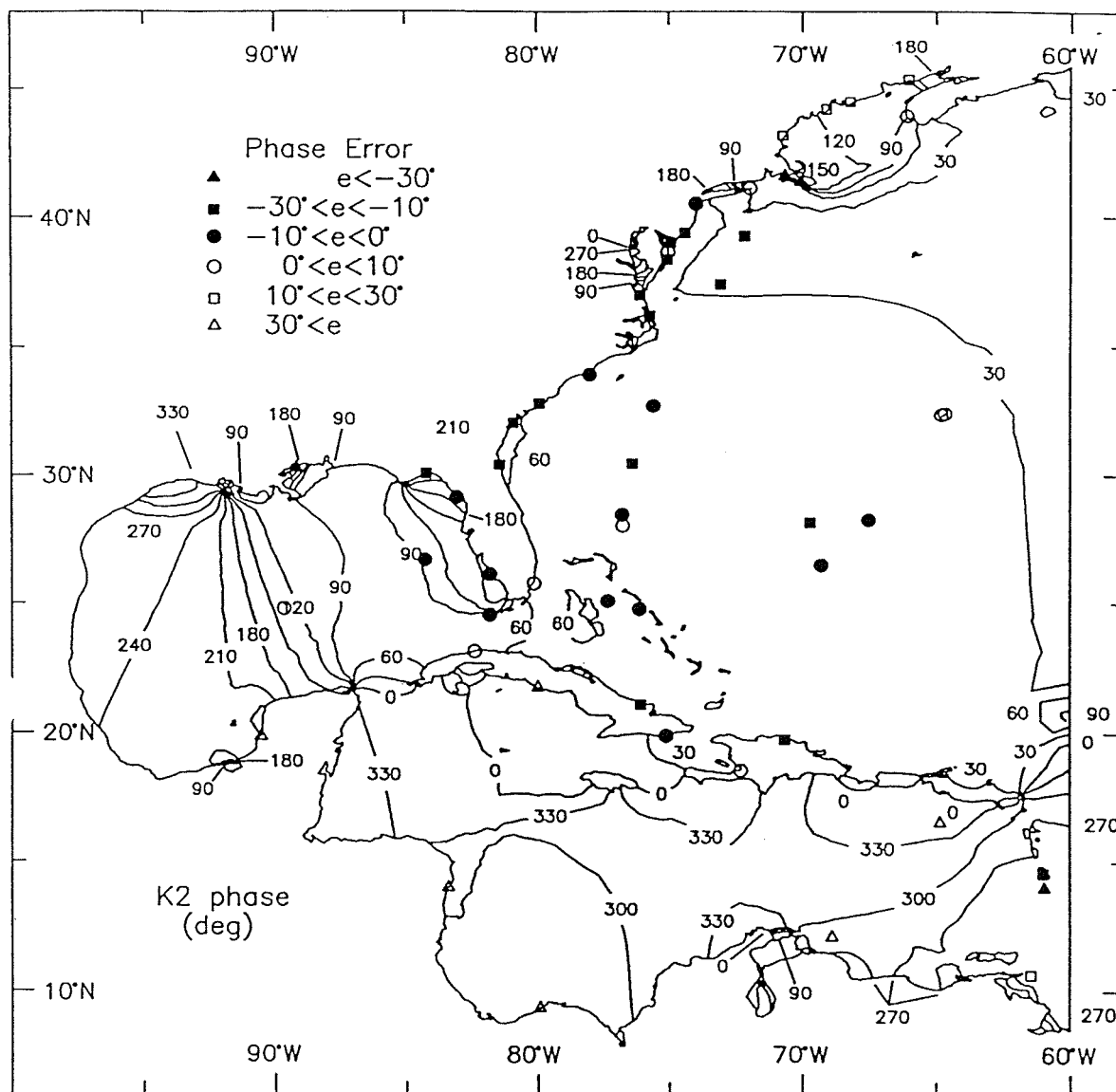
Figure 13. (Sheet 8 of 8)
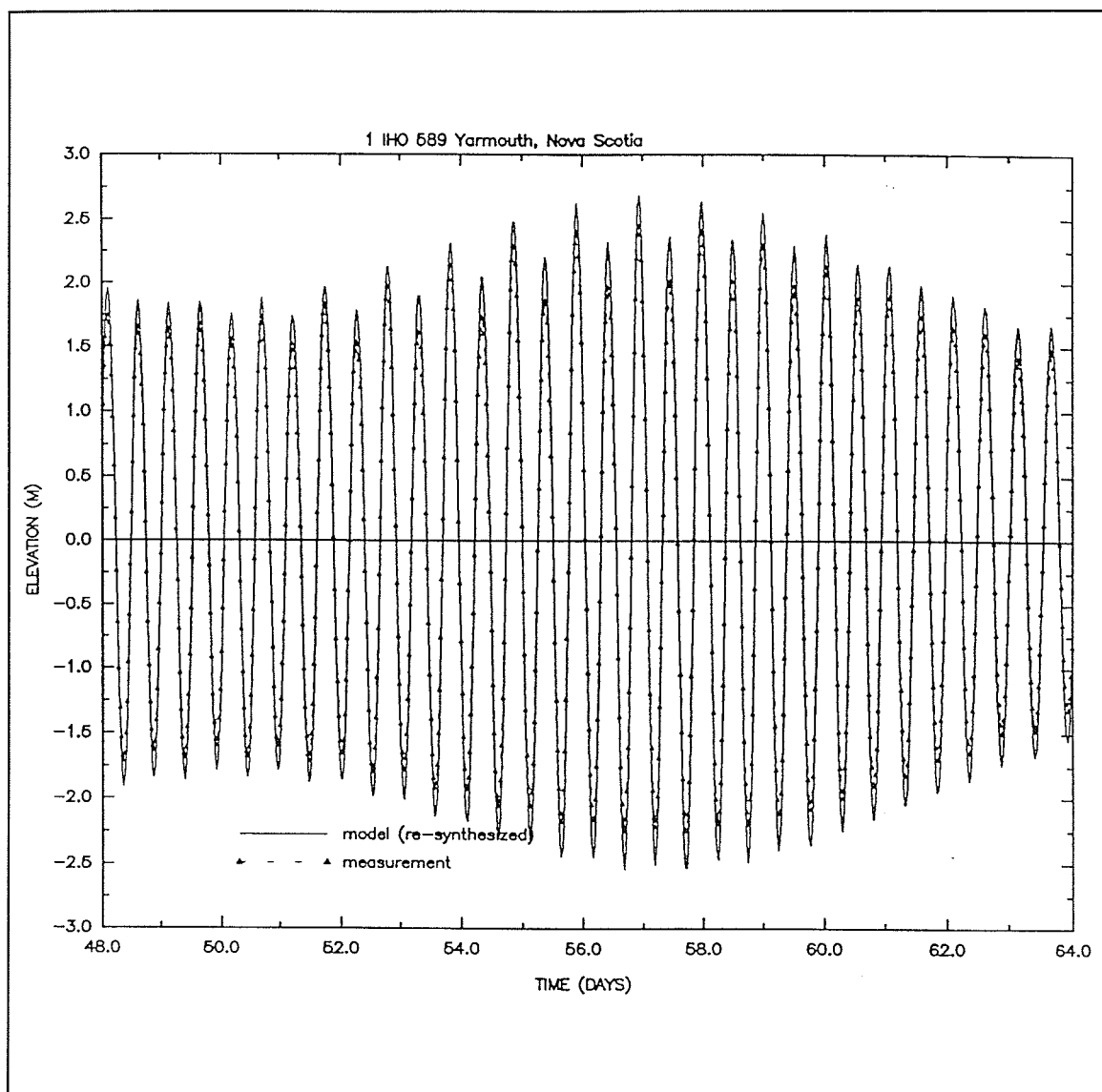
Figure 14.   Comparisons of time histories of resynthesized surface elevations from harmon-
ically decomposed computed constituent data and of synthesized surface
elevations from harmonically decomposed measured constituent data (using
the K_1, O_1, P_1, Q_1, M_2, N_2, S_2, and K_2 constituents) at representative tidal
stations within the Western North Atlantic tidal model domain (Sheet 1 of 39)
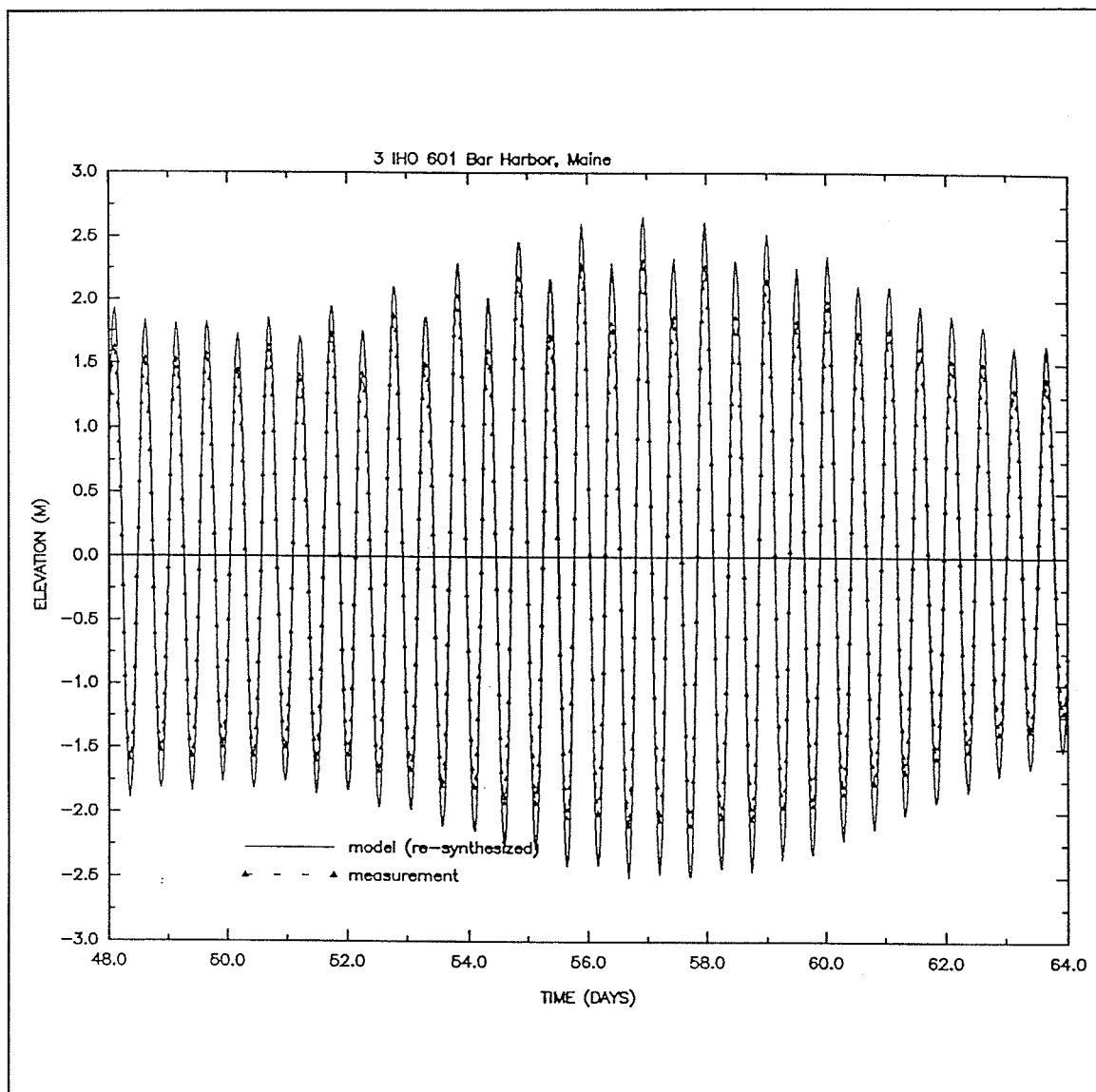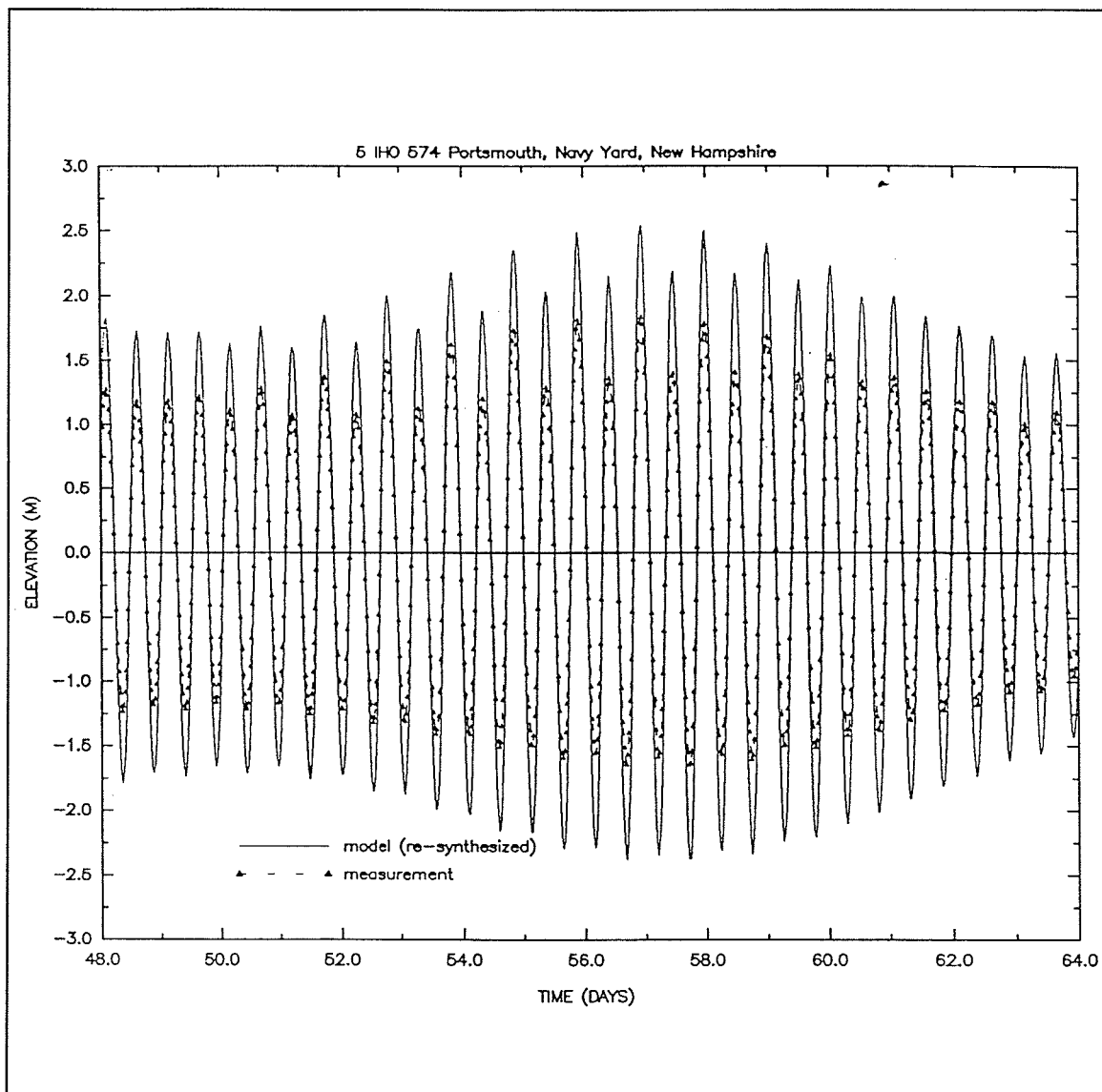
3 IHO 601 Bar Harbor, Maine

model (re-synthesized)
measurement

Figure 14.   (Sheet 2 of 39)

5 IHO 574 Portsmouth, Navy Yard, New Hampshire

model (re-synthesized)
measurement

ELEVATION (M)

TIME (DAYS)

Figure 14.   (Sheet 3 of 39)

7 NOAA 10 Nantucket Island, MA

model (re-synthesized)
measurement

ELEVATION (M)

TIME (DAYS)

Figure 14. (Sheet 4 of 39)

9 IHO 529 Sandy Hook, NJ

ELEVATION (M)

TIME (DAYS)

model (re-synthesized)
measurement

Figure 14.   (Sheet 5 of 39)

11 IHO 503 Cape May Ferry Terminal, NJ

Figure 14.   (Sheet 6 of 39)

13 NOAA 22 Fishing Pier Ocean City, MD
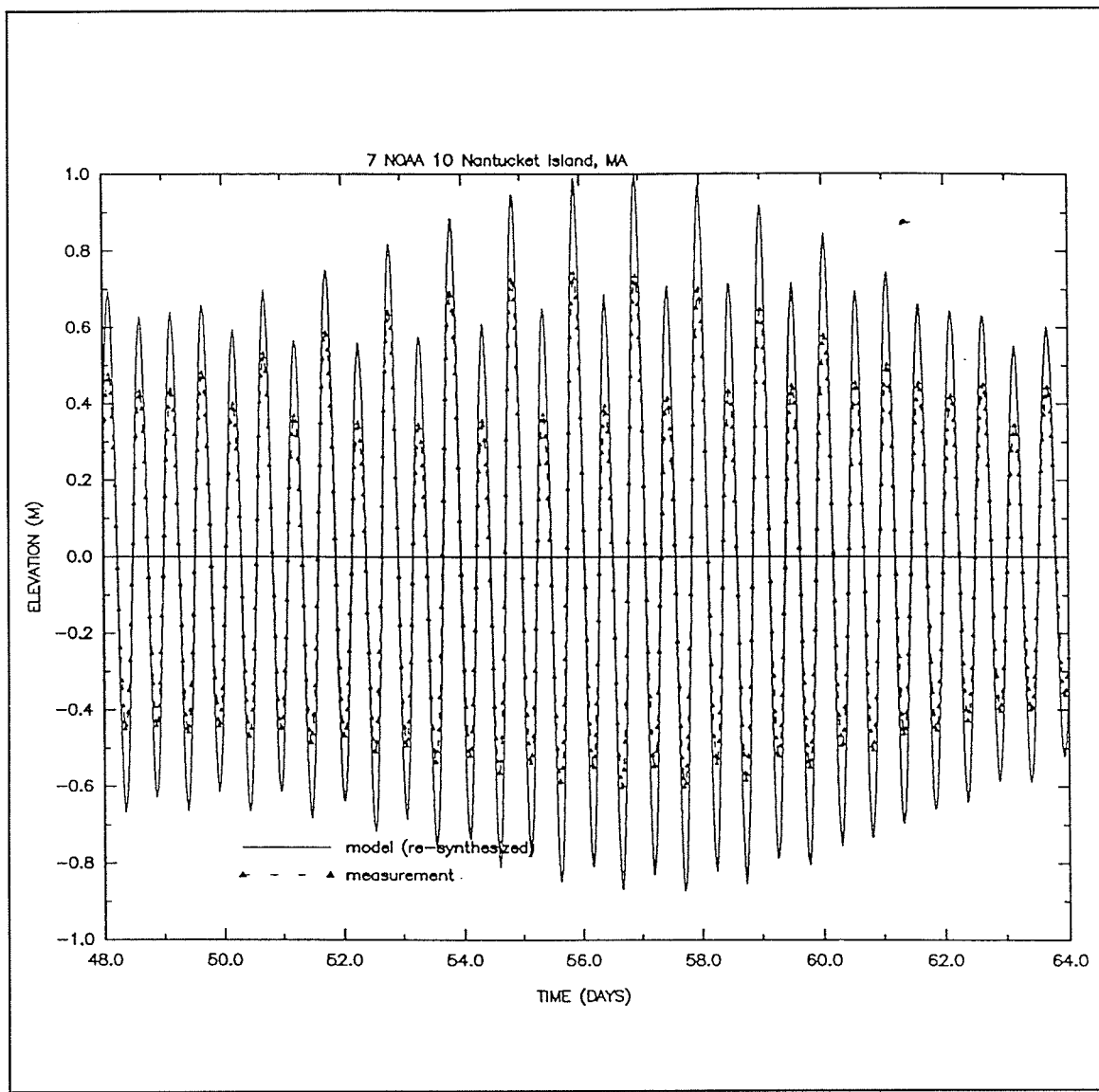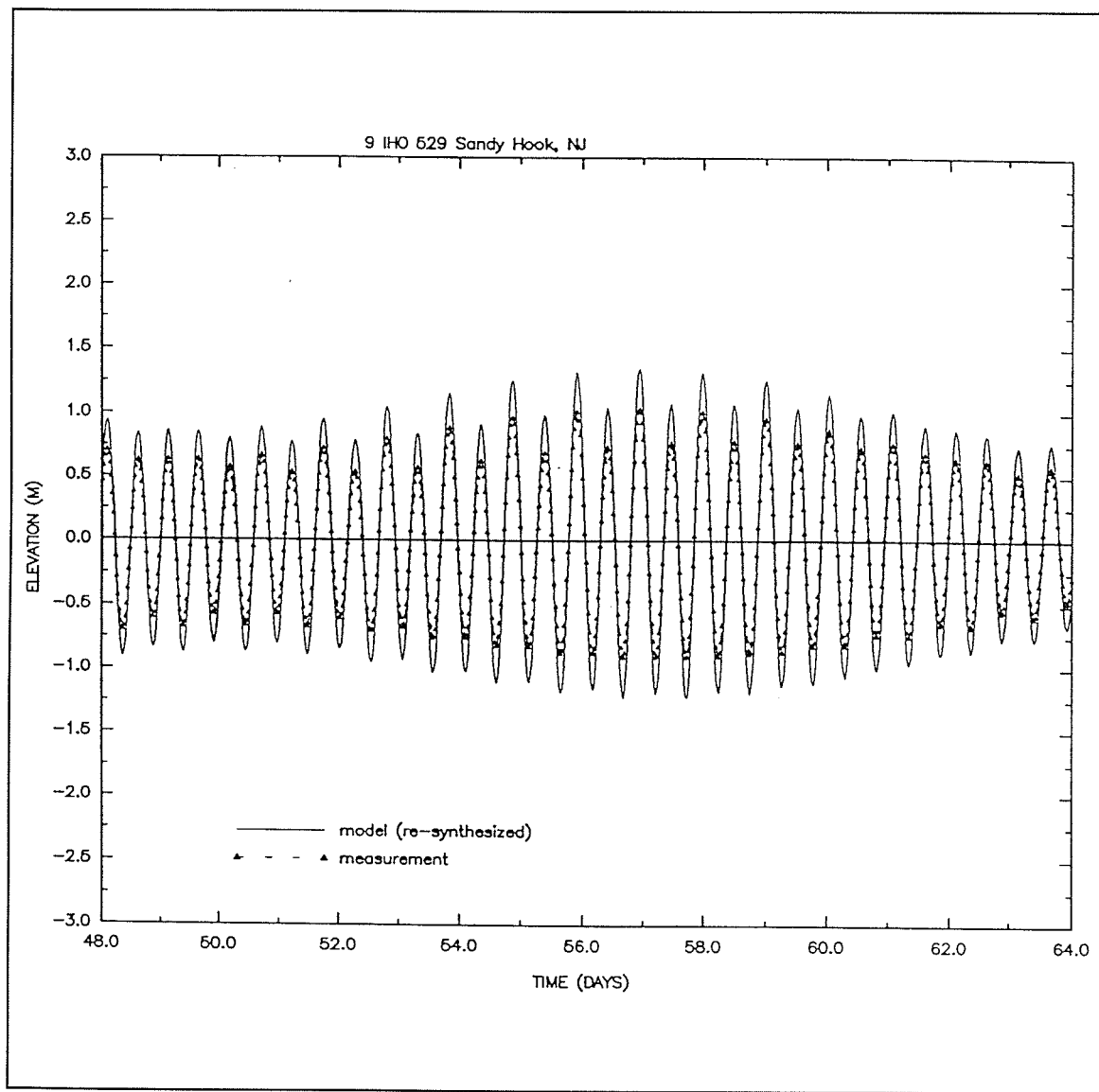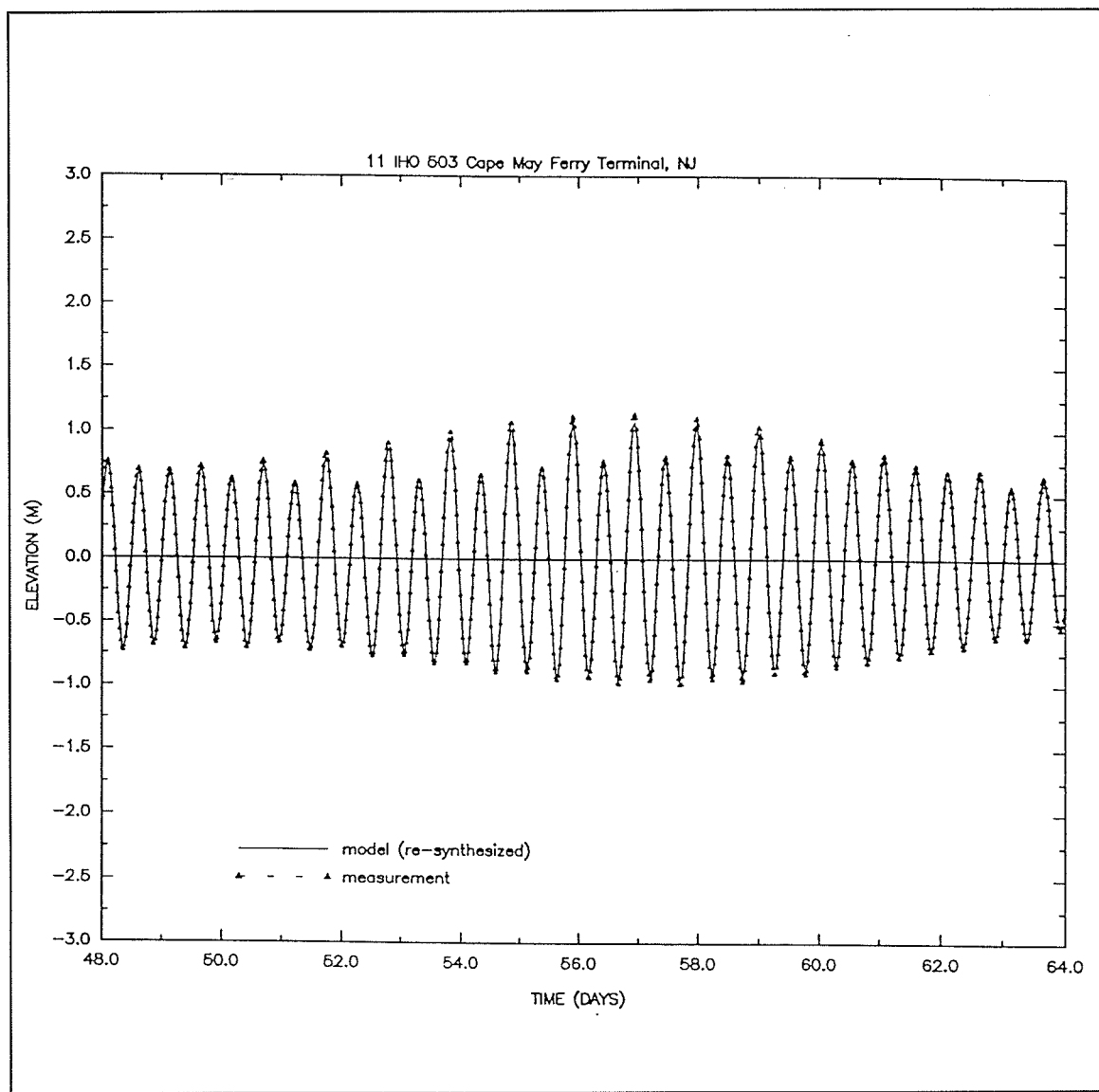
Figure 14.   (Sheet 7 of 39)

Figure 14. (Sheet 8 of 39)

17 IHO 424 Charleston, SC

model (re-synthesized)
measurement

Figure 14. (Sheet 9 of 39)

19 IHO 407 Mayport, FL

Figure 14.   (Sheet 10 of 39)
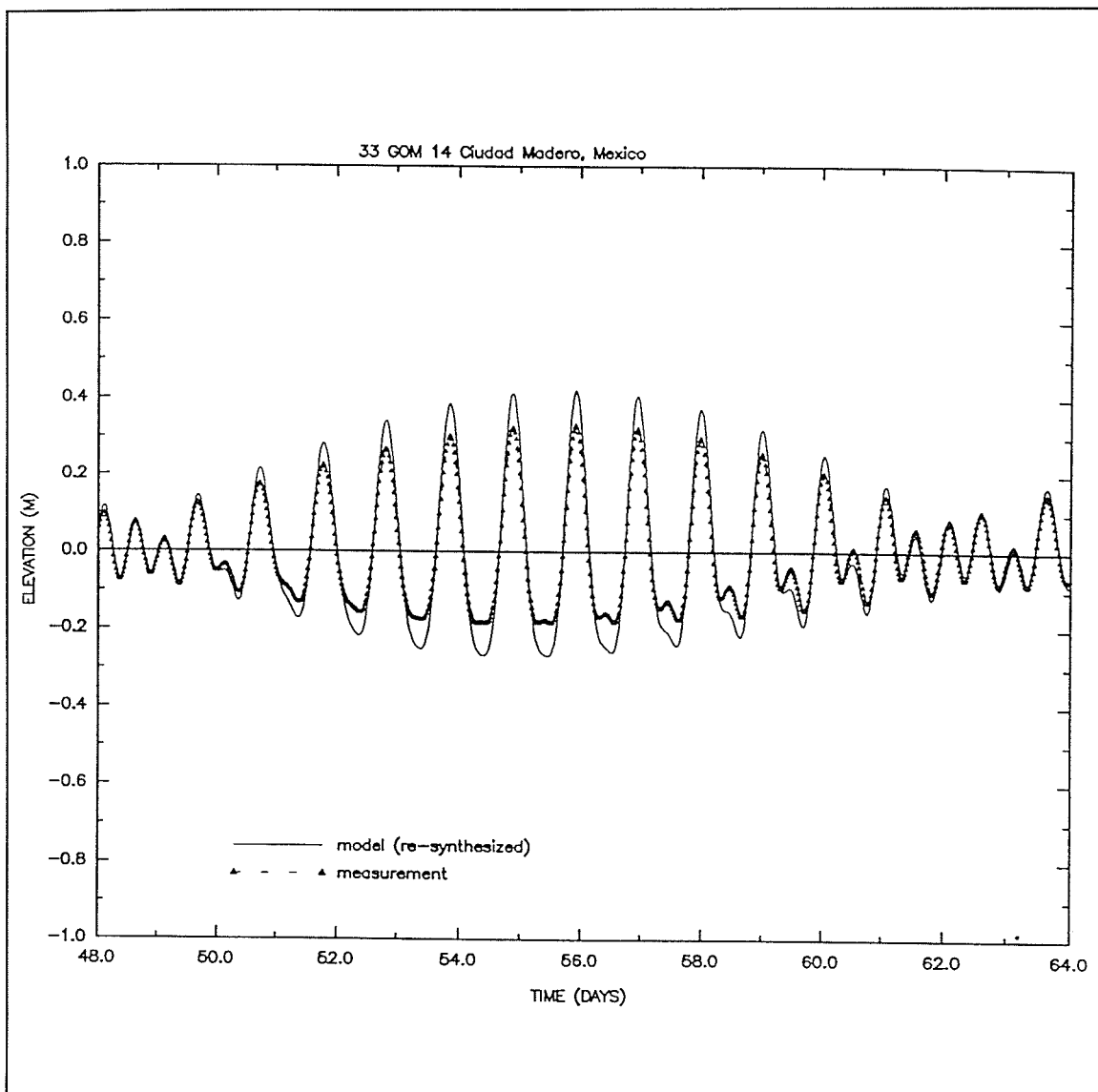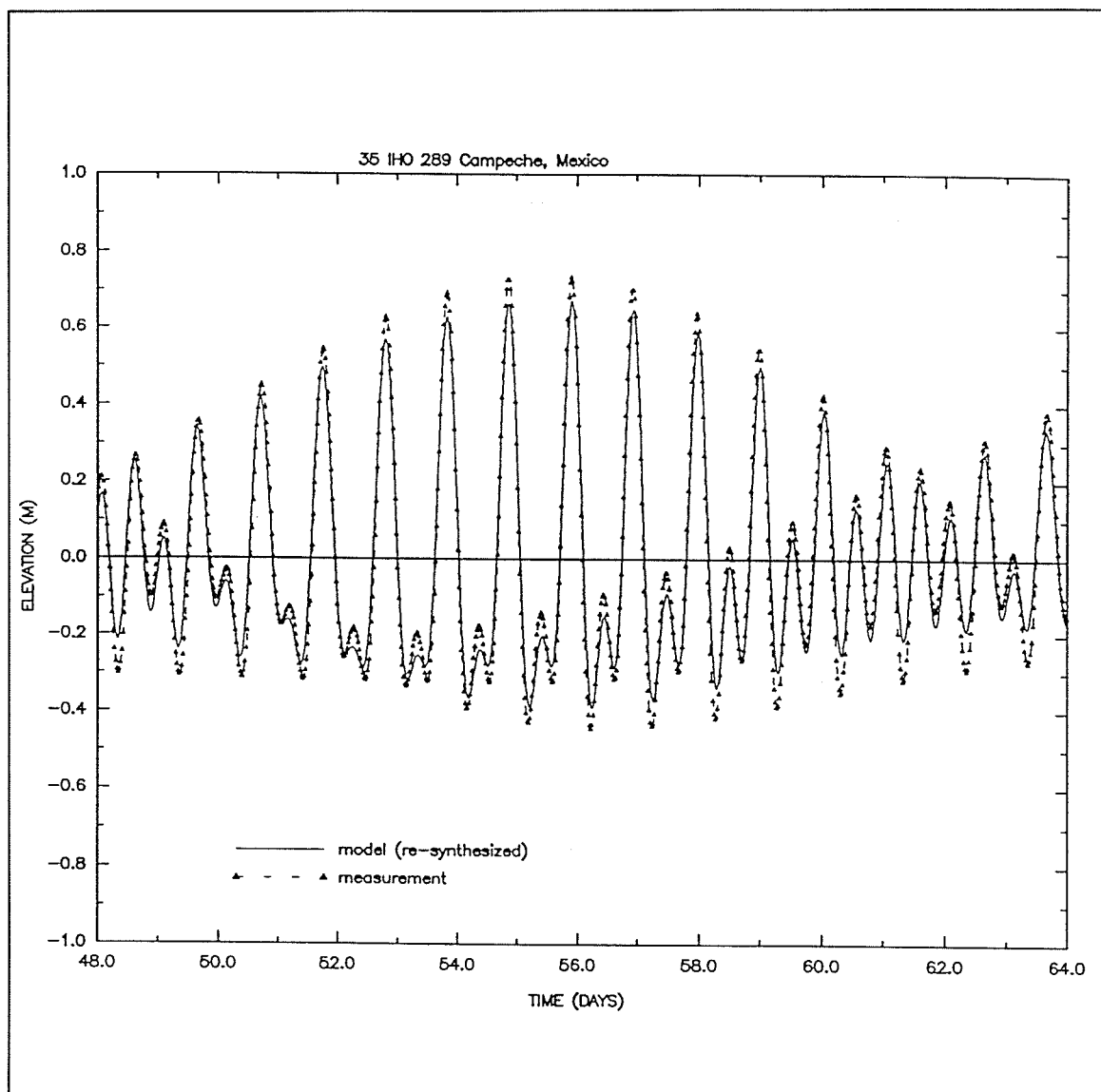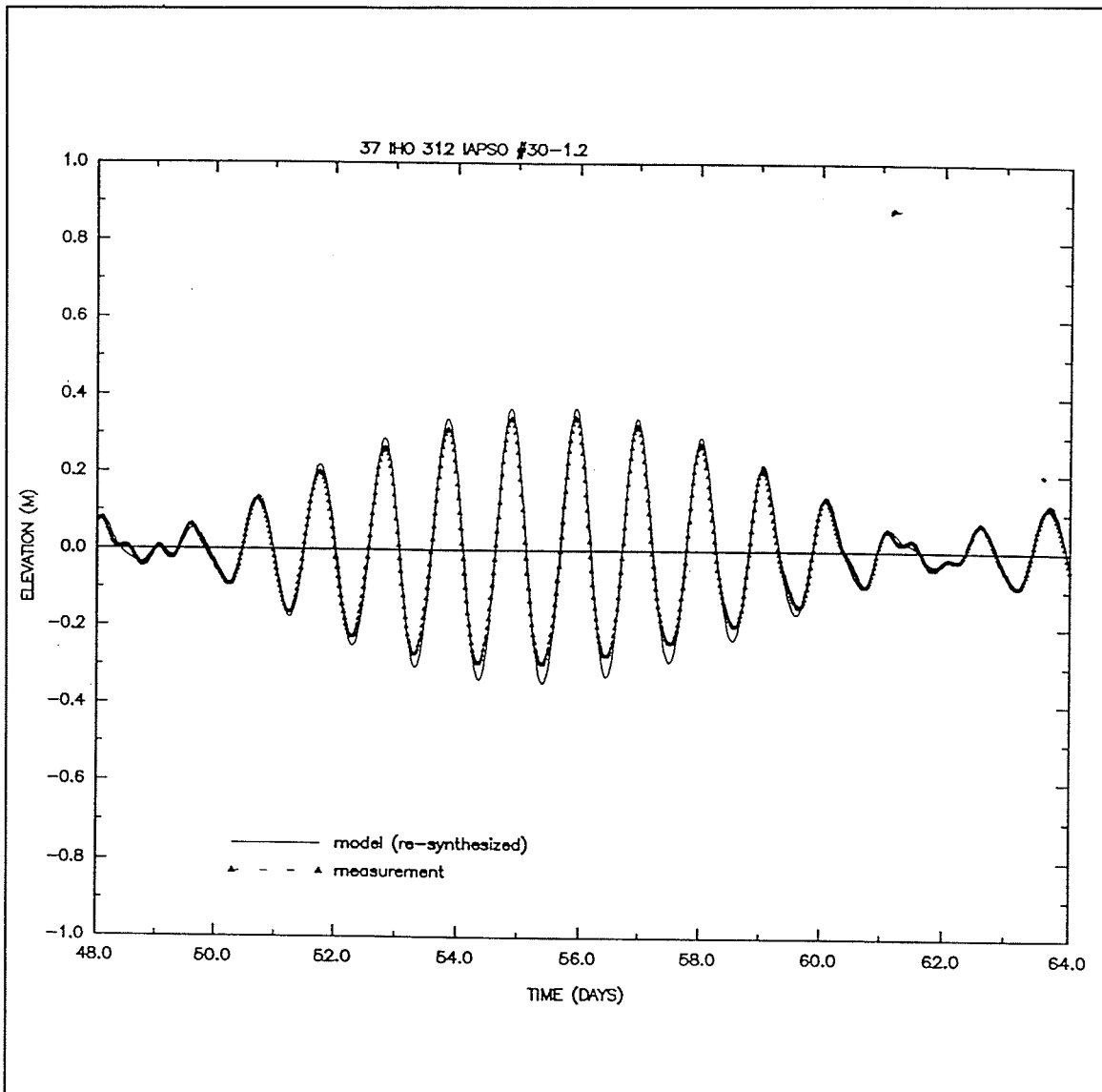
Figure 14. (Sheet 11 of 39)

Figure 14. (Sheet 12 of 39)

25 IHO 400 Alligator Bayou

Figure 14. (Sheet 13 of 39)

27 IHO 402 Cat Island, Mississippi

model (re—synthesized)
measurement

Figure 14.　(Sheet 14 of 39)

29 IHO 378 Point au Fer, Louisiana

model (re-synthesized)
measurement
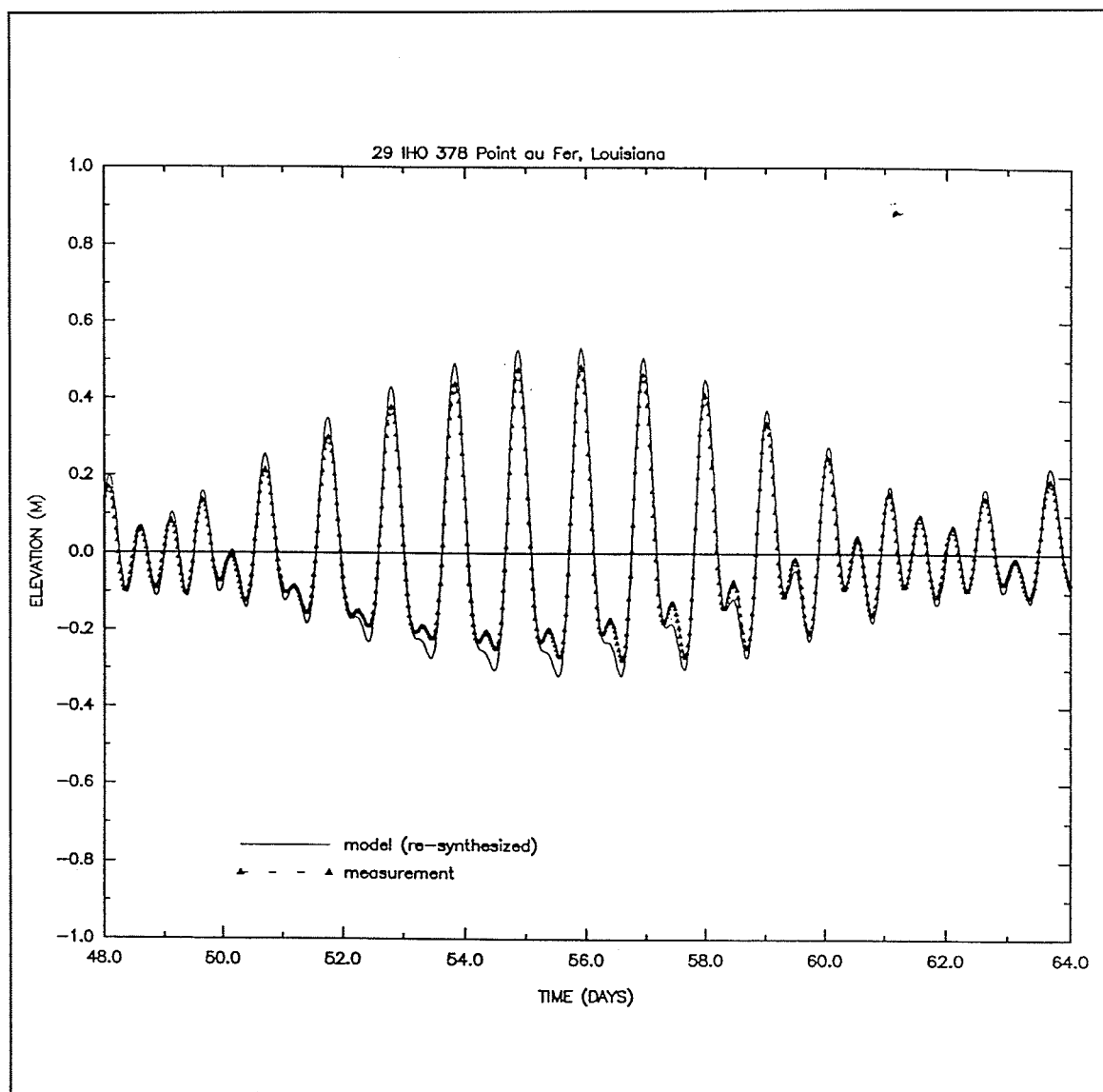
Figure 14.   (Sheet 15 of 39)

31 GOM 12 Port Aransas
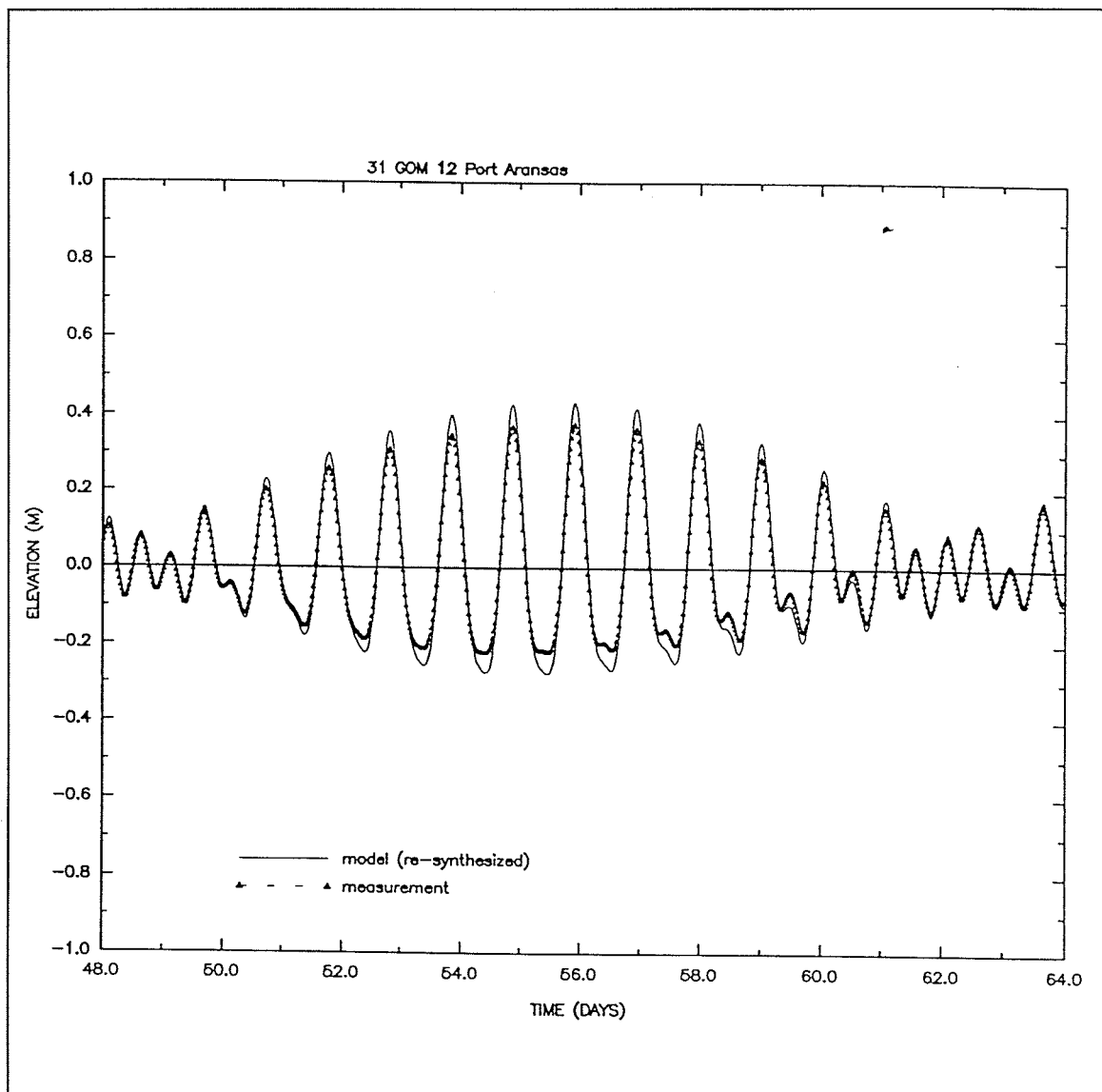
Figure 14.   (Sheet 16 of 39)

Figure 14.   (Sheet 17 of 39)

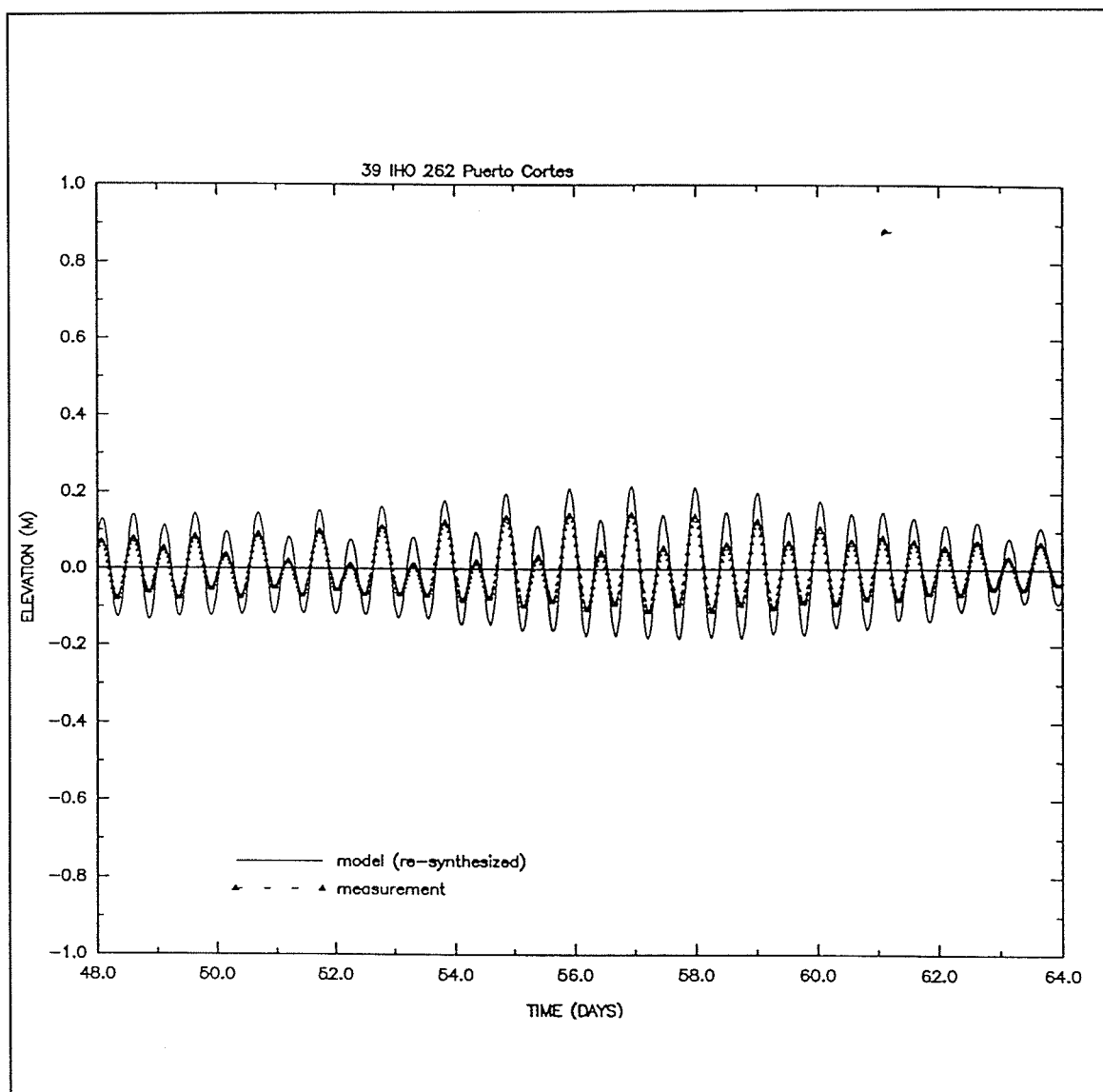Figure 14. (Sheet 18 of 39)

Figure 14.   (Sheet 19 of 39)

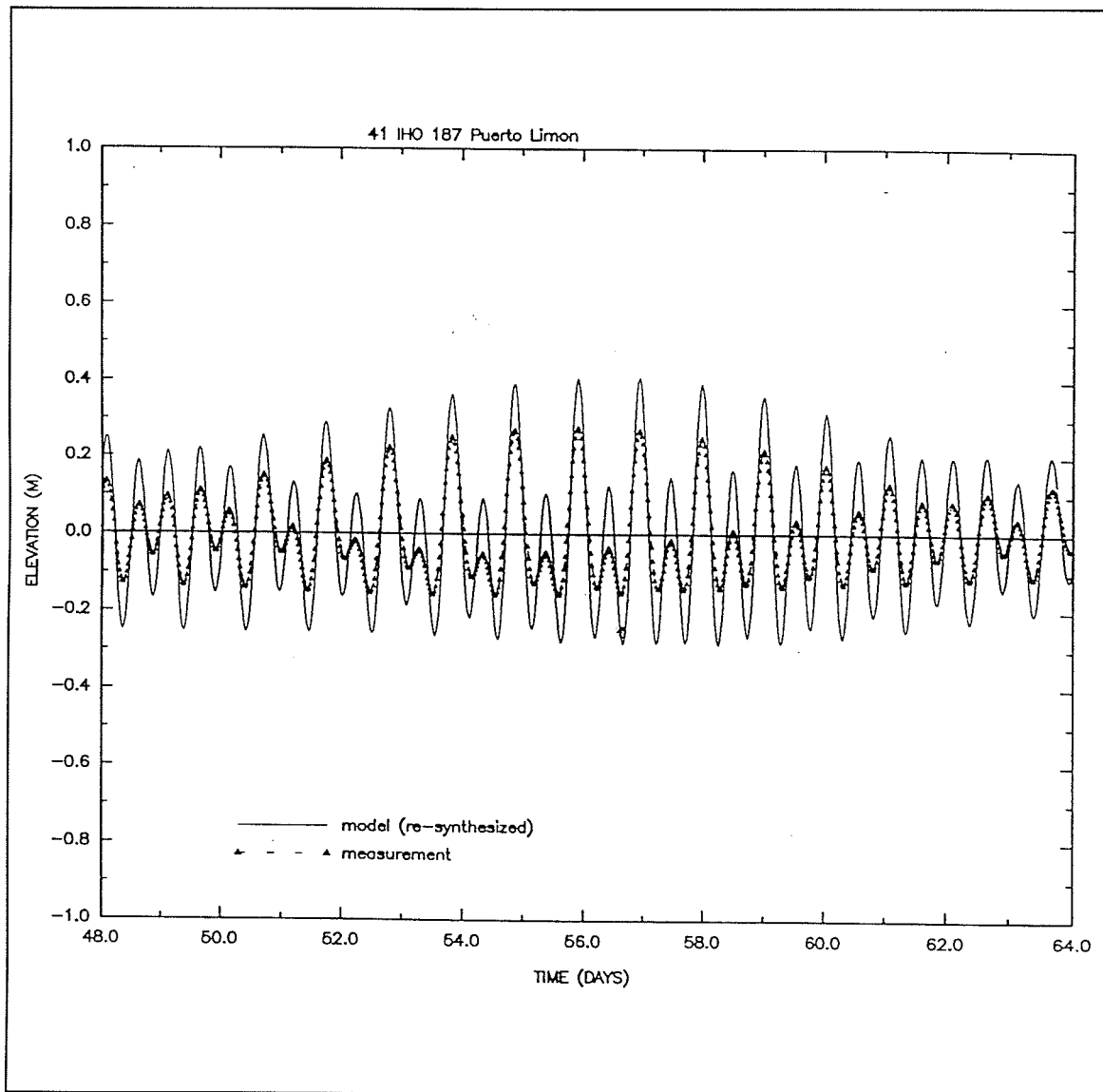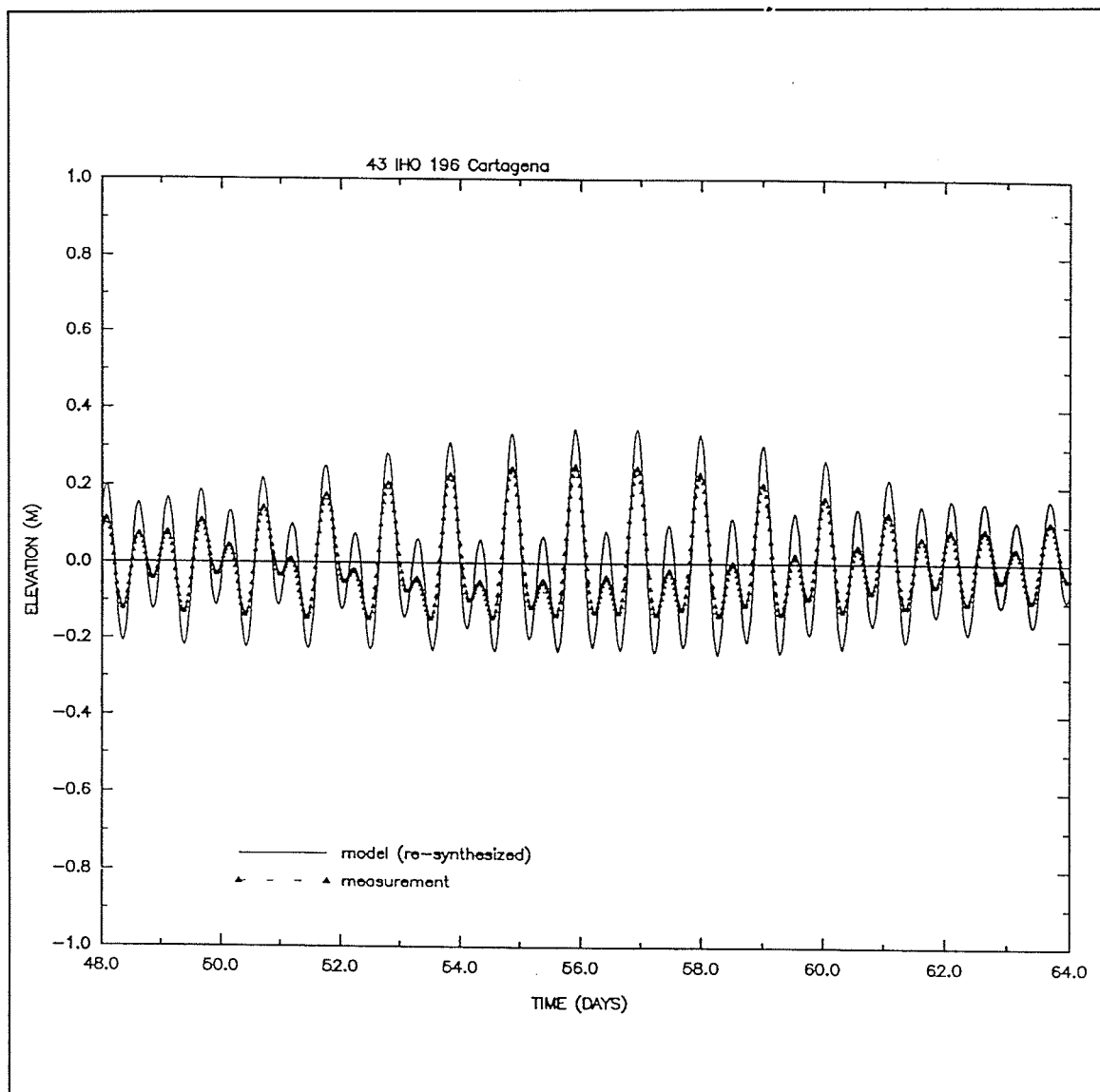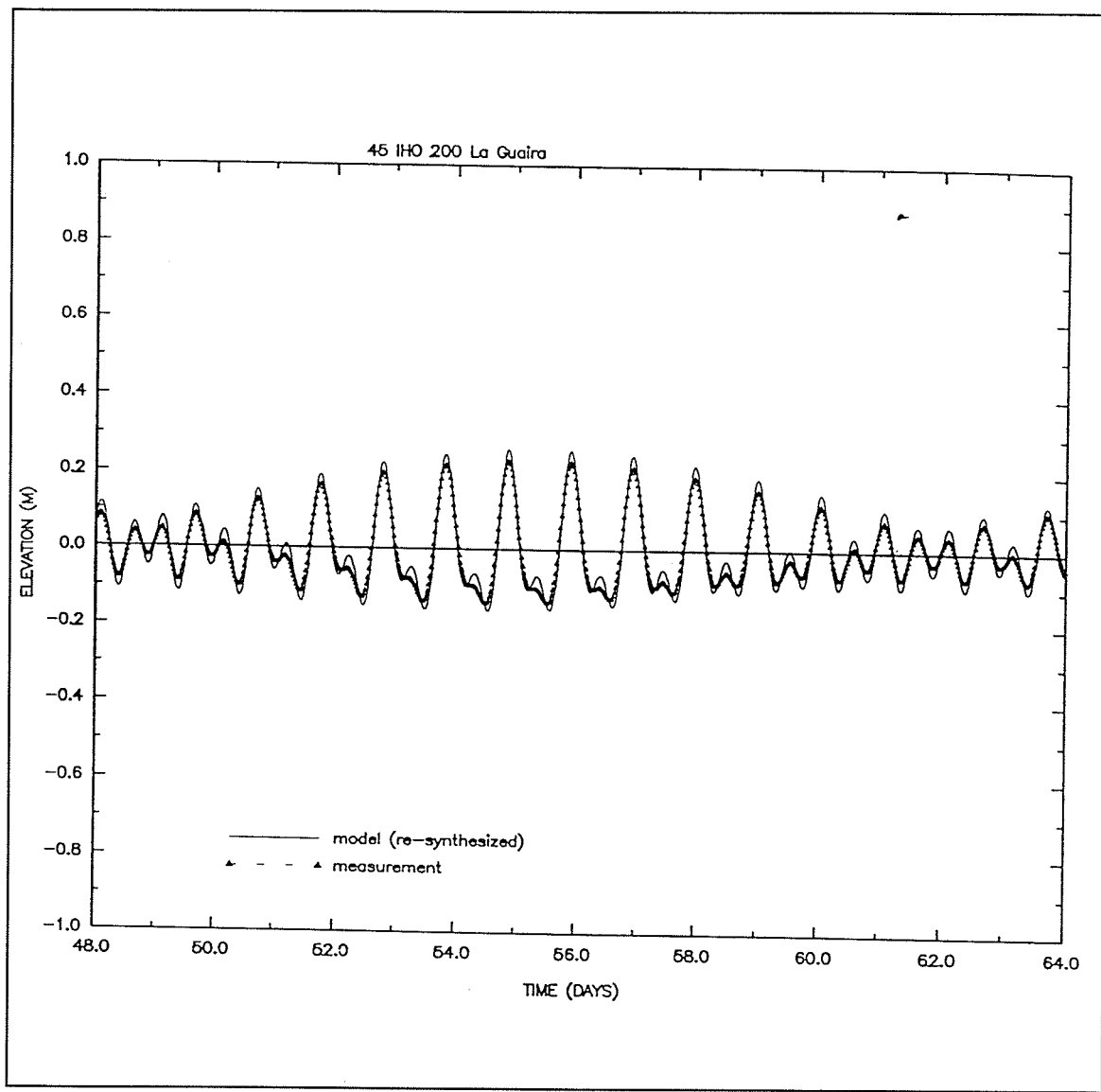39 IHO 262 Puerto Cortes

Figure 14.   (Sheet 20 of 39)

Figure 14. (Sheet 21 of 39)

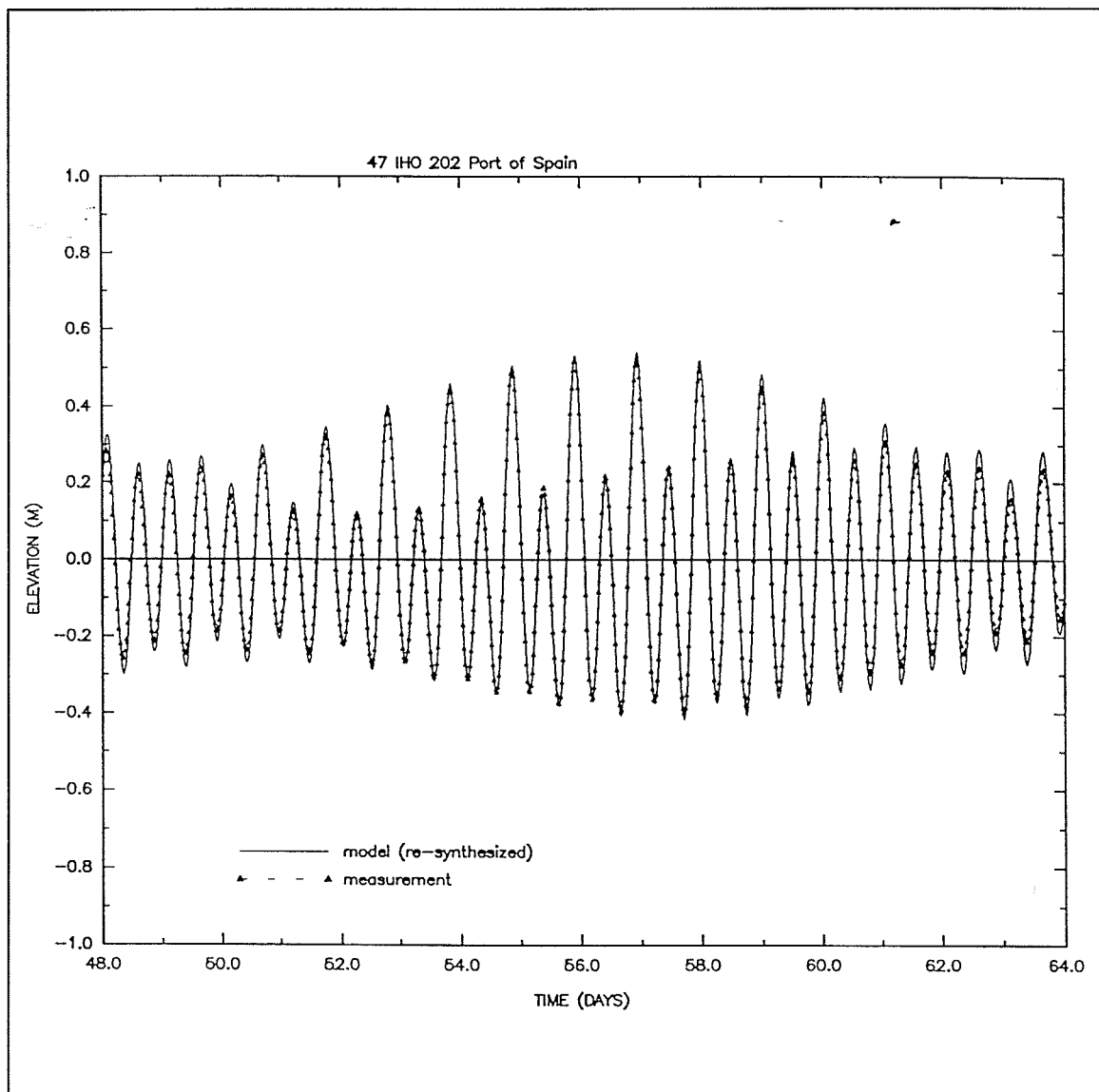Figure 14.   (Sheet 22 of 39)

Figure 14. (Sheet 23 of 39)
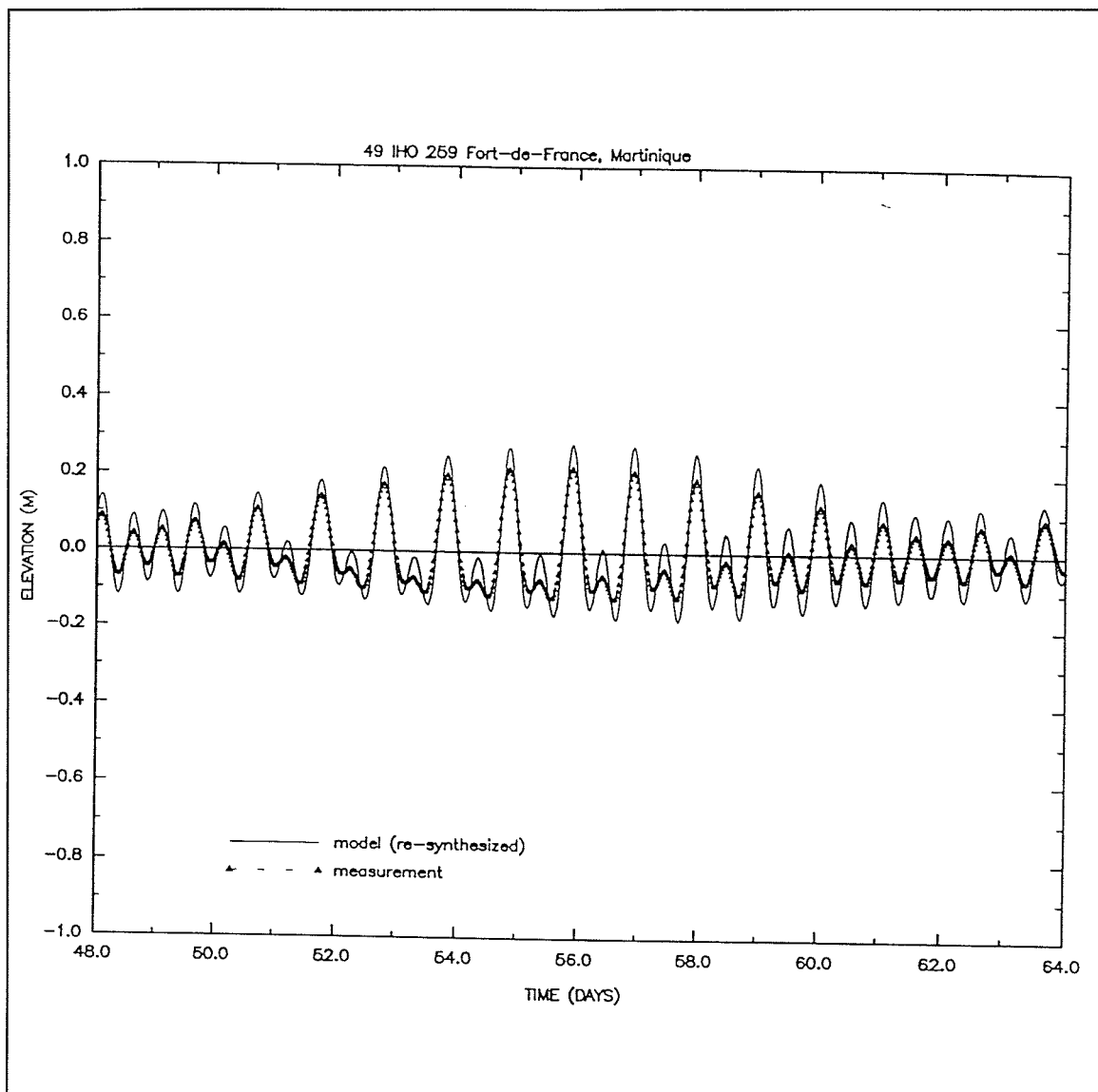
Figure 14.   (Sheet 24 of 39)

49 IHO 259 Fort-de-France, Martinique

model (re-synthesized)
measurement

Figure 14. (Sheet 25 of 39)

51 IHO 274 Magueyes Island, Puerto Rico

Figure 14.   (Sheet 26 of 39)

Figure 14. (Sheet 27 of 39)

55 IHO 290 Guantanomo Bay

model (re-synthesized)
measurement

Figure 14.   (Sheet 28 of 39)

Figure 14. (Sheet 29 of 39)

Figure 14.   (Sheet 30 of 39)

61 IHO 417 Ireland Island, Bermuda

Figure 14.   (Sheet 31 of 39)

Figure 14. (Sheet 32 of 39)

65 IHO 348 IAPSO #30-1.2.13

Figure 14. (Sheet 33 of 39)

67 IHO 357 IAPSO #30-1.2.4

Figure 14.   (Sheet 34 of 39)

69 IHO 360 IAPSO #30-1.2.15
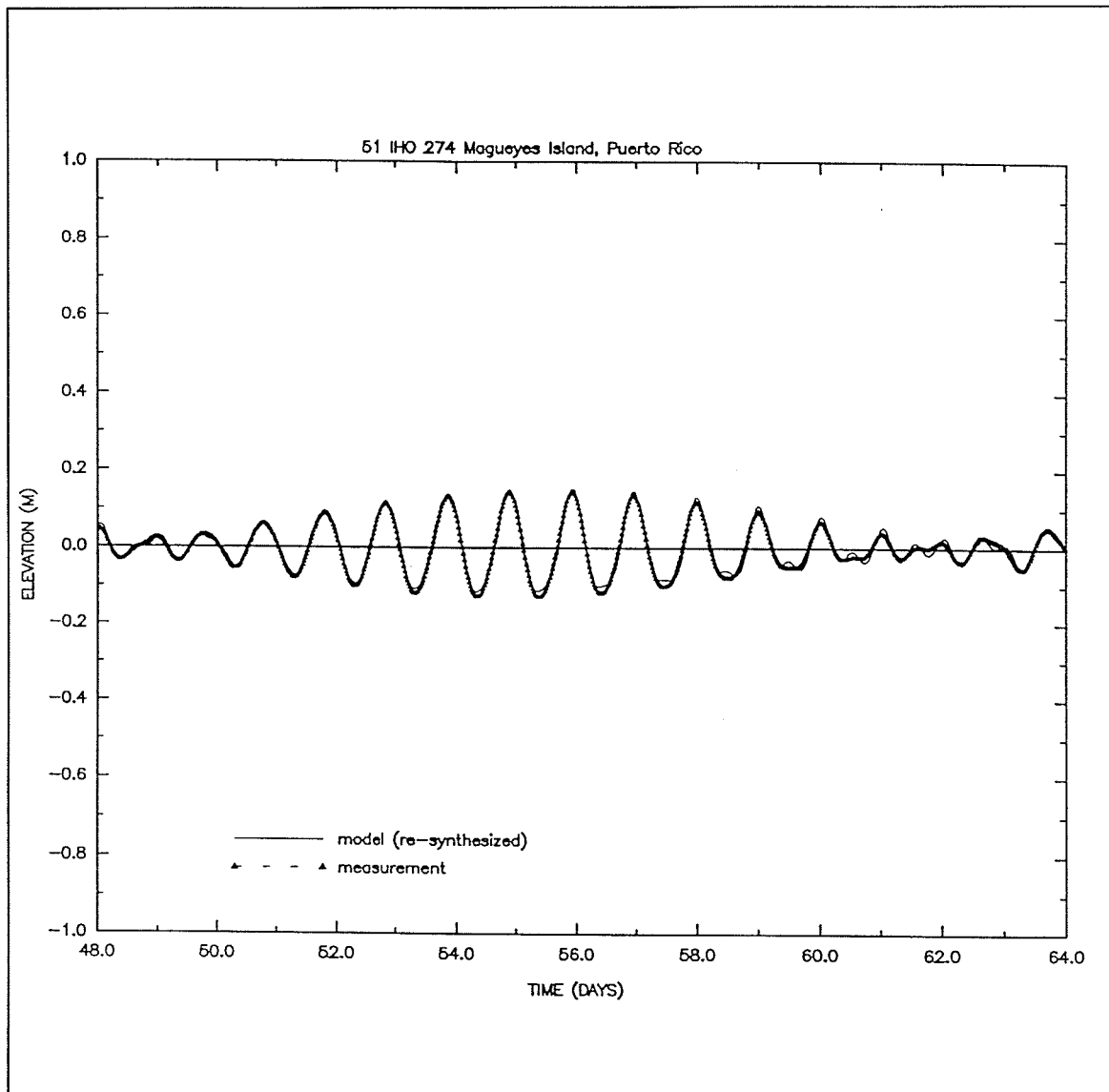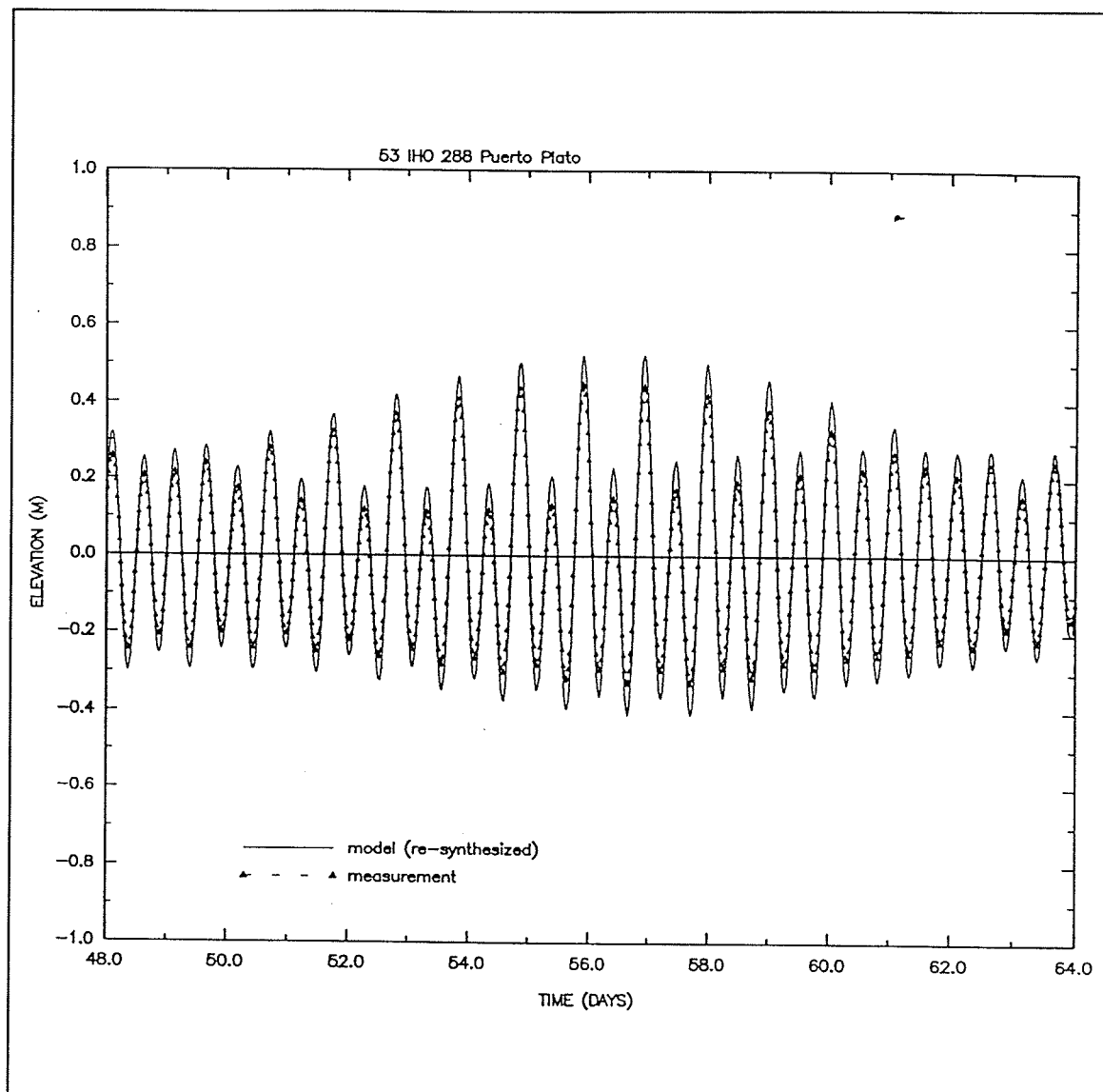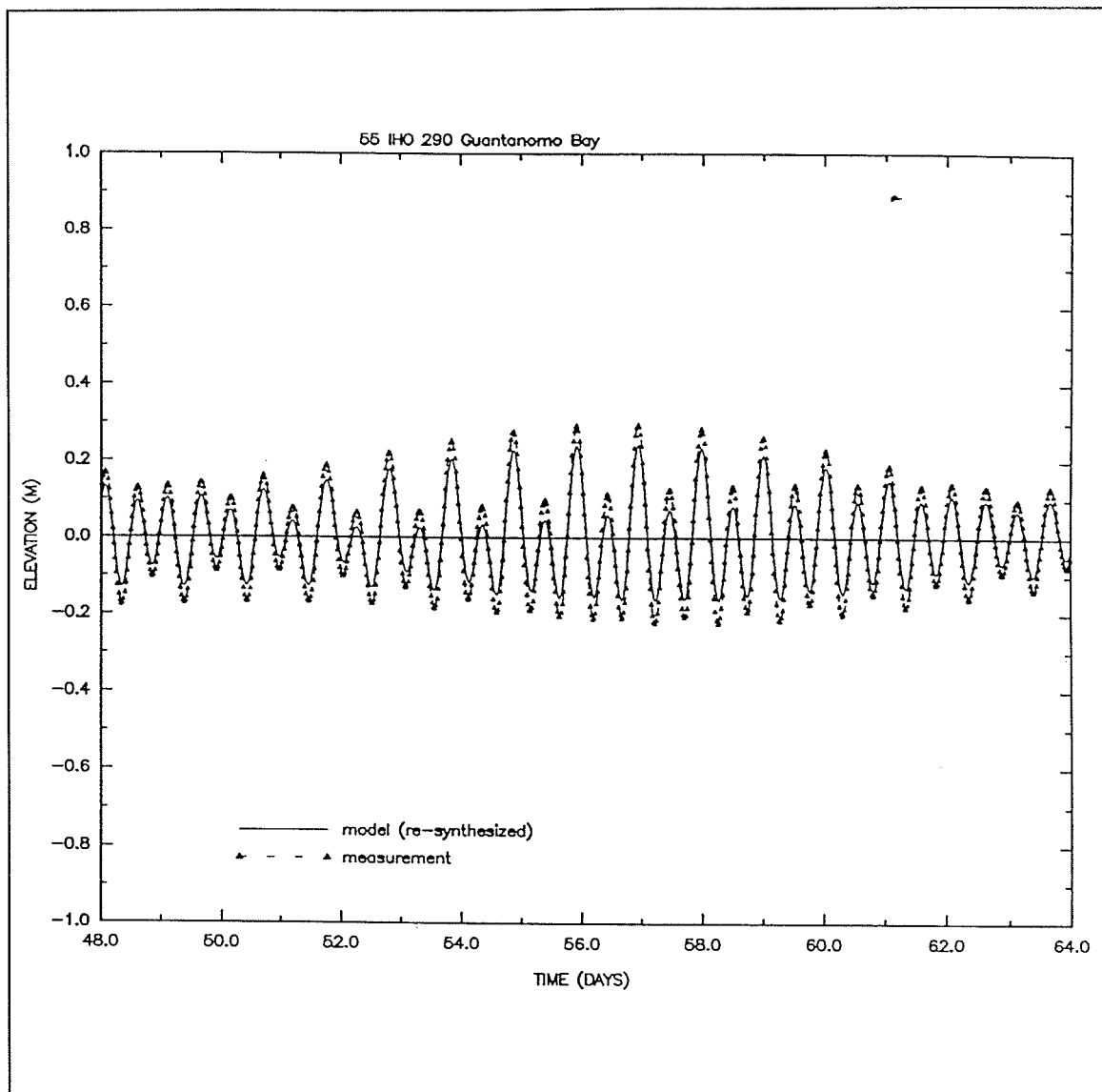
Figure 14.   (Sheet 35 of 39)

Figure 14. (Sheet 36 of 39)
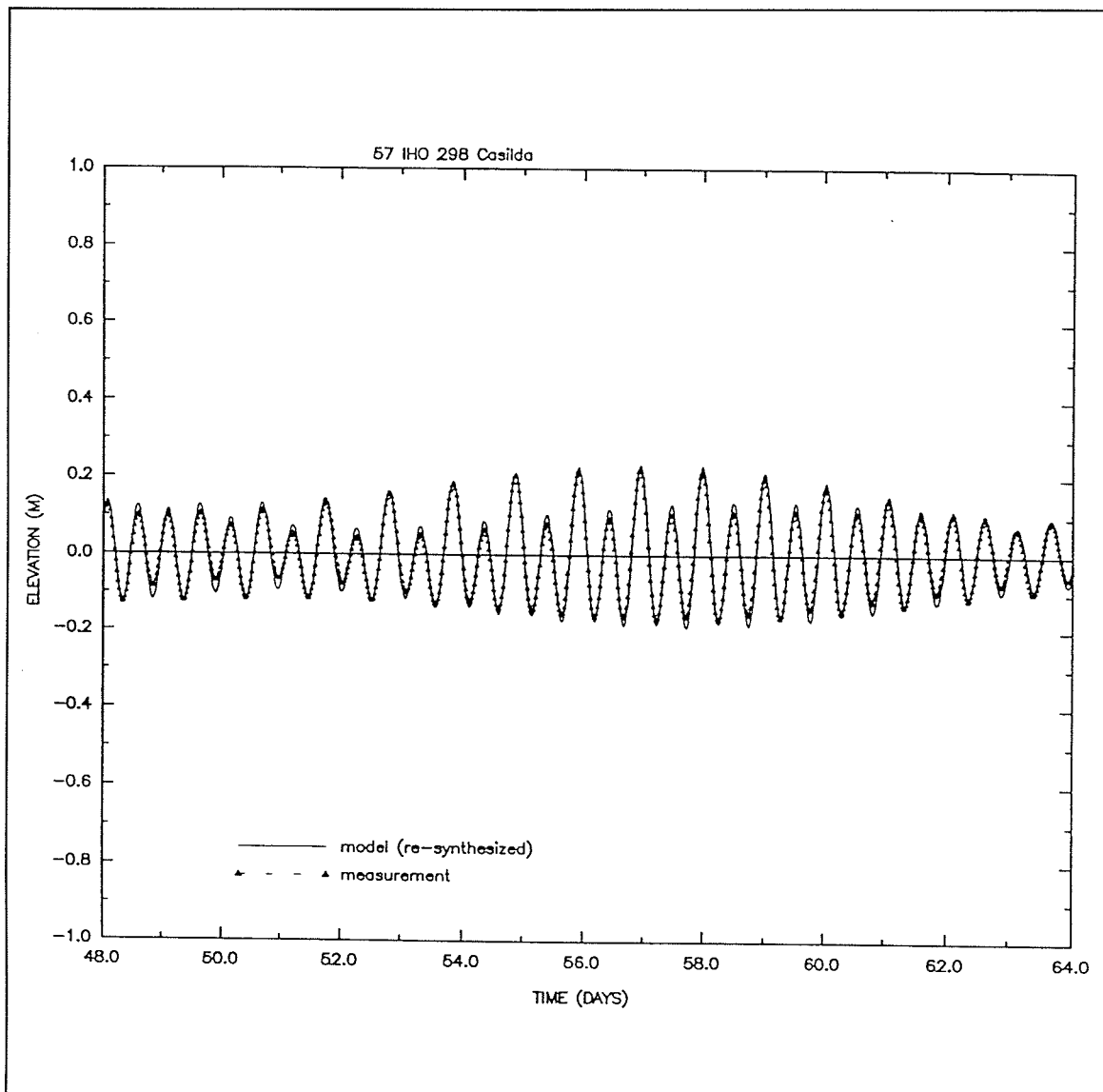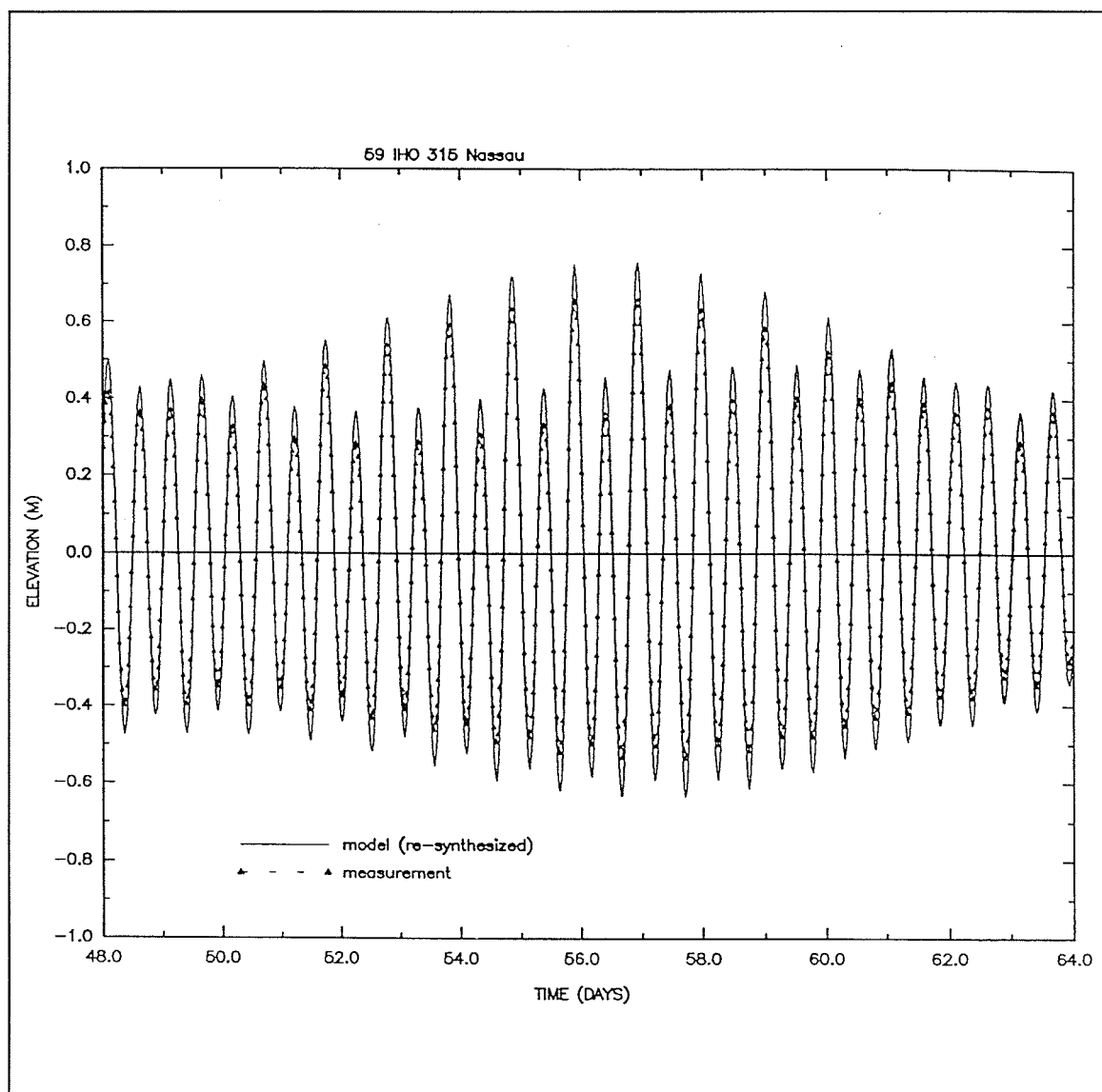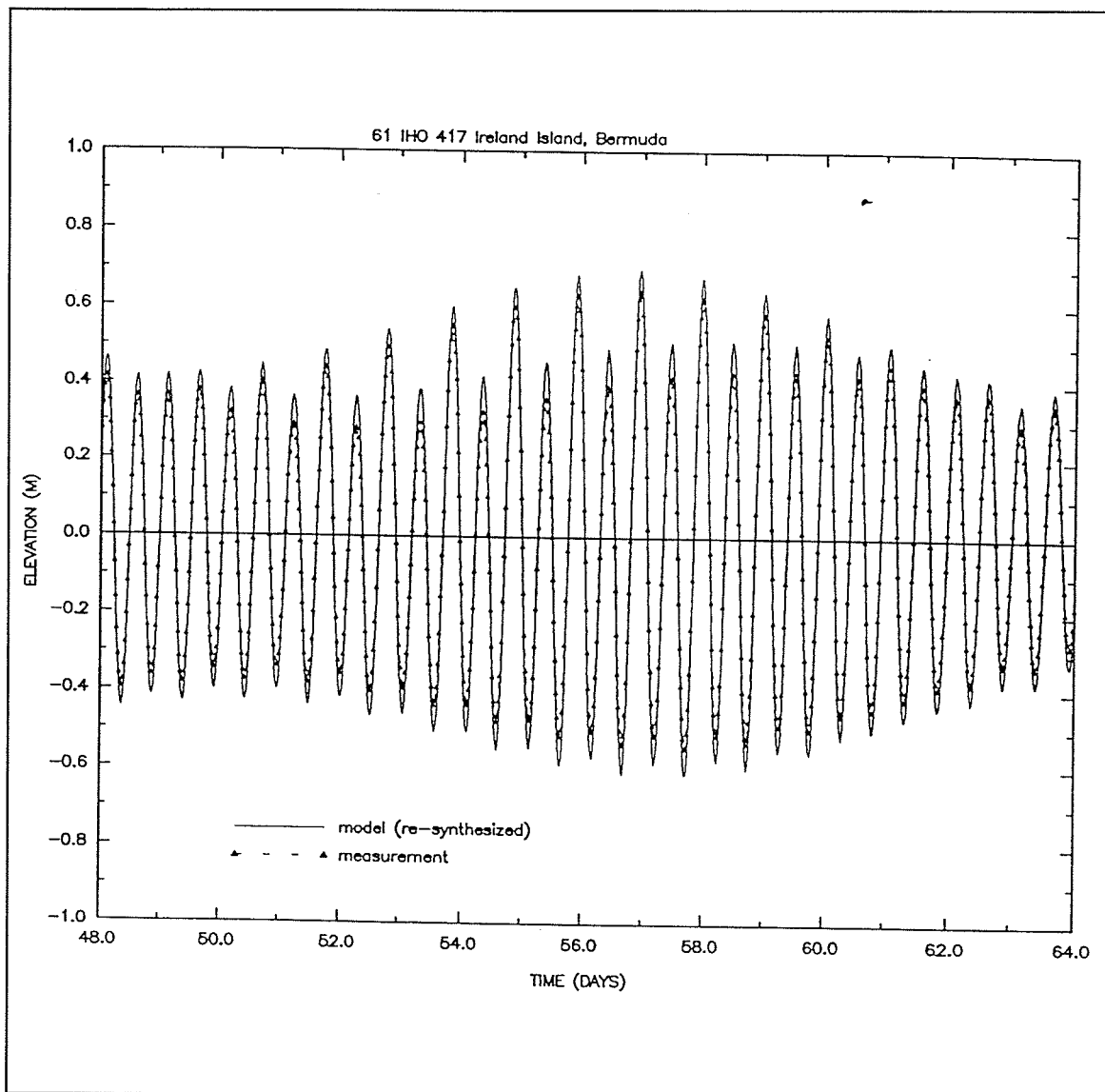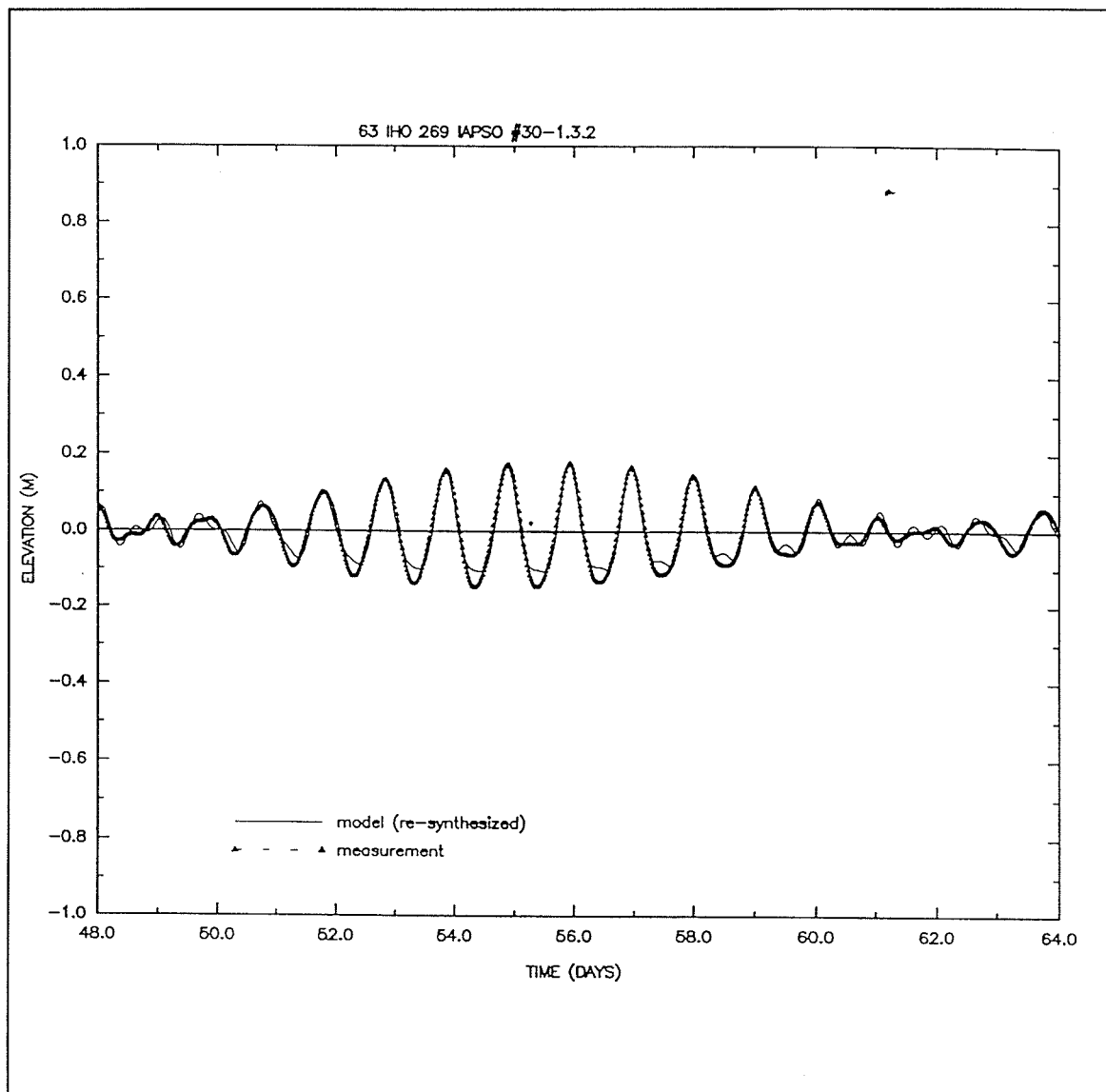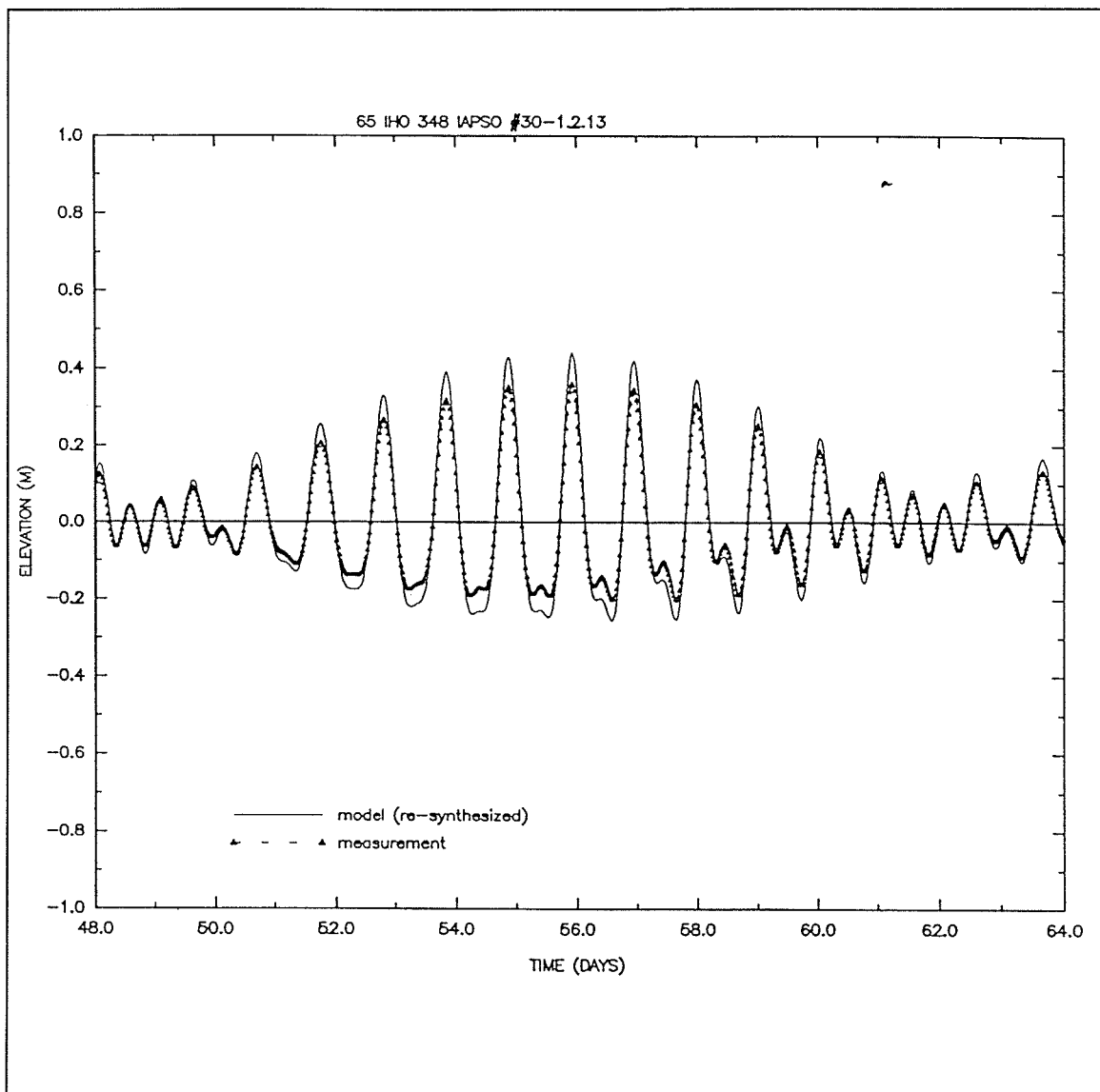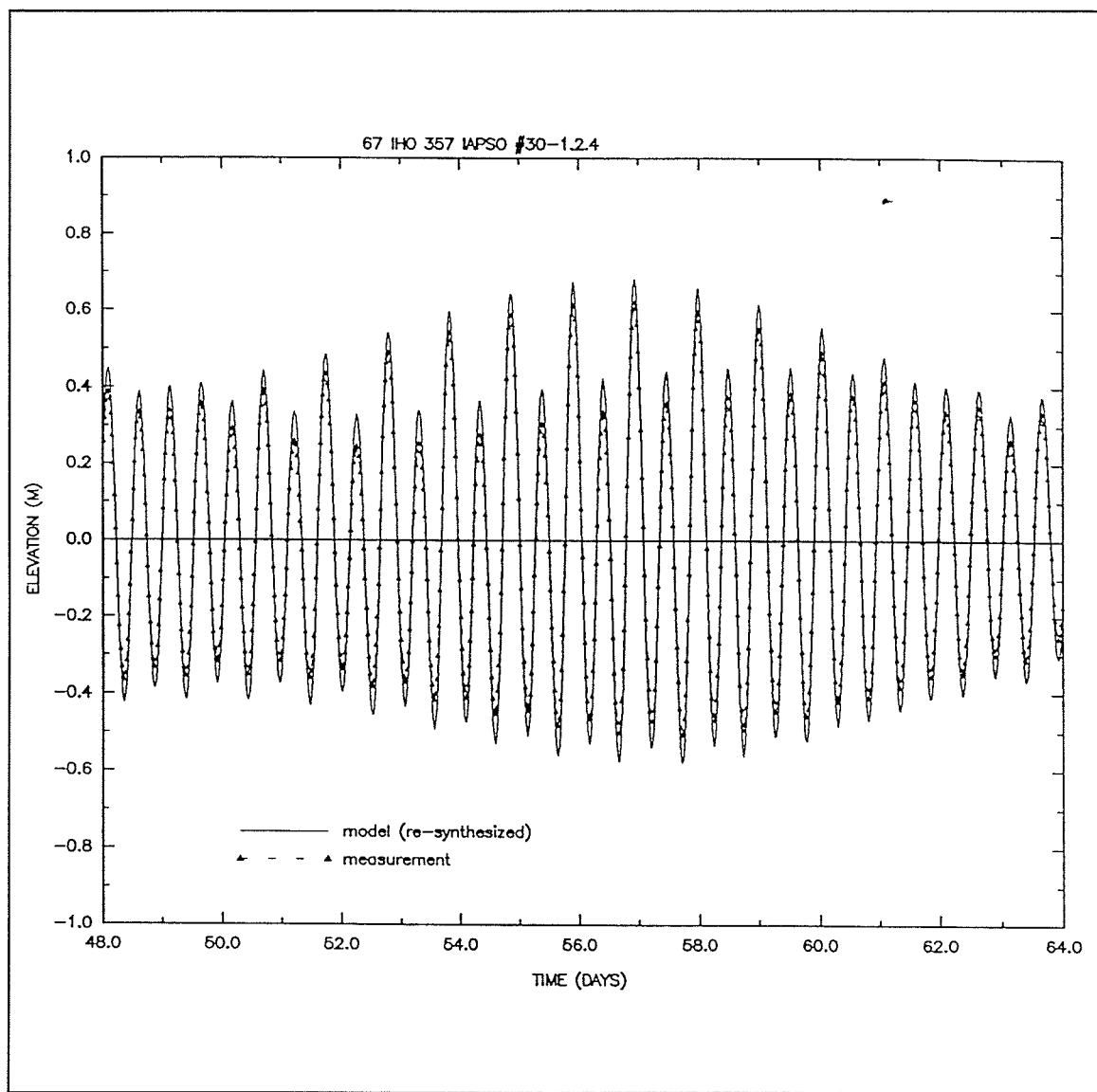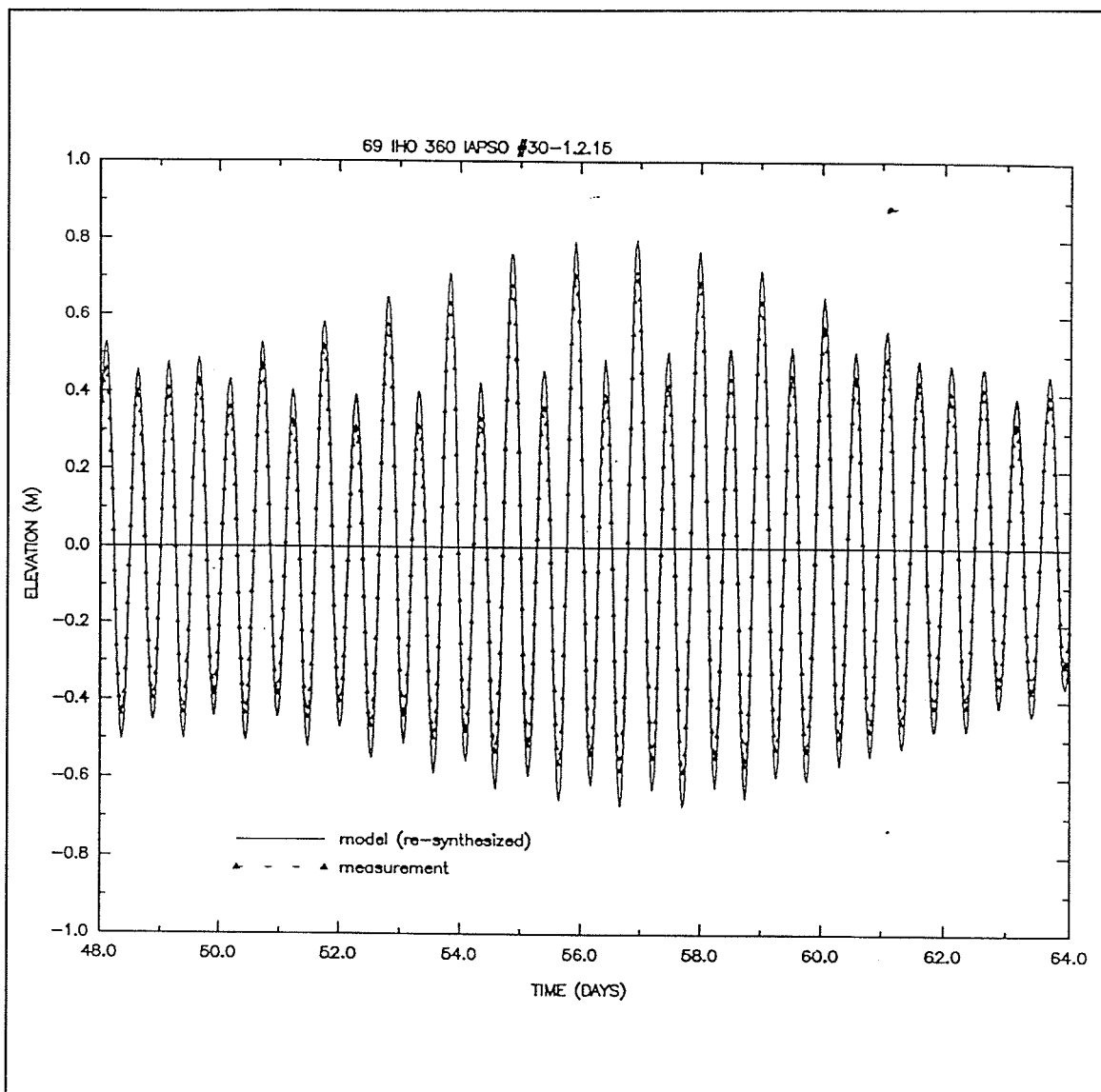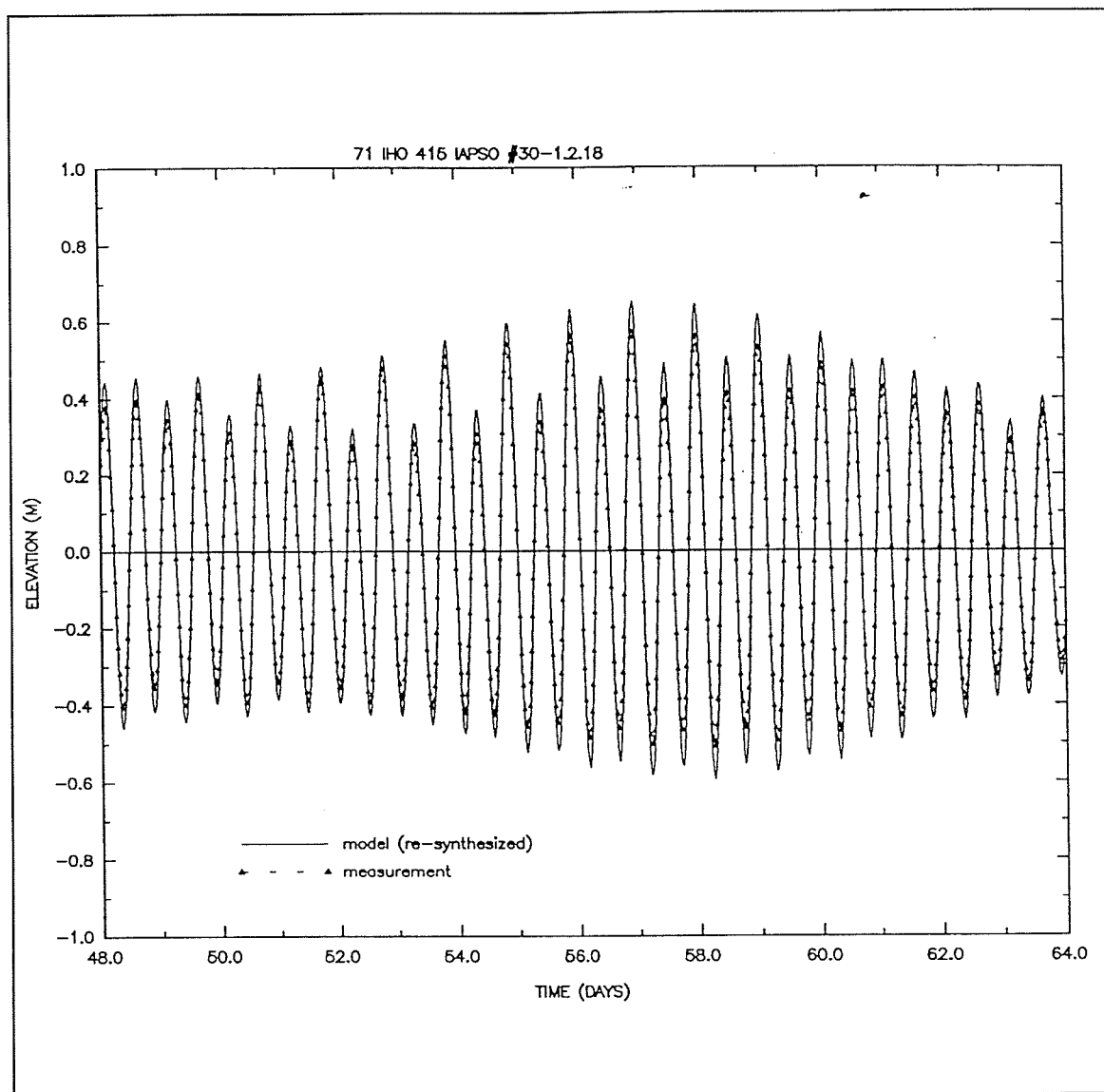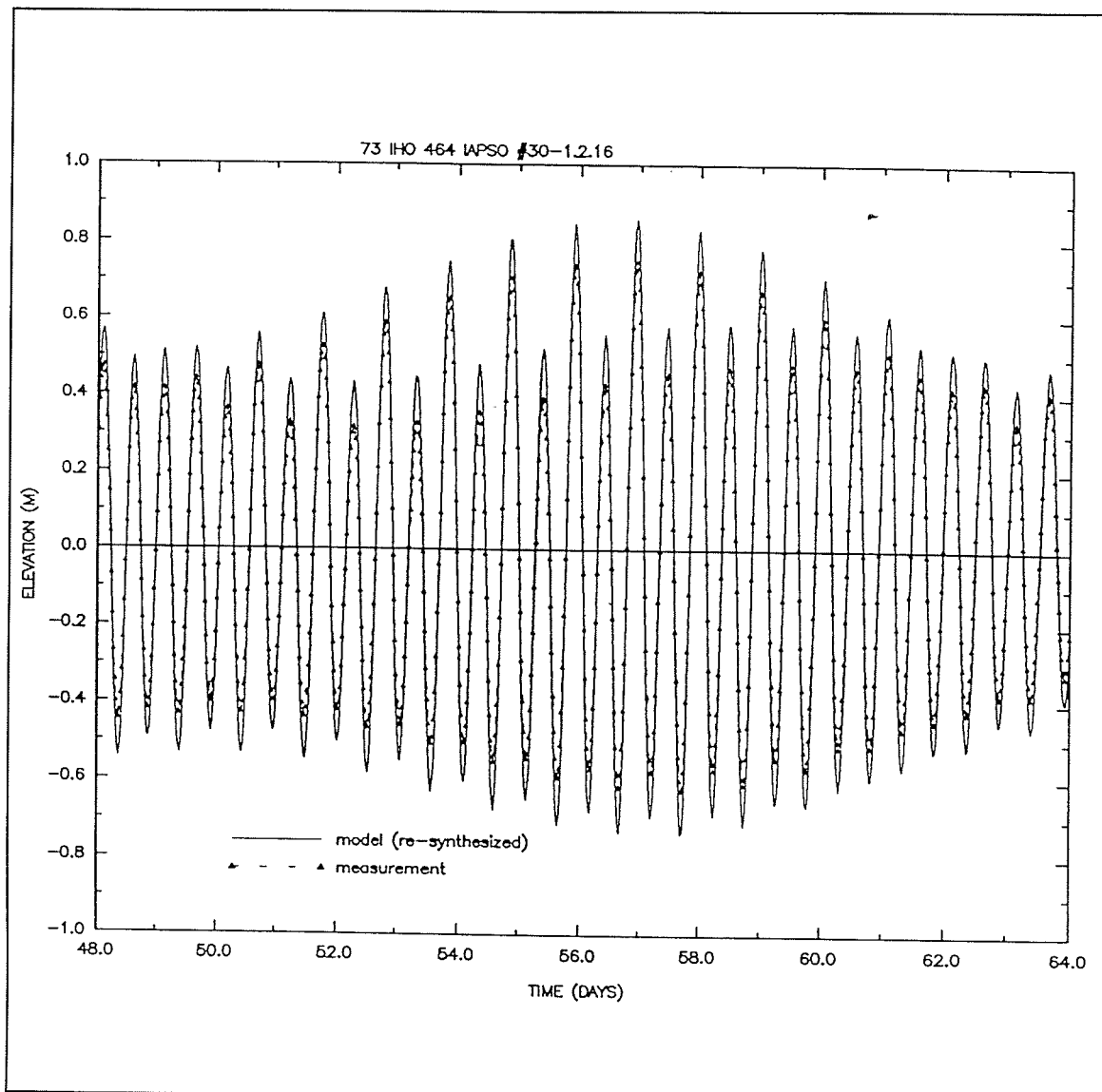
Figure 14.   (Sheet 37 of 39)
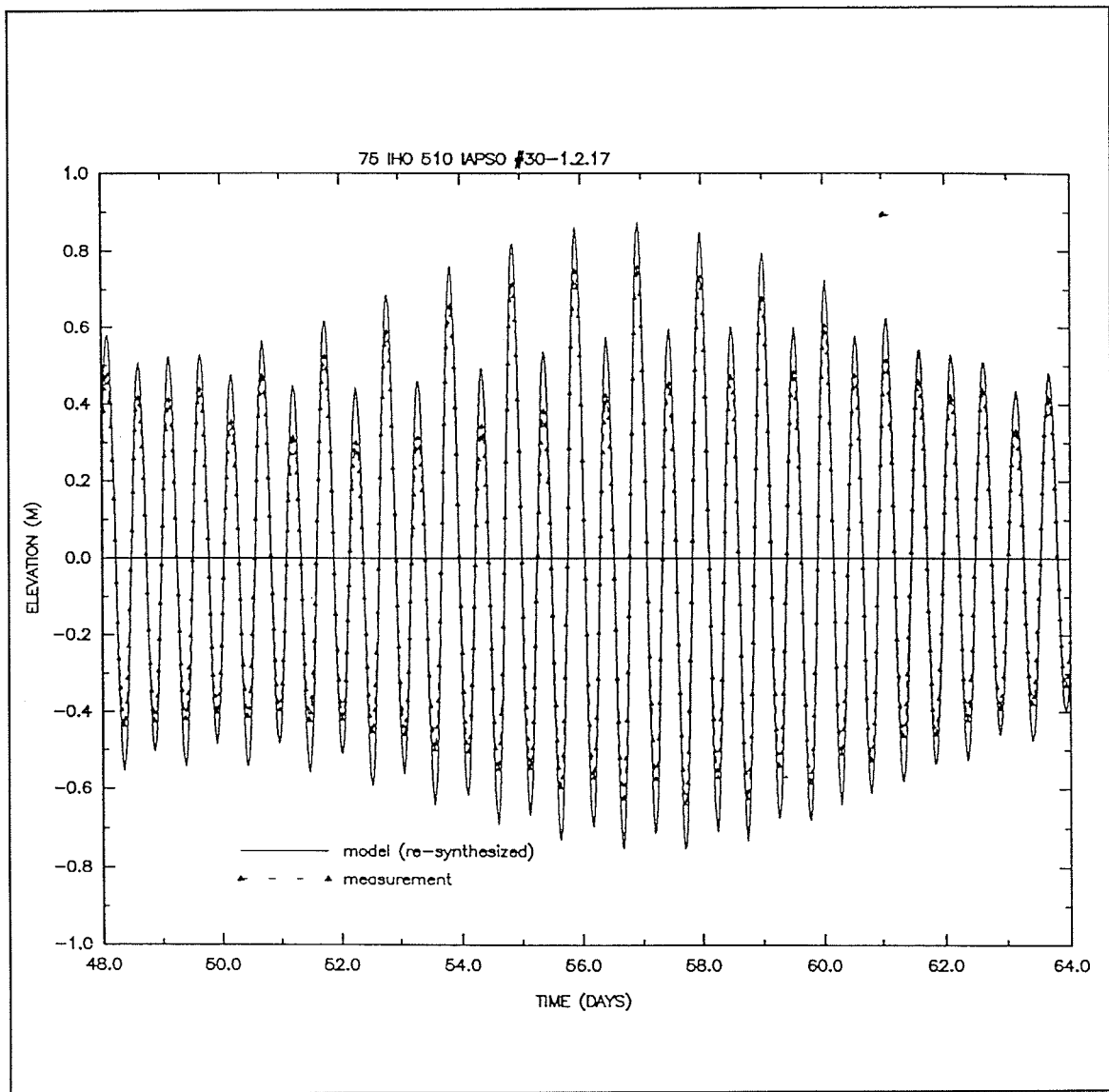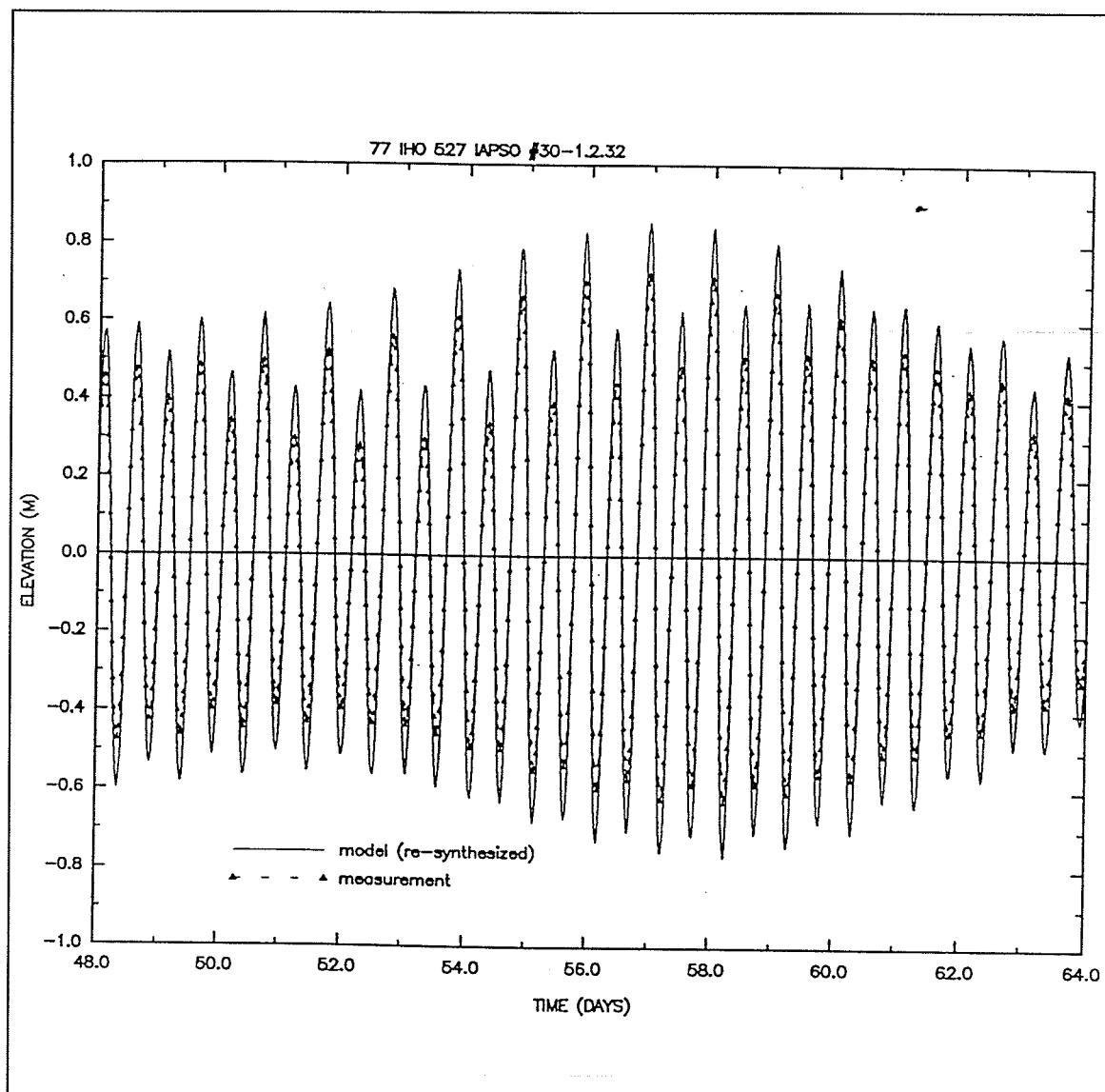
Figure 14.　(Sheet 38 of 39)

Figure 14. (Sheet 39 of 39)

Table 1
Location of Tidal Elevation Stations with Measured Data

Station No.	Station Name	Position (longitude/latitude)	Location	Source[1] of Tidal Data
1	Yarmouth, Nova Scotia	66°7′ - 43°50′	Coast	IHO, USGS
2	St. John, New Brunswick	66°3′ - 45°16′	Coast	IHO
3	Bar Harbor, ME	68°12′ - 44°24′	Coast	IHO, USGS, NOAA
4	Rockland, ME	69°6′ - 44°6′	Coast	IHO, NOAA
5	Portsmouth, Navy Yard, NH	70°44′ - 43°5′	Coast	IHO, USGS, NOAA
6	Woods Hole, Ocean Institute, MA	70°40′ - 41°30′	Coast	IHO, NOAA
7	Nantucket, Nantucket Island, MA	70°6′ - 41°17′	Coast	NOAA
8	Montauk, NY	71°58′ - 41°3′	Coast	IHO, NOAA
9	Sandy Hook, NJ	74°1′ - 40°28′	Coast	IHO, USGS, NOAA
10	Atlantic City, NJ	74°25′ - 39°21′	Coast	IHO, USGS, NOAA
11	Cape May Ferry Terminal, NJ	74°57′ - 38°58′	Coast	IHO, USGS, NOAA
12	Indian River Inlet, DE	75°4′ - 38°36′	Coast	IHO, NOAA
13	Ocean City Fishing Pier, MD	75°5′ - 38°19′	Coast	USGS, NOAA
14	Chesapeake Bay Bridge Tunnel, VA	76°7′ - 38°58′	Coast	NOAA
15	Duck Pier, NC	75°45′ - 36°11′	Coast	NOAA
16	Southport, NC	78°1′ - 33°55′	Coast	IHO, NOAA
17	Charleston, SC	79°55′ - 32°47′	Coast	IHO, NOAA
18	Savannah River Entrance, GA	80°54′ - 32°2′	Coast	IHO, NOAA
19	Mayport, FL	81°26′ - 30°24′	Coast	IHO, NOAA
20	Miami Harbour Entrance, FL	80°8′ - 25°46′	Coast	IHO, NOAA
21	Key West, FL	81°48′ - 24°33′	Coast	IHO, GOM, NOAA
22	Naples, FL	81°48′ - 26°8′	Coast	IHO, GOM
23	Cedar Key, FL	83°2′ - 29°8′	Coast	IHO, GOM
24	St. Marks Light, FL	84°11′ - 30°4′	Coast	IHO, GOM, NOAA
25	Alligator Bayou, FL	85°45′ - 30°10′	Coast	IHO, GOM
26	Bay St. Louis, MS	89°20′ - 30°18′	Coast	IHO, GOM
27	Cat Island, MS	89°10′ - 30°14′	Coast	IHO, GOM
28	Southwest Pass, LA	89°25′ - 28°56′	Coast	IHO, GOM

(Continued)

[1] Sources of Tidal Data: IHO—International Hydrographic Organization Tidal Constituent Bank (1991); USGS: U.S. Geological Survey (1984); NOAA: National Ocean Survey, National Oceanographic and Atmospheric Administration; GOM: Reid and Whitaker (1981).

Table 1 (Continued)

Station No.	Station Name	Position (longitude/latitude)	Location	Source of Tidal Data
29	Point au Fer, LA	91°21' - 29°20'	Coast	IHO, GOM
30	Galveston, TX	94°47' - 29°19'	Coast	IHO, GOM, NOAA
31	Port Aransas, TX	97°3' - 27°49'	Coast	GOM
32	South Padre Island, TX	97°9' - 26°4'	Coast	IHO, GOM
33	Ciudad Madero, Mexico	97°51' - 22°13'	Coast	GOM
34	Coatzacoalcos, Mexico	94°25' - 18°9'	Coast	IHO, GOM
35	Campeche, Mexico	90°32' - 19°50'	Coast	IHO, GOM
36	Progreso, Mexico	89°40' - 21°17'	Coast	IHO, GOM
37	IAPSO #30-1.2.6, GOM Pelagic	89°39' - 24°46'	Deep ocean	IHO,GOM
38	IAPSO #30-1.2.13, Western Florida Outer Shelf	84°15' - 26°42'	Shelf	IHO, GOM
39	Puerto Cortes, Honduras	87°57' - 15°50'	Coast	IHO
40	Puerto Cabezas, Nicaragua	83°22' - 14°1'	Coast	IHO
41	Puerto Limon, Costa Rica	83°2' - 9°60'	Coast	IHO
42	Cristobal (Canal Zone), Panama	79°55' - 9°21'	Coast	IHO
43	Cartagena, Colombia	75°32' - 10°23'	Coast	IHO
44	Willemstad, Curacao, Netherlands Antilles	68°56' - 12°6'	Coast	IHO
45	La Guaira, Venezula	66°56' - 10°37'	Coast	IHO
46	Cumana, Venezuela	64°10' - 10°27'	Coast	IHO
47	Port of Spain, Trinidad	61°31' - 10°39'	Coast	IHO
48	Castries, St. Lucia, B.W.I.	61°0' - 14°1'	Coast	IHO
49	Fort-de-France, Martinique	61°3' - 14°35'	Coast	IHO
50	St. Thomas, Virgin Islands	64°56' - 18°20'	Coast	IHO
51	Magueyes Island, Puerto Rico	67°3' - 17°58'	Coast	IHO
52	Ciudad Trujillo, Dominican Republic	69°53' - 18°28'	Coast	IHO
53	Puerto Plata, Dominican Republic	70°41' - 19°45'	Coast	IHO
54	Port-au-Prince, Haiti	72°21' - 18°33'	Coast	IHO
55	Guantanamo Bay, Cuba	75°9' - 19°54'	Coast	IHO
56	Gibara, Cuba	76°7' - 21°6'	Coast	IHO
57	Casilda,Cuba	79°59' - 21°45'	Coast	IHO

(Continued)

Table 1 (Concluded)

Station No.	Station Name	Position (longitude/ latitude)	Location	Source of Tidal Data
58	Havana, Cuba	82°20' - 23°9'	Coast	IHO, GOM
59	Nassau, Bahamas	77°21' - 25°5'	Coast	IHO
60	Eleuthera, Bahamas	76°9' - 24°56'	Coast	IHO
61	Ireland Island, Bermuda	64°50' - 32°19'	Coast	IHO
62	St. David's Island, Bermuda	64°39' - 32°22'	Coast	IHO
63	IAPSO #30-1.3.2	64°53' - 16°32'	Toe of slope	IHO
64	IAPSO #30-1.2.10, South Bermuda Rise Region	69°20' - 26°28'	Deep ocean	IHO
65	IAPSO #30-1.2.13	84°15' - 26°42'	Shelf	IHO
66	IAPSO #30-1.2.14, Rim of Blake Escarpment	76°47' - 28°1'	Slope	IHO
67	IAPSO #30-1.2.4, Hatteras Plain - Bermuda Rise	69°45' - 28°8'	Deep ocean	IHO
68	IAPSO #30-1.2.5, Bermuda Rise Region	67°32' - 28°14'	Deep ocean	IHO
69	IAPSO #30-1.2.15, Rim of Blake Escarpment	76°48' - 28°27'	Slope	IHO
70	IAPSO #30-1.2.11, East of Blake Plateau	76°25' - 30°26'	Toe of slope	IHO
71	IAPSO #30-1.2.18, Near Bermuda	64°26' - 32°1'	Deep ocean	IHO
72	IAPSO #30-1.2.3	75°37' - 32°41'	Toe of slope	IHO
73	IAPSO #30-1.2.16, East of Cape Hatteras	73°5' - 37°22'	Slope	IHO
74	IAPSO #30-1.2.19, East of New York Bight	71°22' - 39°10'	Slope	IHO
75	IAPSO #30-1.2.17, Outer New York Bight	72°10' - 39°13'	Slope	IHO
76	IAPSO #30-1.2.1, Off Long Island, NY	68°38' - 40°7'	Shelf break	IHO
77	IAPSO #30-1.2.32	70°54' - 40°18'	Shelf	IHO

Table 2
Properties of Grids R1 through R5 and V1 through V3

Grid	Nodes	Boundary	Grid Structure	Approximate Grid Size		Resolution		Time-step sec
				degrees/min	km	$\left(\frac{\lambda_{M_2}}{\Delta x}\right)_{max}$	$\left(\frac{\lambda_{M_2}}{\Delta x}\right)_{min}$	
R1	434	Coarse	Uniform	1.6°	140	78	1.5	600
R2	1611	Coarse	Uniform	0.8°	70	162	2.9	300
R3	6191	Coarse	Uniform	24′	35	341	5.7	150
R4	24255	Coarse	Uniform	12′	17	704	11.3	75
R5	64065	Coarse	Semi-uniform	6′→12′	8→17	1322	22.6	37.5
V1	10147	Coarse	Graded	5′→1.6°	7→140	1184	16.0	37.5
V2	27816	Coarse	Graded	5′→1.6°	7→140	1013	16.0	37.5
V3	19858	Fine	Graded	5′→1.6°	7→140	1344	16.5	37.5

Table 3
M_2 Elevation Amplitude Errors, $E_{M_2-amp}^{grid-R5}$, for the Grids Applied in the Convergence Study as Compared to the Converged Solution Obtained with Grid R5 for Various Regions with the Domain

	$E_{M_2-amp}^{grid-R5}$								
		Stations with Measurement Data				Additional Stations without Measurement Data			
Grid	Entire Domain Stations 1-147	U.S. East Coast Stations 1-20	Gulf of Mexico Stations 21-38	Caribbean Sea Stations 39-58	Remote Stations 59-77	Continental Shelf Stations 78-87	Vicinity of the Shelf Break Stations 88-109	Vicinity of the Toe of Slope Stations 110-130	Deep Ocean Stations 131-147
R1	0.293	0.303	0.593	0.524	0.083	0.339	0.121	0.112	0.091
R2	0.113	0.107	0.423	0.202	0.022	0.102	0.065	0.113	0.089
R3	0.033	0.025	0.139	0.089	0.010	0.032	0.031	0.050	0.039
R4	0.013	0.013	0.026	0.025	0.005	0.008	0.011	0.015	0.012
V1	0.022	0.022	0.037	0.042	0.008	0.025	0.013	0.015	0.012
V2	0.024	0.024	0.043	0.049	0.011	0.013	0.023	0.033	0.026
V3	0.160	0.170	0.154	0.264	0.032	0.176	0.079	0.111	0.087

Table 4
M_2 Elevation Phase Errors, $E_{M_2\text{-}phase}^{grid-R5}$, for the Grids Applied in the Convergence Study as Compared to the Converged Solution Obtained with Grid R5 for Various Regions within the Domain

	$E_{M_2\text{-}phase}^{grid-R5}$, degrees								
		Stations with Measurement Data				Additional Stations without Measurement Data			
Grids	Entire Domain Stations 1-147	U.S. East Coast Stations 1-20	Gulf of Mexico Stations 21-38	Caribbean Sea Stations 39-58	Remote Stations 59-77	Continental Shelf Stations 78-87	Vicinity of the Shelf Break Stations 88-109	Vicinity of the Toe of Slope Stations 110-130	Deep Ocean Stations 131-147
R1	20.9	31.6	30.1	29.1	8.4	22.4	19.4	15.1	12.0
R2	9.9	11.9	12.9	21.1	2.3	7.2	10.5	6.3	5.3
R3	3.4	4.5	6.8	5.6	0.95	2.5	3.1	1.9	1.7
R4	2.3	1.5	6.3	3.2	0.31	1.9	2.3	2.0	1.2
V1	3.2	1.6	10.4	2.6	0.33	3.0	3.6	2.8	1.3
V2	3.1	3.5	9.6	1.8	0.53	3.3	2.9	2.5	1.4
V3	14.6	16.1	41.5	14.2	2.2	12.2	13.6	10.9	6.2

Table 5
Tidal Potential Constants for the Principal Tidal Constituents (from Reid (1990)) and the Associated Effective Earth Elasticity Factor (from Wahr (1981))

Species, j	n	Constituent	T_{jn}, hr	C_{jn}, m	α_{jn}
1	1	K_1 luni-solar	23.934470	0.141565	0.736
	2	O_1 principal lunar	25.819342	0.100514	0.695
	3	P_1 principal solar	24.065890	0.046843	0.706
	4	Q_1 elliptical lunar	26.868357	0.019256	0.695
2	1	M_2 principal lunar	12.420601	0.242334	0.693
	2	S_2 principal solar	12.000000	0.112841	0.693
	3	N_2 elliptical lunar	12.658348	0.046398	0.693
	4	K_2 luni-solar	11.967235	0.030704	0.693

Table 6
Amplitude Errors, $E_{j-amp}^{V3-meas}$, for Constituent j Computed Using Grid V3 as Compared to Field Measured Values for Various Regions within the Domain

j	Constituent	$E_{j-amp}^{V3-meas}$				
		Entire Domain Stations 1-77	U.S. East Coast Stations 1-20	Gulf of Mexico Stations 21-38	Caribbean Sea Stations 39-58	Remote Stations 59-77
1	K_1	0.182	0.220	0.199	0.077	0.131
2	O_1	0.205	0.212	0.218	0.109	0.199
3	P_1	0.345	0.289	0.453	0.167	0.235
4	Q_1	0.324	0.336	0.356	0.131	0.251
5	M_2	0.270	0.266	0.278	0.652	0.204
6	S_2	0.290	0.288	0.407	0.529	0.122
7	N_2	0.244	0.234	0.124	0.741	0.154
8	K_2	0.453	0.444	0.546	0.455	0.407

Table 7
Phase Errors, $E_{j-phase}^{V3-meas}$, for Constituent j Computed Using Grid V3 as Compared to Field Measured Values for Various Regions within the Domain

j	Constituent	$E_{j-phase}^{V3-meas}$				
		Entire Domain Stations 1-77	U.S. East Coast Stations 1-20	Gulf of Mexico Stations 21-38	Caribbean Sea Stations 39-58	Remote Stations 59-77
1	K_1	9.5	17.6	7.8	5.6	6.7
2	O_1	8.3	9.5	7.2	9.9	6.3
3	P_1	12.4	23.4	7.5	7.1	9.4
4	Q_1	8.6	8.0	9.6	9.4	7.5
5	M_2	22.4	15.1	33.1	31.2	10.8
6	S_2	27.5	20.2	28.7	40.8	20.6
7	N_2	19.6	13.6	37.4	23.9	8.0
8	K_2	23.6	15.0	44.5	35.8	12.7

Table 8

Distribution of Amplitude Ratio Error, $R_a = \hat{\eta}_j^{V3}(x_\iota, y_\iota)/\hat{\eta}_j^{meas}(x_\iota, y_\iota)$, for the Measurement Stations

j	Constituent	% Distribution of R_a												
		$R_a < 0.5$	$0.5 \le R_a < 0.6$	$0.6 < R_a \le 0.7$	$0.7 < R_a \le 0.8$	$0.8 < R_a \le 0.9$	$0.9 < R_a \le 1.0$	$1.0 < R_a \le 1.1$	$1.1 < R_a \le 1.2$	$1.2 < R_a \le 1.3$	$1.3 < R_a \le 1.4$	$1.4 < R_a \le 1.5$	$1.5 < R_a \le 2.0$	$2.0 < R_a$
1	K_1	0.0	0.0	2.6	7.9	11.8	21.1	26.3	11.8	10.5	6.6	1.3	0.0	0.0
2	O_1	0.0	0.0	1.3	11.8	22.4	21.1	10.5	18.4	9.2	5.3	0.0	0.0	0.0
3	P_1	0.0	0.0	0.0	1.4	4.3	14.3	11.4	10.0	25.7	10.0	5.7	17.1	0.0
4	Q_1	0.0	6.4	8.1	9.7	17.7	14.5	12.9	9.7	6.5	3.2	4.8	6.5	0.0
5	M_2	1.3	2.6	0.0	3.9	2.6	7.8	6.5	23.4	15.6	11.7	3.9	9.1	13.7
6	S_2	2.6	1.3	0.0	2.6	9.2	10.5	18.4	13.1	7.9	11.8	2.6	9.2	10.5
7	N_2	1.4	2.9	1.4	5.7	5.7	7.1	17.1	20.0	11.4	10.0	4.3	7.1	5.7
8	K_2	7.2	7.1	3.6	0.0	5.4	5.4	7.1	3.6	7.1	10.7	7.1	28.6	7.1

Table 9
Distribution of Phase Error, $P_d = \varphi_j^{V3}(x_\iota, y_\iota) - \varphi_j^{meas}(x_\iota, y_\iota)$, for the Measurement Stations

j	Consti-tuent	% Distribution of R_a											
		-180 $< P_d$ ≤ -60	-60 $< P_d$ ≤ -40	-40 $< P_d$ ≤ -30	-30 $< P_d$ ≤ -20	-20 $< P_d$ ≤ -10	-10 $< P_d$ ≤ 0	0 $< P_d$ ≤ 10	10 $< P_d$ ≤ 20	20 $< P_d$ ≤ 30	30 $< P_d$ ≤ 40	40 $< P_d$ ≤ 60	60 $< P_d$ ≤ 180
1	K_1	0.0	0.0	0.0	0.0	3.9	15.8	51.3	13.2	10.5	1.3	3.9	0.0
2	O_1	0.0	0.0	1.3	2.6	0.0	22.4	55.3	13.2	2.6	1.3	1.3	0.0
3	P_1	0.0	0.0	0.0	0.0	0.0	15.7	50.0	12.9	8.6	10.0	2.9	0.0
4	Q_1	0.0	0.0	1.6	1.6	12.9	37.1	30.6	14.5	1.6	0.0	0.0	0.0
5	M_2	2.6	7.8	3.6	13.0	14.3	26.0	15.6	2.6	5.2	2.6	2.6	3.9
6	S_2	2.6	1.3	9.2	15.8	14.5	11.8	11.8	7.9	3.9	9.2	5.3	6.6
7	N_2	1.4	14.3	4.3	14.3	8.6	27.1	15.7	8.6	2.9	0.0	2.9	0.0
8	K_2	1.8	1.8	1.8	7.1	21.4	25.0	17.9	5.4	3.6	3.6	3.6	7.1

Appendix A
Resynthesis of Time Histories
Using the Cotidal Charts

In order to resynthesize a time history from the cotidal charts presented in Figures 12 and 13 in the main text and the more detailed cotidal charts for the U.S. east coast in Figures B1 and B2 and the Gulf of Mexico in Figures C1 and C2, the following steps are applied.

Step 1

Interpolate amplitudes and phases for the eight astronomical constituents presented in this report using the most detailed set of cotidal charts available. For example, in order to obtain values for Duck Pier, NC (located 75°7'W and 36°11'N), the set of cotidal charts presented in Figures B1 and B2 are interpolated. The adjacent amplitudes A_i and phases Ψ_i can be readily obtained:

Constituent	A_i, m	Ψ_i, deg
K_1	0.092	179
O_1	0.066	183
P_1	0.038	175
Q_1	0.012	179
N_2	0.14	354
M_2	0.63	14
S_2	0.11	57
K_2	0.037	48

Step 2

Surface elevations as a function of time can now be computed using the following relationship:

$$\zeta(x, y, t) = \sum_{i}^{8} A_i(x, y) \, f_i(t_0)$$

$$\cos\left[\omega_i(t - t_0) + v_i(t_0) - \Psi_i^{(radians)}(x, y)\right]$$

(A1)

where $\zeta(x, y, t)$ equals the free surface elevation at the site of interest as a function of time, $A_i(x, y)$ equals the amplitude for the ith constituent, $\Psi_i(x, y)$ equals the phase for the ith constituent (in radians per second), $f_i(t_0)$ equals the nodal factor relative to reference time t_0 for the ith constituent, and $v_i(t_0)$ equals the equilibrium argument relative to reference time t_0 for the ith constituent. For the eight constituents of interest, ω_i has the following values:

Constituent	ω_i, radians/second)
K_1	0.000072921158358
O_1	0.000067597744151
P_1	0.000072522945975
Q_1	0.000064958541129
N_2	0.000137879699487
M_2	0.000140518902509
S_2	0.000145444104333
K_2	0.000145842317201

Guidelines as to how to compute f_i^{BF} and v_i^{BF} are given by Schureman (1941) and Foreman (1977). If equilibrium tides are computed, f_i^{BF} and v_i^{BF} should be specified as 1.0 and 0.0 for all constituents. A resynthesized signal for the data is presented between 50 and 60 days in Figure A1.

Step 2 (Alternate)

An alternate procedure to computing a time series according to Equation A1 is to use the constituent tide record generation program of the Automated Coastal Engineering System (ACES) (Leenknecht, Szuwalski, and Sherlock 1990). This program requires constituent data for the particular desired location to predict a tide elevation at that locale for the period of time specified by the user. The tidal constituents contained in this report can be used as input to the ACES program with one exception. The Greenwich epochs Ψ shown in Equation A1 must be converted to local epochs κ. This transformation is according to the following relationship:

$$Greenwich\,epoch\,\Psi_i = \kappa_i + pL \qquad (A2)$$

where κ is the local epoch needed for input to the ACES program to reconstruct a local tide, p is the coefficient of the constituent (i.e., 2 for M_2, 1 for κ_1, etc.), and L is the longitude of the location for which a tidal prediction is desired. By making the above adjustment, this report can be used in conjunction with the ACES program to yield tidal predictions at any location along the east coast of the United States and Gulf of Mexico.
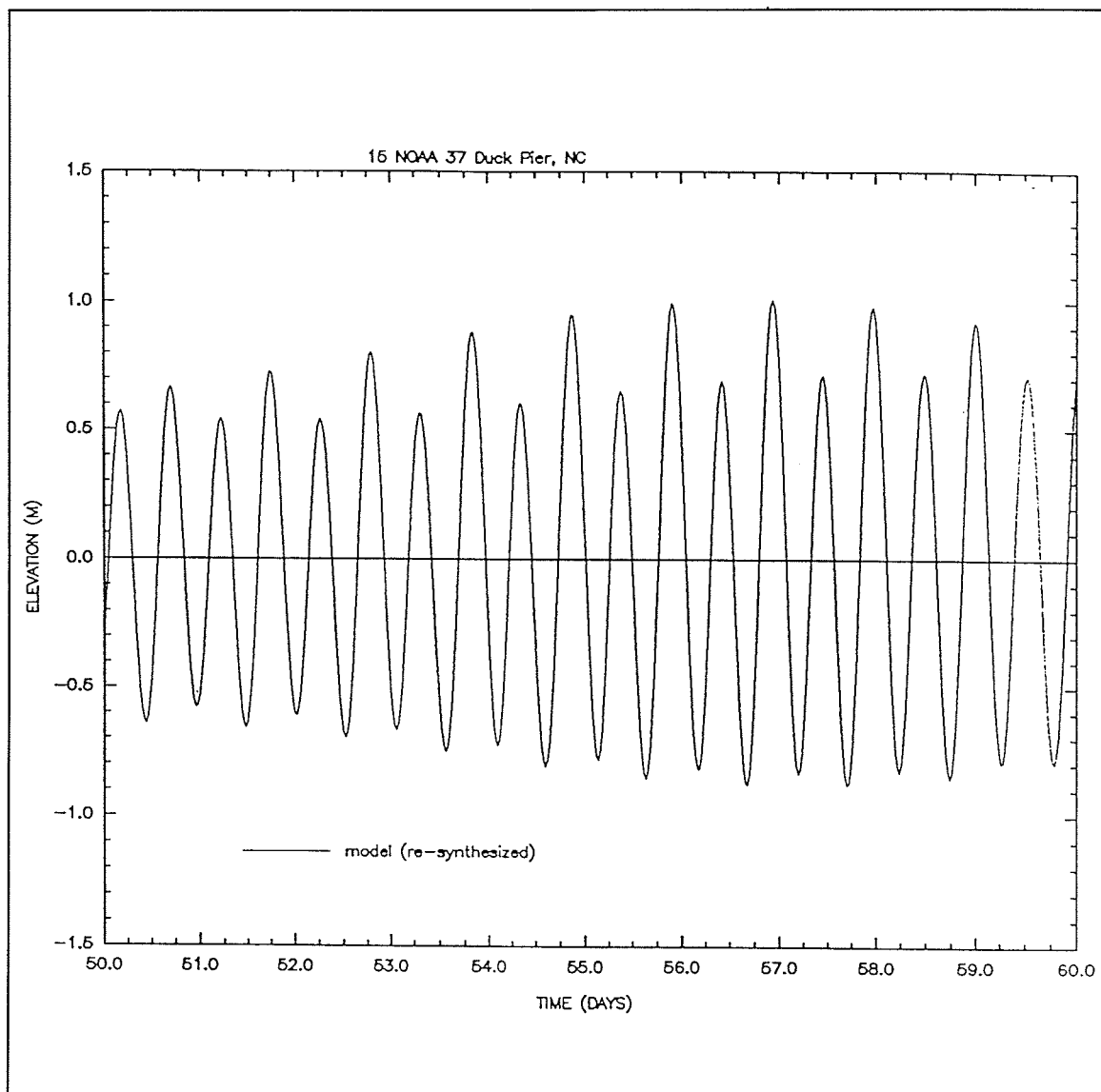
Figure A1. Sample time history of resynthesized surface elevations from harmonically decomposed computed constituent data (using the K_1, O_1, P_1, Q_1, M_2, N_2, S_2, and K_2 constituents) at an example station within the Western North Atlantic
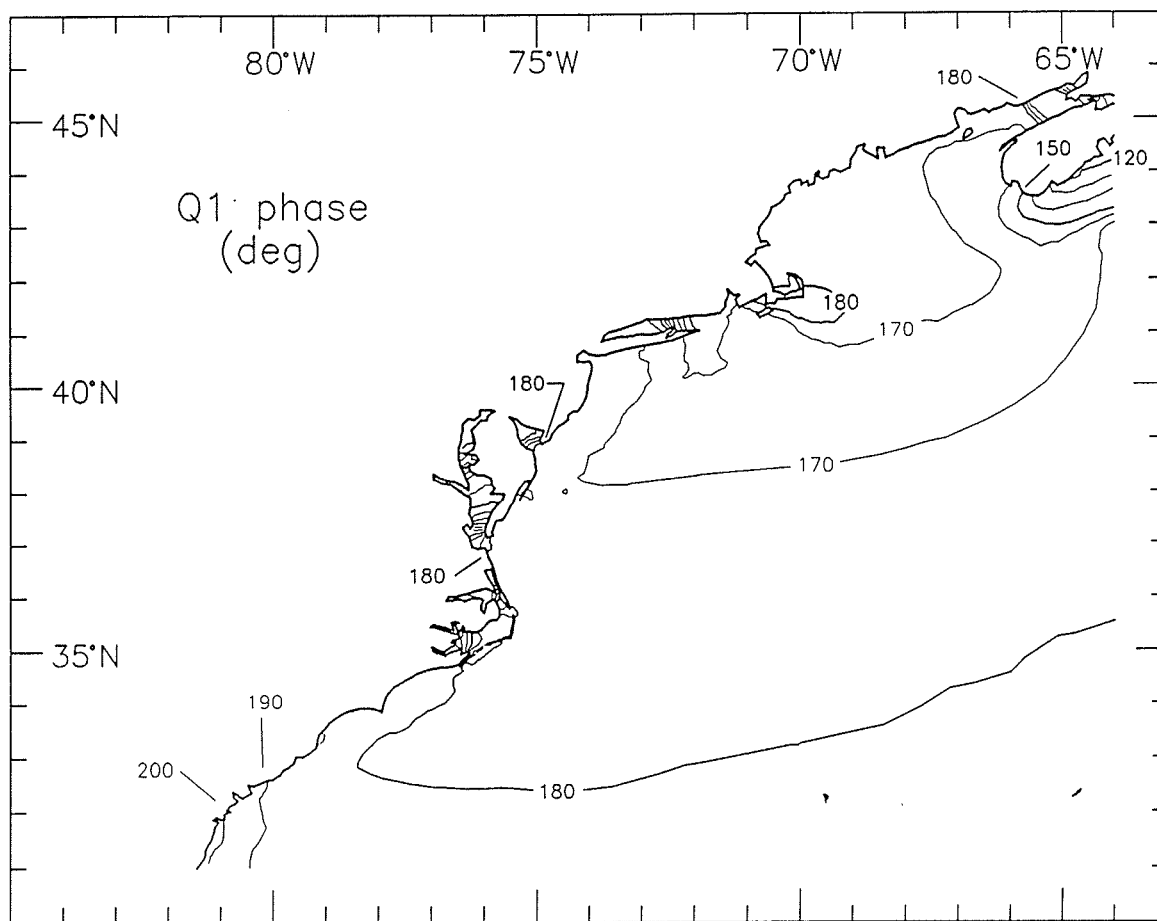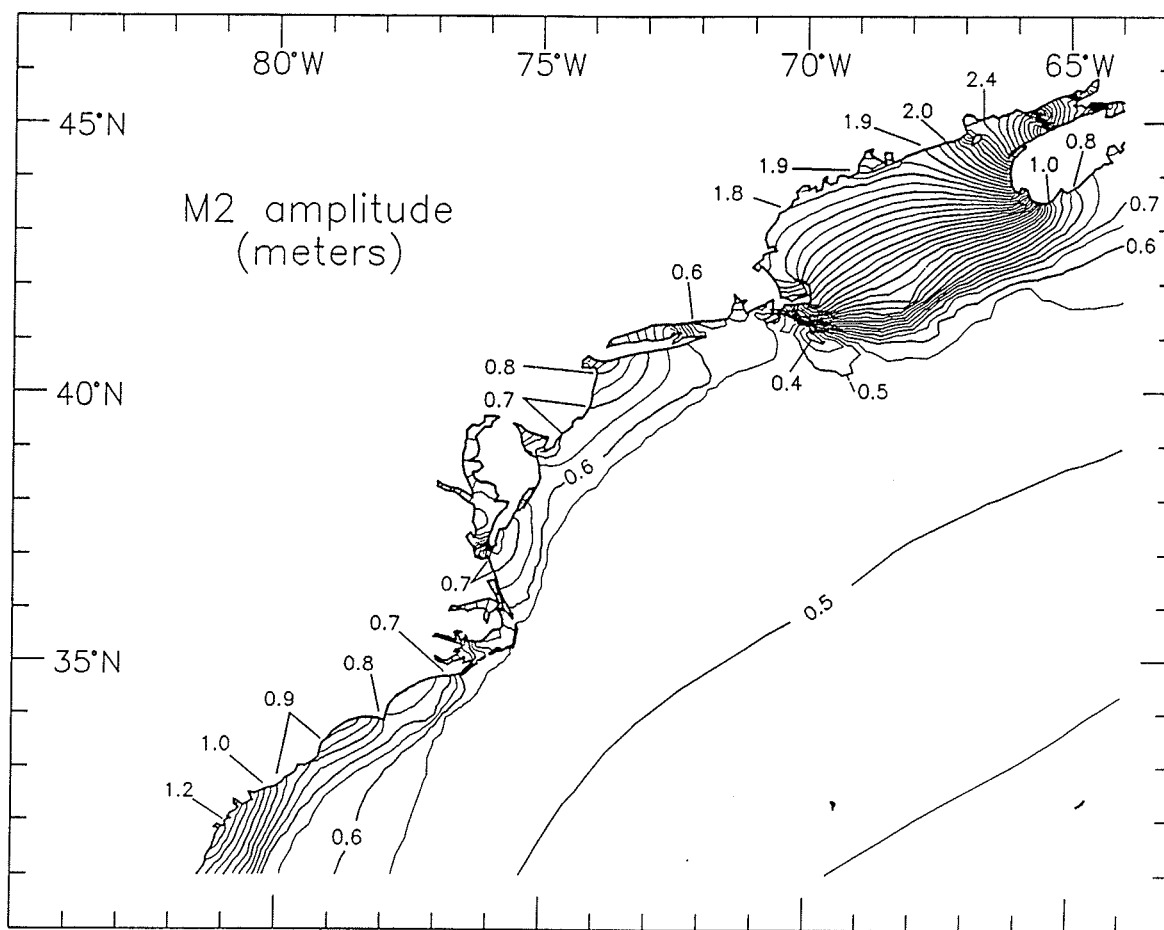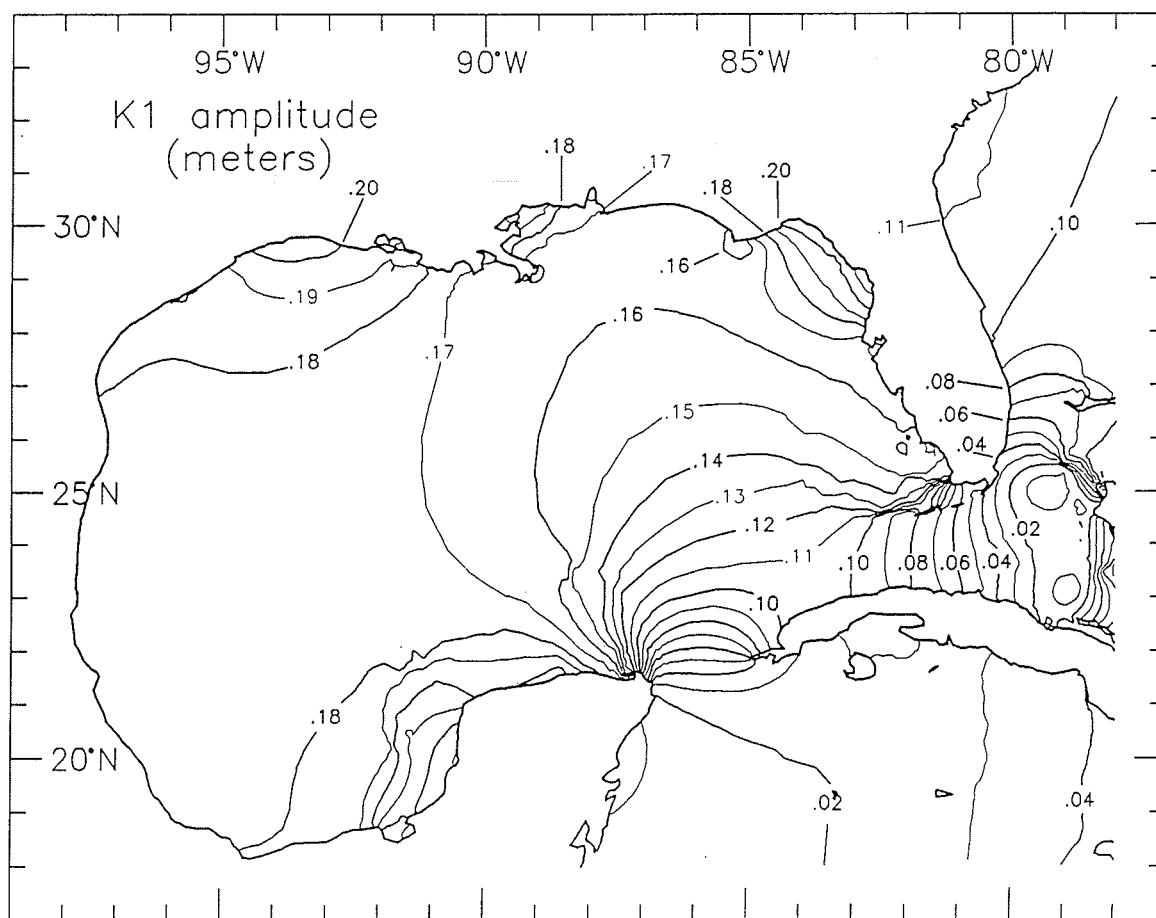
Appendix B
Cotidal Charts
for the U.S. East Coast
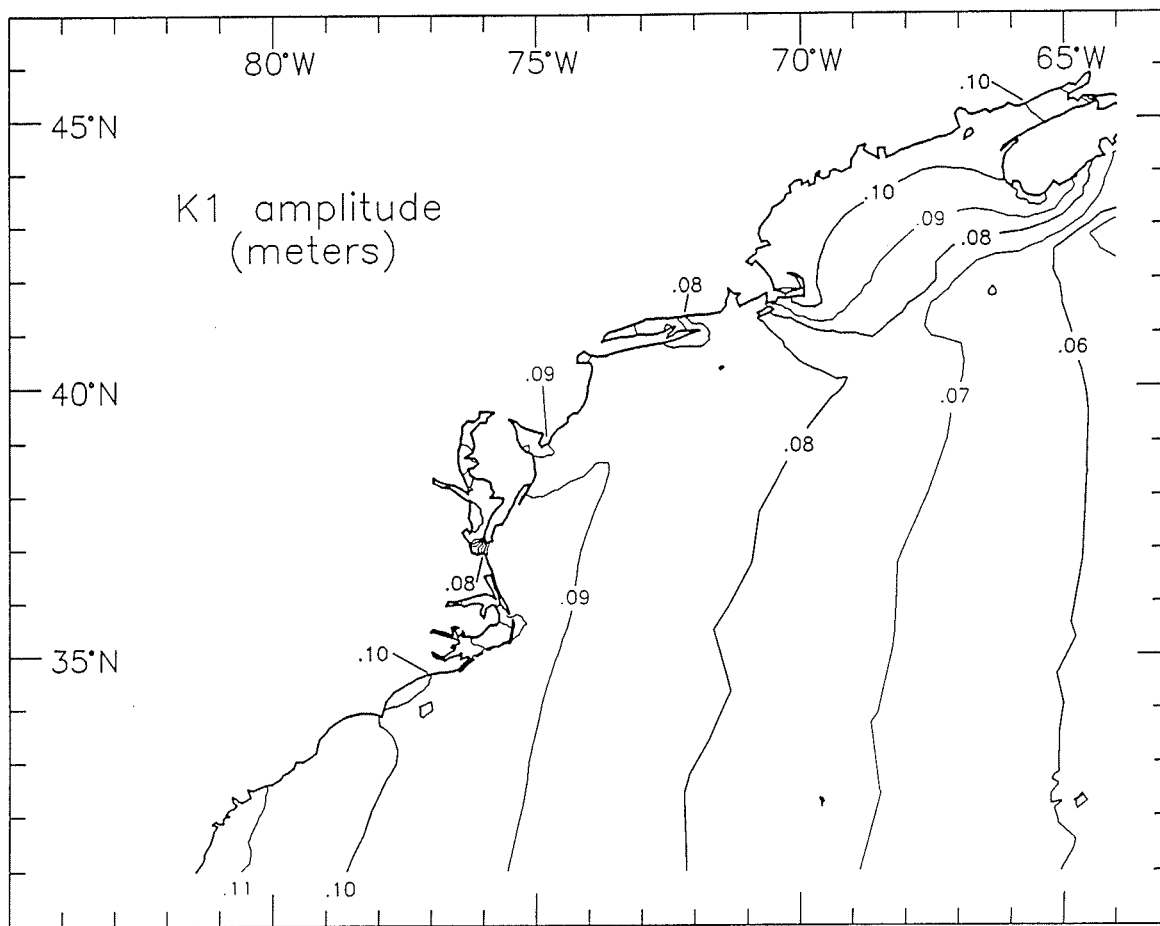
Figure B1. Computed contours for elevation amplitudes (in meters) and phases (in degrees relative to GMT) for the K_1, O_1, P_1, and Q_1 diurnal astronomical tidal constituents for the U.S. east coast (Sheet 1 of 8)
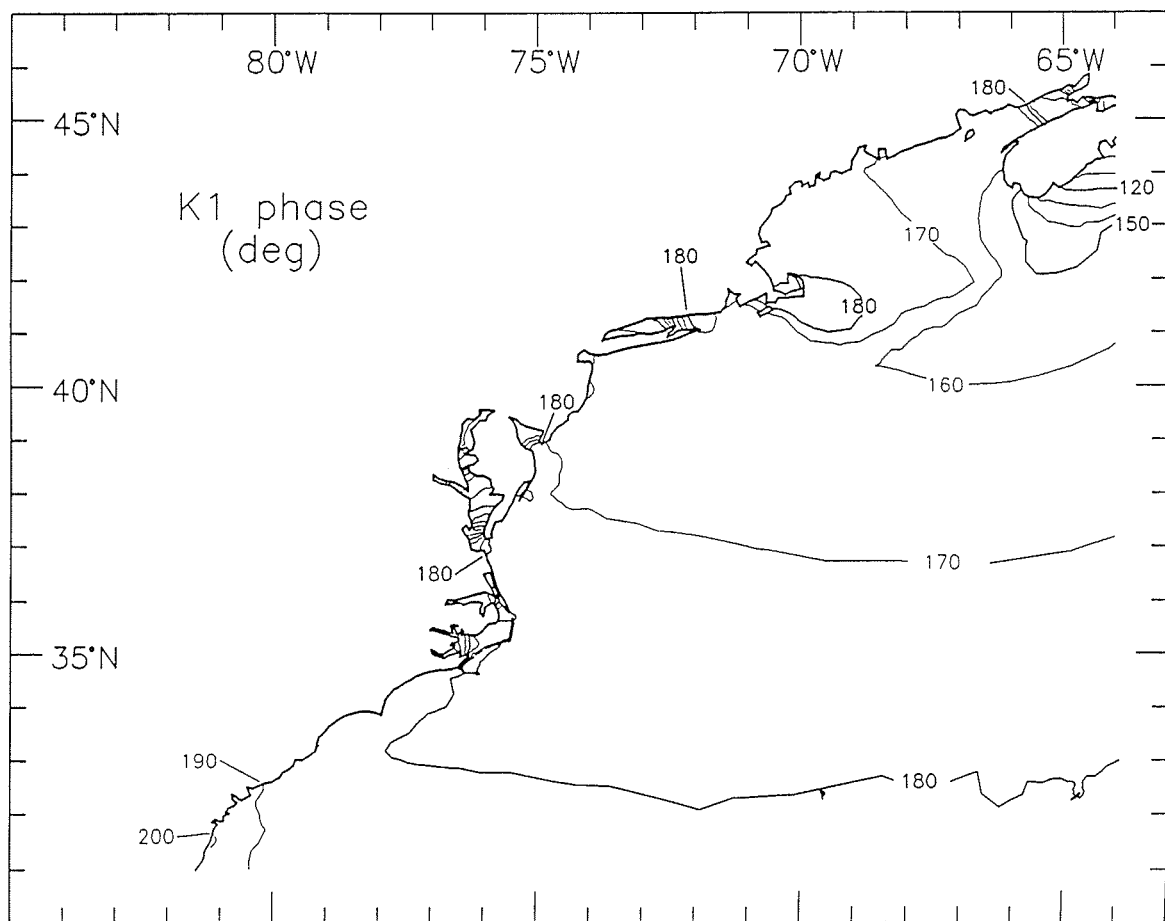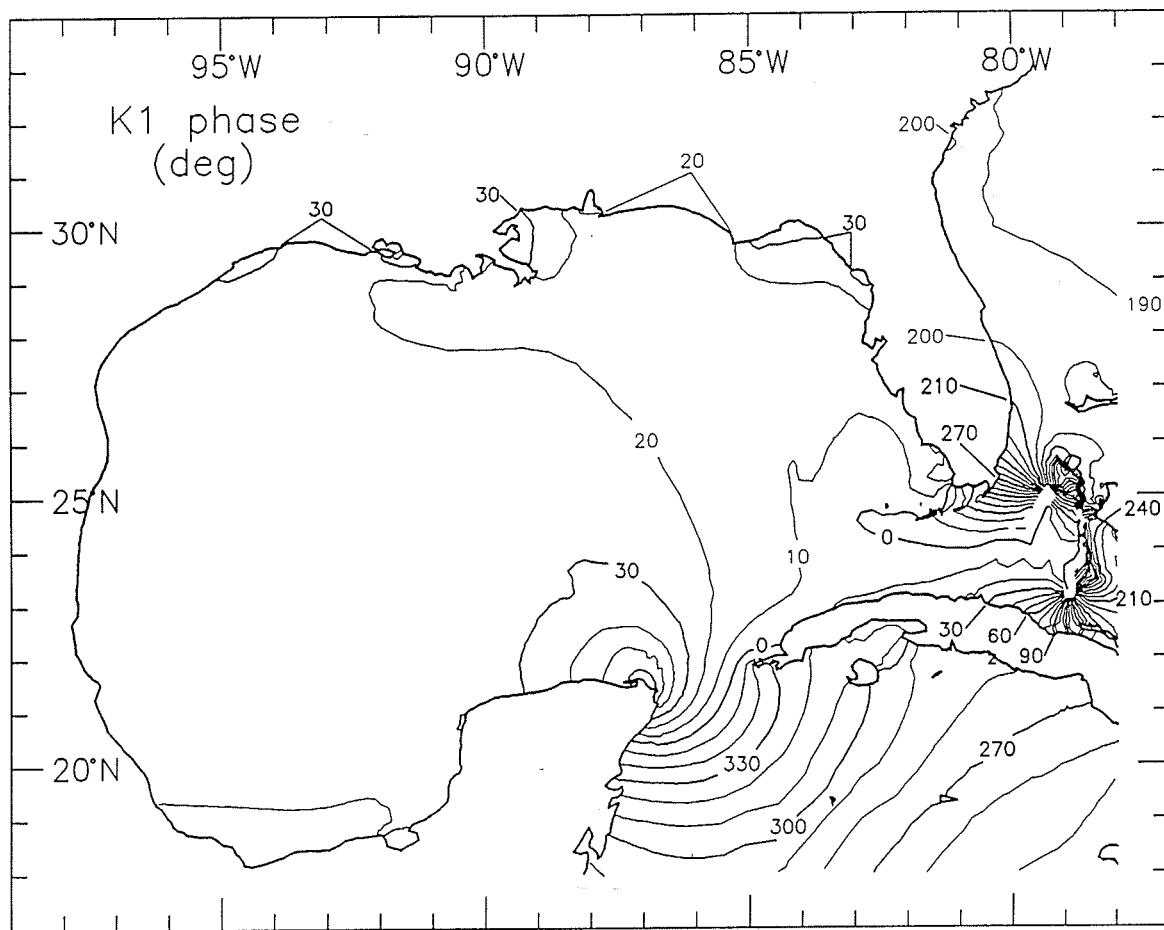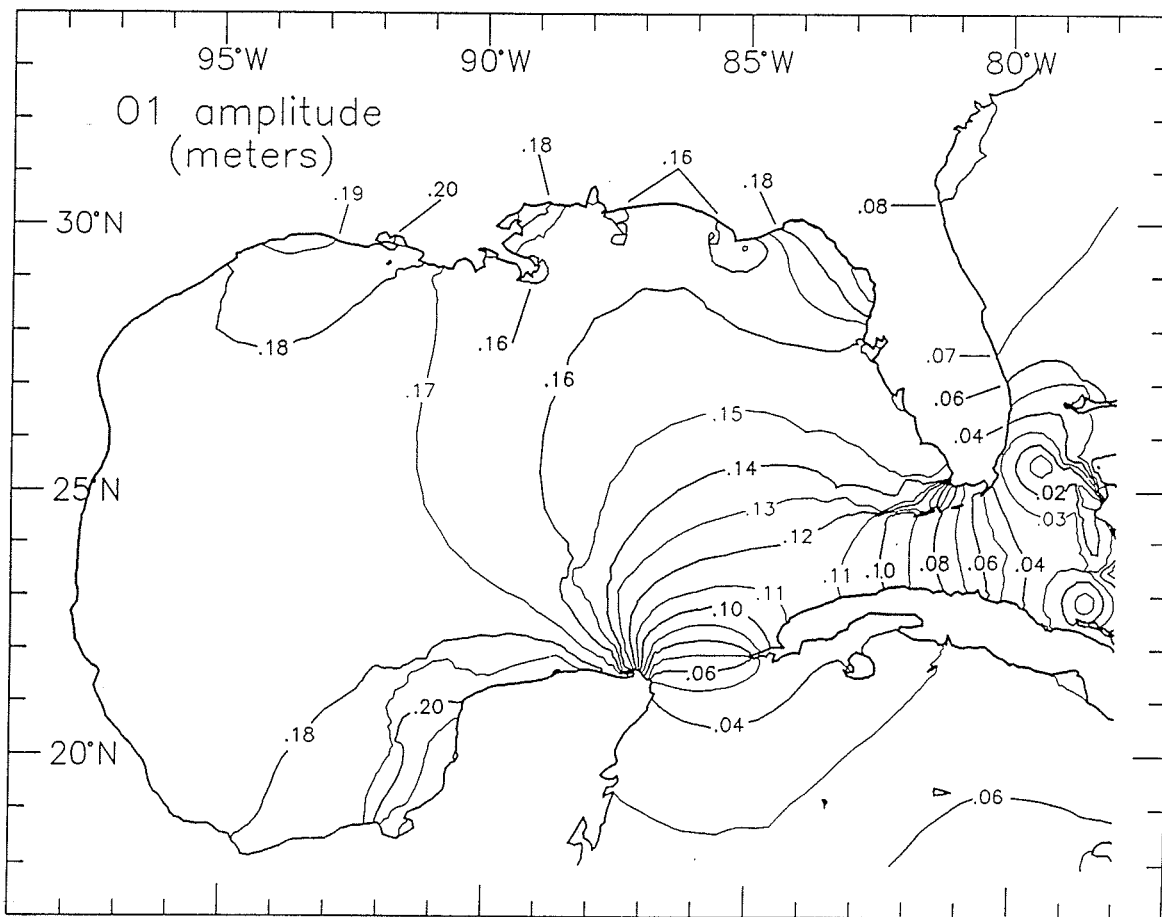
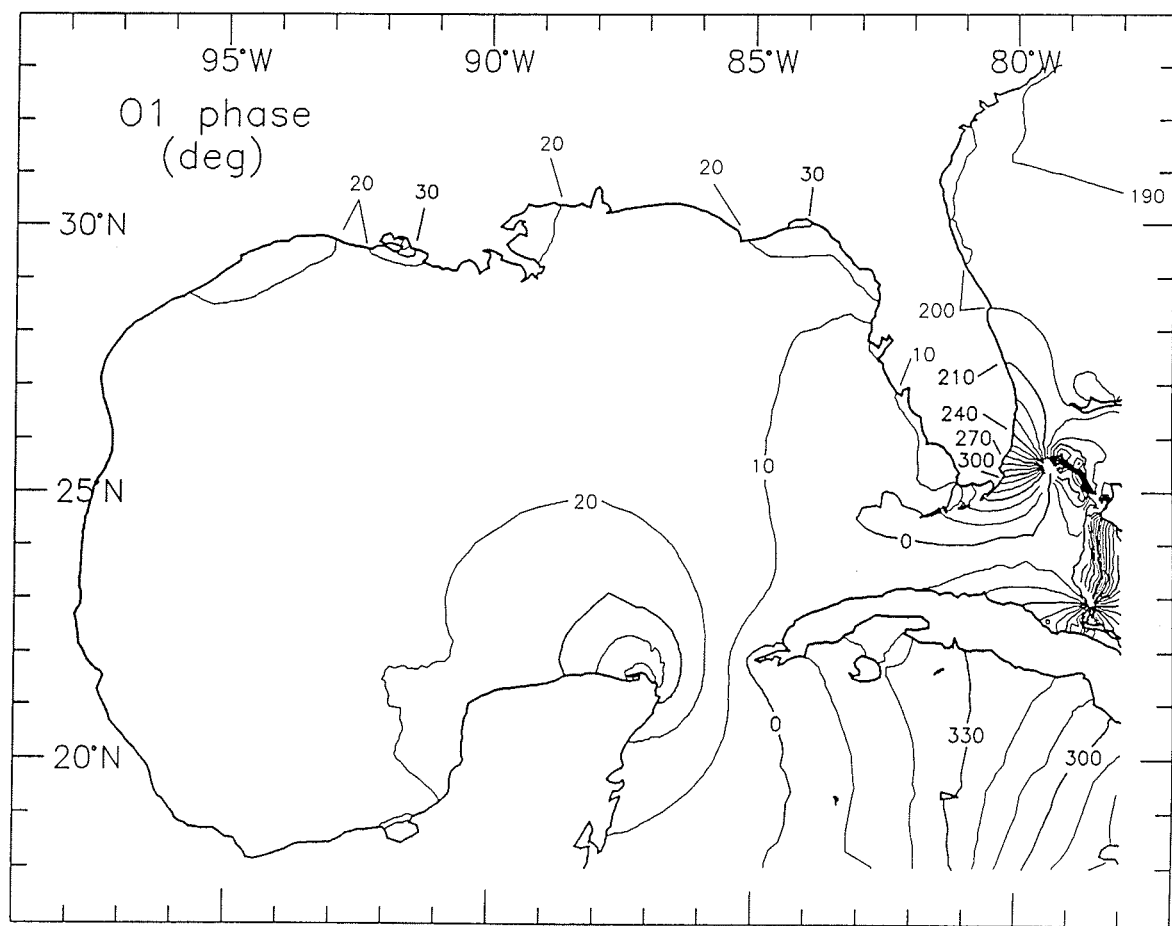Figure B1. (Sheet 2 of 8)
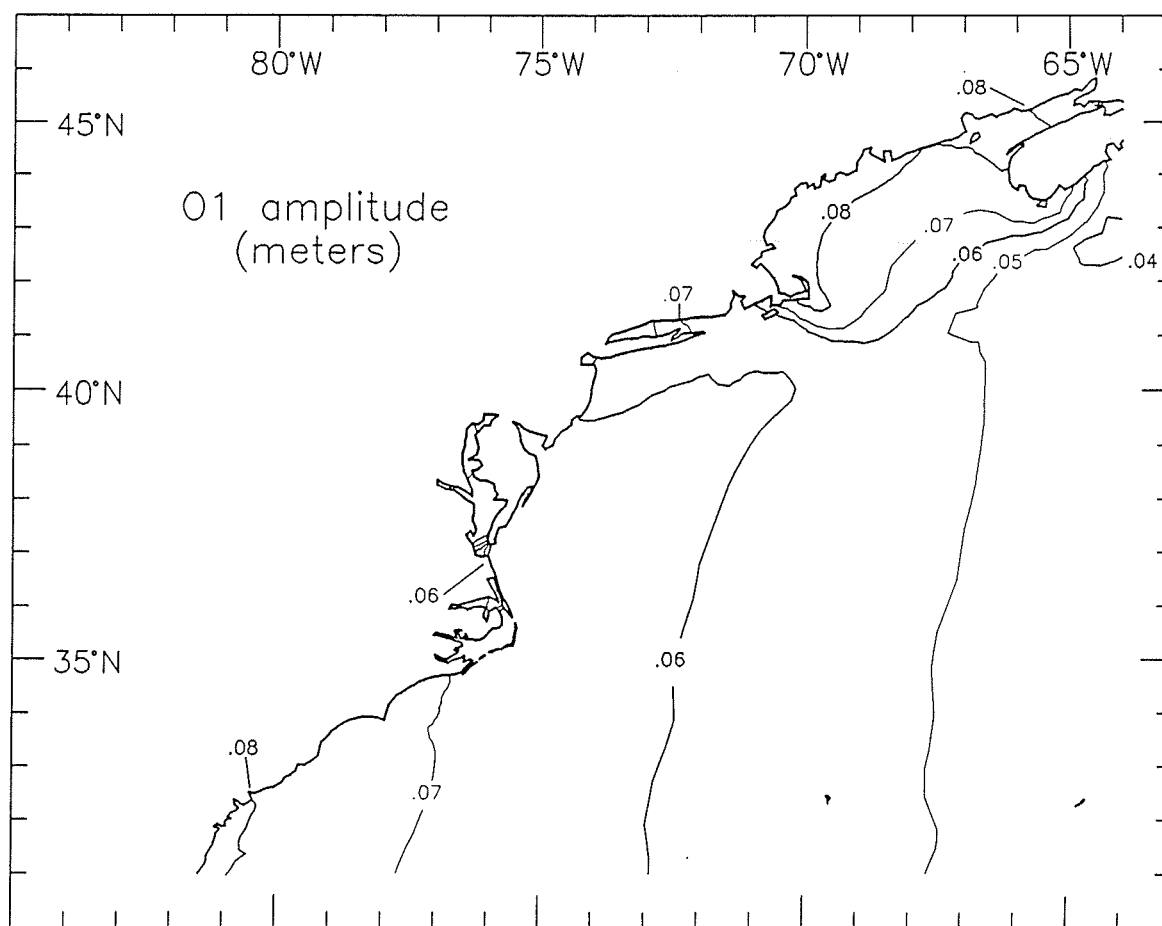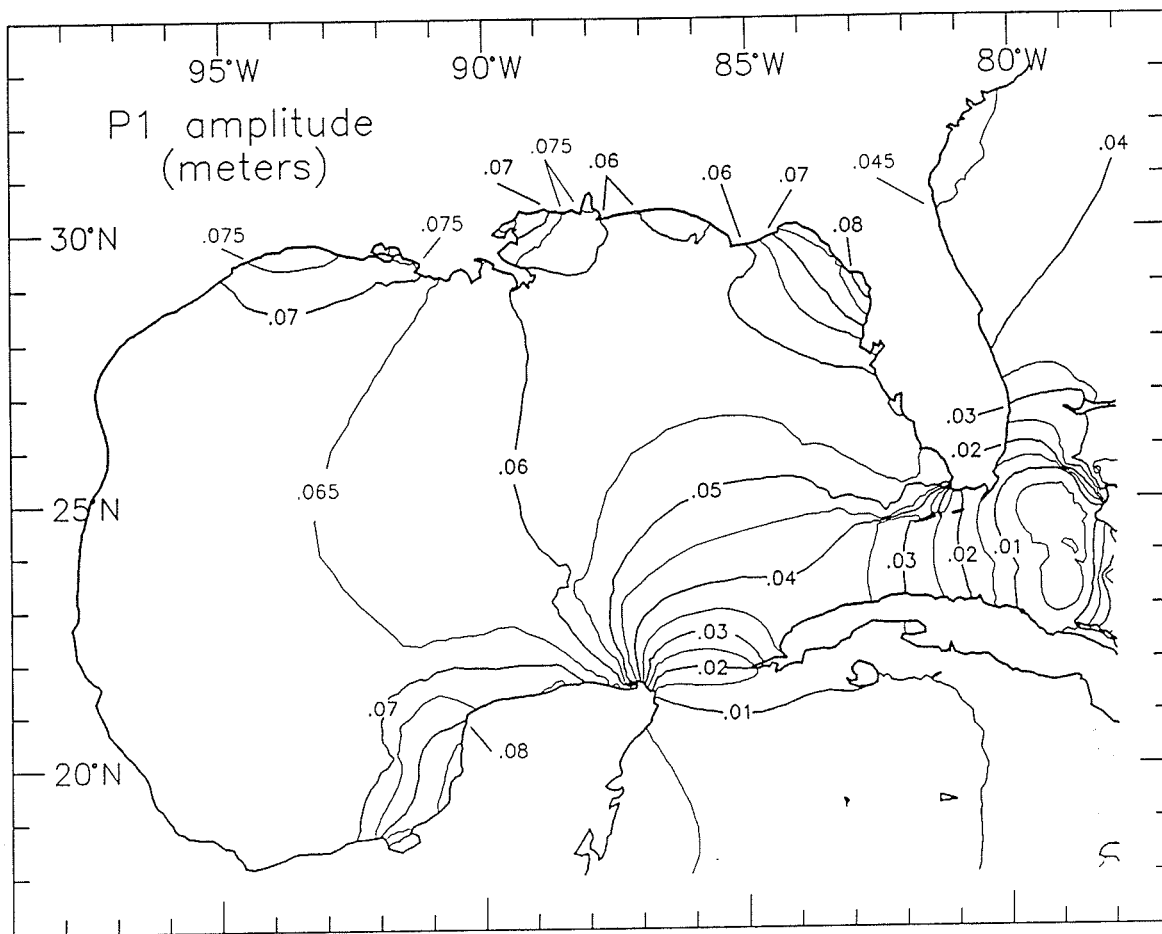
Figure B1. (Sheet 3 of 8)
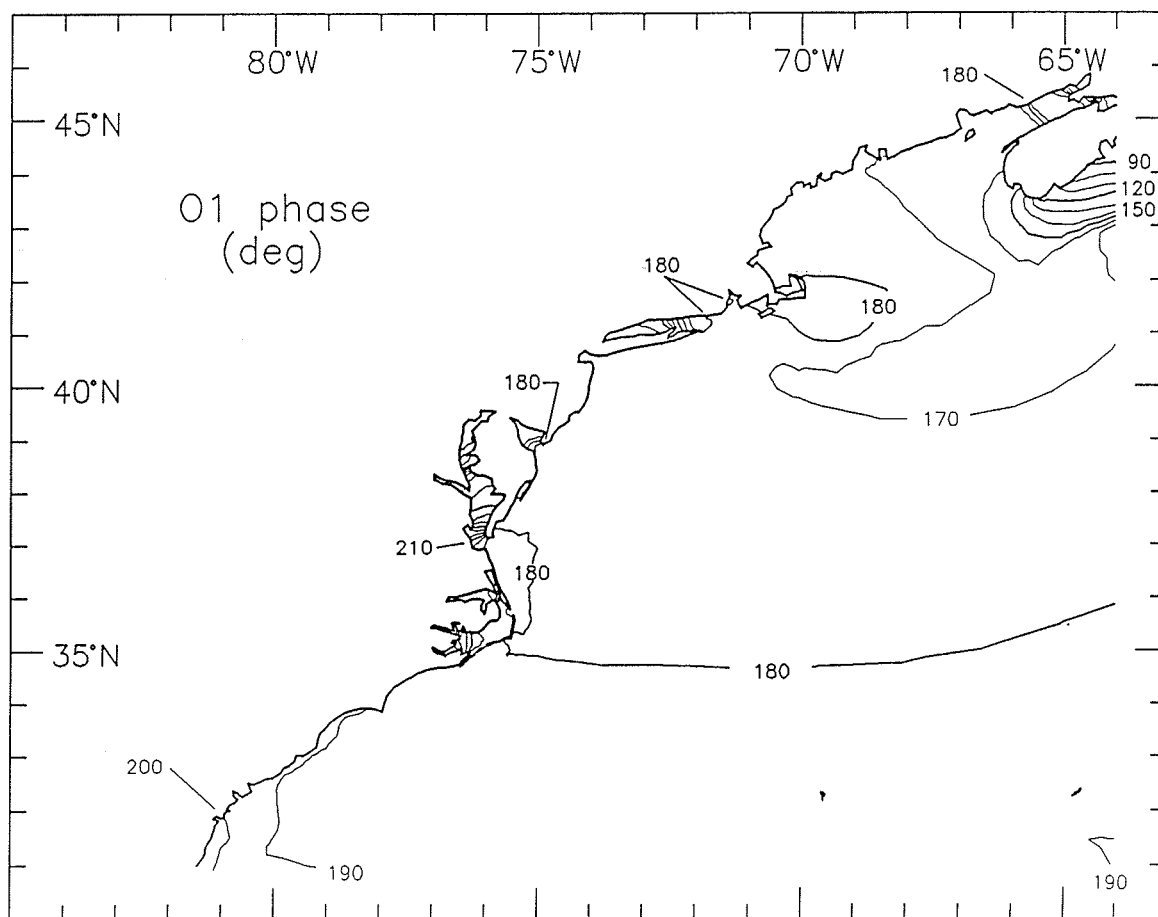
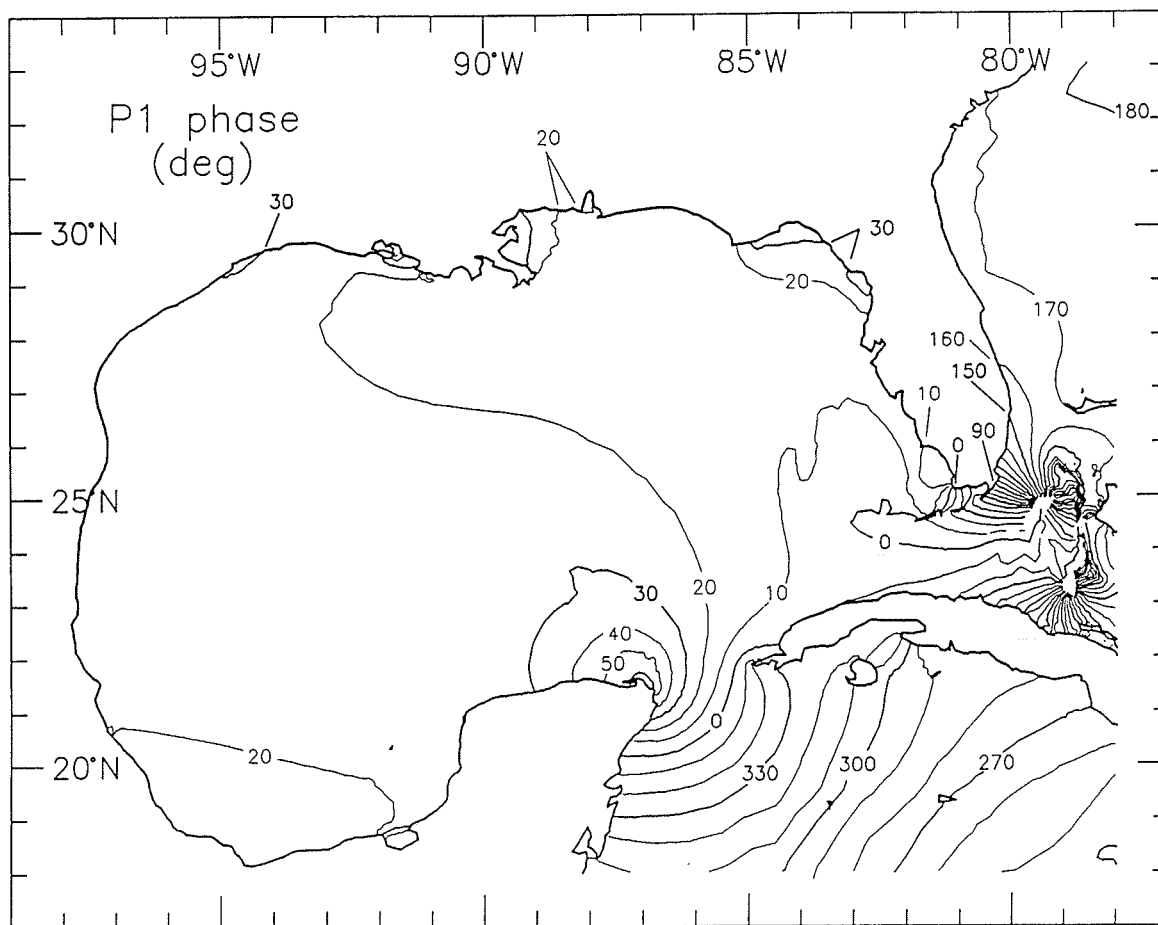Figure B1. (Sheet 4 of 8)
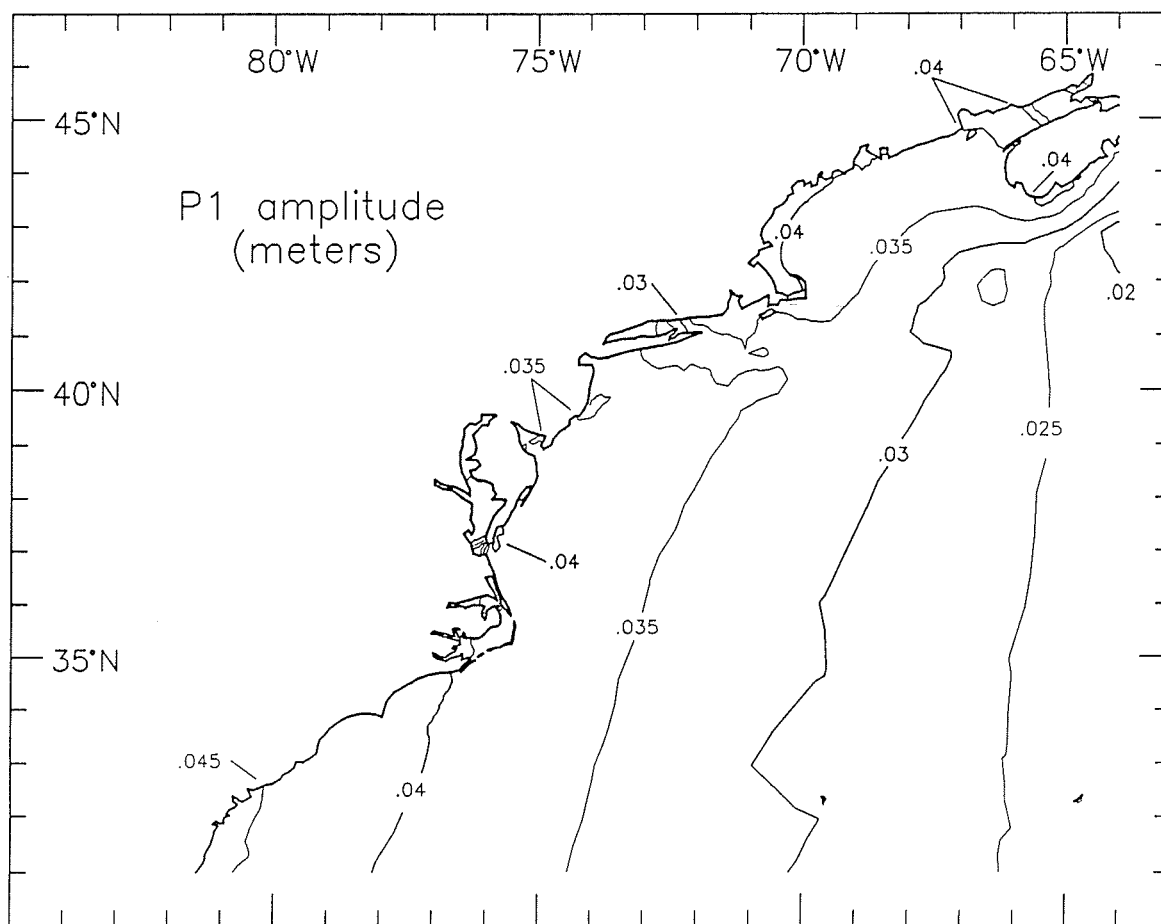
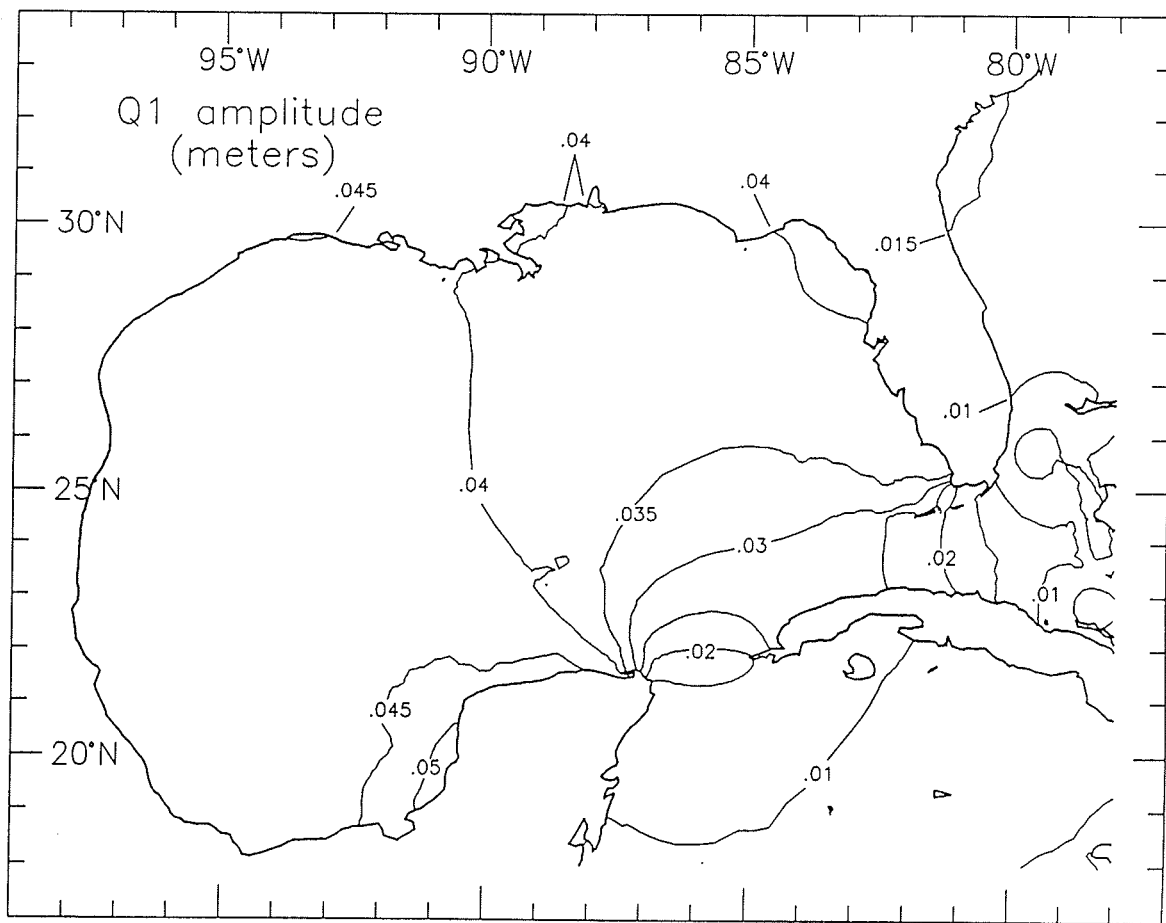Figure B1. (Sheet 5 of 8)
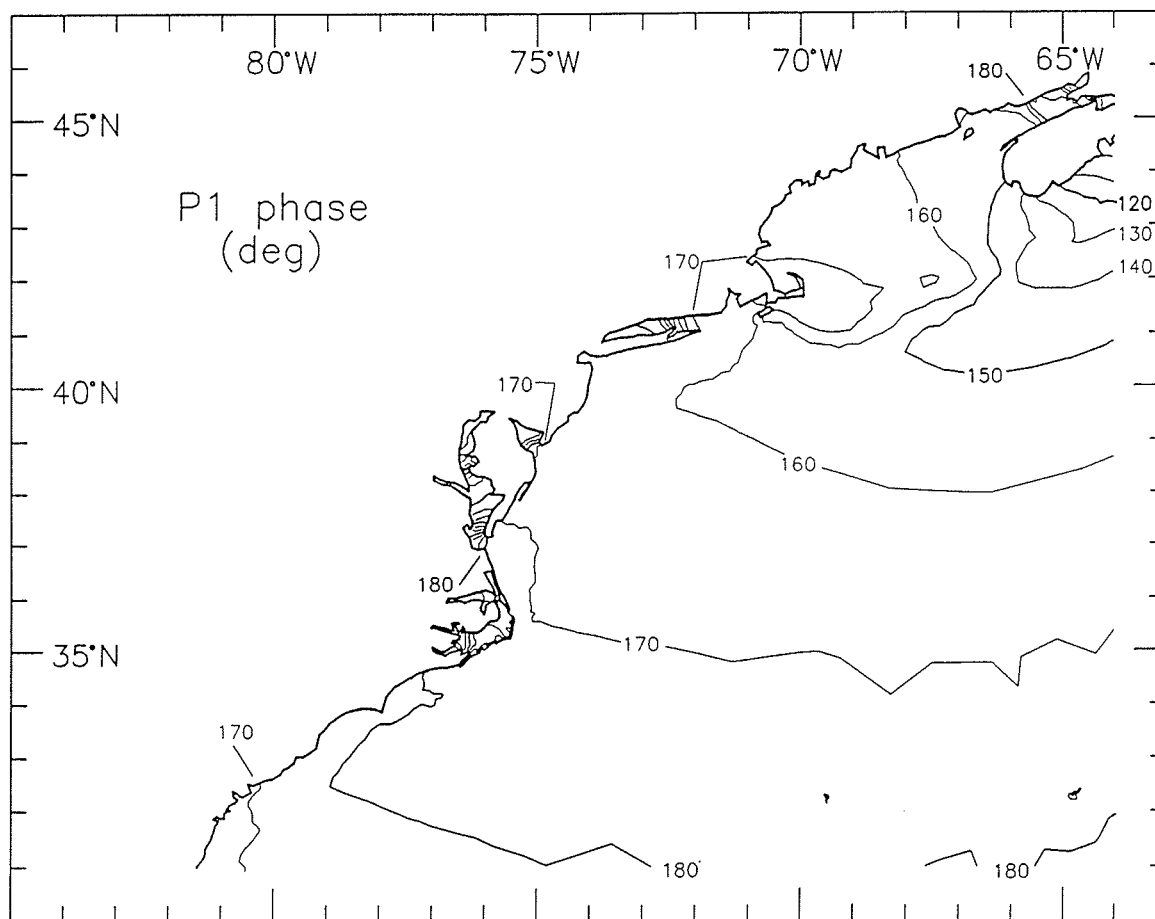
Figure B1. (Sheet 6 of 8)
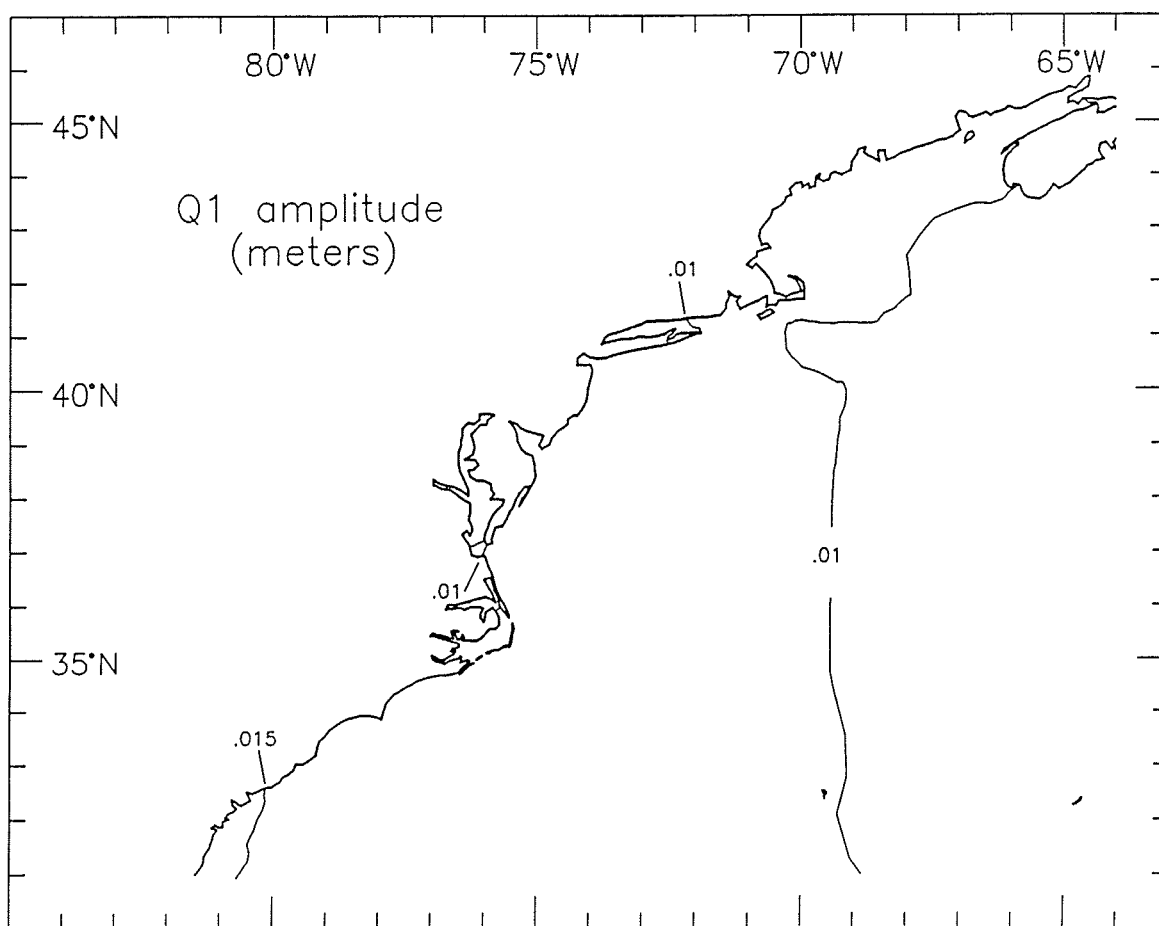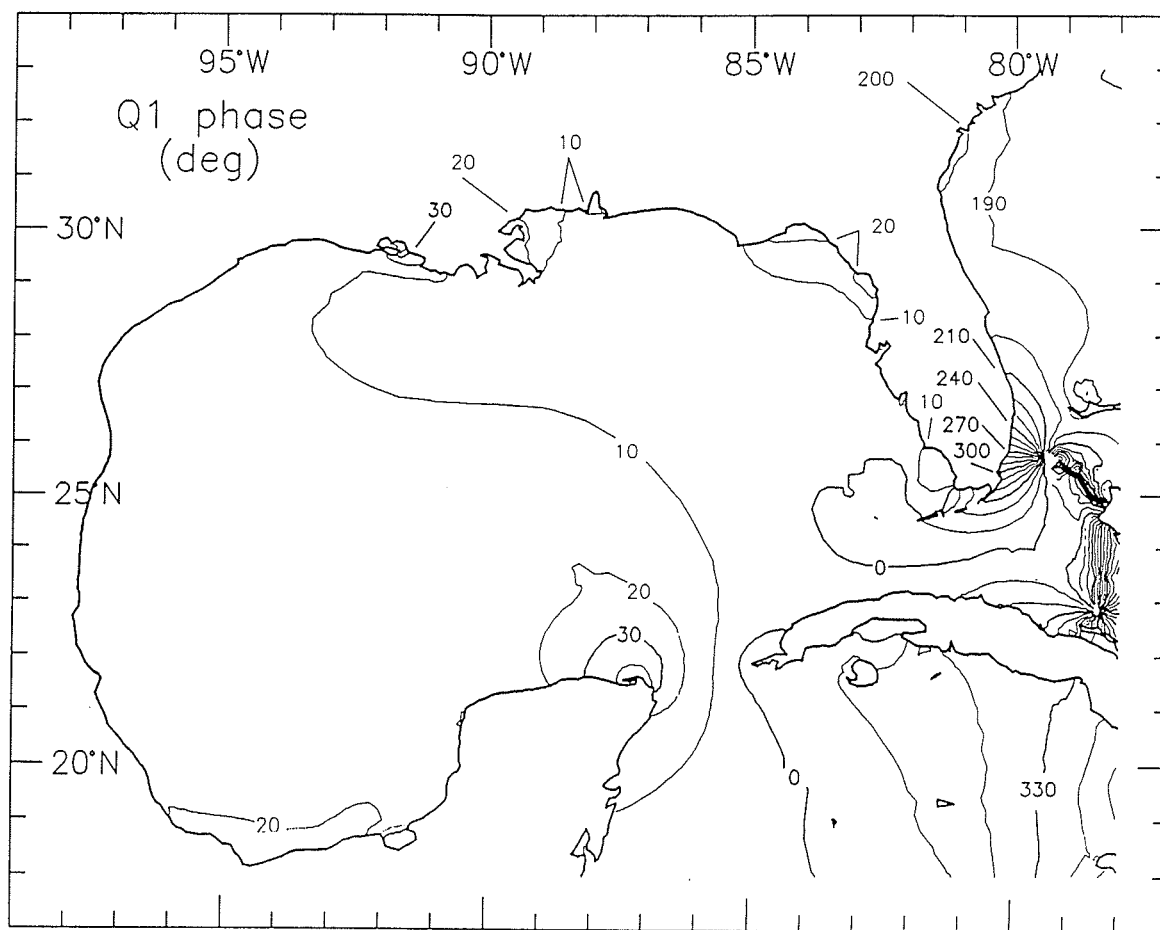
Figure B1. (Sheet 7 of 8)

Figure B1. (Sheet 8 of 8)

Figure B2. Computed contours for elevation amplitudes (in meters) and phases (in degrees relative to GMT) for the M_1, N_1, S_1, and K_1 semidiurnal astronomical tidal constituents for the U.S. east coast (Sheet 1 of 8)
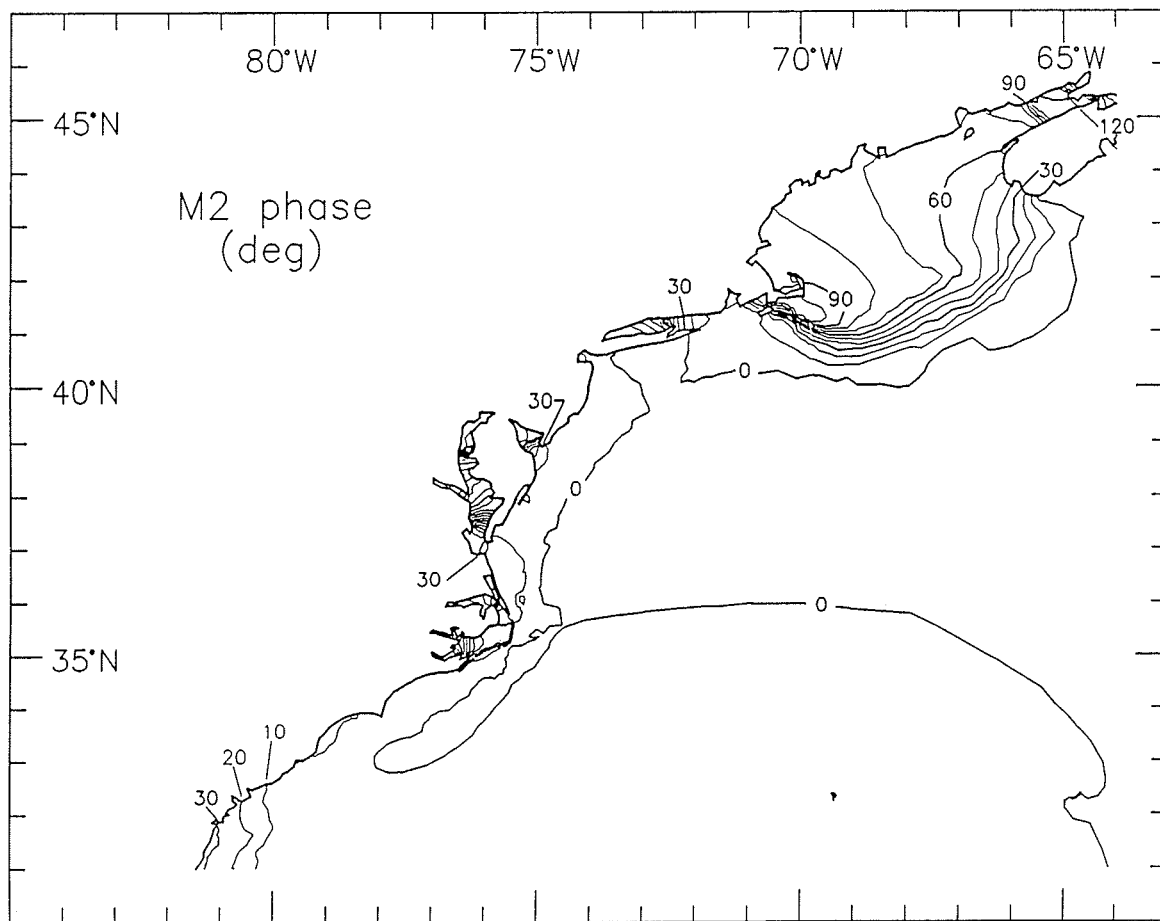
Figure B2. (Sheet 2 of 8)
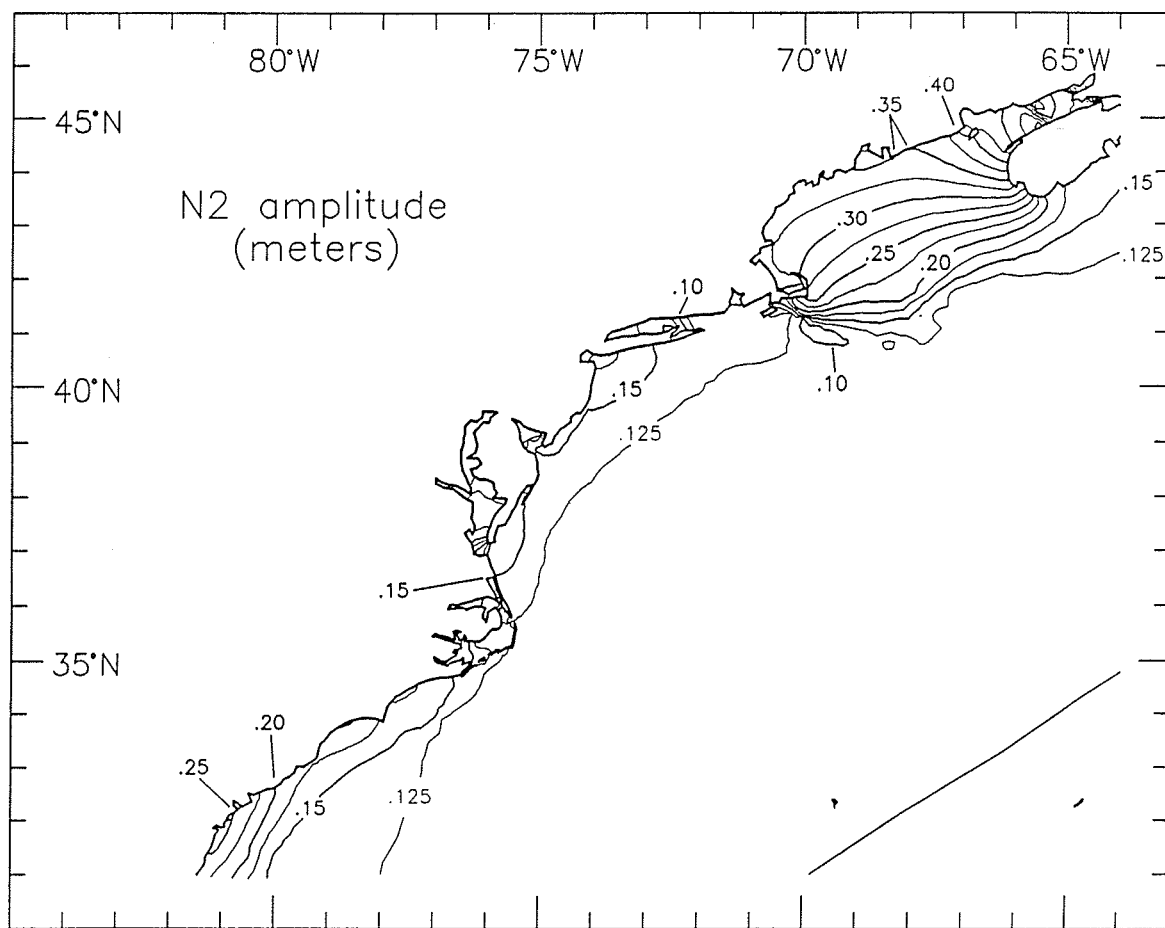
Figure B2. (Sheet 3 of 8)
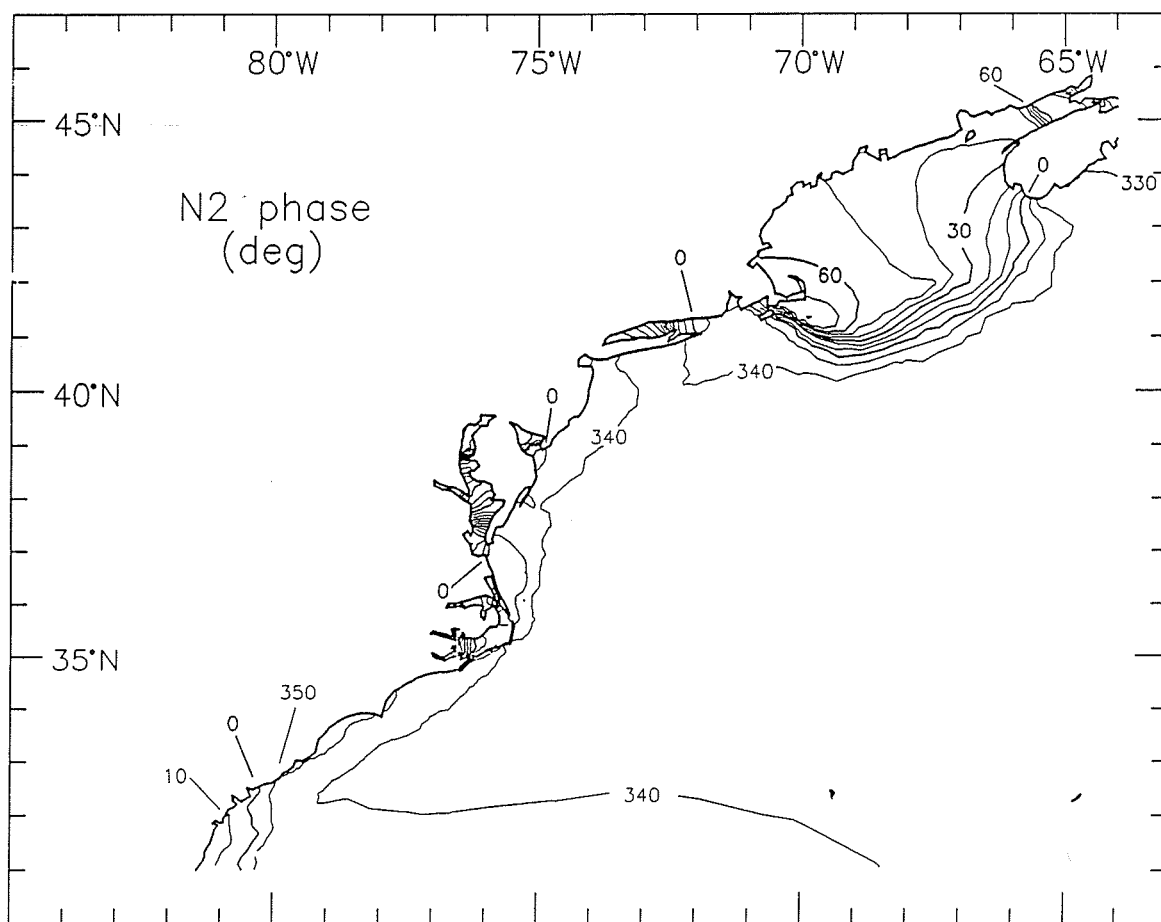
Figure B2. (Sheet 4 of 8)
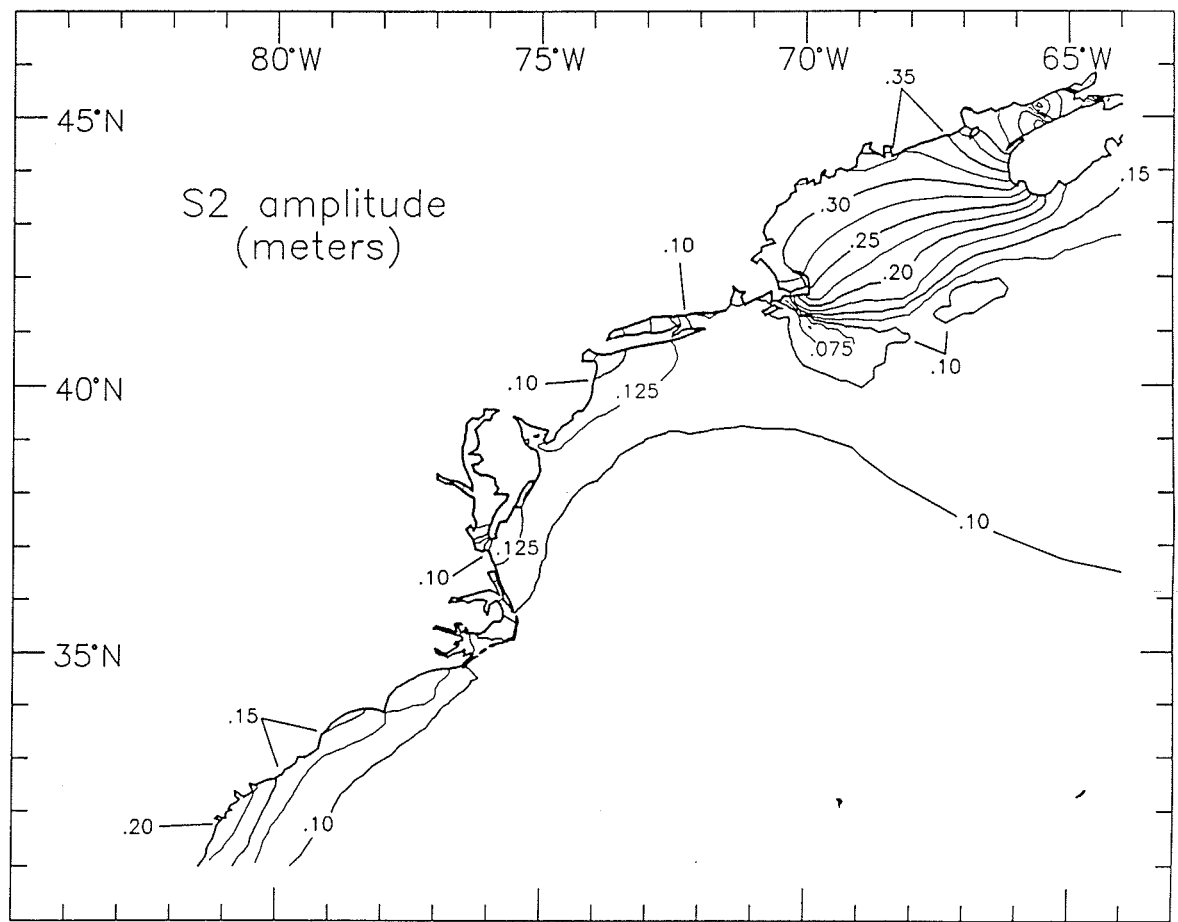
Figure B2. (Sheet 5 of 8)
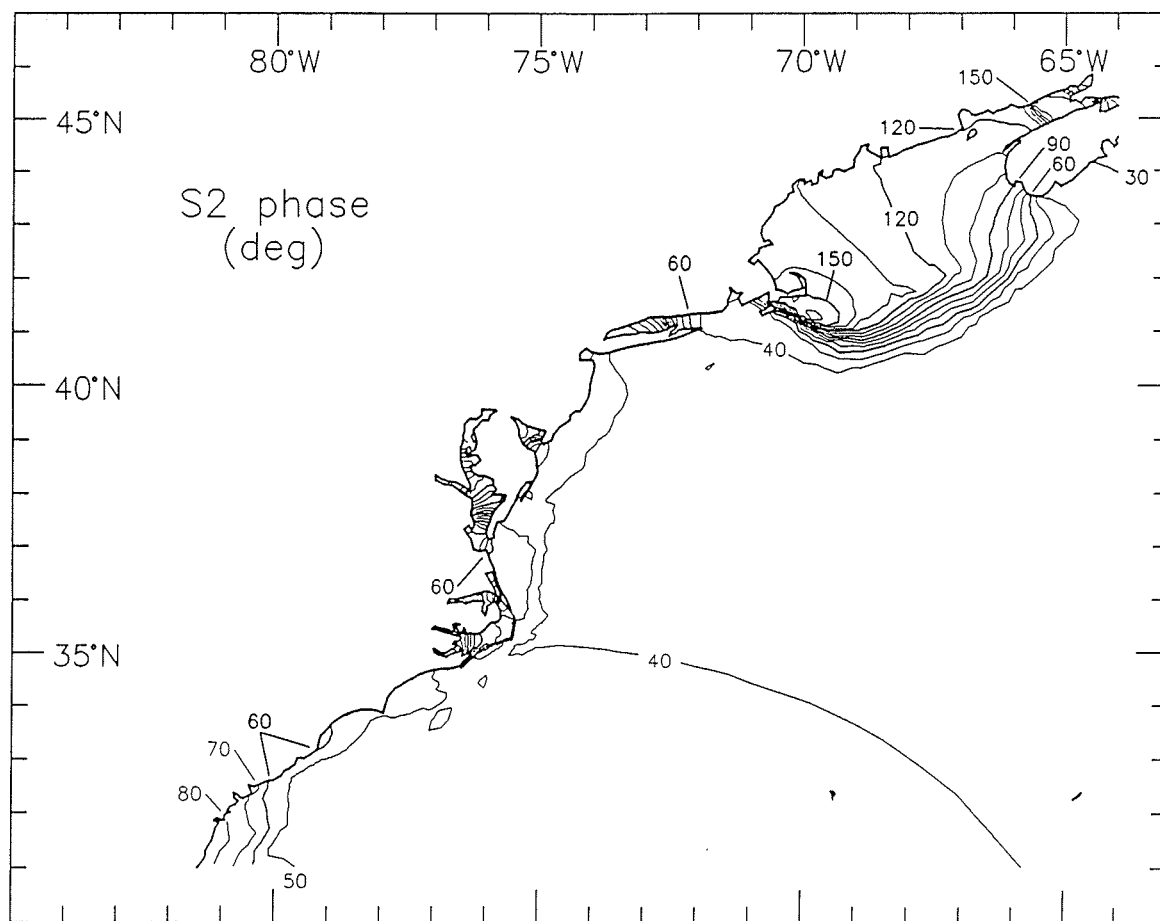
Figure B2. (Sheet 6 of 8)
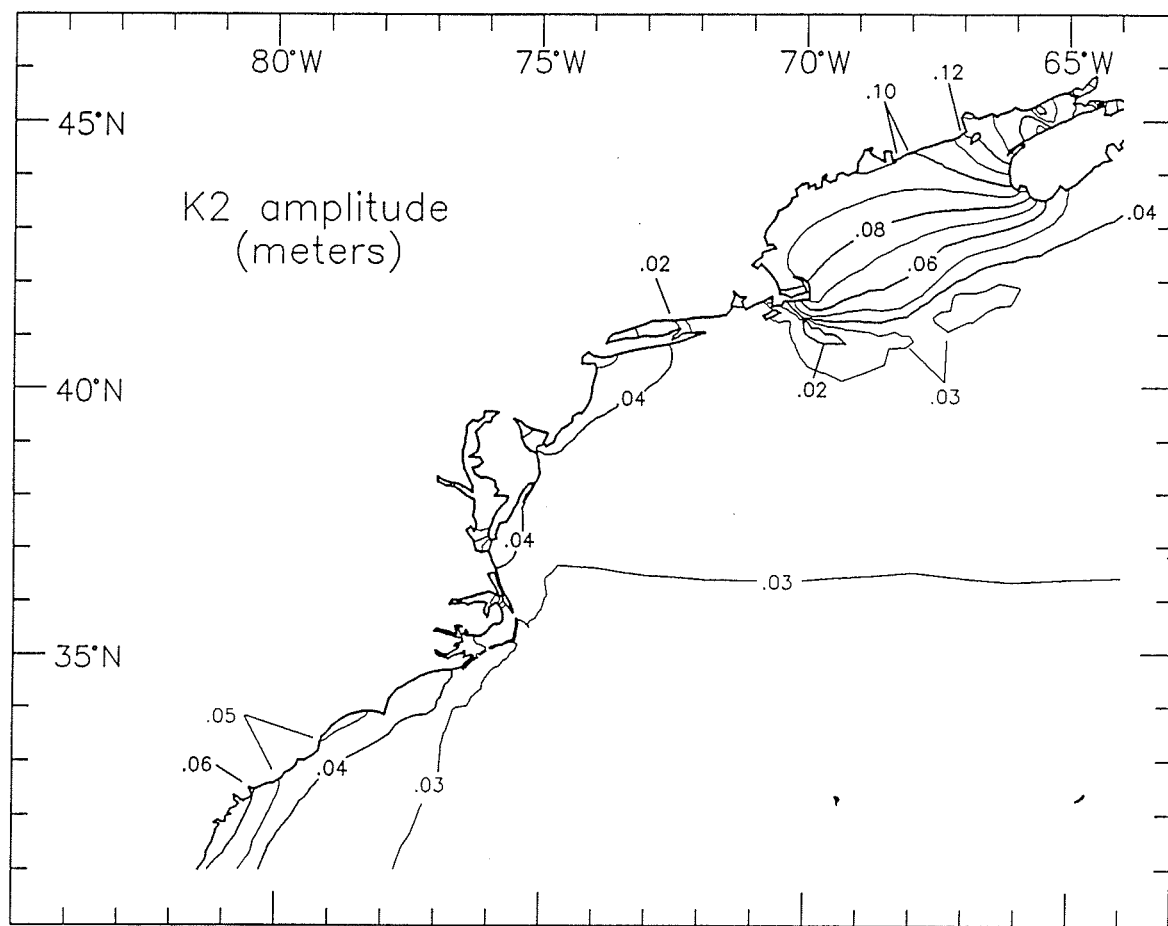
Figure B2. (Sheet 7 of 8)
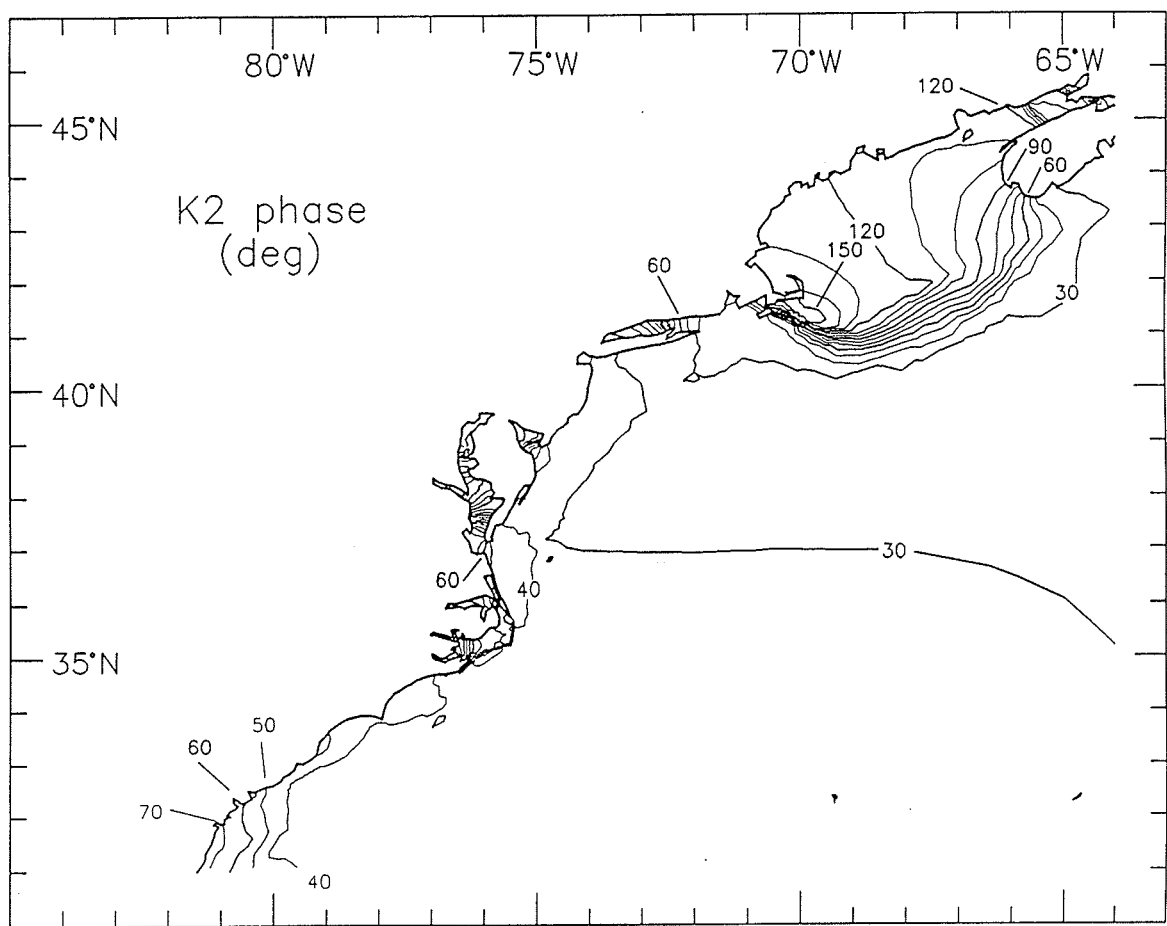
Figure B2. (Sheet 8 of 8)

Appendix C
Cotidal Charts
for the Gulf of Mexico

Figure C1. Computed contours for elevation amplitudes (in meters) and phases (in degrees relative to GMT) for the K_1, O_1, P_1, and Q_1 diurnal astronomical tidal constituents for the Gulf of Mexico (Sheet 1 of 8)

Figure C1. (Sheet 2 of 8)

Figure C1. (Sheet 3 of 8)

Figure C1. (Sheet 4 of 8)

Figure C1. (Sheet 5 of 8)

Figure C1. (Sheet 6 of 8)
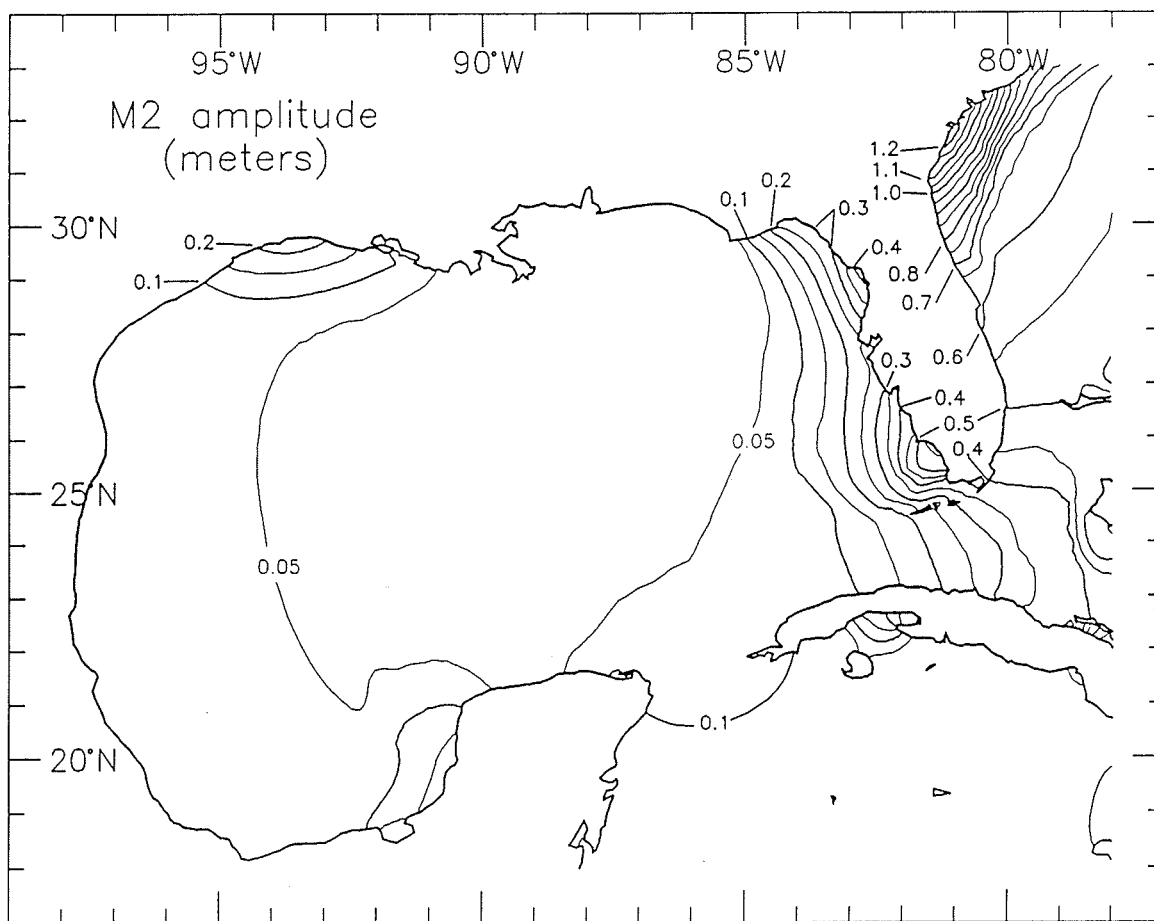
Figure C1. (Sheet 7 of 8)

Figure C1. (Sheet 8 of 8)

Figure C2. Computed contours for elevation amplitudes (in meters) and phases (in degrees relative to GMT) for the M_1, N_1, S_1, and K_1 semidiurnal astronomical tidal constituents for the Gulf of Mexico (Sheet 1 of 8)
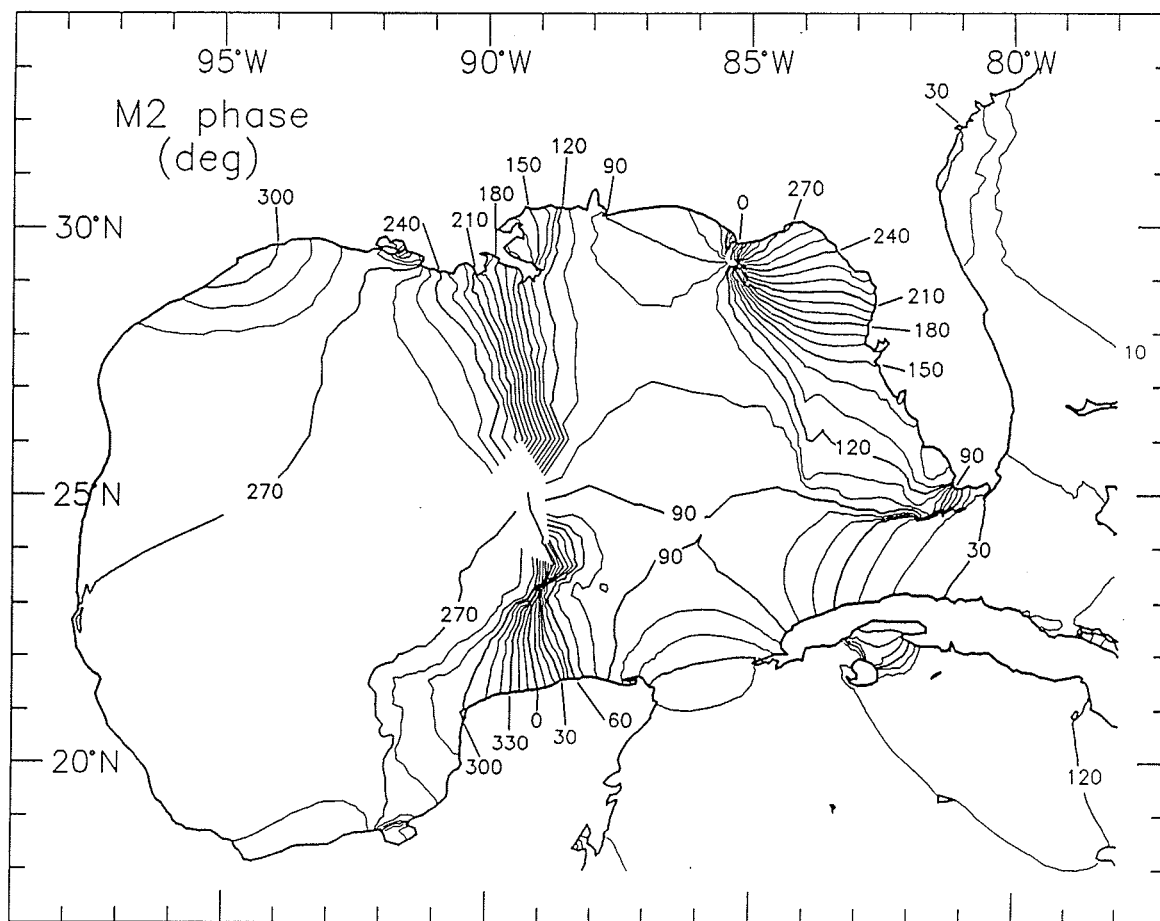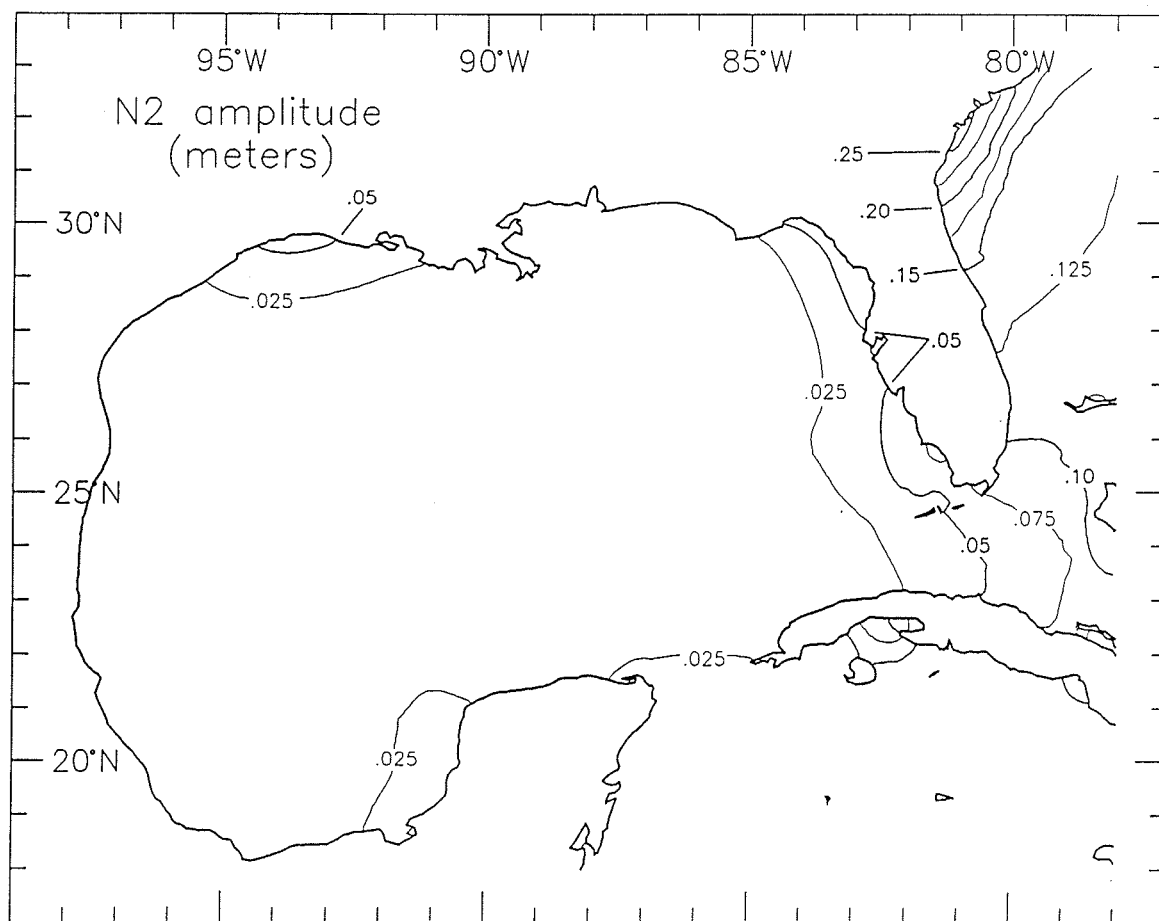
Figure C2. (Sheet 2 of 8)
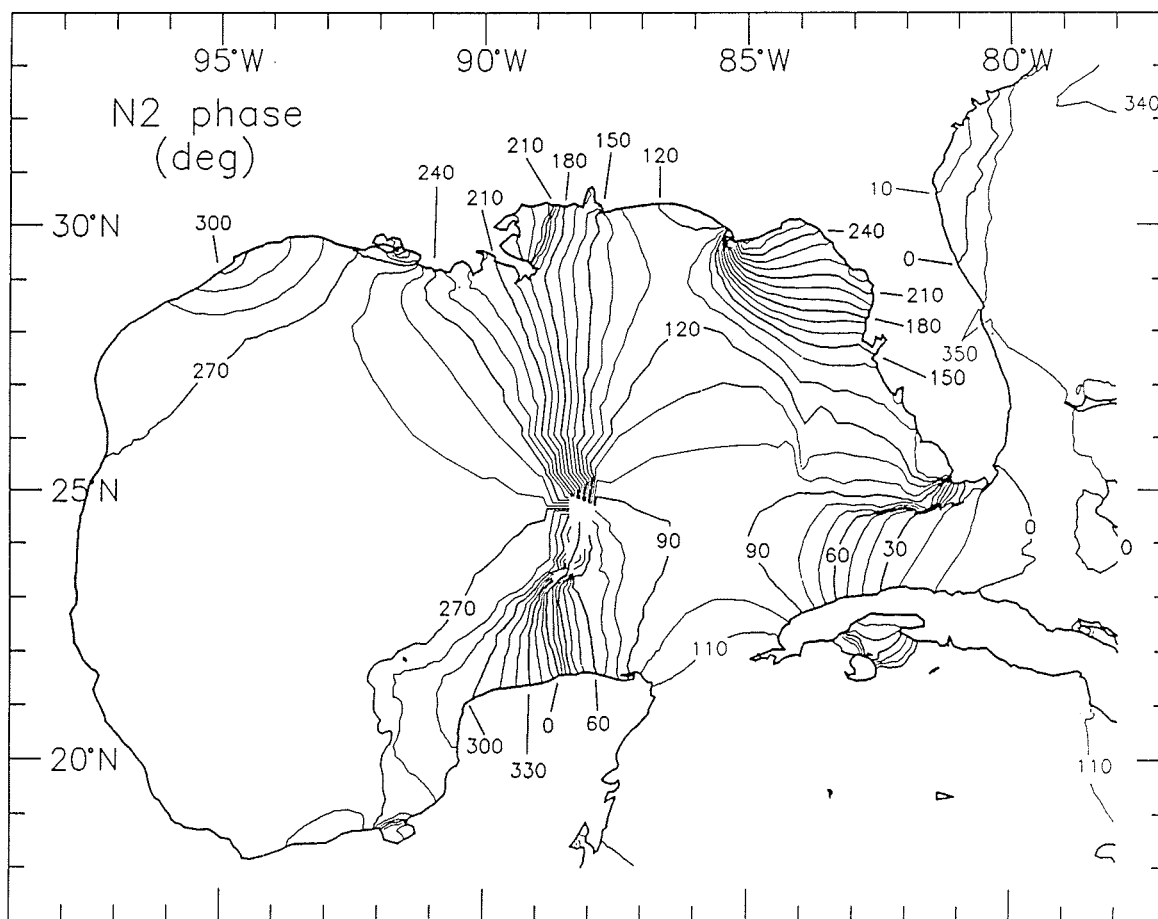
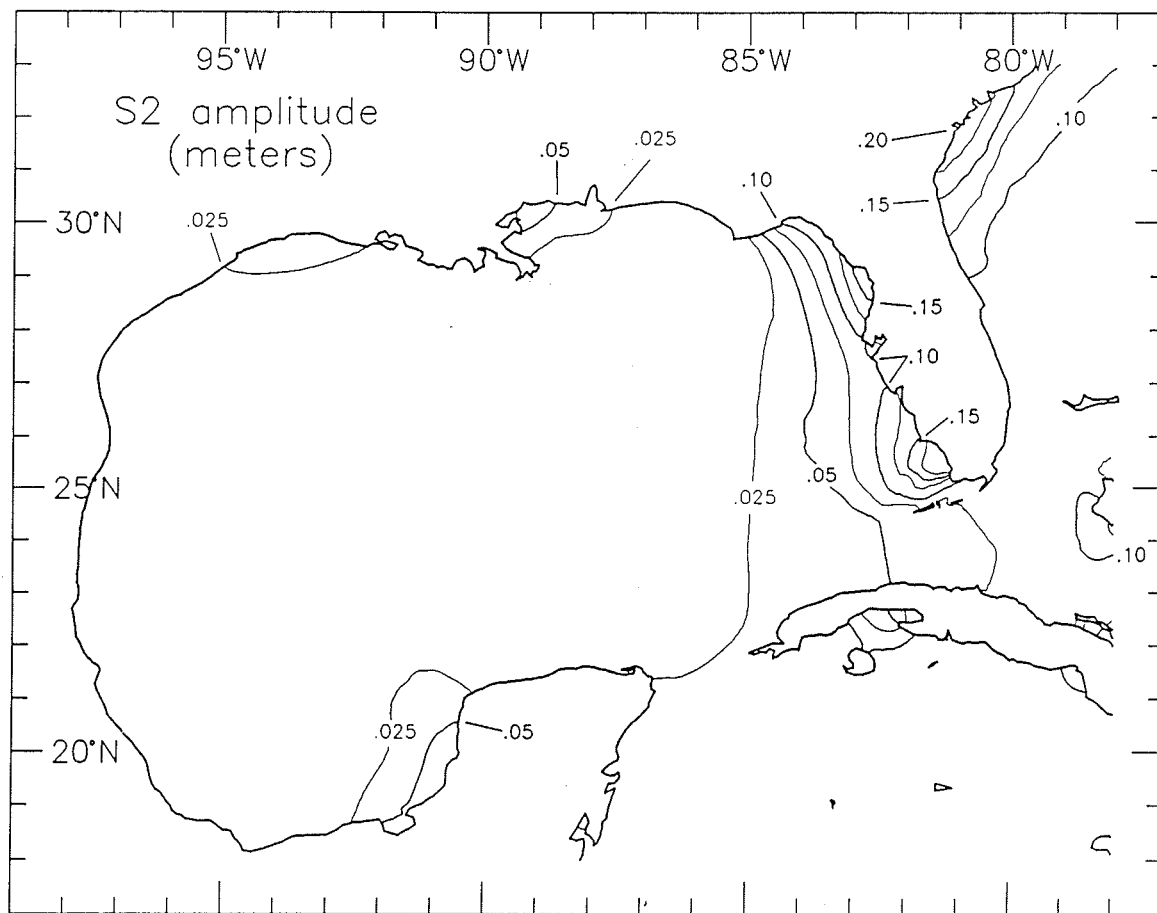Figure C2. (Sheet 3 of 8)

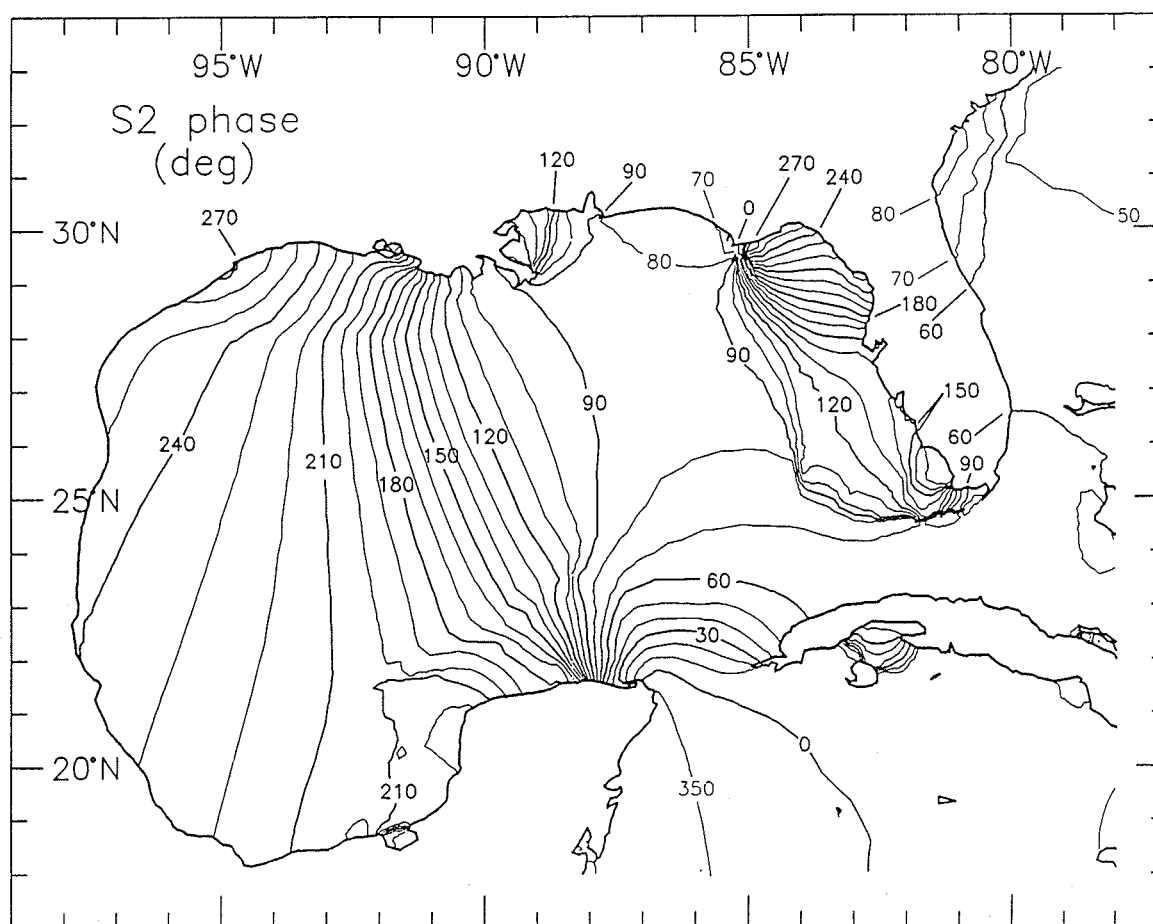Figure C2. (Sheet 4 of 8)

Figure C2. (Sheet 5 of 8)
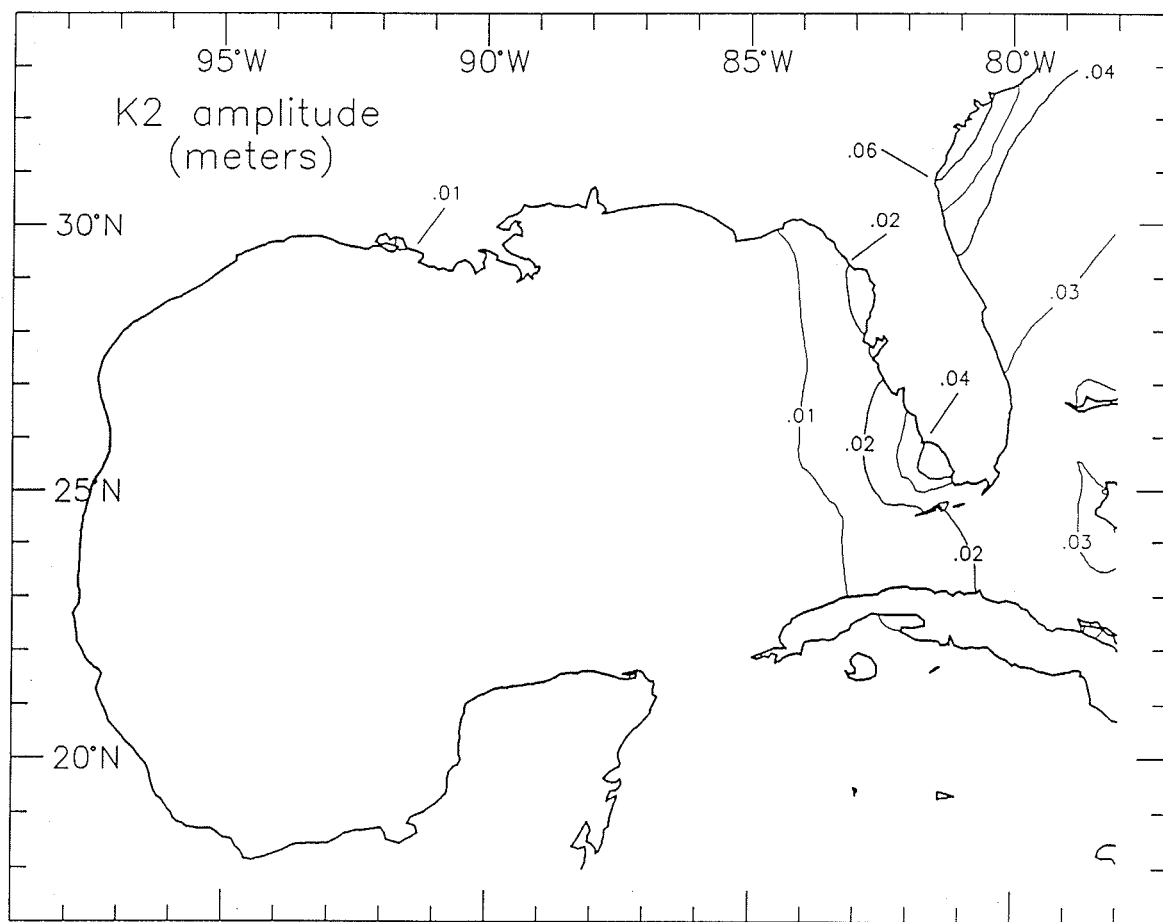
Figure C2. (Sheet 6 of 8)
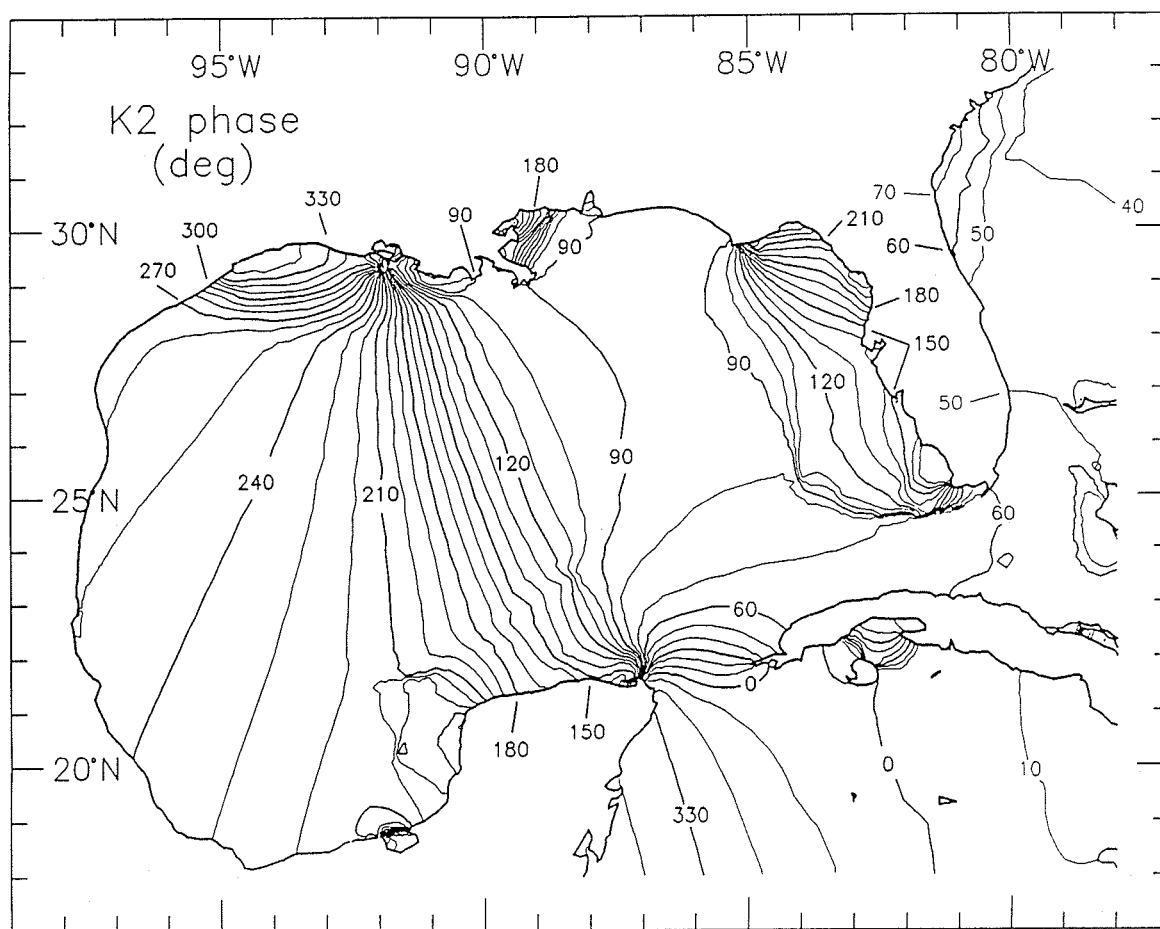
Figure C2. (Sheet 7 of 8)

Figure C2. (Sheet 8 of 8)

REPORT DOCUMENTATION PAGE

Public reporting burden for this collection of information is estimated to average 1 hour per response, including the time for reviewing instructions, searching existing data sources, gathering and maintaining the data needed, and completing and reviewing the collection of information. Send comments regarding this burden estimate or any other aspect of this collection of information, including suggestions for reducing this burden, to Washington Headquarters Services, Directorate for Information Operations and Reports, 1215 Jefferson Davis Highway, Suite 1204, Arlington, VA 22202-4302, and to the Office of Management and Budget, Paperwork Reduction Project (0704-0188), Washington, DC 20503.

1. AGENCY USE ONLY (Leave blank)	2. REPORT DATE June 1993	3. REPORT TYPE AND DATES COVERED Report 3 of a series

4. TITLE AND SUBTITLE
ADCIRC: An Advanced Three-Dimensional Circulation Model for Shelves, Coasts, and Estuaries; Report 3, Development of a Tidal Constituent Database for the Western North Atlantic and Gulf of Mexico

5. FUNDING NUMBERS
WU 32466

6. AUTHOR(S)

J. J. Westerink, R. A. Luettich, Norman W. Scheffner

7. PERFORMING ORGANIZATION NAME(S) AND ADDRESS(ES)

University of Notre Dame, Notre Dame, IN 46556;
University of North Carolina at Chapel Hill, Morehead City, NC 27514;
U.S. Army Engineer Waterways Experiment Station, Coastal Engineering Research Center, 3909 Halls Ferry Road, Vicksburg, MS 39180-6199

8. PERFORMING ORGANIZATION REPORT NUMBER

Technical Report DRP-92-6

9. SPONSORING / MONITORING AGENCY NAME(S) AND ADDRESS(ES)

US Army Corps of Engineers
Washington, DC 20314-1000

10. SPONSORING / MONITORING AGENCY REPORT NUMBER

11. SUPPLEMENTARY NOTES

Available from National Technical Information Service, 5285 Port Royal Road, Springfield, VA 22161

12a. DISTRIBUTION / AVAILABILITY STATEMENT

Approved for public release; distribution is unlimited

12b. DISTRIBUTION CODE

13. ABSTRACT (Maximum 200 words)

This report describes the application of model ADCIRC-2DDI, a two-dimensional, depth-integrated, finite-element-based hydrodynamic circulation code, to the western North Atlantic, Gulf of Mexico and Caribbean Sea in order to develop a tidal constituent database. Issues that are emphasized in the development of the Western North Atlantic Tidal (WNAT) model include the definition of hydrodynamically simple open ocean boundaries; the use of large domains; the importance of a high degree of grid resolution in coastal regions; and the use of finite element meshes with highly varying nodal densities in order to minimize the size of the discrete problem. The development of an optimal graded finite element mesh is based on regular and graded grid convergence studies using an M_2 tidal forcing function on the boundary and within the domain.

The optimal graded mesh is then forced for eight diurnal and semidiurnal astronomical tidal constituents (K_1, O_1, P_1, Q_1, M_2, S_2, N_2, and K_2) on the open ocean boundary by coupling to Schwiderski's (1979; 1981 a-g) global model results as well as within the interior domain using a tidal potential forcing function. The structure of the various tides is examined and results are compared to field data at 77 stations.

14. SUBJECT TERMS
See reverse.

15. NUMBER OF PAGES
154

16. PRICE CODE

17. SECURITY CLASSIFICATION OF REPORT UNCLASSIFIED	18. SECURITY CLASSIFICATION OF THIS PAGE UNCLASSIFIED	19. SECURITY CLASSIFICATION OF ABSTRACT	20. LIMITATION OF ABSTRACT

NSN 7540-01-280-5500

Standard Form 298 (Rev. 2-89)
Prescribed by ANSI Std. Z39-18
298-102

14. (Concluded).

Bottom stress
Circulation model
Direct stress solution

Finite element method
Hydrodynamic model
Numerical model

Three-dimensional model
Two-dimensional model